Model-Based Fault Detection and Isolation for a Novel X-by-Wire Road Vehicle Architecture

by

Lok Man Ho

Thesis

submitted in fulfilment

of the requirements for the Degree of

Doctor of Philosophy

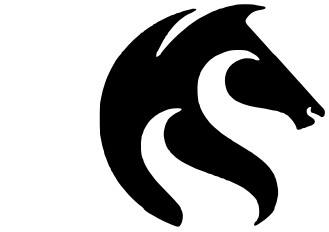

THE UNIVERSITY OF
NEWCASTLE
AUSTRALIA

School of Electrical Engineering and Computing

June, 2017

This research was conducted at and funded by

Deutsches Zentrum
für Luft- und Raumfahrt
German Aerospace Center

Declaration

Statement of Originality

This work contains no material which has been accepted for the award of any other degree or diploma in any university or other tertiary institution and, to the best of my knowledge and belief, contains no material previously published or written by another person, except where due reference has been made in the text. I give consent to the final version of my thesis being made available worldwide when deposited in the University's Digital Repository, subject to the provisions of the Copyright Act 1968.

Lok Man Ho
11th June 2017

Acknowledgements

First of all I would like to express my gratitude to my supervisors at the University of Newcastle. I thank my principle supervisor Prof. Kaushik Mahata for his guidance, encouragement and invaluable advice on the theoretical aspects of this thesis. I also thank my secondary supervisor Prof. Graham Goodwin for deciding to take me on as an external PhD student, and the motivating, open and frank discussions about PhD research during my visits to the bush campus.

I would like to thank the German Aerospace Center (DLR) for funding my PhD. I am grateful for my many colleagues at the DLR that I have learnt a great deal from and shared many memories with during my PhD journey. First and foremost I would like to thank Dr. Ricardo de Castro and Dr. Tilman Bünte, whom I could always rely on for insightful advice and feedback for topics ranging from vehicle dynamics and control theory through to scientific publishing. I thank Dr. Andras Varga for introducing me to the principles of model-based fault diagnosis with his workshop seminars, and Dr. Daniel Ossmann for our enjoyable and fruitful cooperation on this topic and for his thesis review. I am also grateful to my office roommate Dr. Alexander Schaub, whose passion for grammar and willingness for discussions helped improve the quality of my research and publications.

I was fortunate to have had a great team of colleagues to share the rewards and toils of the ROboMObil project, and I thank all the team members for making the experimental validations possible. My gratitude goes especially to the original core team of Jonathan Brembeck, Alexander Schaub and Clemens Satzger, with whom I shared many laughs and proud moments through the initial challenges of building and showcasing our test vehicle. I also extend my appreciation to my master thesis students Daniel Baumgartner and Tobias Lenz. Last but not least, I thank my institute director Dr. Johann Bals for his support of the ROboMObil project and my research.

I am grateful to have also had fruitful exchanges with colleagues outside the DLR. I thank the generous support and in-depth explanations on robust LPV estimator synthesis from Raghu Venkataraman of the University of Minnesota, and also Prof. Harald Pfifer for initiating this contact. I am very thankful for my friends and colleagues who generously

offered their time to review my thesis chapters with such short lead times. Those of you that I have not already mentioned above are: Dr. Richard Roberts, Dr. Neal Lii, Dr. Jakub Tobolář, and Michael Fleps-Dezasse.

Finally I would like to thank my family and friends for their patience, understanding, encouragement, and support throughout the duration of my PhD.

Lok Man Ho
The University of Newcastle
June 2017

Contents

Abstract

Faults in actuators and sensors of vehicle dynamics control systems can result in erroneous control, leading to degraded control performance or even loss of vehicle stability. While many faults in a vehicle dynamics system can be adequately diagnosed at a component level, treating the diagnosis problem using model-based methods on a global vehicle level can offer significant improvements in detectability and sensitivity for certain faults.

This thesis presents two model-based approaches for fault detection and isolation (FDI) design, each using a vehicle dynamics model which cover different operating regions of horizontal vehicle motion. The first approach is based on the linear parameter-varying (LPV) single track model (STM), which adequately models cruising operation with moderate lateral accelerations, low path curvature, and time-varying longitudinal velocity. The design method also accounts for parameter uncertainties arising from variabilities in the tyre cornering stiffness.

This application motivates the main theoretical contribution of this thesis, which is concerned with developing a generic FDI design approach for uncertain LPV systems. Methods are proposed to cover the components of the residual-based FDI with structured residuals, comprising the residual generator, single residual evaluation function, and residual pattern evaluation for fault isolation. The residual generator design method takes a reference model following approach, in which the fault-to-residual responses are optimised to follow a specified reference. The synthesis procedure exploits recent developments in robust LPV estimator synthesis that account for uncertainties by means of Integral Quadratic Constraints. To reduce the potential conservatism caused by fixed residual references, this work extends the common formulation by allowing magnitude parameters from the reference model to be optimised concurrently in the semi-definite programs of the synthesis.

For residual evaluation, the proposed norm-based evaluation function follows the same robust control paradigm, and a model-based procedure is proposed for the determination of evaluation and threshold parameters. Lastly, for residual structure design, an algorithm is presented to find the smallest set of feasible residuals that achieves the best possible fault isolation. These residual generation and evaluation methods are then applied to the uncertain LPV STM to design the FDI functions.

The second presented FDI design approach is based on a nonlinear kinematic model (NKM), which relates wheel speeds and steering angles to the horizontal motion of the vehicle body. The absence of linearisation makes this model valid over all motion directions, but only under the constraint that the tyre slips are negligible. In order to account for the influence of deviations from the model such as small tyre slips and measurement tolerances, this work presents a method to check the feasibility of sets of measurements

with respect to the NKM, under the assumption that the deviations are bounded. Functions are also provided to recognise and exclude operating states when low tyre slip is improbable. Fault isolation is achieved by means of structured residuals.

After analysing the fault diagnosis requirements of the German Aerospace Center's (DLR's) ROboMObil, a highly actuated and manoeuvrable X-by-Wire test platform, the two model-based FDI approaches are implemented for this application. Their effectiveness is demonstrated using simulations and experimental data.

Publications

The following lists the author's contributions to the literature in the areas of this thesis during the research timeframe.

Conference Papers

Ho, Lok Man. "Application of Adaptive Thresholds in Robust Fault Detection of an Electro-Mechanical Single-Wheel Steering Actuator". In: *IFAC Symposium on Fault Detection, Supervision and Safety of Technical Processes*. 2012.

Ho, Lok Man. "Structural Analysis of a Vehicle Dynamics Model for Fault Detection and Isolation on the RObоMObil". In: *International Conference on Control and Fault-Tolerant Systems (SysTol)*. IEEE, 2013.

Ho, Lok Man and Ossmann, Daniel. "Fault Detection and Isolation of Vehicle Dynamics Sensors and Actuators for an Overactuated X-by-Wire Vehicle". In: *IEEE Conference on Decision and Control*. 2014.

Ho, Lok Man. "H-infinity Structured Residual Generator Synthesis Using Residual Reference Models with Application to Lateral Vehicle Dynamics". In: *European Control Conference*. 2016.

Ho, Lok Man and Bünte, Tilman. "Sensor Fault Detection and Isolation using a Non-linear Planar Kinematic Model of Vehicle Dynamics". In: *IEEE Multi-Conference on Systems and Control*. 2016.

Brembeck, J, Ho, L M, Schaub, A, Satzger, C, Tobolar, J, Bals, J and Hirzinger, G. "ROMO - The robotic electric vehicle". In: *IAVSD International Symposium on Dynamics of Vehicle on Roads and Tracks*. 2011.

Bünte, Tilman, Brembeck, Jonathan and Ho, Lok Man. "Human machine interface concept for interactive motion control of a highly maneuverable robotic vehicle". In: *IEEE Intelligent Vehicles Symposium*. 2011.

Peer-Reviewed Articles

Bünte, Tilman, Ho, Lok Man, Satzger, Clemens and Brembeck, Jonathan. "Central Vehicle Dynamics Control of the Robotic Research Platform ROboMObil". In: *ATZ Elektronik* 9.3 (2014), pp. 58–64.

Under Review

Ho, Lok Man. "Robust Residual Generator Synthesis for Uncertain LPV Systems Applied to Lateral Vehicle Dynamics". In: *submitted to IEEE Transactions on Control Systems Technology* (2017).

List of Abbreviations

Abbreviation	Description
ABS	Anti-lock braking system
BRL	Bounded real lemma
CoG	Centre of gravity
CAN	Control area network
DB(-A)(-VD)	Disc brake (-actuator) (-vehicle dynamics)
DLR	Deutsches Zentrum für Luft- und Raumfahrt (German Aerospace Center)
DOB	Disturbance observer
DOF	Degree of freedom
DTM	Double track model
EMA	Electromechanic actuator
ESP	Electronic stability program
FAR	False alarm rate
FDI	Fault detection and isolation
FMEA	Failure modes and effects analysis
FPRG	Fundamental problem of residual generation
FTC	Fault tolerant control
GDC	Generalised diagnostic component
GPS	Global positioning system
I/O	input / output
ICR	Instantaneous centre of rotation
IMU	Inertial measurement unit
INS	Inertial navigation system
IQC	Integral quadratic constraint
LFR	Linear fractional representation
LFT	Linear fractional transformation
LMI	Linear matrix inequality
LP	Linear programming problem
LPV	Linear parameter-varying
LTI	Linear time-invariant
LV	Low voltage
MDR	Missed detection rate
MISO	Multiple input single output
MOPS	Multi-objective parameter search
MSO	Minimally structurally overdetermined

Abbreviation	Description
NKM	Nonlinear kinematic model
NKMFDI	FDI approach based on the NKM
NSKC	No-slip kinematically consistent
NTSA	Negligible tyre slip assumption
OS	Optical sensor
PMSM	Permant magnet synchronous machine
RMS	Root mean square
S(-A)(-VD)	Steering (-actuator) (-vehicle dynamics)
SDP	Semi-definite program
SISO	Single input single output
STM	Single Track Model
STMFDI	FDI approach based on the STM
TMD(-A)(-VD)	Traction motor drive (-actuator) (-vehicle dynamics)
VLA	Vehicle-level application

List of Frequently Used Symbols

Symbol	Description
a	Scalar
$\bar{a}$	Complex conjugate of a
$\boldsymbol{a}$	Vector
$\boldsymbol{A}$	Matrix
$\boldsymbol{A}^T$	Transpose of $\boldsymbol{A}$
$\boldsymbol{A}^*$	Complex conjugate transpose of $\boldsymbol{A}$
$\star$	Symmetric matrix block
$\boldsymbol{I}_n$	Identity matrix of size $n \times n$
$\boldsymbol{0}$	Zero matrix
$\mathbb{R}$	Set of real numbers
$\mathbb{C}$	Set of complex numbers
$\mathbb{R}^n$	Set of $n \times 1$ real vectors
$\mathbb{R}^{m \times n}$	Set of $m \times n$ real matrices
$\mathbb{S}^n$	Set of $n \times n$ symmetric real matrices
$\mathcal{L}_2^l$	Set of $[0, \infty) \to \mathbb{R}^l$ Lebesgue integrable vector functions
$\mathcal{L}_{2e}^l$	Extended $\mathcal{L}_2^l$ space
$\mathrm{diag}(\cdot)$	Block diagonal concatenation of its arguments
$\mathrm{sgn}(\cdot)$	Sign of its argument
$\mathrm{Re}(\cdot)$	Real part of its argument
$\mathrm{Im}(\cdot)$	Imaginary part of its argument
$\lvert \cdot \rvert$	Absolute value
$\lVert \cdot \rVert$	Norm
$\lVert \cdot \rVert_2$	Vector or signal 2-norm
$\lVert \cdot \rVert_{i2}$	Induced-$\mathcal{L}_2$ system norm

List of Tables

List of Figures

List of Procedures

Chapter 1

Introduction

1.1 Motivation

The automation of automobile functions has seen steady growth in the past decades, and this is set to intensify in the future with the expansion of driver assistance functionalities and proliferation of autonomous driving vehicles. The automated functions range from the compartmentalised traction control (TCS) and anti-lock brake (ABS) systems, through to more integrated functions such as electronic stability systems (ESP) and adaptive cruise control (ACC), stretching further to more recent highway driving assistance, parking assistance and fully automated driving functions [Ben14; GL15]. While these developments are placing ever increasing demands on environment perception and sensor fusion algorithms, as well as the computational resources on which they run, they also demand an increased level of control authority over the dynamics of the vehicle via by-Wire powertrain and chassis actuators. Combined with developments to improve convenience of city vehicles through manoeuvrability enhancements that exploit an increase in steered and propelled wheels, this brings the industry into a period of renewed challenges for the design of X-by-Wire chassis systems.

The ability of an X-by-Wire chassis system to guide and stabilise the vehicle on its desired trajectory depends critically on the integrity of the actuators and sensors employed in the control loops. Despite improvements to the reliability of automotive actuators and sensors, the appearance of faults during operation cannot be ruled out. Faulty actuators and sensors compromise the authority of the controller, degrade the achievable performance and potentially trigger instabilities. In an age of strict requirements on comfort, safety and efficiency, it is crucial to diagnose the relevant faults before their effects on the vehicle become critical. This enables effective mitigation through adaptation and reconfiguration of hardware and controllers. This demand for timeliness and fault sensitivity poses a challenge for the fault diagnosis task.

Concurrently, automotive control architectures are shifting from distributed towards centralised designs [Buc12]. Such architectures have long been the standard in many industries, such as aerospace [RTC05] and robotics [SK16]. Vehicle functions in traditionally

separate areas are now treated as interdependent functions, including powertrain, braking, steering, driver interfaces and sensing. This shift is driven by the quest to deliver optimal control performance and cross-disciplinary driver assistance and automation functionalities, and simultaneously reduce costs by sharing sensing and controller resources between functions.

The architectural shift presents an opportunity to exploit the benefits of centralised fault diagnosis. Illustrative examples of distributed and centralised diagnostic architectures are depicted in Figure 1.1. A centralised or global diagnostic module exploits the possibility of accessing information across functional divisions to draw conclusions about the fault state and availability of the vehicle. The larger pool of available measurements allows effective use of analytical redundancy for consistency checks, which can reveal fault information without directly measuring the phenomenon. A well-known example of this is the use of ABS wheel speed sensors to indirectly monitor tyre pressure issues [IWI09]. Such approaches are classified as model-based fault diagnosis, as knowledge of the fault-free (and possibly faulty) system behaviour is used in carrying out the diagnosis.

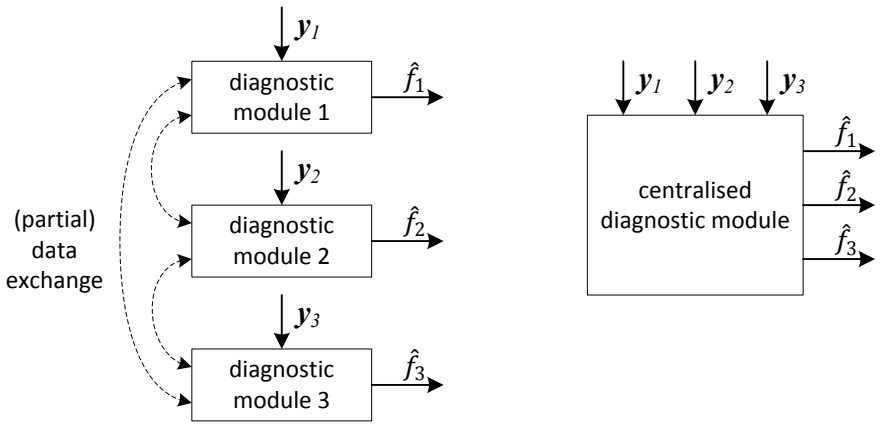

Figure 1.1: Types of diagnostic architectures, left: distributed, right: centralised. $\boldsymbol{y}_*$ denotes a set of available measurement, and $\hat{f}_*$ a diagnostic output.

Having already operated with digital Fly-by-Wire controls and centralised flight computers for some decades, advances in aerospace applications represent valuable knowledge in dealing with such architectures and offer opportunities for technological transfers. More specifically, the aerospace research community has been actively exploiting the potentials of model-based diagnosis for tackling challenges in Fly-by-Wire flight control systems. In recent EU projects ADDSAFE [GM11] and RECONFIGURE [Gou15], it has been demonstrated that model-based diagnosis using analytical redundancy complements established model-free, hardware redundancy based methods by providing higher sensitivity and broadening the spectrum of diagnosable faults.

In automotive applications, promising investigations have been made into model-based diagnosis for chassis control systems, including ESP, brake-by-wire and steer-by-wire. The extension to integrated chassis control systems on highly actuated X-by-Wire architectures is a logical step. A wide variety of configurations exist for the actuation, sensing and

control of such architectures, each suitable for certain vehicle classes, levels of automation and types of propulsion technologies. To handle this broad spectrum, it would be highly desirable to have flexible methodologies and tools to assist designers with tackling the diagnosis design task systematically.

1.2 Goals of the Thesis

The application-oriented goal of this thesis is to propose systematic design methods for model-based fault diagnosis of horizontal vehicle dynamics control systems, that are capable of handling highly actuated X-by-Wire architectures. The designed functions should complement the diagnostic modules on subsystem levels and the model-free diagnostics in the central controller, in order to broaden the diagnostic coverage. Furthermore, they should also cope with the common range of motion possibilities during the operation of such road vehicles, which are captured by the regimes of medium-to-high speed cruising as well as low speed manoeuvring that permits tight path curvatures.

For medium to high speed cruising operation, the design of fault diagnosis is based on the force-based lateral dynamics behaviour represented by the linearised single track model (STM). To account for a vehicle's time-varying speed during its typical operation, the STM is scheduled by this parameter and therefore becomes a linear parameter-varying (LPV) system. Furthermore, the model requires knowledge of the *cornering stiffness* parameters, which is dependent on the uncertain tyre-road contact characteristics. The chosen design method makes use of developments in robust estimator synthesis for uncertain LPV systems, which can be solved by efficient numerical routines that pose it as a semi-definite program. The robust estimator synthesis procedures are adapted to cope with the additional degrees of freedom present in the residual generation problem compared to a standard estimator synthesis problem. Since the presented method is applicable to generic LPV systems regardless of their structure, it can be readily applied to different actuation and sensing architectures for X-by-Wire vehicles. The performances of the residual generators are assessed by applying them to data from nonlinear simulations of vehicle manoeuvres and experimental test drives.

At low speeds, a road vehicle can engage in parking type manoeuvres with high path curvatures and body side-slip angles. These motion parameters can become even more severe for vehicles equipped with high angle range four wheel steering. Such motion falls outside the validity region of the linearised STM, which is linearised about the straight-ahead driving condition. To handle the challenge of low speed manoeuvring over the entire possible motion range, a method is proposed for diagnosing sensor faults based on the nonlinear kinematic model (NKM). Again the robustness to model and measurement uncertainty is handled explicitly — on this occasion the tolerances for small tyre slips and permissible sensor measurement deviations during fault-free operation are propagated to permissible bounds on the residuals.

In order to demonstrate and validate the proposed methods, they are applied to fault diagnosis design for the "ROboMObil", a test vehicle of the German Aerospace Center's (DLR's) Robotic and Mechatronics Center. This is a test platform not only for highly redundant X-by-Wire vehicle dynamics systems and their control, but also for electric propulsion, autonomous driving and driver interaction concepts [Bre11] (see Figure 1.2). The methods are then validated using simulations and experimental test drive data.

The main contributions of this thesis are listed at the end of Chapter 2, after an overview of fault diagnosis and relevant literature has been provided.

Figure 1.2: The DLR's ROboMObil undergoing vehicle dynamics testing

1.3 Thesis Outline

Following this introduction and a background overview chapter, the remainder of the thesis is organised into two parts. The first is concerned with robust fault detection and isolation (FDI) design for linear parameter-varying (LPV) systems. Together, the contained chapters address the stages of residual generation, residual evaluation, and residual structure design. The second part presents the development and validation of a fault diagnosis system for an X-by-Wire test vehicle, using a combination of methods including those proposed in Part I. Here are the chapter contents in more detail:

Chapter 2 provides a background overview of fault diagnosis, including important definitions. Approaches for the sequential stages of the design and implementation of model-based fault detection and isolation are reviewed. The chapter closes with a brief look at the use of these approaches in the application area of automotive vehicle dynamics, before the main contributions of this thesis are listed.

In Part I, Chapter 3 introduces the basic theory required for robust estimator synthesis for uncertain LPV systems. The thoeretical background is formulated into procedures that are used in residual generators synthesis in Chapter 4.

Chapter 4 presents a residual generator design method for uncertain LPV systems, by reformulating its requirements into that of an estimator and thereby recasting it as a

robust estimator synthesis. The chapter integrates an additional degree of freedom into the model-reference tracking representation of the fault sensitivity constraint, which reduces conservatism and is one of the key theoretical contributions of this thesis.

Chapter 5 examines the two stages of processing residuals using the structured residuals approach to achieve fault detection and isolation. The first part concerns the selection and parametrisation of the residual evaluation and threshold functions. The presented approach exploits analytical system properties to compute a dynamic threshold for the evaluated residual. The second part addresses the issues related to the design of residual signature structures for fault isolation. I show how, by exploiting the information about the robustness of each residual in the signature structure design process, the designer can systematically handle the necessary trade-offs.

In Part II, Chapter 6 outlines the application problem which motivates this thesis, namely that of FDI design for the vehicle dynamics system of the ROboMObil. Relevant details of the ROboMObil are described, including its control architecture and layout of the diagnostic software module. The model-based vehicle dynamics FDI problem to be tackled in the following chapters is specified in the final section.

Chapter 7 is concerned with mathematical modelling of the relevant systems. The described models either play a role in the development and design process, or in the test and validation stage as a simulation model. Besides various descriptions of vehicle dynamics, models for actuators, sensors, disturbances and faults are also discussed and presented. Furthermore, identification of the cornering stiffness parameters of the single-track model from experimental data is also covered.

Chapter 8 describes the application of the robust fault detector design approach presented in Part-I to the STM describing the ROboMObil's vehicle dynamics system. Besides residual generator and evaluation function design and parametrisation, it is demonstrated how structured residuals can be used to isolate faults on this highly actuated vehicle, albeit with some limitations.

Chapter 9 presents a FDI method for vehicle dynamics suitable for low speed manoeuvring, using the NKM as the basis. The resulting static parity relations are augmented with dynamic thresholds determined by propagating modelling and measurement errors to the residual. Also presented are some relevant metrics that indicates the validity of the NKM given a set of vehicle states, as well as auxiliary results on vehicle motion estimation based on this model. The chapter closes with a discussion on the consolidation of diagnostic results from STM-based and NKM-based diagnosis.

Finally, Chapter 10 presents a discussion of the outcomes of the thesis and recommendations of future research directions.

The structure of this thesis is depicted in Figure 1.3, which illustrates the dependencies between the chapters.

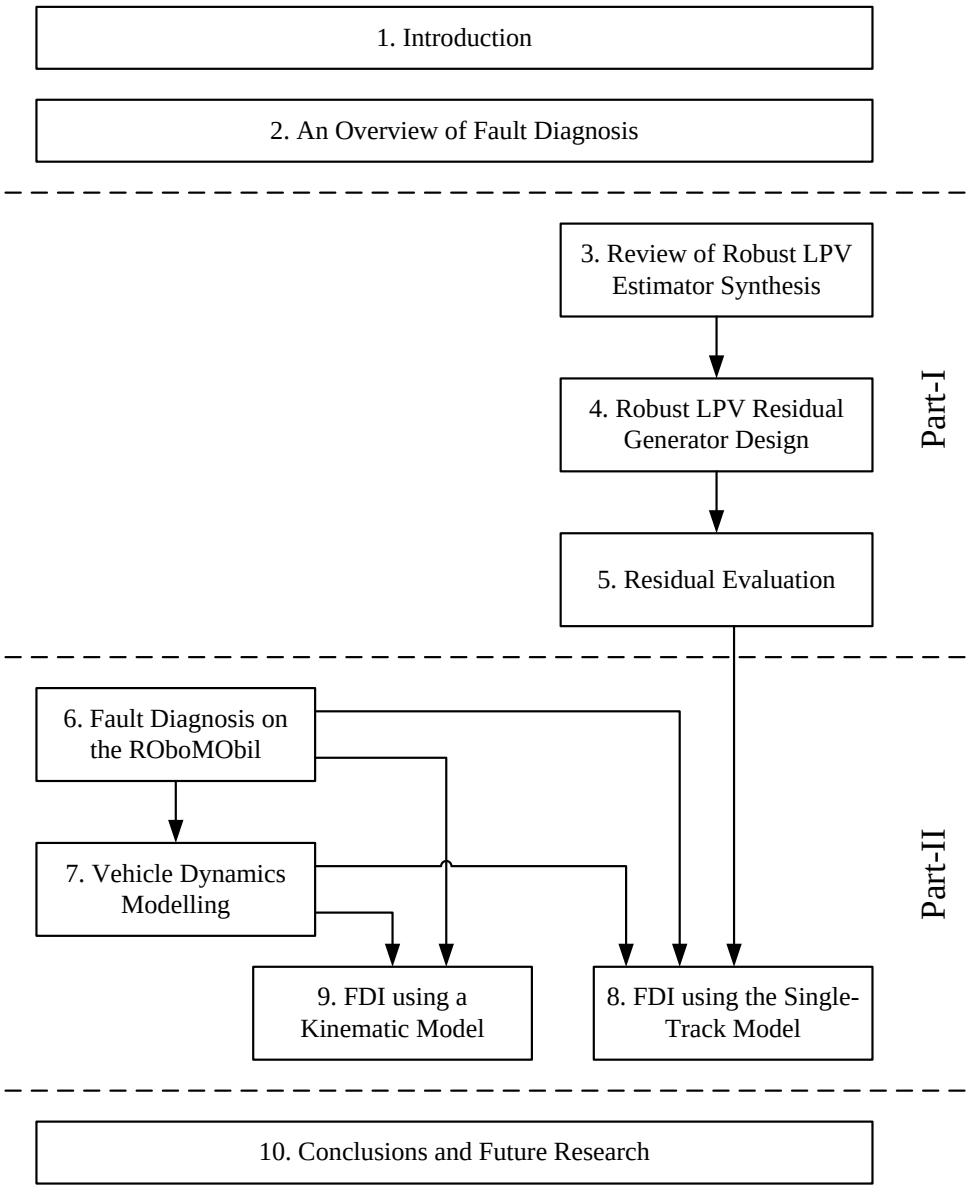

Figure 1.3: Structure of this thesis

Chapter 2

An Overview of Fault Diagnosis

This chapter gives a brief overview for the state of the art and developments in the area of fault diagnosis, as well as its applications in automotive and related applications. To place the role of fault diagnosis into context, we begin with a short look into the topic of fault tolerance.

2.1 Fault Tolerance

As the concept of a *fault* is central to this work, we begin by clarifying its meaning and its distinction from a *failure* in the field of fault diagnosis. These terms are defined in [CP99] as:

- fault: an unexpected change in system function, which may be tolerable
- failure: a complete breakdown of a system component or function

The occurrence of faults in a system may undermine the system's ability to fulfil its performance requirements, and could even lead to unsafe situations. The aim of fault-tolerant control is to detect such faults and take actions to stop or inhibit the propagation of their effects. While robust control and adaptive control techniques can be applied to achieve fault tolerance, they are only suitable for mild and slowly changing faults respectively. On the other hand, severe faults can disrupt and modify the system structure, and abrupt faults cannot be adequately estimated by adaptive control methods. For such cases, an architecture consisting of a combination of fault diagnosis and controller reconfiguration methods must be used [Bla06]. The diagnosis and reconfiguration can be considered to be acting on a supervisory level, while the controller acts on the execution level. Figure 2.1 illustrates this layout.

The fault-tolerant behaviour of a system may be classified into several degradation levels, namely *fail-operational*, *fail-safe*, or *fail-silent* [Kop97; ISS02]. As the name suggests, a *fail-operational* system remains operational after the fault. In contrast, a *fail-safe* system is brought into a safe state after a failure, and a *fail-silent* system appears passive from an external perspective to avoid adversely affecting other components.

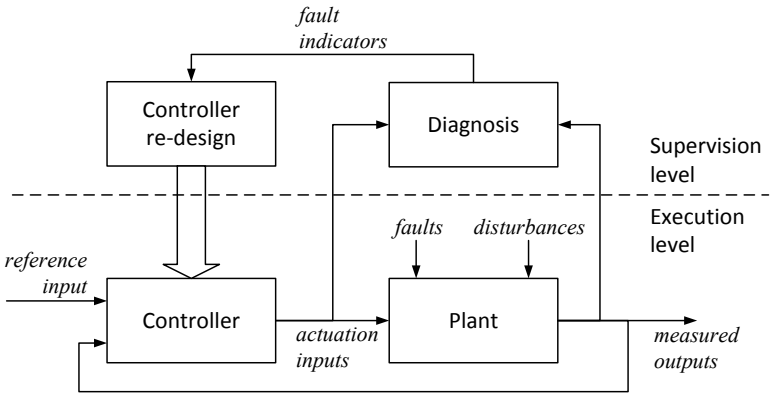

Figure 2.1: Architecture of fault-tolerant control by controller reconfiguration [Bla06]

In the transportation sector, fault tolerance has been a key consideration in system design in both the aeronautical and automotive industries. In particular, aircraft apply hardware redundancy, i.e. by employing redundant hardware components, to ensure safety and availability of their critical actuators and sensor [Gou11]. An example of actuator redundancy is the fault-tolerant electrically actuated cabin outflow valve described in [MBI09], implemented using redundant motors in a parallel configuration. Fault-tolerance of the angle of attack and airspeed sensors are handled in [VOJ14] by model-based diagnosis and virtual sensors, when multiple sensor failures exceed the hardware fault-tolerance capability of the triplex redundant sensor configurations. When the physical sensor output is unavailable, virtual sensors are used to estimate the measured quantity from other healthy sensors [Bla06]. When further sensors are lost such that even the virtual sensors are inoperable, then the final degradation level is activated. In this instance, this involves switching the controller to a backup control law requiring only a restricted set of scheduling parameter measurements.

In automotive applications, the subject of fault tolerance has gained importance due to the proliferation of mechatronic and controlled systems in vehicles, and the impending introduction of Drive-by-Wire systems without mechanical backup. The challenges differ somewhat from those for aerospace applications. Fault handling in automobiles requires shorter reaction times due to their faster dynamics and lower tolerance for trajectory deviations, but has less stringent demands for the tolerance of multiple faults due to the possibility of reaching a safe state more easily and swiftly. For most road vehicles, standstill or low speed at a non-hazardous place can be regarded as a safe state. This permits a less restrictive standard in which generally only combinations of up to two independent faults are considered, according to the ISO26262 Functional Safety Standard [ISO09]. Much of fault-tolerant control literature considers only the case of single (independent) faults, due to the low probability of a second fault occurring within a short time interval after the first, before mitigation measures can be imposed. For Drive-by-Wire vehicles without driver-operable mechanical backup, the vehicle must be *fail-operational* to this first fault, at least for sufficiently long to bring the vehicle to a safe state. This is achieved by an

architecture of fault-tolerant subsystems and components with an appropriate combination of degradation levels.

There are extensive research, literature, and concepts that cover the prominent topic of automotive fault tolerance in communication buses and computation software and hardware (e.g. [Kop94; Arm06; Che08; Wil05; Tou05]). This level of fault tolerance is addressed in software and electronic hardware architecture design. It will not be covered here as the focus of this thesis lies with "physical" faults in actuators, sensors and the plant. For these types of subsystems, there are established methods for fault tolerance relying on hardware redundancy, which can be classified into static and dynamic redundancy [ISS02]. In static redundancy, at least two independent components operate in parallel. An example of this is a voting scheme, in which a voter compares the output signals from several active, independent sensor or computation modules and decides by majority on the correct value. The number of parallel modules determines the degree of redundancy, and in general fail operational systems require a higher degree of redundancy than fail silent ones. Some examples of voting schemes are majority [ISS02], median, and plurality voting, while extensions with fuzzy reasoning can also be found in literature [LSC10]. In contrast, dynamic redundancy seeks to first diagnose the fault before reconfiguring the system to use a healthy standby component in place of the faulty one, in either a hot or cold standby configuration. Timely and reliable fault diagnosis is paramount for the success of such a scheme.

The literature provides insights into how individual fault tolerance measures are applied to achieve system level safety and reliability goals. For example, [ISS02] describes fault-tolerant designs for an electrical throttle actuator and a Brake-by-Wire system. A redundant Steer-by-Wire solution is presented in [ZA08], while [LSC10] provides a concept for fault-tolerant driver input sensing on the Brake-by-Wire pedal.

Even though hardware redundancy is necessary for fault tolerance for many combinations of architectures and faults, there is growing interest in using built-in analytical redundancies of highly actuated vehicles to diagnose and handle actuator and sensor faults. Such designs lower costs and physical complexity by eliminating the need for additional hardware components. The feasibility of such a design requires the system to be operable using the remaining healthy elements such that the system's objectives can be fully or partially met (fail operational), or at least the remaining system must have sufficient control authority to be gracefully degraded and brought to an acceptable safe state (fail safe). An example of this type of fault-tolerant control is investigated in [Wan15] and [JW08] for vehicles with in-wheel electric motors.

2.2 Model-based Fault Diagnosis

We will now consider the diagnosis component of fault tolerant control in more detail. Fault diagnosis is the combination of the tasks of fault detection, isolation and identification [CP99]. Fault detection is the decision of whether a fault has occurred, and isolation

seeks to determine the location of the fault. These two tasks are essential for deciding on actions to mitigate an occurred fault. The identification task, which involves the estimation of the size and type or nature of the fault, is significant if fault effects are to be compensated through control adaptation or reconfiguration. In this work the focus will lie with the detection and isolation stages, and thus diagnosis will refer only to these two tasks.

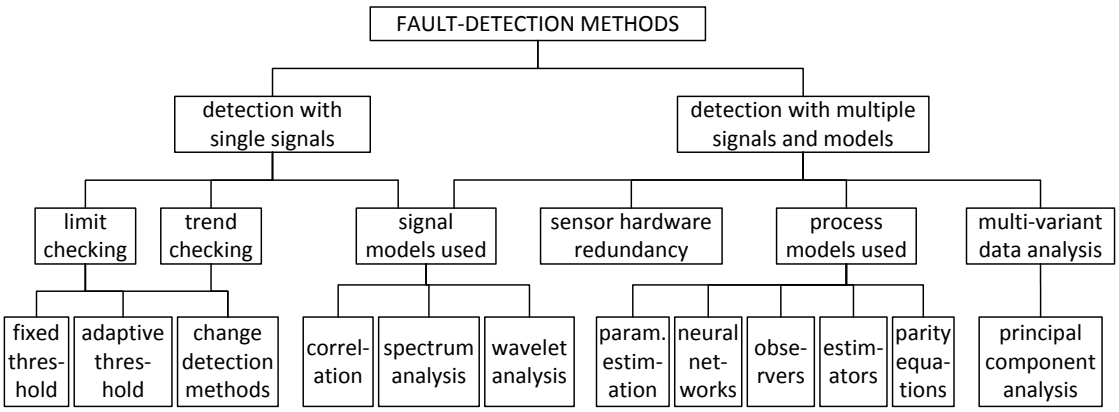

Figure 2.2: Taxonomy of fault detection methods (adapted from [Ise06b])

Fault detection methods can be broadly divided into model-free and model-based categories. Figure 2.2 shows a taxonomy of fault detection methods from [Ise06b]. Model-free, signal-based approaches examine properties of individual or multiple signals to reach fault conclusions, without a mathematical model of the system under consideration. Methods include limit and trend checking, examination of correlation and spectral properties, as well as principle component analysis. On the other hand, hardware redundancy based approaches compare equivalent signals obtained from independent sources to check for inconsistencies, and in the provided taxonomy they can be considered as the use of a simple equality model to check for consistency between the signals. These approaches are often incorporated into fault-tolerance schemes such as voting algorithms, as mentioned in the previous section. Usually, the term "model-based" approaches refer to those that rely on a less trivial mathematical model of the relationships between measurements and known variables to determine consistency among them. By making use of this *analytical redundancy*, model-based approaches can potentially detect and isolate additional faults, detect small faults where the measured signals are within normal operating range, as well as detect plant faults located away from the actuators and sensors. The drawback is that the robustness of the diagnosis is sensitive to modelling errors and unknown disturbances, which have to be suppressed in the design procedure. Prominent approaches for model-based diagnosis include parameter estimation, which is suited for parametric (multiplicative) faults, and residual-based methods which are more suitable for additive faults. Common realisations of residual-based methods include observers, estimators, and parity equations. This thesis will cover residual-based methods since these are relevant to the types of faults to be diagnosed in the vehicle dynamics application.

The residual-based method usually comprises the stages of residual generation and residual evaluation. If an array of residuals is involved, then there is the additional stage of decision making based on patterns in the evaluation outcomes. Each of these stages is discussed in more detail later. For larger systems it is often useful, when this is possible, to first divide the diagnosis problem into smaller, decoupled or weakly coupled sub-problems. Systematic approaches for achieving this include the use of structural methods such as hierarchical decomposition or structural analysis, and these will be briefly introduced in the next subsection.

2.2.1 Structural Methods

Fault diagnosis is often applied to large engineering systems with a high number of measurements and potential faults. As a preliminary step to numerical FDI design, it is advantageous to decompose the full system into smaller and more manageable units, thus reducing the size and complexity of the numerical problems for fault detector design. To this end, structural analysis methods can be employed to computationally find sets of equations with redundant variables. Using such sets, inconsistency between the contained variables can then be detected and flagged as a fault. Among the methods are the *matching algorithm* [Bla06] and the *MSO algorithm* [KAN08], both of which are based on results from graph theory. In particular, the latter determines Minimally Structurally Overdetermined (MSO) sets, each containing one more equation than the number of variables. Several other further methods for finding decompositions are presented in [Arm09].

Alternatively, in some applications it may be possible to decompose a system hierarchically using design knowledge of the system, often along the divisions of a decentralised or distributed control system. In such schemes, the diagnostic results from the smaller lower-level subsystems are aggregated at higher levels to draw a diagnostic conclusion at the system-level. [Nas10] applies this to the components of a smart distance keeping function, while [YJ04] formalises this into design guidelines for a standardised, reuseable software module called a *Generalised Diagnostic Component*. For each unit resulting from the decomposition, residual-based FDI methods can then be applied. This is discussed in the next sections.

2.2.2 Residual Generation

Residual-based methods involve the computation and analysis of residuals, which are quantities which represent the inconsistency between the actual system variables and its mathematical model [CP99]. They can be viewed as auxiliary signals calculated from known system inputs and measurements and, in the ideal case, they are decoupled from disturbances and uncertainties while being sensitive to faults. The commonly accepted layout for residual-based FDI is a two-stage process, with residual generation followed by decision making including residual evaluation [CW84]. This layout is illustrated schematically in Figure 2.3. The residual generator shown in this figure is the simplest possible

model-based layout, in which the residual is computed as the difference between the plant and a parallel model of the process. More sophisticated and robust designs are usually employed.

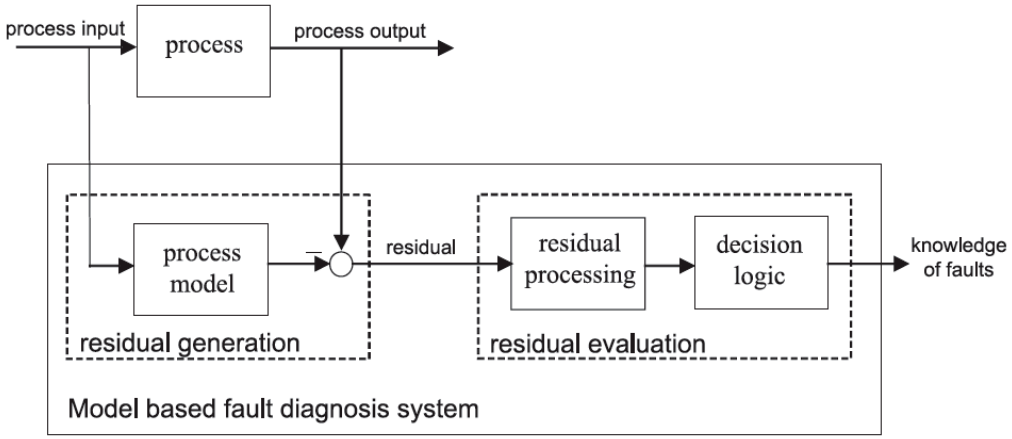

Figure 2.3: Schematic diagram of model-based FDI [Din13]

The computation of residuals with the aforementioned characteristics is referred to as the Fundamental Problem of Residual Generation (FPRG). Methods have been developed since the 1970s to deal with this problem. These include but are not limited to the Beard-Jones fault detection filter [Bea71], parity equations [CW84], the geometric filter [Mas86], Unknown Input Observer (UIO) [CP99], parameter estimation [Fra96], and factorisation-based methods [FD97]. In the LTI context, the approaches using parity equations, observers, and parameter estimation are actually closely related and even equivalent under some conditions [Fra96]. Where an exact decoupling solution is not possible, approximate methods can be applied, which maximise sensitivity to faults while attenuating disturbance effects using numerical optimisation methods [FD97]. Model uncertainties may be handled by representing them as additive disturbances entering through distribution matrices [CP99], or alternatively by employing robust estimation methods which minimise certain norms of estimation errors in the presence of structured or unstructured uncertainties [Man95]. Across the listed methods, there are wide variations in robustness to model uncertainties and noise, computation complexity and other properties. The suitable methods in a particular application depends on many factors including model form and complexity, present uncertainty types, and performance requirements.

Most of the earlier work was dedicated to linear time-invariant (LTI) systems. While there is no universal solution for nonlinear systems, more recent advances have seen development of solutions for certain classes of such systems. Nonlinear parity relations and the dynamic inversion based approach are examples of proposed methods [BS09]. Observer-based residual generation techniques have also been extended to affine and bilinear systems using geometric concepts [BS09]. In particular, a substantial body of literature describes the extension of the LTI results to linear parameter-varying (LPV) systems, and these will be described in more detail in the next section. In general, residual generation and fault detection for nonlinear systems is still an active field of research.

For diagnosis in stochastic systems, stochastic filters / estimators can be combined with statistical residual evaluation techniques. One such technique is to use the innovation of a Kalman filter as the residual signal. By first extracting a sub-model without unknown inputs from the plant model and using this in the Kalman Filter design, it is possible to achieve decoupling from disturbances [Bla06]. With the incorporation of probability information into the design, an advantage of stochastic methods is their ability to estimate not just the mean value of the states and residuals, but also their probability distributions. This then allows straightforward calculations of metrics such as false alarm rates (FAR) and missed detection rates (MDR), which can be naturally interpreted as performance indicators for a fault detection system. For nonlinear systems, there exist designs which employ nonlinear stochastic filters such as the unscented Kalman filter [LT10] and the particle filter [Kad02; OV09].

2.2.3 Linear Parameter-Varying (LPV) Approaches

LPV systems represent a class or representation of nonlinear systems where some parameters of a linear system are known but time-varying quantities. This representation allows many LTI results to be extended and applied to these systems, which is particularly relevant to this research, since its main application of road vehicle lateral dynamics can be represented as an LPV model with vehicle speed as the main scheduling parameter. Much of the development of LPV methods was initially driven by the aeronautical sector. The dynamics of aircraft and their components on various levels (e.g. actuators for wing and rudder elements) can often be represented by models that are scheduled by a small number of parameters that can be measured or readily estimated, a dominant one being air speed. These methods have since been shown to be applicable to a diverse range of applications, from automotive [VKM14] to fuel cells [De 11] and winding machines [Rod13].

Most observer-based methods handle the LPV property explicitly in the residual generator synthesis phase to achieve desired properties over all admissible parameter trajectories, which are defined by bounds on parameter values and in some cases also rates of parameter variation. Some of these methods are:

- exact decoupling using geometric subspace methods for parameter-affine LPV systems [BB04]
- approximate decoupling using robust methods based on minimisation of induced norms [GHZ08; Cas08]

Alternatively, an LPV residual generator may be designed by interpolation of LTI counterparts synthesised at each point on a parameter grid [Var11c]. While interpolation is generally seen as an ad-hoc, albeit widely applied method to deal with LPV systems, stability can be proven for sufficiently slow parameter variations. Furthermore, stability preserving interpolation methods exist [RS00; LL00]. Yet another possibility is to retain the scheduling parameter as a symbol throughout the synthesis process, either for specific problem structures [VO14; Sch05] or for a general class of methods (e.g. the rational

nullspace approach [Var11b]), although both these approaches are only tractable for small system dimensions and low parameter counts.

2.2.4 Residual Evaluation

The role of the evaluation step is to take the continuous residual signal and transform it into a binary decision variable that indicates whether or not a fault has occurred. Residual evaluation is approached differently for deterministic and stochastic methods. In deterministic methods, usually a measure of residual size is calculated by the evaluation function and compared to a threshold. In directional residual approaches such as [Bea71; GM95], the directional information of the residual vector is also exploited for fault isolation. Common evaluation functions found in the literature include norms [Din13], their approximation through recursive filters [Oss14], and wavelets [Kab02; YDW02]. Thresholds can in some cases be determined theoretically from analysis of the residual generator to obtain the maximum fault-free value of the evaluated residual. However, often they are determined as the worst-case value from detailed simulations with representative input signals and model parameters, in order to avoid false alarms under realistic operating conditions and yet avoid excessively conservative theoretical values. Another approach that reduces conservatism is the use of dynamic or adaptive thresholds [FD97]. Since non-zero residual values on a fault-free plants are caused in part by plant-model mismatch, a description of the model uncertainty would allow the residual to be bounded as a function of plant inputs and / or outputs. Using such a bound as a dynamic threshold can improve fault sensitivity by lowering the constant component, which would otherwise have to account for the effects the worst-case inputs and outputs on the residual.

In stochastic methods the residual evaluation makes use of the available probability information through hypothesis testing, which requires at least some of distributions of the residual signal in fault-free and faulty states to be known. Change detection algorithms such as Cumulative Sum (CUSUM), Likelihood Ratio and Generalised Likelihood Ratio exploit this information in a recursive manner, making them suitable for online calculations [Bla06]. The fault detection threshold can be set directly based on the desired trade-off between FAR and MDR.

2.2.5 Structured Residuals for Fault Isolation

Besides the already mentioned method of directional residuals, another fault isolation technique is that of structured residuals. In this concept, an array of residuals is designed where each is sensitive to a different subset of faults, such that each fault triggers a reaction in a different combination of residuals [Ger98]. Under some assumptions, the occurred fault can be determined by matching the pattern of triggered residuals to each fault's "residual signature", which is the supposed response of the residual array to that fault. This scheme is implemented as a bank of residual generators and evaluation functions operating in parallel, and can be combined with any residual generation method and evaluation function

that produces a binary decision. Some residual structures have particular configurations and provide guaranteed isolation properties, and carry special designations such as the Dedicated Observer Scheme and the Generalised Observer Scheme. However, other more general structures exist and are also useful for fault isolation when certain requirements are fulfilled. This will be discussed in more detail in Chapter 5.

In literature, the residual structure design stage is usually separated from that of residual generation and evaluation. Procedures for designing the bank of residual generators generally require the residual structure to be known *a priori*. This results in an iterative design process in which structures are selected heuristically until all the contained residual generators can be successfully synthesised with the prescribed fault sensitivity and decoupling characteristics. More recently the developments in [Var11a] provide a connection by numerically calculating all feasible signatures from the model definition, while the works of [HO14; SNF13; Kho14] consider the realisability and performance properties of the corresponding residual generators at the stage of residual selection. These developments provide the means for more systematic approaches to residual structure design, which can prove especially beneficial for large systems with higher numbers of potential faults.

2.3 Automotive Vehicle Dynamics Applications

The topic of fault diagnosis using vehicle dynamics relations has gathered momentum with the introduction and proliferation of lateral dynamics stabilisation systems. Advanced methods applied in series-production systems are presented in [DFD04] for diagnosis of the suite of sensors used for the ESP functions, namely the wheel speeds, steering wheel angle, lateral acceleration and yaw rate sensors. The work employs a bank of static parity equations based on vehicle motion geometry and steady-state cornering characteristics, similar to that described in [Fis07].

More advanced developments saw the introduction of the dynamic, fixed velocity single track model (STM), also known as the *bicycle model*, to describe vehicle behaviour and dynamics. Observed-based or parity equation-based LTI residual generators can then be synthesised based on this LTI model. This basic approach has been extended in literature by a multitude of directions. In a bid to improve the correlation with real vehicle behaviour, [Sch05] and [ZP09] extend the model to include a roll degree of freedom in order to replicate its effects on the sensor measurements. Other literature investigates specific aspects of the residual generator using the roll-free single track model, including the estimation of uncertainty in the residuals [Din05], integrated handling of residual generation and evaluation design [Ma07] and the use of a Proportional-Integral observer [Kas06]. Practical implementation of these fault detectors on an actual road vehicle requires additional measures. Since the velocity typical varies during normal operation, this has to be handled by either switching or interpolating between an array of fixed velocity fault detectors synthesised at points in the velocity range encountered during normal driving.

To explicitly handle the time-varying velocity at the synthesis stage, the single track model can be treated as an LPV model with velocity as a scheduling parameter. This is done in [Abd09; VKM14], both of which synthesised the residual generators using a parity space approach. [Abd09] additionally demonstrates that the generated parity relations can be translated into an equivalent observer implementation, which has a more efficient online implementation.

Besides the use of variations on the STM to represent horizontal lateral dynamics, some approaches make use of alternative vehicle dynamics representations to exploit novel sensor configurations or to fulfil particular requirements. For example, [Vie12] employs a model that only involves yaw and roll dynamics to achieve decoupling from uncertain parameters, on the assumption that lateral tire force sensors are available. In instances where information on the relative or absolute position is available from functions such as platooning or path following, they can also be integrated into the model-based fault diagnosis [GR03; Raj01]. The integration of component dynamics descriptions into the vehicle dynamics model can also bring benefits through a holistic perspective on fault diagnosis, especially if the two dynamics possess strong interactions. In [LT10], braking dynamics is integrated and a diagnostic observer based on an unscented Kalman filter is designed to monitor disc-pad friction coefficient in a brake-by-wire system. [CMA91; GYG04; Khe11] propose the diagnosis of steer-by-wire system faults by concurrently considering both the steering system and vehicle models in the linear or sliding-mode observed-based FDI approaches.

With the increasing relevance of electrically driven, X-by-Wire and autonomous vehicles, applications with such additional sensors and actuators are becoming more commonplace and provide opportunities for approaches based on such alternative or extended representations. Furthermore, the higher degrees of actuation and sensing result in more complex plant models. This in turn leads to higher dimensional fault diagnosis problems in which more faults can occur, offset by the availability of more known quantities that can be employed in analytical redundancy relations. This thesis aims to tackle the challenges and exploit the opportunities posed by such contemporary applications.

2.4 Main Contributions of the Thesis

The main contributions of this work can be divided into three aspects - a theoretical one that proposes a generic residual generator design method for LPV systems, and application related aspects that are specific to vehicle dynamics systems. Each is described below together with the chapters and publications in which it is presented.

Robust residual generation: An approximate decoupling approach is proposed for residual generator synthesis for uncertain LPV systems. The method aims to produce a residual with behaviour that follows a specified fault-to-residual reference model, and exploits recent advances in robust LPV estimator synthesis that formulates it as an optimisation in the format of a semi-definite program (SDP). The novelty in the presented approach is that the fault-to-residual gains within the reference model are concurrently

optimised, providing an efficient method to reduce the conservatism of the solution when the optimal reference is not known in advance. (Chapter 4; [Ho16; Ho17])

Robust FDI using the LPV STM with time-varying velocity: By applying the proposed design procedures for robust residual generation, residual evaluation and structured residuals to the LPV STM, a vehicle-level FDI is designed for the ROboMObil's vehicle dynamics system during variable speed cruising operation. Compared to the existing literature, the contribution of this work lies with handling both the time-varying vehicle speed and uncertainties in the residual generator design process. The approach also addresses the isolation of a greater number of sensor and actuator faults to cope with the configuration of the ROboMObil. (Chapter 5, 8; [HO14; Ho17])

Sensor FDI for highly manoeuvrable non-holonomic vehicles: Based on the nonlinear kinematic model (NKM), an FDI approach is proposed that remains valid over the entire horizontal motion range of four-wheeled non-holonomic vehicles with large steering angle ranges such as the ROboMObil. This is achieved by retaining the nonlinear trigonometric relationships in the model, rather than using the linearisation approaches often found in literature. Furthermore, empirical tuning of residual bounds is avoided by directly embedding physically motivated uncertainty parameters of the sensors and vehicle into the fault detector computations. (Chapter 9; [HB16])

Part I

Robust LPV Fault Detector Design

Chapter 3

Review of Robust LPV Estimator Synthesis

The residual generator synthesis approach to be presented in Chapter 4 is a special case of linear parameter-varying (LPV) estimator synthesis. To prepare for that development, this chapter introduces the basic theory required for solving the general robust estimator synthesis problem for uncertain LPV systems. First, LPV systems are introduced, alongside methods for their stability and performance analysis. The representation of uncertain systems in the linear fractional form is then covered, followed by the use of integral quadratic constraints in their analysis.

This chapter culminates in a procedure to solve the robust estimator synthesis problem, the essence of which is illustrated in Figure 3.1. Let $\boldsymbol{P}(\boldsymbol{\rho}, \Delta)$ be an uncertain LPV plant with known scheduling parameters $\boldsymbol{\rho}$, uncertain parameters Δ, unknown disturbance inputs $\bar{\boldsymbol{d}}$, measured outputs $\bar{\boldsymbol{y}}$, and an auxiliary output $\boldsymbol{z}$. The synthesis task involves finding an LPV estimator $\boldsymbol{F}(\boldsymbol{\rho})$ that computes $\hat{\boldsymbol{z}}$, the estimate of $\boldsymbol{z}$, which minimises the size of the estimation error $\boldsymbol{e} = \boldsymbol{z} - \hat{\boldsymbol{z}}$.

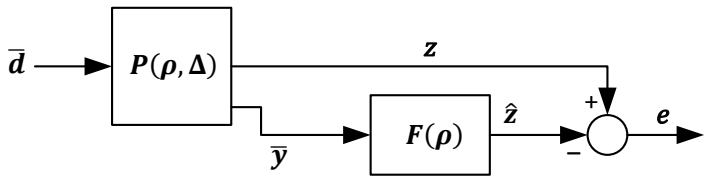

Figure 3.1: The robust LPV estimator synthesis problem

3.1 Preliminaries

3.1.1 Notation

Although standard notation is used in most of this and the next chapter, some are stated here to ensure clarity. $\mathbb{R}$ and $\mathbb{C}$ denote the set of real and complex numbers respectively. $\mathbb{RH}_\infty$ denotes the set of proper rational functions with real coefficients, have no poles on the imaginary axis, and are analytic on the closed right half of the complex plane. $\mathbb{R}^{m\times n}$, $\mathbb{C}^{m\times n}$ and $\mathbb{RH}_\infty^{m\times n}$ denote the set of $m\times n$ matrices whose elements are in $\mathbb{R}$, $\mathbb{C}$, and $\mathbb{RH}_\infty$ respectively. $\mathbb{R}^n$ denotes the set of all $n\times 1$ vectors with elements in $\mathbb{R}$, while the set of $n\times n$ symmetric matrices is denoted $\mathbb{S}^n$. The transpose of a matrix $\boldsymbol{M}$ is denoted $\boldsymbol{M}^T$. Symmetric matrix blocks are denoted as $\star$. The complex conjugate of $s\in\mathbb{C}$ is denoted $\bar{s}$. An operator F from one space to another, e.g. $\mathbb{R}$ to $\mathbb{R}^n$, is denoted $F:\mathbb{R}\to\mathbb{R}^n$. $\mathcal{L}_2^l[0,\infty)$ is the space of $\mathbb{R}^l$-valued functions $f:[0,\infty)\to\mathbb{R}^l$ of finite energy. That is, if $f\in\mathcal{L}_2^l[0,\infty)$ then $\|f\|_2<\infty$ where

$$\|f\|_2 := \left(\int_0^\infty f(t)^T f(t)dt\right)^{\frac{1}{2}} .$$

It is a subset of the space $\mathcal{L}_{2e}^l[0,\infty)$, whose members only need to be square integrable on every finite interval.

3.1.2 Linear Matrix Inequalities (LMIs)

A symmetric matrix $\boldsymbol{M}\in\mathbb{S}^n$ is positive definite if $\boldsymbol{u}^T\boldsymbol{M}\boldsymbol{u}>0$ for all non-zero $\boldsymbol{u}\in\mathbb{R}^n$, and is denoted $\boldsymbol{M}>0$. A positive semi-definite matrix requires $\boldsymbol{u}^T\boldsymbol{M}\boldsymbol{u}\geq 0$, and is denoted $\boldsymbol{M}\geq 0$. Negative definite and semi-definite matrix are analogously defined with $<$ and $\leq$ respectively.

The following definition of a linear matrix inequality (LMI) is taken from [Boy94]. An LMI has the form

$$\boldsymbol{M}(\boldsymbol{x}) := \boldsymbol{M}_0 + \sum_{i=1}^m x_i\boldsymbol{M}_i > 0 \tag{3.1}$$

where $\boldsymbol{x}=[x_1\ \ldots\ x_m]^T\in\mathbb{R}^m$ is the variable and $\boldsymbol{M}_i\in\mathbb{S}^n$ are given. The LMI is a convex constraint on $\boldsymbol{x}$. LMIs can also be written equivalently in a condensed form with matrices as variables, replacing $x_i\boldsymbol{M}_i$ in (3.1) with $\boldsymbol{M}_i\boldsymbol{X}_i$ where $\boldsymbol{X}_i$ is a matrix variable.

Many of the constraints presented in this chapter are matrix inequalities that are transformed into LMIs for integration into a semi-definite program (SDP). An SDP is an optimisation problem with a linear objective function and LMI constraints, i.e.,

$$\min_{\boldsymbol{x}} \boldsymbol{c}^T\boldsymbol{x} \quad s.t. \quad \boldsymbol{M}(\boldsymbol{x})>0\ . \tag{3.2}$$

They can be solved efficiently via convex optimisation algorithms [Boy94]. The SDPs in this thesis are solved with the help of the optimisation toolbox YALMIP [Löf04].

3.2 LPV Systems

Linear parameter-varying (LPV) systems are finite-dimensional linear time-varying systems whose states space matrices are functions of measurable time-varying parameters. Many classes of nonlinear systems can be represented as LPV systems. Their prevalence in literature can be attributed to the possibility of extending many mature LTI theories to their LPV counterparts, providing a paradigm for systematic analysis, control and estimation of compatible nonlinear systems.

Definition 3.1 (LPV system [Wu95])**.** *Let $\boldsymbol{\rho} \in \mathcal{P}$ be a time-varying, measurable scheduling parameter vector, where the parameter space $\mathcal{P} \in \mathbb{R}^{n_\rho}$ is a closed and bounded set. Furthermore, the parameter rate of change $\dot{\boldsymbol{\rho}}$ resides in a bounded set $\dot{\mathcal{P}}$. With system state $\boldsymbol{x} \in \mathbb{R}^n$, input $\boldsymbol{d} \in \mathbb{R}^{n_d}$ and output $\boldsymbol{e} \in \mathbb{R}^{n_e}$, an LPV system $\boldsymbol{P}(\boldsymbol{\rho})$ is given by*

$$\boldsymbol{P}(\boldsymbol{\rho}) : \left\{ \quad \begin{bmatrix} \dot{\boldsymbol{x}} \\ \boldsymbol{e} \end{bmatrix} = \left[\begin{array}{c|c} \boldsymbol{A}(\boldsymbol{\rho}) & \boldsymbol{B}(\boldsymbol{\rho}) \\ \hline \boldsymbol{C}(\boldsymbol{\rho}) & \boldsymbol{D}(\boldsymbol{\rho}) \end{array}\right] \begin{bmatrix} \boldsymbol{x} \\ \boldsymbol{d} \end{bmatrix} \quad , \quad \boldsymbol{x}(0) = \boldsymbol{x}_0 \right. \tag{3.3}$$

where $\boldsymbol{A} : \mathcal{P} \to \mathbb{R}^{n \times n}$, $\boldsymbol{B} : \mathcal{P} \to \mathbb{R}^{n \times n_d}$, $\boldsymbol{C} : \mathcal{P} \to \mathbb{R}^{n_e \times n}$, $\boldsymbol{D} : \mathcal{P} \to \mathbb{R}^{n_e \times n_d}$ are matrix valued functions of $\boldsymbol{\rho}$.

Note that the set $\dot{\mathcal{P}}$ is often defined as a hyperbox and is independent to $\mathcal{P}$. Another technicality is that strictly speaking, $\boldsymbol{\rho}$ is assumed to be a continuously differentiable function of time, whose admissible trajectories are defined by

$$\mathcal{A} := \{\boldsymbol{\rho} | \boldsymbol{\rho}(t) \in \mathcal{P},\ \dot{\boldsymbol{\rho}}(t) \in \dot{\mathcal{P}}\ \ \forall t \geq 0\} \ . \tag{3.4}$$

To simplify the notation, the time dependence of $\boldsymbol{\rho}$ will be omitted. Reference to the function or its value can be readily determined from context.

LPV models can be obtained analytically from nonlinear systems by Jacobian linearisation, velocity-based linearisation, state transformation techniques, and function substitution techniques [LBC13; RS00; LL00]. In some cases, as with the application study in Chapter 8 of this thesis, the state space equations naturally take on an LPV form with exogenous measurable scheduling parameters. Methods also exist to obtain LPV models directly from experimental data [LBC13]. It is worth mentioning that representations whose scheduling parameters are partially dependent on the system states are commonly referred to as quasi-LPV systems. In the rest of Part-I, the LPV representation will be taken as the starting point, and no distinction will be made between the methods used in obtaining this representation.

3.2.1 Stability

Lyapunov stability theory can be used as the basis for deriving the stability condition for LPV systems [Bec93; RS00]. It is an extension to quadratic stability for LTI systems, which defines the quadratic Lyapunov function $V(\boldsymbol{x}) = \boldsymbol{x}^T \boldsymbol{X} \boldsymbol{x}$, where $\boldsymbol{X}$ is a positive

definite matrix. Lemma 3.1 states the conditions for quadratic stability. Note that the time derivative of an LTI system $\dot{\boldsymbol{x}} = \boldsymbol{A}\boldsymbol{x}$ is given by $\dot{V}(\boldsymbol{x}) = \boldsymbol{A}^T\boldsymbol{X} + \boldsymbol{X}\boldsymbol{A}$.

Lemma 3.1 (Quadratic stability [Boy94])**.** *The autonomous LTI system $\dot{\boldsymbol{x}} = \boldsymbol{A}\boldsymbol{x}$ is exponentially stable if there exists a matrix $\boldsymbol{X} \in \mathbb{S}^n$, $\boldsymbol{X} > 0$ such that*

$$\boldsymbol{A}^T\boldsymbol{X} + \boldsymbol{X}\boldsymbol{A} < 0 \ . \tag{3.5}$$

A common approach for analysing the stability of LPV systems is to extend the notion of quadratic stability in Lemma 3.1. The constant Lyapunov matrix $\boldsymbol{X}$ is changed to a matrix function $\boldsymbol{X} : \mathcal{P} \to \mathbb{S}^n$, so that the Lyapunov function $V(\boldsymbol{x}, \boldsymbol{\rho})$ for an LPV system is given in terms of $\boldsymbol{X}(\boldsymbol{\rho}) > 0$ for all $\boldsymbol{\rho}$ as

$$V(\boldsymbol{x}, \boldsymbol{\rho}) = \boldsymbol{x}^T\boldsymbol{X}(\boldsymbol{\rho})\boldsymbol{x} \ . \tag{3.6}$$

Its derivative with respect to time along the system trajectories is given by

$$\begin{aligned} \dot{V}(\boldsymbol{x}, \boldsymbol{\rho}, \dot{\boldsymbol{\rho}}) &= \frac{\partial V(\boldsymbol{x}, \boldsymbol{\rho})}{\partial \boldsymbol{x}}\boldsymbol{A}\boldsymbol{x} + \frac{\partial V(\boldsymbol{x}, \boldsymbol{\rho})}{\partial \boldsymbol{\rho}}\dot{\boldsymbol{\rho}} \\ &= \boldsymbol{x}^T(\boldsymbol{A}(\boldsymbol{\rho})^T\boldsymbol{X}(\boldsymbol{\rho}) + \boldsymbol{X}(\boldsymbol{\rho})\boldsymbol{A}(\boldsymbol{\rho}))\boldsymbol{x} + \boldsymbol{x}^T\partial\boldsymbol{X}(\boldsymbol{\rho}, \dot{\boldsymbol{\rho}})\boldsymbol{x} \end{aligned} \tag{3.7}$$

where the following operator notation was introduced to improve clarity, with p_i and $\bar{p}_i$ denoting the i-th elements of $\boldsymbol{p}$ and $\bar{\boldsymbol{p}}$ respectively:

$$\partial\boldsymbol{X}(\boldsymbol{p}, \bar{\boldsymbol{p}}) := \sum_{i=1}^{s} \frac{\partial \boldsymbol{X}(\boldsymbol{p})}{\partial p_i}\bar{p}_i \ . \tag{3.8}$$

The symbols $\boldsymbol{p}$ and $\bar{\boldsymbol{p}}$ are used in (3.8) in place of $\boldsymbol{\rho}$ and $\dot{\boldsymbol{\rho}}$ to emphasise that they are values as opposed to functions of time. Given these expressions, the application of Lyapunov stability conditions results in the conditions for *parameter-dependent stability*. In order for the analysis to be tractable, in these conditions $\dot{\boldsymbol{\rho}}$ is treated as a parameter that varies independently from $\boldsymbol{\rho}$.

Lemma 3.2 (Parameter-dependent stability)**.** *If there exists a continuously differentiable Lyapunov matrix function $\boldsymbol{X} : \mathcal{P} \to \mathbb{S}^n$, such that $\forall(\boldsymbol{p}, \bar{\boldsymbol{p}}) \in \mathcal{P} \times \dot{\mathcal{P}}$*

$$\boldsymbol{X}(\boldsymbol{p}) > 0 \tag{3.9}$$

$$\boldsymbol{A}(\boldsymbol{p})^T\boldsymbol{X}(\boldsymbol{p}) + \boldsymbol{X}(\boldsymbol{p})\boldsymbol{A}(\boldsymbol{p}) + \partial\boldsymbol{X}(\boldsymbol{p}, \bar{\boldsymbol{p}}) < 0 \tag{3.10}$$

then the system (3.3) is exponentially stable.

Proof. A proof can be found in [Wu96]. □

Remark 3.1. *For unbounded parameter rates of change, the satisfaction of (3.10) for all permissible $\bar{\boldsymbol{p}}$ requires that $\frac{\partial \boldsymbol{X}(\boldsymbol{p})}{\partial p_i} = 0, \ i = 1, \ldots, s \ , \ \forall \boldsymbol{p} \in \mathcal{P}$. These conditions correspond to a constant Lyapunov matrix $\boldsymbol{X}(\boldsymbol{\rho}) = \boldsymbol{X}$.*

3.2.2 Dynamic Behaviour

The notion of stability for LPV systems can be augmented using *LMI regions*, which provide conditions to ensure the eigenvalues of the frozen parameter LPV system (with $\boldsymbol{\rho}$ fixed at one value) lie within specified convex regions on the complex plane. Even though the concept of eigenvalues is defined for LTI systems only and therefore not strictly valid in the LPV context, these conditions nonetheless provide a useful characterisation of the system dynamics. The eigenvalue requirements are mapped into LMI constraints on the constant state space matrix $\boldsymbol{A}$ of the frozen parameter LPV system [CG96; SGC97].

Lemma 3.3 (LMI region [SW05])**.** *Given a symmetric matrix $\boldsymbol{L}$ and a matrix $\boldsymbol{M}$ define*

$$\mathcal{R} = \{s \in \mathbb{C} | \boldsymbol{L} + s\boldsymbol{M} + \bar{s}\boldsymbol{M}^T < 0\} \ . \tag{3.11}$$

Then the eigenvalues of $\boldsymbol{A}$ are confined in $\mathcal{R}$ if and only if there exists a symmetric $\boldsymbol{X}$ such that

$$\boldsymbol{X} > 0 \tag{3.12}$$

$$\boldsymbol{L} \otimes \boldsymbol{X} + \boldsymbol{M}^T \otimes (\boldsymbol{A}^T\boldsymbol{X}) + \boldsymbol{M} \otimes (\boldsymbol{X}\boldsymbol{A}) < 0 \ . \tag{3.13}$$

The symbol $\otimes$ denotes the Kronecker product.

Values of $\boldsymbol{L}$ and $\boldsymbol{M}$ for some commonly encountered elementary regions are listed in [CG96] and [SW05]. Several cases used later in this thesis are listed in Table 3.1 together with their accompanying LMI constraints (3.13). Composite regions constructed by intersecting multiple elementary regions can be handled by enforcing their LMI constraints concurrently. For example, the eigenvalues can be restricted to the shaded region in Figure 3.2 by combining all three constraints listed in Table 3.1.

Table 3.1: Parameters for selected LMI regions

	Description	$\mathcal{R}$	$\boldsymbol{L}$	$\boldsymbol{M}$
1	Minimum real part α_1	$s: \ Re(s) > \alpha_1$	$2\alpha_1$	-1
2	Maximum real part α_2	$s: \ Re(s) < \alpha_2$	$-2\alpha_2$	1
3	Conic sector with angle 2θ	$s: \ \frac{\lvert Im(s)\rvert}{-Re(s)} < \tan(\theta)$	0	$\begin{bmatrix} \sin(\theta) & \cos(\theta) \\ -\cos(\theta) & \sin(\theta) \end{bmatrix}$

The LMIs corresponding to each of these regions are respectively

$$1: \quad 2\alpha_1\boldsymbol{X} - \boldsymbol{X}\boldsymbol{A} - \boldsymbol{A}^T\boldsymbol{X} < 0 \tag{3.14}$$

$$2: \quad -2\alpha_2\boldsymbol{X} + \boldsymbol{X}\boldsymbol{A} + \boldsymbol{A}^T\boldsymbol{X} < 0 \tag{3.15}$$

$$3: \quad \begin{bmatrix} \sin(\theta)(\boldsymbol{X}\boldsymbol{A} + \boldsymbol{A}^T\boldsymbol{X}) & \cos(\theta)(\boldsymbol{X}\boldsymbol{A} - \boldsymbol{A}^T\boldsymbol{X}) \\ -\cos(\theta)(\boldsymbol{X}\boldsymbol{A} - \boldsymbol{A}^T\boldsymbol{X}) & \sin(\theta)(\boldsymbol{X}\boldsymbol{A} + \boldsymbol{A}^T\boldsymbol{X}) \end{bmatrix} < 0 \tag{3.16}$$

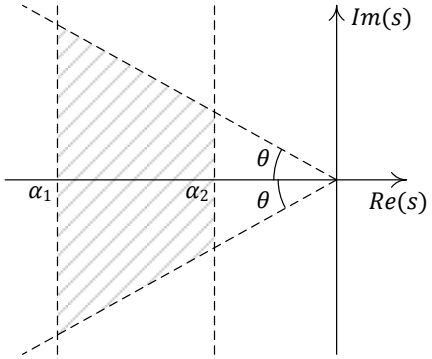

Figure 3.2: An LMI region constructed by intersecting the elementary regions from Table 3.1.

3.2.3 Induced $\mathcal{L}_2$ Performance

A useful characterisation of system performance is the input-to-output energy gain, where the energy of a signal given by its 2-norm $\|\cdot\|_2$. When applied to the closed-loop systems in regulation or estimation problems, this can be interpreted as the energy gain from the disturbance signals $\boldsymbol{d}$ to some performance outputs $\boldsymbol{e}$. An example would be plant disturbance to estimation error for the estimation problem. The largest energy gain of the LPV system $\boldsymbol{P}(\boldsymbol{\rho})$ over all possible admissible system trajectories is given by its induced-$\mathcal{L}_2$ norm, denoted $\|\cdot\|_{i2}$. It is defined as

$$\|\boldsymbol{P}(\boldsymbol{\rho})\|_{i2} := \sup_{\substack{\boldsymbol{d}\in\mathcal{L}_2(0,\infty) \\ \boldsymbol{\rho}\in\mathcal{P}}} \frac{\|\boldsymbol{e}\|_2}{\|\boldsymbol{d}\|_2} \,. \tag{3.17}$$

Note that the induced-$\mathcal{L}_2$ norm of an LTI system is simply the H_∞ norm.

The Bounded Real Lemma (BRL) [Boy94] provides for an LTI system a necessary and sufficient condition for stability and the existence of an upper bound on the H_∞ norm. It can be extended for parameter-varying systems into what will hereafter be referred to as the *generalised* Bounded Real Lemma. As in the case of parameter-dependent stability, $\dot{\boldsymbol{\rho}}$ is treated as a parameter that varies independently of $\boldsymbol{\rho}$. In part due to this source of conservatism, the generalised BRL now only represents a sufficient condition for the upper bound. A variety of representations for the BRL can be found in literature, related to each other by algebraic manipulations and/or the Schur Complement [Boy94]. The presented lemma is based on the form used in [AGB95].

Lemma 3.4 (Generalised Bounded Real Lemma)**.** *The LPV system $\boldsymbol{P}(\boldsymbol{\rho})$ is exponentially stable and satisfies $\|\boldsymbol{P}(\boldsymbol{\rho})\|_{i2} < \gamma$ if there exists a continuously differentiable Lyapunov*

matrix function $\boldsymbol{X} : \mathcal{P} \to \mathbb{S}^n$ *such that* $\forall (\boldsymbol{p}, \bar{\boldsymbol{p}}) \in \mathcal{P} \times \dot{\mathcal{P}}$

$$\boldsymbol{X}(\boldsymbol{p}) > 0 \tag{3.18}$$

$$\begin{bmatrix} \boldsymbol{A}(\boldsymbol{p})^T \boldsymbol{X}(\boldsymbol{p}) + \boldsymbol{X}(\boldsymbol{p}) \boldsymbol{A}(\boldsymbol{p}) + \partial \boldsymbol{X}(\boldsymbol{p}, \bar{\boldsymbol{p}}) & \boldsymbol{X}(\boldsymbol{p}) \boldsymbol{B}(\boldsymbol{p}) & \boldsymbol{C}(\boldsymbol{p})^T \\ \boldsymbol{B}(\boldsymbol{p})^T \boldsymbol{X}(\boldsymbol{p}) & -\gamma \boldsymbol{I}_{n_d} & \boldsymbol{D}(\boldsymbol{p})^T \\ \boldsymbol{C}(\boldsymbol{p}) & \boldsymbol{D}(\boldsymbol{p}) & -\gamma \boldsymbol{I}_{n_e} \end{bmatrix} < 0 \tag{3.19}$$

Proof. See [PS14] for a proof based on the dissipation inequality. □

It is remarked that the above matrix inequalities are infinite dimensional, as the conditions apply to all $(\boldsymbol{p}, \bar{\boldsymbol{p}}) \in \mathcal{P} \times \dot{\mathcal{P}}$, which constitutes a continuous parameter space. Furthermore, for the same reasons as parameter-dependent stability, the satisfaction of (3.19) for unbounded parameter rates of change demands $\boldsymbol{X}(\boldsymbol{\rho}) = \boldsymbol{X}$.

3.2.4 Stability and Performance Analysis

Based on the conditions defined so far for the stability, dynamic behaviour, and performance of an LPV system, the analysis of these three aspects of an LPV system amounts to a search for a Lyapunov matrix function $\boldsymbol{X} : \mathcal{P} \to \mathbb{S}^n$ which satisfies the LMIs (3.18) and (3.19). Furthermore, since the generalised Bounded Real Lemma provides a test for the validity of a given upper bound γ on the induced-$\mathcal{L}_2$ norm, the minimisation of γ subject to the LMIs of the generalised BRL allows the norm to be computed to an arbitrary level of accuracy. For the LPV system $\boldsymbol{P}(\boldsymbol{\rho})$ defined by (3.3), an upper bound γ for $\|\boldsymbol{P}(\boldsymbol{\rho})\|_{i2}$ can be calculated by

$$\min_{\gamma, \boldsymbol{X}(\boldsymbol{p})} \gamma \quad \text{s.t.} \quad \text{(3.18) and (3.19) hold } \forall \boldsymbol{p}, \bar{\boldsymbol{p}} \in \mathcal{P} \times \dot{\mathcal{P}} \ . \tag{3.20}$$

LMI region constraints, such as the examples (3.14), (3.15) and (3.16), can be added to the optimisation to confine the eigenvalues of the system at selected frozen parameter values to the corresponding regions of $\mathbb{C}$.

It is simple to verify that the constraint (3.19) represents an LMI for any fixed value of $(\boldsymbol{p}, \bar{\boldsymbol{p}})$. Since the search space $\mathcal{P} \times \dot{\mathcal{P}}$ is continuous, and moreover the dependency of $X(\boldsymbol{\rho})$ on $\boldsymbol{\rho}$ is arbitrary, the optimisation (3.20) is intractable. In order to reduce this to a finite number of inequality constraints, so-called *relaxations* are employed. In literature, three relaxation approaches are commonly encountered, namely gridding, the full block S-procedure, and the polytopic approach.

The gridding approach approximates the parameter space $\mathcal{P}$ with a sufficiently dense grid of parameter points $\{\boldsymbol{\rho_1} \ \cdots \ \boldsymbol{\rho}_m\} \in \mathcal{P}$, while $\dot{\mathcal{P}}$ is generally assumed to be a polytope. The parametrised inequality constraints (3.18) and (3.19) are approximated by their instances at each point of the finite parameter grid. Although this approach lacks a theoretical guarantee of stability and performance due to the unknown behaviours between the grid points, in practice a sufficiently dense grid provides enough certainty for smooth

parameter dependencies. An advantage of the gridding approach is that it can be applied to arbitrary parameter dependencies of the plant matrices. Interested readers are referred to [Wu95] for details.

In contrast, the approach based on the full block S-procedure is able to guarantee stability and performance over the permissible parameter space for systems with rational parameter dependence. However, the algebraic manipulations introduce additional multipliers and hence increase the number of optimisation variables. Readers are referred to [Sch01] for further details on this method.

The third common approach is to apply polytopic relaxation, which is used in the rest of this work. This approach is restricted to systems with affine parameter dependencies. When the sets $\mathcal{P}$ and $\dot{\mathcal{P}}$ are defined by convex polytopes, the inequality constraints (3.18) and (3.19) are guaranteed to hold on its interior if they are satisfied at its vertices and certain constraints are placed on the Lyapunov matrices. The most commonly found constraint in literature is the restriction to constant Lyapunov matrices [Bec93; AGB95]. Since this corresponds to unbounded parameter rates $\dot{\boldsymbol{\rho}}$, it leads to an increase in conservatism if the parameter rates are actually bounded by low known limits. Nonetheless, if the conservatism proves to be acceptable, this represents an attractive approach for some applications due to its simplicity. Otherwise, parameter rate bounds can be incorporated via affine parameter-dependent Lyapunov matrix functions to reduce the conservatism [GAC96]. The coefficient matrices of the affine function must be chosen such that the function $\boldsymbol{A}(\boldsymbol{\rho})^T\boldsymbol{X}(\boldsymbol{\rho}) + \boldsymbol{X}(\boldsymbol{\rho})\boldsymbol{A}(\boldsymbol{\rho})$ is *multiconvex*, which can be enforced by means of LMIs. To reduce the problem complexity, this extension is not used in the remainder of this thesis. Nevertheless we refer the interested readers to [GAC96] for details.

The application of any of these relaxation approaches to the induced-$\mathcal{L}_2$ norm calculation (3.20) produces an optimisation problem with a linear objective function and an array of LMI constraints. Such an optimisation problem is known as a semi-definite program (SDP). Algorithm 3.1 presents a method to compute the induced-$\mathcal{L}_2$ norm by applying the polytopic relaxation with a constant Lyapunov matrix.

Algorithm 3.1 (Performance analysis of a polytopic LPV system)**.** *Let $\boldsymbol{P}(\boldsymbol{\rho})$ be an LPV system defined by (3.3). Let $\mathcal{P}$ be a polytope with vertices $\mathcal{V}_\rho = \{\boldsymbol{\rho}_1 \ \ldots \ \boldsymbol{\rho}_m\}$. An upper bound for the induced-$\mathcal{L}_2$ norm $\|\boldsymbol{P}(\boldsymbol{\rho})\|_{i2}$ can be calculated by:*

$$\min_{\substack{\gamma \\ \boldsymbol{X}\in\mathbb{S}^n}} \gamma \quad s.t.$$

$$\boldsymbol{X} > 0$$

$$\begin{bmatrix} \boldsymbol{A}(\boldsymbol{p})^T\boldsymbol{X} + \boldsymbol{X}\boldsymbol{A}(\boldsymbol{p}) & \boldsymbol{X}\boldsymbol{B}(\boldsymbol{p}) & \boldsymbol{C}(\boldsymbol{p})^T \\ \boldsymbol{B}(\boldsymbol{p})^T\boldsymbol{X} & -\gamma\boldsymbol{I}_d & \boldsymbol{D}(\boldsymbol{p})^T \\ \boldsymbol{C}(\boldsymbol{p}) & \boldsymbol{D}(\boldsymbol{p}) & -\gamma\boldsymbol{I}_e \end{bmatrix} < 0, \quad \forall \boldsymbol{p} \in \mathcal{V}_\rho \ .$$

3.3 Uncertain LPV systems

Up until this point only the analysis of nominal systems has been treated. Real systems are inevitably affected by uncertainties, which may have significant effects on system characteristics. The goal of robust analysis is to investigate whether stability holds over all permissible uncertainties and to determine the worst-case performance. To this end, a model of the uncertainties and their constraints is required. Detailed treatments of uncertainty modelling can be found in robust control texts such as [ZDG95]. Uncertainties can generally be divided into unmodelled dynamics and parametric uncertainties. The former type is typically characterised by unstructured complex perturbations. In this work, the uncertainties of interest are restricted to parametric uncertainties, which are manifested as dependencies of the system state matrices on the uncertain parameters $\boldsymbol{\delta}$.

This section introduces the linear fractional representation, which is used for analysis of uncertain systems and other perturbed linear systems. It allows such systems to be separated into the nominal part, whose properties can be readily analysed using results for LTI or LPV systems, and the perturbation, which has to be handled by additional measures. The integral quadratic constraint is then introduced as a means to incorporate knowledge about the uncertain component into the LPV system analysis. Subsequently the analysis of the uncertain LPV system is treated.

3.3.1 Linear Fractional Representation

The linear fractional representation (LFR) is the standard form of a dynamical system for the application of many modern robust control techniques. It consists of a feedback interconnection between the nominal and perturbed parts of a system. The LFR is based on the linear fractional transformation (LFT) which will first be described below.

Definition 3.2 (Linear fractional transformation)**.** *For a partitioned matrix*

$$\boldsymbol{M} = \left[\begin{array}{c|c} \boldsymbol{M}_{11} & \boldsymbol{M}_{12} \\ \hline \boldsymbol{M}_{21} & \boldsymbol{M}_{22} \end{array}\right] \in \mathbb{C}^{(n_v+n_e)\times(n_w+n_d)} \tag{3.21}$$

and $\Delta \in \mathbb{R}^{n_w \times n_v}$*, the upper LFT is defined as*

$$\mathcal{F}_u(\boldsymbol{M}, \Delta) := \boldsymbol{M}_{22} + \boldsymbol{M}_{21}\Delta(\boldsymbol{I} - \boldsymbol{M}_{11}\Delta)^{-1}\boldsymbol{M}_{12} \ , \tag{3.22}$$

provided that the inverse $(\boldsymbol{I} - \boldsymbol{M}_{11}\Delta)^{-1}$ *exists.*

By defining inputs $\boldsymbol{w},\ \boldsymbol{d}$ and outputs $\boldsymbol{v},\ \boldsymbol{e}$ such that

$$\begin{bmatrix} \boldsymbol{v} \\ \boldsymbol{e} \end{bmatrix} = \left[\begin{array}{c|c} \boldsymbol{M}_{11} & \boldsymbol{M}_{12} \\ \hline \boldsymbol{M}_{21} & \boldsymbol{M}_{22} \end{array}\right] \begin{bmatrix} \boldsymbol{w} \\ \boldsymbol{d} \end{bmatrix} \ ,$$

$\mathcal{F}_u(\boldsymbol{M}, \Delta)$ represents the input / output mapping from $\boldsymbol{d}$ to $\boldsymbol{e}$ in the block diagram connection in Figure 3.3.

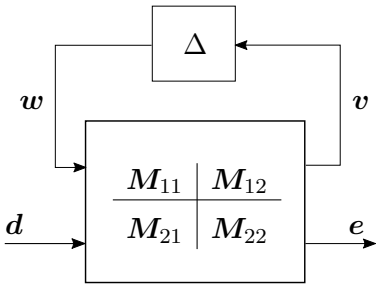

Figure 3.3: Graphical representation of an upper LFT

A linear parametric system with rational parameter dependencies can be written in its LFR form by "pulling out" the integration operator $\frac{1}{s}\boldsymbol{I}$ and the parameters into the Δ matrix [ZDG95; HV06]. Consider a system $\boldsymbol{P}_{\delta,\rho}$, which is dependent on both its uncertain parameters $\boldsymbol{\delta} = [\delta_1 \ \dots \ \delta_{n_\delta}]$ and scheduling parameters $\boldsymbol{\rho}$. It is given by

$$\boldsymbol{P}_{\delta,\rho} : \left\{ \quad \begin{bmatrix} \dot{\boldsymbol{x}} \\ \boldsymbol{e} \end{bmatrix} = \begin{bmatrix} \boldsymbol{A}_\delta(\boldsymbol{\delta},\boldsymbol{\rho}) & \boldsymbol{B}_\delta(\boldsymbol{\delta},\boldsymbol{\rho}) \\ \boldsymbol{C}_\delta(\boldsymbol{\delta},\boldsymbol{\rho}) & \boldsymbol{D}_\delta(\boldsymbol{\delta},\boldsymbol{\rho}) \end{bmatrix} \begin{bmatrix} \boldsymbol{x} \\ \boldsymbol{d} \end{bmatrix} \right. . \tag{3.23}$$

To reach the required format for the later analysis, only the parameter $\boldsymbol{\delta}$ is extracted from the state space matrices while $\boldsymbol{\rho}$ remains. The resulting LFR is represented by the interconnection of two systems with the following state space equations:

$$\left[\begin{array}{c} \dot{\boldsymbol{x}} \\ \hline \boldsymbol{v} \\ \boldsymbol{e} \end{array}\right] = \left[\begin{array}{cc|c} \bar{\boldsymbol{A}}(\boldsymbol{\rho}) & \bar{\boldsymbol{B}}_1(\boldsymbol{\rho}) & \bar{\boldsymbol{B}}_2(\boldsymbol{\rho}) \\ \bar{\boldsymbol{C}}_1(\boldsymbol{\rho}) & \bar{\boldsymbol{D}}_{11}(\boldsymbol{\rho}) & \bar{\boldsymbol{D}}_{12}(\boldsymbol{\rho}) \\ \hline \bar{\boldsymbol{C}}_2(\boldsymbol{\rho}) & \bar{\boldsymbol{D}}_{21}(\boldsymbol{\rho}) & \bar{\boldsymbol{D}}_{22}(\boldsymbol{\rho}) \end{array}\right] \left[\begin{array}{c} \boldsymbol{x} \\ \hline \boldsymbol{w} \\ \boldsymbol{d} \end{array}\right] \tag{3.24}$$

$$\boldsymbol{w} = \Delta(\boldsymbol{\delta})\boldsymbol{v} \ , \tag{3.25}$$

where $\Delta(\boldsymbol{\delta})$ has the form

$$\Delta(\boldsymbol{\delta}) = \mathrm{diag}(\delta_1 \boldsymbol{I}_{m_1} \ \dots \ \delta_{n_\delta} \boldsymbol{I}_{m_{n_\delta}}) \ . \tag{3.26}$$

The order of the LFR is defined as $\sum_{i=1}^{n_\delta} m_i$. In addition, we also have the relation $\boldsymbol{x} = \left(\frac{1}{s}\boldsymbol{I}\right)\dot{\boldsymbol{x}}$. The relations are summarised in the depiction of the LFR in Figure 3.4.

The LFR for a given system is not unique, and efficient numerical tools with symbolic pre-processing are available to generate low order LFRs (e.g. [HV06]). This is favourable because it reduces the problem sizes for the computationally intensive robust control synthesis algorithms. To use these numerical tools to extract $\boldsymbol{\delta}$ into the Δ block while keeping $\boldsymbol{\rho}$ in the state space matrices, the combined parameter vector $[\boldsymbol{\delta}^T \ \boldsymbol{\rho}^T]^T$ is first pulled out into $\Delta(\boldsymbol{\delta},\boldsymbol{\rho}) = diag(\Delta(\boldsymbol{\delta}),\Delta(\boldsymbol{\rho}))$. Then the $\Delta(\boldsymbol{\rho})$ block is reintegrated into the system matrices by symbolically applying the upper LFT (3.22) with $\Delta = \Delta(\boldsymbol{\rho})$ and appropriate partitioning.

Although the LFR has only been presented here for the treatment of rational uncertain parameters, it can also be used to represent other classes of perturbations such as

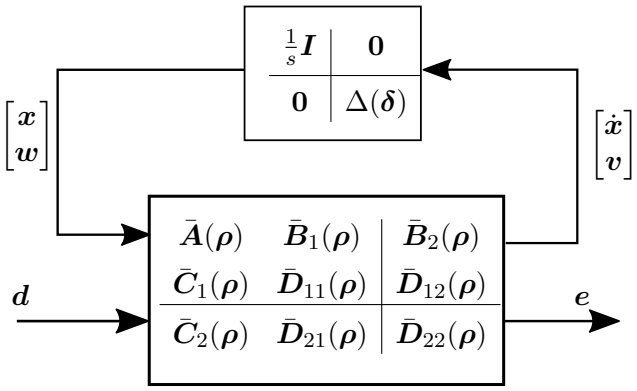

Figure 3.4: LFR of the uncertain LPV system $\boldsymbol{P}_{\delta,\rho}$

norm-bounded complex uncertainties and nonlinearities (e.g. saturation, rate limits, and deadzones). In the case of the nonlinearities, Δ is treated as a general causal operator [MR97].

For LTI systems, the well-known μ-synthesis technique can be employed to handle systems in the LFR form. However, this is not applicable for LPV systems. In this case, another powerful approach that is available to us is analysis with the help of integral quadratic constraints, and this is the subject of the next subsection.

3.3.2 Integral Quadratic Constraints (IQCs)

Integral quadratic constraints (IQCs) can be used to describe the input / output relationships of perturbations, and provide a means of incorporating such descriptions into the LMI-based framework for system analysis [MR97]. Maintaining the block and signal names from the previous section, an IQC describes $\boldsymbol{w} = \Delta\boldsymbol{v}$ (see (3.25)) by means of an inequality constraint on an integral quadratic expression on $[\boldsymbol{v}\ \boldsymbol{w}]^T$. Consider an example where Δ is a norm-bounded uncertainty, whose input and output are constrained by $\|\boldsymbol{w}\|_2 \leq b\|\boldsymbol{v}\|_2$. This can be written as

$$\int_0^\infty (b^2\boldsymbol{v}^T\boldsymbol{v} - \boldsymbol{w}^T\boldsymbol{w})dt \geq 0\ ,$$

which can be expressed in matrix form as

$$\int_0^\infty \begin{bmatrix}\boldsymbol{v}\\ \boldsymbol{w}\end{bmatrix}^T \begin{bmatrix}b^2\boldsymbol{I} & \mathbf{0}\\ \mathbf{0} & -\boldsymbol{I}\end{bmatrix} \begin{bmatrix}\boldsymbol{v}\\ \boldsymbol{w}\end{bmatrix} dt \geq 0\ .$$

In its more general form, the integral quadratic constraints are imposed not on $[\boldsymbol{v}\ \boldsymbol{w}]^T$ directly, but on a signal $\boldsymbol{q}$ produced by filtering $[\boldsymbol{v}\ \boldsymbol{w}]^T$ through a dynamic system $\boldsymbol{\Psi}$. Expressed in such a form, the information on Δ can be integrated into the LMI-based analysis framework via the dissipation inequality formulation. This is the topic of the next section.

By Parseval's theorem, an equivalent constraint holds for the Fourier transforms of $\boldsymbol{v}$ and $\boldsymbol{w}$ in the frequency domain. Now we provide a formal definition of both frequency domain and time-domain IQCs. It is more convenient to start with the former.

Definition 3.3 (Frequency domain IQC)**.** *Let $\boldsymbol{\Pi} : j\mathbb{R} \longrightarrow \mathbb{C}^{(n_v+n_w)\times(n_v+n_w)}$ be a measurable Hermitian matrix-valued function. A bounded causal operator $\Delta : \mathcal{L}_{2e}^{n_v} \to \mathcal{L}_{2e}^{n_w}$ is said to satisfy an IQC defined by $\boldsymbol{\Pi}$, if the following inequality holds for all $\boldsymbol{v} \in \mathcal{L}_{2e}^{n_v}[0,\infty)$, $\boldsymbol{w} = \Delta(\boldsymbol{v})$:*

$$\int_{-\infty}^{\infty} \begin{bmatrix} \hat{\boldsymbol{v}}(j\omega) \\ \hat{\boldsymbol{w}}(j\omega) \end{bmatrix}^* \boldsymbol{\Pi}(j\omega) \begin{bmatrix} \hat{\boldsymbol{v}}(j\omega) \\ \hat{\boldsymbol{w}}(j\omega) \end{bmatrix} d\omega \geq 0 \tag{3.27}$$

where $\hat{\boldsymbol{v}}(j\omega)$ and $\hat{\boldsymbol{w}}(j\omega)$ are the Fourier transforms of $\boldsymbol{v}$ and $\boldsymbol{w}$ respectively.

Any rational multiplier $\boldsymbol{\Pi}(j\omega)$ that is bounded on the imaginary axis $\mathbb{C}^0$ can be factorised as

$$\boldsymbol{\Pi}(j\omega) = \boldsymbol{\Psi}(j\omega)^* \boldsymbol{M} \boldsymbol{\Psi}(j\omega) \ , \tag{3.28}$$

where $\boldsymbol{\Psi}(j\omega)$ is a stable linear system and $\boldsymbol{M}$ is a symmetric real matrix. This allows the inequality (3.27) to be written in the time-domain.

Definition 3.4 (Time domain IQC)**.** *Let $\boldsymbol{\Psi}$ be a stable linear system and $\boldsymbol{M} \in \mathbb{S}^{(n_v+n_w)}$. A bounded causal operator $\Delta : \mathcal{L}_{2e}^{n_v} \to \mathcal{L}_{2e}^{n_w}$ is said to satisfy an IQC defined by $(\boldsymbol{\Psi}, \boldsymbol{M})$, denoted by $\Delta \in IQC(\boldsymbol{\Psi}, \boldsymbol{M})$, if the following inequality holds for all $\boldsymbol{v} \in \mathcal{L}_{2e}^{n_v}[0,\infty)$, $\boldsymbol{w} = \Delta(\boldsymbol{v})$:*

$$\int_0^{\infty} \boldsymbol{q}(t)^T \boldsymbol{M} \boldsymbol{q}(t) dt \geq 0 \tag{3.29}$$

where $\boldsymbol{q}$ is the output of the following linear system:

$$\boldsymbol{\Psi} : \begin{cases} \dot{\boldsymbol{x}}_\Psi = \boldsymbol{A}_\Psi \boldsymbol{x}_\Psi + \boldsymbol{B}_{\Psi 1} \boldsymbol{v} + \boldsymbol{B}_{\Psi 2} \boldsymbol{w} \\ \boldsymbol{q} = \boldsymbol{C}_\Psi \boldsymbol{x}_\Psi + \boldsymbol{D}_{\Psi 1} \boldsymbol{v} + \boldsymbol{D}_{\Psi 2} \boldsymbol{w} \\ \boldsymbol{x}_\Psi(0) = 0 \ . \end{cases} \tag{3.30}$$

If the integral in (3.29) also holds for all finite horizons $T \geq 0$, then $(\boldsymbol{\Psi}, \boldsymbol{M})$ is a hard *IQC factorisation of $\boldsymbol{\Pi}$. Otherwise it is known as a* soft *IQC factorisation.*

Figure 3.5 provides a graphical representation of the signals involved in the time-domain IQC.

The stability and performance conditions presented in the next section require the more restrictive hard IQC factorisation, which allows a dissipation inequality formulation to be applied [Sei15]. The distinction between hard and soft IQCs is discussed in more detail in [MR97; Sei15]. Here, it suffices to note that the IQCs used in this work all admit hard factorisations.

The IQCs that are satisfied by a given Δ are not unique. The class of all rational Hermitian matrix functions $\boldsymbol{\Pi}$ that define a valid IQC for a given Δ is convex and usually infinite-dimensional. Furthermore, factorisations of $\boldsymbol{\Pi}$ into $(\boldsymbol{\Psi}, \boldsymbol{M})$ are generally non-unique [MR97]. The choice of $\boldsymbol{\Pi}$ and the corresponding $(\boldsymbol{\Psi}, \boldsymbol{M})$ for relevant forms of Δ in this work will be treated later in the chapter appendix (Section 3.5.1). It will now be explained how the IQC descriptions of uncertainty can be applied to extend the LPV system analysis results from nominal to uncertain systems.

3.3.3 Robust Analysis for Uncertain LPV Systems Using IQCs

Consider an uncertain LPV system in an LFR form, given by the interconnection between the nominal plant $\boldsymbol{P}(\boldsymbol{\rho})$ and the uncertainty Δ. This interconnection is denoted by $\mathcal{F}_u(\boldsymbol{P}(\boldsymbol{\rho}), \Delta)$ and shown in Figure 3.4. Robustness analysis is concerned with determining its stability and performance, as defined in Lemmas 3.2 and 3.4, under the influence of the worst-case perturbation Δ within its permissible set $\mathcal{D}$. More specifically, an uncertain system is robustly stable if it remains stable for all permissible variations of Δ and all permissible trajectories of $\boldsymbol{\rho}$. That is,

$$\mathcal{F}_u(\boldsymbol{P}(\boldsymbol{\rho}), \Delta) \text{ is stable} \quad \forall \Delta \in \mathcal{D}, \boldsymbol{\rho} \in \mathcal{A} \ .$$

Moreover, the system achieves robust performance of γ if its induced-$\mathcal{L}_2$ norm is at most γ under those same permissible variations of Δ and $\boldsymbol{\rho}$. That is,

$$\|\mathcal{F}_u(\boldsymbol{P}(\boldsymbol{\rho}), \Delta)\|_{i2} < \gamma \qquad \forall \Delta \in \mathcal{D}, \boldsymbol{\rho} \in \mathcal{A} \ .$$

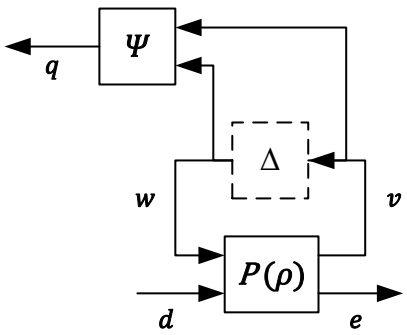

Figure 3.5: Interconnection of nominal plant $\boldsymbol{P}(\boldsymbol{\rho})$, perturbation Δ, and dynamic IQC factor $\boldsymbol{\Psi}$. The dotted outline of the Δ block indicates that it is removed in the analysis structure.

Analysis of stability and performance for uncertain systems can be tackled by extending the conditions for the nominal systems, namely the generalised Bounded Real Lemma for LPV systems, with IQCs representing the effects of uncertainties. It is assumed that an appropriate IQC multiplier $\boldsymbol{\Pi}$ and its hard IQC factorisation $\boldsymbol{\Psi}^* \boldsymbol{M} \boldsymbol{\Psi}$ have been selected. In preparation for the analysis, , the system interconnection $\mathcal{F}_u(\boldsymbol{P}(\boldsymbol{\rho}), \Delta)$ is augmented with $\boldsymbol{\Psi}$ while the Δ block is removed, turning $\boldsymbol{w}$ into an external input signal subject

to the IQC. This operation is illustrated in Figure 3.5. In the ensuing discussion, it is assumed that the resultant system $\boldsymbol{P}(\boldsymbol{\rho})\boldsymbol{\Psi}$ has the state space representation

$$\boldsymbol{P}(\boldsymbol{\rho})\boldsymbol{\Psi}: \left\{ \begin{bmatrix} \dot{\boldsymbol{x}} \\ \boldsymbol{q} \\ \boldsymbol{e} \end{bmatrix} = \begin{bmatrix} \boldsymbol{A}(\boldsymbol{\rho}) & \boldsymbol{B}_1(\boldsymbol{\rho}) & \boldsymbol{B}_2(\boldsymbol{\rho}) \\ \boldsymbol{C}_1(\boldsymbol{\rho}) & \boldsymbol{D}_{11}(\boldsymbol{\rho}) & \boldsymbol{D}_{12}(\boldsymbol{\rho}) \\ \boldsymbol{C}_2(\boldsymbol{\rho}) & \boldsymbol{D}_{21}(\boldsymbol{\rho}) & \boldsymbol{D}_{22}(\boldsymbol{\rho}) \end{bmatrix} \begin{bmatrix} \boldsymbol{x} \\ \boldsymbol{w} \\ \boldsymbol{d} \end{bmatrix} , \right. \tag{3.31}$$

where $\boldsymbol{x} = [\boldsymbol{x}_p \ \boldsymbol{x}_\Psi]^T$, with $\boldsymbol{x}_p$ being the state vector of $\boldsymbol{P}(\boldsymbol{\rho})$.

The conditions for robust stability and performance for $\mathcal{F}_u(\boldsymbol{P}(\boldsymbol{\rho}), \Delta)$ are now stated. In the following, "well-posedness" of an interconnection refers to the existence, uniqueness and continuability of the underlying differential equations [MR97]. Most problems representing meaningful physical processes can be assumed to be well-posed, based on physical plausibility [Leo68, p.223]. Applied to $\mathcal{F}_u(\boldsymbol{P}(\boldsymbol{\rho}), \Delta)$, it essentially means that it has a causal solution. Lemma 3.2 is extended by the IQC condition on Δ to give the robust stability result in Theorem 3.1.

Theorem 3.1 (Robust stability - Parameter-dependent stability with IQC [Sei15])**.** *Assume that $\mathcal{F}_u(\boldsymbol{P}(\boldsymbol{\rho}), \Delta)$ is well-posed for all $\Delta \in IQC(\boldsymbol{\Psi}, \boldsymbol{M})$, and let $\boldsymbol{P}(\boldsymbol{\rho})\boldsymbol{\Psi}$ be given by the state space equations (3.31). $\mathcal{F}_u(\boldsymbol{P}(\boldsymbol{\rho}, \Delta))$ is asymptotically stable for all $\Delta \in IQC(\boldsymbol{\Psi}, \boldsymbol{M})$ if there exists a scalar $\zeta > 0$ such that $\forall (\boldsymbol{p}, \bar{\boldsymbol{p}}) \in \mathcal{P} \times \dot{\mathcal{P}}$*

$$\boldsymbol{X}(\boldsymbol{p}) > 0 \ , \tag{3.32}$$

$$\begin{bmatrix} \boldsymbol{A}(\boldsymbol{p})^T \boldsymbol{X}(\boldsymbol{p}) + \boldsymbol{X}(\boldsymbol{p}) \boldsymbol{A}(\boldsymbol{p}) + \partial \boldsymbol{X}(\boldsymbol{p}, \bar{\boldsymbol{p}}) & \star \\ \boldsymbol{B}_1(\boldsymbol{p})^T \boldsymbol{P}(\boldsymbol{p}) & \boldsymbol{0} \end{bmatrix} + \begin{bmatrix} \boldsymbol{C}_1(\boldsymbol{p})^T \\ \boldsymbol{D}_{11}(\boldsymbol{p})^T \end{bmatrix} \zeta \boldsymbol{M} \begin{bmatrix} \boldsymbol{C}_1(\boldsymbol{p}) & \boldsymbol{D}_{11}(\boldsymbol{p}) \end{bmatrix} < 0 \ . \tag{3.33}$$

Proof. See [Sei15] for a proof based on the dissipation inequality. □

Extension of the generalised BRL in Lemma 3.4 in a similar vein arrives at the robust performance result in Theorem 3.2.

Theorem 3.2 (Robust performance - Generalised Bounded Real Lemma with IQC [PS14])**.** *Assume $\mathcal{F}_u(\boldsymbol{P}(\boldsymbol{\rho}), \Delta)$ is well-posed for all $\Delta \in IQC(\boldsymbol{\Psi}, \boldsymbol{M})$, and let $\boldsymbol{P}(\boldsymbol{\rho})\boldsymbol{\Psi}$ be given by the state space equations (3.31). Then, the interconnection is stable and its worst-case induced $\mathcal{L}_2$ gain satisfies*

$$\sup_{\Delta \in IQC(\boldsymbol{\Psi}, \boldsymbol{M})} \|\mathcal{F}_u(\boldsymbol{P}(\boldsymbol{\rho}), \Delta)\|_{i2} < \gamma$$

if there exists a scalar $\zeta > 0$ *such that* $\forall (\boldsymbol{p}, \bar{\boldsymbol{p}}) \in \mathcal{P} \times \dot{\mathcal{P}}$

$$\boldsymbol{X}(\boldsymbol{p}) > 0 \;, \tag{3.34}$$

$$\begin{bmatrix} \boldsymbol{A}(\boldsymbol{p})^T \boldsymbol{X}(\boldsymbol{p}) + \boldsymbol{X}(\boldsymbol{p}) \boldsymbol{A}(\boldsymbol{p}) + \partial \boldsymbol{X}(\boldsymbol{p}, \bar{\boldsymbol{p}}) & \star & \star & \star \\ \boldsymbol{B}_1(\boldsymbol{p})^T \boldsymbol{X}(\boldsymbol{p}) & \boldsymbol{0} & \star & \star \\ \boldsymbol{B}_2(\boldsymbol{p})^T \boldsymbol{X}(\boldsymbol{p}) & \boldsymbol{0} & -\gamma \boldsymbol{I}_{n_d} & \star \\ \boldsymbol{C}_2(\boldsymbol{p}) & \boldsymbol{D}_{21}(\boldsymbol{p}) & \boldsymbol{D}_{22}(\boldsymbol{p}) & -\gamma \boldsymbol{I}_{n_e} \end{bmatrix} + \begin{bmatrix} \boldsymbol{C}_1(\boldsymbol{p})^T \\ \boldsymbol{D}_{11}(\boldsymbol{p})^T \\ \boldsymbol{D}_{12}(\boldsymbol{p})^T \\ \boldsymbol{0} \end{bmatrix} \zeta \boldsymbol{M} \begin{bmatrix} \boldsymbol{C}_1(\boldsymbol{p}) & \boldsymbol{D}_{11}(\boldsymbol{p}) & \boldsymbol{D}_{12}(\boldsymbol{p}) & \boldsymbol{0} \end{bmatrix} < 0 \;. \tag{3.35}$$

Proof. See [PS14] for a proof based on the dissipation inequality. □

The preceding theorems are given in terms of a single IQC $(\boldsymbol{\Psi}, \boldsymbol{M})$. However, they can be readily extended to handle multiple IQCs. The reasons that this would be necessary are two-fold. The first is that in the general case, a given Δ may satisfy an infinite number of IQCs, and the form of the optimal IQC within this space for the stability or performance analysis is not known *a priori*. A tractable analysis approach is to define a finite dimensional basis of satisfied IQCs $(\boldsymbol{\Psi}_i, \boldsymbol{M}_i)$, $i = 1, \ldots, n_{IQC}$, and search for linear combinations that yield the best stability or performance result. In order to minimise conservatism in the analysis, Δ should be described as accurately as possible by the IQCs in the basis. [MR97] provides a library of frequency domain IQCs that are satisfied by many basic system components. The second source of multiple IQCs is the handling of multiple perturbations contained in Δ, each of which defines its own set of IQCs.

Each IQC $(\boldsymbol{\Psi}_i, \boldsymbol{M}_i)$ from the set corresponds to a $\boldsymbol{\Psi}_i$ that is connected to $\boldsymbol{v}$ and $\boldsymbol{w}$, and its output $\boldsymbol{q}_i$ is given by its output equation

$$\boldsymbol{q}_i = \boldsymbol{C}_{1i}(\boldsymbol{p})\boldsymbol{x} + \boldsymbol{D}_{11i}(\boldsymbol{p})\boldsymbol{w} + \boldsymbol{D}_{12i}(\boldsymbol{p})\boldsymbol{d}$$

where $\boldsymbol{x} = [\boldsymbol{x}_p \; \boldsymbol{x}_{\Psi_1} \; \ldots \; \boldsymbol{x}_{\Psi_{n_{IQC}}}]$. Theorem 3.2 is then modified by changing the second summand of (3.35) to:

$$\sum_{i=1}^{n_{IQC}} \begin{bmatrix} \boldsymbol{C}_{1i}(\boldsymbol{p})^T \\ \boldsymbol{D}_{11i}(\boldsymbol{p})^T \\ \boldsymbol{D}_{12i}(\boldsymbol{p})^T \\ \boldsymbol{0} \end{bmatrix} \zeta_i \boldsymbol{M}_i \begin{bmatrix} \boldsymbol{C}_{1i}(\boldsymbol{p}) & \boldsymbol{D}_{11i}(\boldsymbol{p}) & \boldsymbol{D}_{12i}(\boldsymbol{p}) & \boldsymbol{0} \end{bmatrix} \;.$$

Theorem 3.1 can also be adapted analogously. To bring this term into a universal form in agreement with that of the single IQC, $\boldsymbol{\Psi}$ and $\boldsymbol{M}(\boldsymbol{\zeta})$ are defined by joining the

$\boldsymbol{\Psi}_i, \boldsymbol{M}_i, \zeta_i,\ i = 1, \ldots, n_{IQC}$ as

$$\boldsymbol{\Psi} = \begin{bmatrix} \boldsymbol{\Psi}_1 \\ \vdots \\ \boldsymbol{\Psi}_r \end{bmatrix}, \quad \boldsymbol{M}(\boldsymbol{\zeta}) = \begin{bmatrix} \zeta_1 \boldsymbol{M}_1 & & \boldsymbol{0} \\ & \ddots & \\ \boldsymbol{0} & & \zeta_{n_{IQC}} \boldsymbol{M}_{n_{IQC}} \end{bmatrix}, \quad \boldsymbol{\zeta} = \begin{bmatrix} \zeta_1 \\ \vdots \\ \zeta_r \end{bmatrix}. \tag{3.36}$$

More generally, $\boldsymbol{M}(\boldsymbol{\zeta})$ is described as a matrix variable $\boldsymbol{M}$ subject to structure restrictions and LMI constraints. The notation $\boldsymbol{M}(\boldsymbol{\zeta})$ will be retained to indicate the parametrisation of this matrix variable.

Section 3.5.1 of the chapter appendix deals with the multiple IQCs arising when Δ consists of multiple blocks of repeated constant scalars. Both the issues of multiple sub-elements in Δ as well as the multi-dimensional basis for $(\boldsymbol{\Psi}, \boldsymbol{M})$ for each sub-element are treated.

From Theorem 3.2, the worst-case induced-$\mathcal{L}_2$ norm can be computed by minimising γ subject to the constraints (3.34) and (3.35). Where a polytopic approach is taken for LPV relaxation, the Lyapunov matrix functions $\boldsymbol{X}(\boldsymbol{\rho})$ are replaced by real matrices $\boldsymbol{X}$. The resulting SDP is described in Algorithm 3.2.

Algorithm 3.2 (Performance analysis of an uncertain polytopic LPV system)**.** *Let an uncertain LPV system be defined by $\mathcal{F}_u(\boldsymbol{P}(\boldsymbol{\rho}), \Delta)$, where the state space matrices of $\boldsymbol{P}(\boldsymbol{\rho})$ are affinely dependent on $\boldsymbol{\rho} \in \mathcal{P}$, with $\mathcal{P}$ a polytope with vertices $\mathcal{V}_\rho = \{\boldsymbol{\rho}_1 \ \ldots \ \boldsymbol{\rho}_m\}$. Define a list of IQCs $(\boldsymbol{\Psi}_i, \boldsymbol{M}_i),\ i = 1, \ldots, r$ that are satisfied by $\Delta \in \mathcal{D}$. Let $\boldsymbol{\Psi} = [\boldsymbol{\Psi}_1^T \ldots \boldsymbol{\Psi}_r^T]^T$, and construct the connection of $\boldsymbol{P}(\boldsymbol{\rho})\boldsymbol{\Psi}$ with the state space representation (3.31). An upper bound for the worst-case induced-$\mathcal{L}_2$ norm*

$$\sup_{\Delta \in \mathcal{D}} \|\mathcal{F}_u(\boldsymbol{P}(\boldsymbol{\rho}), \Delta)\|_{i2}$$

can be calculated by:

$$\min_{\substack{\gamma,\ \boldsymbol{\zeta} \\ \boldsymbol{X} \in \mathbb{S}^n}} \gamma \quad s.t. \tag{3.37a}$$

$$\boldsymbol{X} > 0 \tag{3.37b}$$

$$\begin{bmatrix} \boldsymbol{A}(\boldsymbol{p})^T \boldsymbol{X} + \boldsymbol{X} \boldsymbol{A}(\boldsymbol{p}) & \star & \star & \star \\ \boldsymbol{B}_1(\boldsymbol{p})^T \boldsymbol{X} & \boldsymbol{0} & \star & \star \\ \boldsymbol{B}_2(\boldsymbol{p})^T \boldsymbol{X} & \boldsymbol{0} & -\gamma \boldsymbol{I}_{n_d} & \star \\ \boldsymbol{C}_2(\boldsymbol{p}) & \boldsymbol{D}_{21}(\boldsymbol{p}) & \boldsymbol{D}_{22}(\boldsymbol{p}) & -\gamma \boldsymbol{I}_{n_e} \end{bmatrix} + \begin{bmatrix} \boldsymbol{C}_1(\boldsymbol{p})^T \\ \boldsymbol{D}_{11}(\boldsymbol{p})^T \\ \boldsymbol{D}_{12}(\boldsymbol{p})^T \\ \boldsymbol{0} \end{bmatrix} \boldsymbol{M}(\boldsymbol{\zeta}) \begin{bmatrix} \boldsymbol{C}_1(\boldsymbol{p}) & \boldsymbol{D}_{11}(\boldsymbol{p}) & \boldsymbol{D}_{12}(\boldsymbol{p}) & \boldsymbol{0} \end{bmatrix} < 0, \quad \forall \boldsymbol{p} \in \mathcal{V}_\rho \tag{3.37c}$$

with $\boldsymbol{M}(\boldsymbol{\zeta})$ defined in (3.36).

3.4 Robust LPV Estimator Synthesis

Based on the previous analysis results, we can now tackle the robust estimator synthesis problem described in the introduction. The synthesis approach presented in this section is primarily based on [VS16]. Application of Algorithm 3.2 to the plant-estimator interconnection provides the basis to search for a stable estimator that minimises the estimation error under uncertainty and parameter variation constraints. We first define the plant-estimator interconnection and the error minimisation set-up and the constraints in Algorithm 3.2 are applied to this set-up. In these steps, the generality for arbitrary parameter dependencies is maintained. The resulting optimisation problem is subsequently transformed into an SDP by applying the polytopic relaxation followed by a convex transformation. After the SDP is solved, the estimator state space matrices are then recovered from the solution. This section describes each of these steps and summarises them into a procedure at the end.

3.4.1 Estimator Synthesis Formulation

Consider the set up in Figure 3.6. The uncertain plant $\boldsymbol{P}(\boldsymbol{\rho}, \Delta)$ is formed by the interconnection of a stable nominal plant $\bar{\boldsymbol{P}}(\boldsymbol{\rho})$ and a bounded perturbation Δ. The to-be-synthesised LPV estimator $\boldsymbol{F}(\boldsymbol{\rho})$ computes the estimate of the auxiliary plant output $\boldsymbol{z}$, denoted $\hat{\boldsymbol{z}}$, from the measurable plant outputs $\bar{\boldsymbol{y}}$. The estimator synthesis task involves finding a $\boldsymbol{F}(\boldsymbol{\rho})$ which minimises the estimation error $\boldsymbol{e} = \boldsymbol{z} - \hat{\boldsymbol{z}}$ in the face of bounded disturbances $\bar{\boldsymbol{d}}$ and perturbations Δ. Let the state-space model of $\bar{\boldsymbol{P}}(\boldsymbol{\rho})$ has the following form:

$$\bar{\boldsymbol{P}}(\boldsymbol{\rho}) : \begin{cases} \dot{\bar{\boldsymbol{x}}} = \bar{\boldsymbol{A}}(\boldsymbol{\rho})\bar{\boldsymbol{x}} + \bar{\boldsymbol{B}}_1(\boldsymbol{\rho})\boldsymbol{w} + \bar{\boldsymbol{B}}_2(\boldsymbol{\rho})\bar{\boldsymbol{d}} \\ \boldsymbol{v} = \bar{\boldsymbol{C}}_1(\boldsymbol{\rho})\bar{\boldsymbol{x}} + \bar{\boldsymbol{D}}_{11}(\boldsymbol{\rho})\boldsymbol{w} + \bar{\boldsymbol{D}}_{12}(\boldsymbol{\rho})\bar{\boldsymbol{d}} \\ \bar{\boldsymbol{y}} = \bar{\boldsymbol{C}}_2(\boldsymbol{\rho})\bar{\boldsymbol{x}} + \bar{\boldsymbol{D}}_{21}(\boldsymbol{\rho})\boldsymbol{w} + \bar{\boldsymbol{D}}_{22}(\boldsymbol{\rho})\bar{\boldsymbol{d}} \\ \boldsymbol{z} = \bar{\boldsymbol{C}}_3(\boldsymbol{\rho})\bar{\boldsymbol{x}} + \bar{\boldsymbol{D}}_{31}(\boldsymbol{\rho})\boldsymbol{w} + \bar{\boldsymbol{D}}_{32}(\boldsymbol{\rho})\bar{\boldsymbol{d}} \end{cases} \tag{3.38}$$

This structure is related to (3.24), but the output $\boldsymbol{e}$ of that system is replaced by the partitioned vector $[\bar{\boldsymbol{y}}^T \ \boldsymbol{z}^T]^T$, $\boldsymbol{d}$ is replaced by $\bar{\boldsymbol{d}}$, and the state space matrices are adapted accordingly. The first change relates to splitting the plant output into the measurement output $\bar{\boldsymbol{y}}$ and the signals to be estimated, denoted auxiliary output $\boldsymbol{z}$. The second change provides consistency with the next chapter, where $\bar{\boldsymbol{d}}$ is an augmented disturbance containing not only the physical disturbances.

Applying the analysis procedure from the previous section, the analysis structure is created by removing Δ and connecting its input $\boldsymbol{v}$ and output $\boldsymbol{w}$ to the IQC factor $\boldsymbol{\Psi}$, which has the state-space representation in (3.30). These additions are shown in dotted

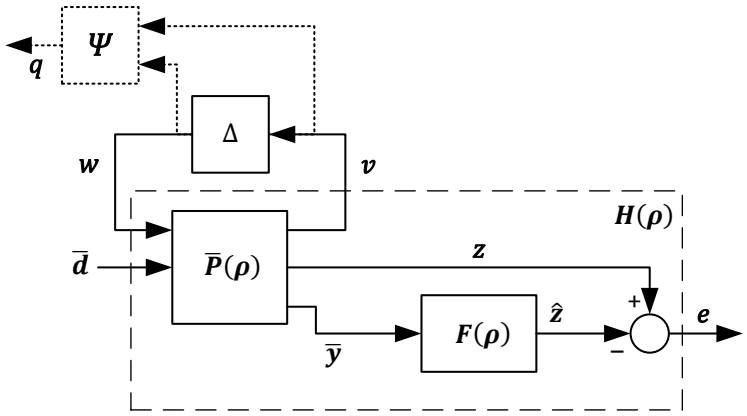

Figure 3.6: Block diagram of the set up for the synthesis of estimator $\boldsymbol{F}(\boldsymbol{\rho})$. The factor $\boldsymbol{\Psi}$ is added to create the IQC analysis structure.

lines in Figure 3.6. The connection of $\bar{\boldsymbol{P}}(\boldsymbol{\rho})$ and $\boldsymbol{\Psi}$ is given by:

$$\bar{\boldsymbol{P}}(\boldsymbol{\rho})\boldsymbol{\Psi}: \begin{cases} \dot{\boldsymbol{x}} = \boldsymbol{A}(\boldsymbol{\rho})\boldsymbol{x} + \boldsymbol{B}_1(\boldsymbol{\rho})\boldsymbol{w} + \boldsymbol{B}_2(\boldsymbol{\rho})\bar{\boldsymbol{d}} \\ \boldsymbol{q} = \boldsymbol{C}_1(\boldsymbol{\rho})\boldsymbol{x} + \boldsymbol{D}_{11}(\boldsymbol{\rho})\boldsymbol{w} + \boldsymbol{D}_{12}(\boldsymbol{\rho})\bar{\boldsymbol{d}} \\ \bar{\boldsymbol{y}} = \boldsymbol{C}_2(\boldsymbol{\rho})\boldsymbol{x} + \boldsymbol{D}_{21}(\boldsymbol{\rho})\boldsymbol{w} + \boldsymbol{D}_{22}(\boldsymbol{\rho})\bar{\boldsymbol{d}} \\ \boldsymbol{z} = \boldsymbol{C}_3(\boldsymbol{\rho})\boldsymbol{x} + \boldsymbol{D}_{31}(\boldsymbol{\rho})\boldsymbol{w} + \boldsymbol{D}_{32}(\boldsymbol{\rho})\bar{\boldsymbol{d}} \end{cases} \tag{3.39}$$

where

$$\boldsymbol{x} = \begin{bmatrix} \bar{\boldsymbol{x}} \\ \boldsymbol{x}_\Psi \end{bmatrix}, \quad \boldsymbol{A} = \begin{bmatrix} \bar{\boldsymbol{A}} & 0 \\ \boldsymbol{B}_{\Psi 1}\bar{\boldsymbol{C}}_1 & \boldsymbol{A}_\Psi \end{bmatrix}, \quad \boldsymbol{B}_1 = \begin{bmatrix} \bar{\boldsymbol{B}}_1 \\ \boldsymbol{B}_{\Psi 2} + \boldsymbol{B}_{\Psi 1}\bar{\boldsymbol{D}}_{11} \end{bmatrix}, \quad \boldsymbol{B}_2 = \begin{bmatrix} \bar{\boldsymbol{B}}_2 \\ \boldsymbol{B}_{\Psi 1}\bar{\boldsymbol{D}}_{12} \end{bmatrix},$$
$$\boldsymbol{C}_1 = \begin{bmatrix} \boldsymbol{D}_{\Psi 1}\bar{\boldsymbol{C}}_1 & \boldsymbol{C}_\Psi \end{bmatrix}, \quad \boldsymbol{D}_{11} = \boldsymbol{D}_{\Psi 2} + \boldsymbol{D}_{\Psi 1}\bar{\boldsymbol{D}}_{11}, \quad \boldsymbol{D}_{12} = \boldsymbol{D}_{\Psi 1}\bar{\boldsymbol{D}}_{12},$$
$$\boldsymbol{C}_2 = \begin{bmatrix} \bar{\boldsymbol{C}}_2 & 0 \end{bmatrix}, \quad \boldsymbol{D}_{21} = \bar{\boldsymbol{D}}_{21}, \quad \boldsymbol{D}_{22} = \bar{\boldsymbol{D}}_{22},$$
$$\boldsymbol{C}_3 = \begin{bmatrix} \bar{\boldsymbol{C}}_3 & 0 \end{bmatrix}, \quad \boldsymbol{D}_{31} = \bar{\boldsymbol{D}}_{31}, \quad \boldsymbol{D}_{32} = \bar{\boldsymbol{D}}_{32}\ .$$

The estimator $\boldsymbol{F}(\boldsymbol{\rho})$ has a form given by:

$$\boldsymbol{F}(\boldsymbol{\rho}): \begin{cases} \dot{\boldsymbol{x}}_F = \boldsymbol{A}_F(\boldsymbol{\rho})\boldsymbol{x}_F + \boldsymbol{B}_F(\boldsymbol{\rho})\bar{\boldsymbol{y}} \\ \hat{\boldsymbol{z}} = \boldsymbol{C}_F(\boldsymbol{\rho})\boldsymbol{x}_F + \boldsymbol{D}_F(\boldsymbol{\rho})\bar{\boldsymbol{y}}\ . \end{cases} \tag{3.40}$$

The nominal closed-loop system $\boldsymbol{H}(\boldsymbol{\rho})$ consists of $\bar{\boldsymbol{P}}(\boldsymbol{\rho})$, $\boldsymbol{F}(\boldsymbol{\rho})$, and the difference block $\boldsymbol{e} = \boldsymbol{z} - \hat{\boldsymbol{z}}$, connected as shown in Figure 3.6. Applying Theorem 3.2 to $\mathcal{F}_u(\boldsymbol{H}(\boldsymbol{\rho}), \Delta)$ provides a way to verify an upper bound γ on the robust performance

$$\sup_{\substack{\boldsymbol{\rho}\in\mathcal{P},\Delta\in\mathcal{D} \\ \bar{\boldsymbol{d}}\in\mathcal{L}_2}} \frac{\|\boldsymbol{e}\|_2}{\|\bar{\boldsymbol{d}}\|_2} = \sup_{\Delta\in\mathcal{D}} \|\mathcal{F}_u\left(\boldsymbol{H}(\boldsymbol{\rho}), \Delta\right)\|_{i2} < \gamma\ . \tag{3.41}$$

To do this, we create the interconnection of $\boldsymbol{H}(\boldsymbol{\rho})$ with $\boldsymbol{\Psi}$, giving the analysis structure analogous to that in (3.31). It has the state space representation given by

$$\boldsymbol{H}(\boldsymbol{\rho})\boldsymbol{\Psi}: \left\{ \quad \begin{bmatrix} \dot{\boldsymbol{x}}_e \\ \hline \boldsymbol{q} \\ \boldsymbol{e} \end{bmatrix} = \left[\begin{array}{c|cc} \boldsymbol{A}_e & \boldsymbol{B}_{1e} & \boldsymbol{B}_{2e} \\ \hline \boldsymbol{C}_{1e} & \boldsymbol{D}_{11e} & \boldsymbol{D}_{12e} \\ \boldsymbol{C}_{2e} & \boldsymbol{D}_{21e} & \boldsymbol{D}_{22e} \end{array}\right] \begin{bmatrix} \boldsymbol{x}_e \\ \hline \boldsymbol{w} \\ \bar{\boldsymbol{d}} \end{bmatrix} \right. \tag{3.42}$$

where

$$\begin{aligned} &\boldsymbol{x}_e = \begin{bmatrix} \boldsymbol{x} \\ \boldsymbol{x}_F \end{bmatrix}, \quad \boldsymbol{A}_e = \begin{bmatrix} \boldsymbol{A} & \boldsymbol{0} \\ \boldsymbol{B}_F\boldsymbol{C}_2 & \boldsymbol{A}_F \end{bmatrix}, \quad \boldsymbol{B}_{1e} = \begin{bmatrix} \boldsymbol{B}_1 \\ \boldsymbol{B}_F\boldsymbol{D}_{21} \end{bmatrix}, \quad \boldsymbol{B}_{2e} = \begin{bmatrix} \boldsymbol{B}_2 \\ \boldsymbol{B}_F\boldsymbol{D}_{22} \end{bmatrix}, \\ &\boldsymbol{C}_{1e} = \begin{bmatrix} \boldsymbol{C}_1 & \boldsymbol{0} \end{bmatrix}, \quad \boldsymbol{D}_{11e} = \boldsymbol{D}_{11}, \quad \boldsymbol{D}_{12e} = \boldsymbol{D}_{12}, \\ &\boldsymbol{C}_{2e} = \begin{bmatrix} (\boldsymbol{C}_3 - \boldsymbol{D}_F\boldsymbol{C}_2) & -\boldsymbol{C}_F \end{bmatrix}, \ \boldsymbol{D}_{21e} = \boldsymbol{D}_{31} - \boldsymbol{D}_F\boldsymbol{D}_{21}, \ \boldsymbol{D}_{22e} = \boldsymbol{D}_{32} - \boldsymbol{D}_F\boldsymbol{D}_{22}\ . \end{aligned} \tag{3.43}$$

Then, the matrix inequality to be satisfied in Theorem 3.2, corresponding to (3.35), reads

$$\begin{aligned} &\begin{bmatrix} \boldsymbol{A}_e(\boldsymbol{p})^T\boldsymbol{X}(\boldsymbol{p}) + \boldsymbol{X}(\boldsymbol{p})\boldsymbol{A}_e(\boldsymbol{p}) + \partial\boldsymbol{X}(\boldsymbol{p},\bar{\boldsymbol{p}}) & \star & \star & \star \\ \boldsymbol{B}_{1e}(\boldsymbol{p})^T\boldsymbol{X}(\boldsymbol{p}) & \boldsymbol{0} & \star & \star \\ \boldsymbol{B}_{2e}(\boldsymbol{p})^T\boldsymbol{X}(\boldsymbol{p}) & \boldsymbol{0} & -\gamma\boldsymbol{I}_{n_{\bar{d}}} & \boldsymbol{0} \\ \boldsymbol{C}_{2e}(\boldsymbol{p}) & \boldsymbol{D}_{21e}(\boldsymbol{p}) & \boldsymbol{D}_{22e}(\boldsymbol{p}) & -\gamma\boldsymbol{I}_{n_z} \end{bmatrix} \\ &\quad + \begin{bmatrix} \boldsymbol{C}_{1e}(\boldsymbol{p})^T \\ \boldsymbol{D}_{11e}(\boldsymbol{p})^T \\ \boldsymbol{D}_{12e}(\boldsymbol{p})^T \\ \boldsymbol{0} \end{bmatrix} \boldsymbol{M}(\boldsymbol{\zeta}) \begin{bmatrix} \boldsymbol{C}_{1e}(\boldsymbol{p}) & \boldsymbol{D}_{11e}(\boldsymbol{p}) & \boldsymbol{D}_{12e}(\boldsymbol{p}) & \boldsymbol{0} \end{bmatrix} < 0\ , \end{aligned} \tag{3.44}$$

where $\boldsymbol{\zeta}\boldsymbol{M}$ is replaced by $\boldsymbol{M}(\boldsymbol{\zeta})$ to account for multiple IQCs.

The other constraint $\boldsymbol{X}(\boldsymbol{p}) > 0$ from Theorem 3.2 is treated differently here, according to the argument in [VS16]. First observe that the estimator does not influence plant dynamics, as confirmed by the coupling term at the $(1,2)$ block of A_e being zero. This, together with the assumption that both $\bar{\boldsymbol{P}}(\boldsymbol{\rho})$ and $\boldsymbol{\Psi}$ are stable, means that only a sub-block of $\boldsymbol{X}(\boldsymbol{\rho})$ corresponding to $\boldsymbol{A}_F(\boldsymbol{\rho})$ must be verified to be positive definite to ensure the stability of $\boldsymbol{F}(\boldsymbol{\rho})$.

To show this, the Lyapunov matrix function $\boldsymbol{X} : \mathcal{P} \to \mathbb{S}^{2n}$ is first partitioned into sub-matrices $\boldsymbol{X}_1 : \mathcal{P} \to \mathbb{S}^n, \boldsymbol{X}_2 : \mathcal{P} \to \mathbb{R}^{n\times n}, \boldsymbol{X}_3 : \mathcal{P} \to \mathbb{S}^n$ as

$$\boldsymbol{X}(\boldsymbol{p}) = \begin{bmatrix} \boldsymbol{X}_1(\boldsymbol{p}) & \boldsymbol{X}_2(\boldsymbol{p}) \\ \boldsymbol{X}_2(\boldsymbol{p})^T & \boldsymbol{X}_3(\boldsymbol{p}) \end{bmatrix}\ . \tag{3.45}$$

Then substitute (3.45) together with the definition of $\boldsymbol{A}_e(\boldsymbol{p})$ and $\boldsymbol{C}_{1e}(\boldsymbol{p})$ from (3.43) into the $(1,1)$ block of the matrix term in (3.44). It can be readily shown that the southeast

sub-block of the $(1,1)$ block of the LMI (3.44) implies

$$\boldsymbol{A}_F(\boldsymbol{p})^T \boldsymbol{X}_3(\boldsymbol{p}) + \boldsymbol{X}_3(\boldsymbol{p})\boldsymbol{A}_F(\boldsymbol{p}) + \partial \boldsymbol{X}_3(\boldsymbol{p}, \bar{\boldsymbol{p}}) < 0 \ , \tag{3.46}$$

because every principle submatrix of a negative definite matrix must also be negative definite [Gan77, p.307]. Hence, enforcing

$$\boldsymbol{X}_3(\boldsymbol{p}) > 0 \tag{3.47}$$

for all $\boldsymbol{p} \in \mathcal{P}$ ensures the stability of $\boldsymbol{A}_F(\boldsymbol{\rho})$ by the condition for parameter-dependent stability (see Lemma 3.2).

With the performance and stability requirements now expressed in LMIs, the estimator $\boldsymbol{F}(\boldsymbol{\rho})$ can be synthesised from the optimisation problem

$$\min_{\boldsymbol{F},\boldsymbol{X},\boldsymbol{M}(\boldsymbol{\zeta}),\gamma} \gamma \quad \text{s.t. (3.44) and (3.47) are satisfied } \forall (\boldsymbol{p}, \bar{\boldsymbol{p}}) \in \mathcal{P} \times \dot{\mathcal{P}} \ . \tag{3.48}$$

3.4.2 Solving the Optimisation

Even with an appropriate LPV relaxation, (3.48) does not yet constitute an SDP since (3.44) contains product terms between the state space matrices of $\{\boldsymbol{A}_F(\boldsymbol{p}), \boldsymbol{B}_F(\boldsymbol{p}), \boldsymbol{C}_F(\boldsymbol{p}), \boldsymbol{D}_F(\boldsymbol{p})\}$ and $\boldsymbol{X}(\boldsymbol{\rho})$, all of which are optimisation variables. To obtain an expression affine in the decision variables as required by an LMI, a convexification procedure employed in [SK08] and [VS16] is applied to (3.44).

Although the congruence transformation and the existence conditions of the estimator $\boldsymbol{F}(\boldsymbol{\rho})$ are valid for parameter-dependent Lyapunov functions (see [VS16]), from this point onwards results will be presented for the polytopic relaxation, which uses a constant Lyapunov matrix $\boldsymbol{X}$.

Define the transformation matrix $\boldsymbol{T}$, where

$$\boldsymbol{T} := \begin{bmatrix} \boldsymbol{I}_n & \boldsymbol{I}_n & \boldsymbol{0} \\ -\boldsymbol{X}_3^{-1}\boldsymbol{X}_2^T & \boldsymbol{0} & \boldsymbol{0} \\ \boldsymbol{0} & \boldsymbol{0} & \boldsymbol{I}_{(n_w+n_z+n_{\tilde{d}})} \end{bmatrix} . \tag{3.49}$$

The congruence transformation right / left multiplies (3.44) by $\boldsymbol{T}$ and $\boldsymbol{T}^T$ respectively, which yields the inequality

$$\begin{bmatrix} \boldsymbol{A}^T\boldsymbol{Y}+\boldsymbol{Y}\boldsymbol{A} & \star & \star & \star & \star \\ \boldsymbol{A}^T\boldsymbol{Y}+\boldsymbol{X}_1\boldsymbol{A}+\bar{\boldsymbol{A}} & (\boldsymbol{A}^T\boldsymbol{X}_1+\bar{\boldsymbol{B}}\boldsymbol{C}_2)+(\star) & \star & \star & \star \\ \boldsymbol{B}_1^T\boldsymbol{Y} & \boldsymbol{B}_1^T\boldsymbol{X}_1+\boldsymbol{D}_{21}^T\bar{\boldsymbol{B}}^T & \boldsymbol{0} & \star & \star \\ \boldsymbol{B}_2^T\boldsymbol{Y} & \boldsymbol{B}_2^T\boldsymbol{X}_1+\boldsymbol{D}_{22}^T\bar{\boldsymbol{B}}^T & \boldsymbol{0} & -\gamma\boldsymbol{I}_{n_{\bar{d}}} & \star \\ \boldsymbol{C}_3-\boldsymbol{D}_F\boldsymbol{C}_2-\bar{\boldsymbol{C}} & \boldsymbol{C}_3-\boldsymbol{D}_F\boldsymbol{C}_2 & \boldsymbol{D}_{31}-\boldsymbol{D}_F\boldsymbol{D}_{21} & \boldsymbol{D}_{32}-\boldsymbol{D}_F\boldsymbol{D}_{22} & -\gamma\boldsymbol{I}_{n_z} \end{bmatrix} + (\star)\boldsymbol{M}(\boldsymbol{\zeta}) \begin{bmatrix} \boldsymbol{C}_1 & \boldsymbol{C}_1 & \boldsymbol{D}_{11} & \boldsymbol{D}_{12} & \boldsymbol{0} \end{bmatrix} < 0 \tag{3.50}$$

with the following changes of variables:

$$\boldsymbol{Y} := \boldsymbol{X}_1 - \boldsymbol{X}_2\boldsymbol{X}_3^{-1}\boldsymbol{X}_2^T \tag{3.51}$$

$$\bar{\boldsymbol{A}} := \boldsymbol{X}_2(\boldsymbol{B}_F\boldsymbol{C}_2 - \boldsymbol{A}_F\boldsymbol{X}_3^{-1}\boldsymbol{X}_2^T) \tag{3.52}$$

$$\bar{\boldsymbol{B}} := \boldsymbol{X}_2\boldsymbol{B}_F \tag{3.53}$$

$$\bar{\boldsymbol{C}} := -\boldsymbol{C}_F\boldsymbol{X}_3^{-1}\boldsymbol{X}_2^T \ . \tag{3.54}$$

The dependence of the matrices on $\boldsymbol{\rho}$ is suppressed to limit the width of the expression.

Then, using a congruence transformation and the change of variable (3.51), $\boldsymbol{X}_3 > 0$ is transformed as follows:

$$\boldsymbol{X}_3 > 0 \Leftrightarrow \boldsymbol{X}_2\boldsymbol{X}_3^{-1}\boldsymbol{X}_2^T > 0 \tag{3.55a}$$

$$\Leftrightarrow \boldsymbol{X}_1 - \boldsymbol{Y} > 0 \ . \tag{3.55b}$$

It is simple to verify that both (3.50) and (3.55b) is, as required for an LMI, affine in the set of variables $\{\bar{\boldsymbol{A}}(\boldsymbol{p}), \bar{\boldsymbol{B}}(\boldsymbol{p}), \bar{\boldsymbol{C}}(\boldsymbol{p}), \boldsymbol{D}_F(\boldsymbol{p}), \boldsymbol{X}_1, \boldsymbol{Y}, \boldsymbol{M}(\boldsymbol{\zeta}), \gamma\}$. This set forms the decision variables in the optimisation.

A further prerequisite for the application of the polytopic relaxation is that (3.50) must be affine in $\boldsymbol{\rho}$. Affineness of (3.50) in $\boldsymbol{\rho}$ demands that no product terms exist between parameter-varying matrices. This is achieved by imposing a constraint for the state space matrices $\boldsymbol{C}_2, \boldsymbol{D}_{21}, \boldsymbol{D}_{22}$ to be parameter-independent. This requirement is not as restrictive as it first appears, as filtering the output of a non-compliant system through signal post-processing would accomplish this [AGB95]. Additionally, it is necessary to define $\boldsymbol{F}(\boldsymbol{\rho})$ to be affine in $\boldsymbol{\rho}$, and this characteristic is then inherited by $\bar{\boldsymbol{A}}(\boldsymbol{p}), \bar{\boldsymbol{B}}(\boldsymbol{p}), \bar{\boldsymbol{C}}(\boldsymbol{p})$ through the affine changes of variables (3.51)-(3.54).

The state space matrices of $\boldsymbol{F}(\boldsymbol{\rho})$ are defined to be convex combinations of those of the vertex estimators, each denoted as $\boldsymbol{F}_i(\boldsymbol{\rho}),\ i = 1, \ldots, m$, yielding:

$$\begin{aligned} \boldsymbol{A}_F &= \sum_{i=1}^{m} \vartheta_i(\boldsymbol{\rho}) \boldsymbol{A}_{F,i} \qquad \boldsymbol{B}_F = \sum_{i=1}^{m} \vartheta_i(\boldsymbol{\rho}) \boldsymbol{B}_{F,i} \\ \boldsymbol{C}_F &= \sum_{i=1}^{m} \vartheta_i(\boldsymbol{\rho}) \boldsymbol{C}_{F,i} \qquad \boldsymbol{D}_F = \sum_{i=1}^{m} \vartheta_i(\boldsymbol{\rho}) \boldsymbol{D}_{F,i} \end{aligned} \tag{3.56}$$

where m is the number of vertices and $\vartheta_i(\boldsymbol{\rho})$ are parameter-dependent interpolation coefficients such that

$$\sum_{i=1}^{m} \vartheta_i(\boldsymbol{\rho}) = 1 \quad \forall \boldsymbol{\rho} \in \mathcal{P} \tag{3.57}$$

$$0 \leq \vartheta_i(\boldsymbol{\rho}) \leq 1, \quad i = 1, \ldots, m\ , \tag{3.58}$$

and at the k-th vertex where $\boldsymbol{\rho} = \boldsymbol{\rho}_k$,

$$\vartheta_i(\boldsymbol{\rho}_k) = \begin{cases} 1, & i = k \\ 0, & \text{otherwise}\ . \end{cases}$$

With the prerequisites satisfied, by the polytopic assumption the parameter-dependent LMIs (3.50) and (3.55b) are equivalent to the set of *vertex LMIs*. These are formed by evaluating the parameter-dependent LMIs at each vertex of the parameter polytope, and each such *vertex LMI* contains the decision variables $\{\bar{\boldsymbol{A}}_i, \bar{\boldsymbol{B}}_i, \bar{\boldsymbol{C}}_i, \boldsymbol{D}_{F,i}\}$ corresponding to that vertex alongside the common decision variables $\{\boldsymbol{X}_1, \boldsymbol{Y}, \boldsymbol{M}(\boldsymbol{\zeta}), \gamma\}$. Theorem 3.3 summarises the existence conditions for a stable estimator with the required performance.

Theorem 3.3 (Robust LPV estimator)**.** *Let an uncertain LPV system be defined by $\mathcal{F}_u(\bar{\boldsymbol{P}}(\boldsymbol{\rho}), \Delta)$, where $\bar{\boldsymbol{P}}(\boldsymbol{\rho})$ has the form (3.38) and is parametrically stable and affinely dependent on $\boldsymbol{\rho} \in \mathcal{P}$, with $\mathcal{P}$ a polytope with vertices $\mathcal{V}_\rho = \{\boldsymbol{\rho}_1\ \ldots\ \boldsymbol{\rho}_m\}$. Moreover, its plant matrices $\bar{\boldsymbol{C}}_2$, $\bar{\boldsymbol{D}}_{21}$ and $\bar{\boldsymbol{D}}_{22}$ are parameter-independent. Let $\Delta \in \mathcal{D}$ satisfy the IQCs defined by $(\boldsymbol{\Psi}, \boldsymbol{M}(\boldsymbol{\zeta}))$. The connection $\bar{\boldsymbol{P}}(\boldsymbol{\rho})\boldsymbol{\Psi}$ has the state space representation in (3.39).*

Then there exists a stable polytopic estimator

$$\boldsymbol{F}(\boldsymbol{\rho}) = \sum_{i=1}^{m} \vartheta_i(\boldsymbol{\rho}) \boldsymbol{F}_i$$

such that the system from disturbance $\bar{\boldsymbol{d}}$ to estimation error $\boldsymbol{e}$, denoted $\mathcal{F}_u(\boldsymbol{H}(\boldsymbol{\rho}), \Delta)$ and formed by connecting $\bar{\boldsymbol{P}}(\boldsymbol{\rho})$, $\boldsymbol{F}(\boldsymbol{\rho})$ and Δ according to Figure 3.6, satisfies

$$\sup_{\Delta \in IQC(\boldsymbol{\Psi}, \boldsymbol{M}(\boldsymbol{\zeta}))} \|\mathcal{F}_u(\boldsymbol{H}(\boldsymbol{\rho}), \Delta)\|_{i2} < \gamma \tag{3.59}$$

if there exist

i) $\bar{\boldsymbol{A}}_i, \bar{\boldsymbol{B}}_i, \bar{\boldsymbol{C}}_i, \boldsymbol{D}_{F,i}$ for $i = 1, \ldots, m$,

ii) $\boldsymbol{X}_1, \boldsymbol{Y}, \boldsymbol{M}(\boldsymbol{\zeta})$, *and*
iii) $\gamma > 0$,

such that (3.50) *and* (3.55b) *hold for all* $\boldsymbol{p} \in \mathcal{V}_\rho$.

In addition to the robust stability and performance constraints, the dynamics of the estimator can be shaped by restricting the eigenvalues of $\boldsymbol{A}_{F,i}$ to desired regions of the complex plane using *LMI regions*. Here the regions presented in Section 3.2.2 are included. The associated LMI constraints are applied to $\boldsymbol{A}_{F,i}$ and $\boldsymbol{X}_3$. Any occurrence of the term $\boldsymbol{X}_3\boldsymbol{A}_{F,i}$ is transformed into the decision variables by left / right multiplying the LMIs by $\boldsymbol{X}_2(\boldsymbol{X}_3^{-1})^T$ and its transpose respectively. The transformed LMIs for the i-th vertex are

Constraint : **LMI**

$$Re(s) > \alpha_1 : 2\alpha_1(\boldsymbol{X}_1 - \boldsymbol{Y}) - (\bar{\boldsymbol{B}}_i\boldsymbol{C}_2 - \bar{\boldsymbol{A}}_i) - (\bar{\boldsymbol{B}}_i\boldsymbol{C}_2 - \bar{\boldsymbol{A}}_i)^T < 0 \tag{3.60}$$

$$Re(s) < \alpha_2 : -2\alpha_2(\boldsymbol{X}_1 - \boldsymbol{Y}) + (\bar{\boldsymbol{B}}_i\boldsymbol{C}_2 - \bar{\boldsymbol{A}}_i) + (\bar{\boldsymbol{B}}_i\boldsymbol{C}_2 - \bar{\boldsymbol{A}}_i)^T < 0 \tag{3.61}$$

$$\tan(\theta) < \frac{|Im(s)|}{-Re(s)} : \begin{bmatrix} \sin(\theta)\boldsymbol{V}_{pT,i} & \cos(\theta)\boldsymbol{V}_{nT,i} \\ -\cos(\theta)\boldsymbol{V}_{nT,i} & \sin(\theta)\boldsymbol{V}_{pT,i} \end{bmatrix} < 0 \tag{3.62}$$

where

$$\boldsymbol{V}_{pT,i} = (\bar{\boldsymbol{B}}_i\boldsymbol{C}_2 - \bar{\boldsymbol{A}}_i) + (\bar{\boldsymbol{B}}_i\boldsymbol{C}_2 - \bar{\boldsymbol{A}}_i)^T$$
$$\boldsymbol{V}_{nT,i} = (\bar{\boldsymbol{B}}_i\boldsymbol{C}_2 - \bar{\boldsymbol{A}}_i) - (\bar{\boldsymbol{B}}_i\boldsymbol{C}_2 - \bar{\boldsymbol{A}}_i)^T$$

The estimator is synthesised by solving an SDP to minimise γ subject to the constraints stated in Theorem 3.3, and optionally the LMI region constraints. From the solutions for the decision variables, the Lyapunov matrices and the estimator matrices are reconstructed. The reconstruction of $\boldsymbol{X}_2$ and $\boldsymbol{X}_3$ is actually underdetermined through (3.51), and this freedom is used to choose $\boldsymbol{X}_3 = \boldsymbol{I}$ as proposed in [VS16]. Then (3.51) is rewritten as

$$\boldsymbol{X}_2\boldsymbol{X}_2^T = \boldsymbol{X}_1 - \boldsymbol{Y} \ , \tag{3.63}$$

allowing $\boldsymbol{X}_2$ to be determined using a Cholesky factorisation from the known solution variables $\boldsymbol{X}_1$ and $\boldsymbol{Y}$. Subsequently the state space matrices of $\boldsymbol{F}_i$ are reconstructed from $\{\bar{\boldsymbol{A}}_i, \bar{\boldsymbol{B}}_i, \bar{\boldsymbol{C}}_i, \boldsymbol{D}_{F,i}\}$ by:

$$\boldsymbol{C}_{F,i} = -\bar{\boldsymbol{C}}_i(\boldsymbol{X}_2^T)^{-1}\boldsymbol{X}_3 \tag{3.64}$$

$$\boldsymbol{B}_{F,i} = \boldsymbol{X}_2^{-1}\bar{\boldsymbol{B}}_i \tag{3.65}$$

$$\boldsymbol{A}_{F,i} = \boldsymbol{X}_2^{-1}(\bar{\boldsymbol{B}}_i\boldsymbol{C}_2 - \bar{\boldsymbol{A}}_i)(\boldsymbol{X}_2^T)^{-1}\boldsymbol{X}_3 \ . \tag{3.66}$$

$\boldsymbol{D}_{F,i}$ is directly a decision variable and no reconstruction is necessary.

During execution, the state space matrices of $\boldsymbol{F}(\boldsymbol{\rho})$ are computed by interpolation from these vertex estimator matrices using (3.56). The expression is provided below again for

convenient reference.

$$\boldsymbol{F}(\boldsymbol{\rho}) = \left[\begin{array}{c|c} \boldsymbol{A}_F(\boldsymbol{\rho}) & \boldsymbol{B}_F(\boldsymbol{\rho}) \\ \hline \boldsymbol{C}_F(\boldsymbol{\rho}) & \boldsymbol{D}_F(\boldsymbol{\rho}) \end{array}\right] = \sum_{i=1}^{m} \vartheta_i(\boldsymbol{\rho}) \left[\begin{array}{c|c} \boldsymbol{A}_{F,i} & \boldsymbol{B}_{F,i} \\ \hline \boldsymbol{C}_{F,i} & \boldsymbol{D}_{F,i} \end{array}\right] \tag{3.67}$$

The polytopic synthesis procedure is summarised in Procedure 3.1 below.

Procedure 3.1 Polytopic Robust LPV Estimator Synthesis

Input: $\bar{\boldsymbol{P}}(\boldsymbol{\rho}), \Delta$

Output: γ, $\{\boldsymbol{F}_i,\ \vartheta_i(\boldsymbol{\rho}),\ i = 1, \ldots, m\}$

1: Describe Δ by a list of IQCs specified by $(\boldsymbol{\Psi}, \boldsymbol{M}(\boldsymbol{\zeta}))$.

2: Combine $\bar{\boldsymbol{P}}(\boldsymbol{\rho})$ and $\boldsymbol{\Psi}$ to form the augmented system according to (3.39).

3: Solve the following SDP:

$$\min_{\substack{\boldsymbol{X}_1, \boldsymbol{Y}, \boldsymbol{M}(\boldsymbol{\zeta}) \\ \{\bar{\boldsymbol{A}}_i, \bar{\boldsymbol{B}}_i, \bar{\boldsymbol{C}}_i, \boldsymbol{D}_{F,i}\}\ i=1,\ldots,m}} \quad \gamma \tag{3.68}$$

subject to

a) $\gamma > 0$

b) $\boldsymbol{X}_1 - \boldsymbol{Y} > 0$ (refer to (3.55b))

c) the transformed generalised Bounded Real Lemma with IQC (3.50) for all $\boldsymbol{p} \in \mathcal{V}_\rho$ (contains state matrices of $\bar{\boldsymbol{P}}(\boldsymbol{\rho})\boldsymbol{\Psi}$)

d) (optional) transformed LMI region constraints on $\boldsymbol{A}_{F,i}$ at each polytope vertex.

4: Reconstruct the vertex estimators $\boldsymbol{F}_i = \{\boldsymbol{A}_{F,i}, \boldsymbol{B}_{F,i}, \boldsymbol{C}_{F,i}, \boldsymbol{D}_{F,i}\}$ for $i = 1, \ldots, m$ using (3.63) - (3.66).

5: Determine a suitable set of interpolation functions $\vartheta_i(\boldsymbol{\rho}),\ i = 1, \ldots, m$ that satisfies (3.57) and (3.58).

3.5 Appendix

3.5.1 Factorisations and State Space Representations of Selected IQC Multipliers

Blocks of Repeated Constant Real Scalar

The section concerns Δ consisting of n_δ diagonal blocks, i.e.,

$$\Delta = \begin{bmatrix} \delta_1 \boldsymbol{I}_{m_1} & \boldsymbol{0} & \cdots & \boldsymbol{0} \\ \boldsymbol{0} & \delta_2 \boldsymbol{I}_{m_2} & & \boldsymbol{0} \\ \vdots & & \ddots & \vdots \\ \boldsymbol{0} & \boldsymbol{0} & \cdots & \delta_{n_\delta} \boldsymbol{I}_{m_{n_\delta}} \end{bmatrix} . \tag{3.69}$$

Consider first the i-th diagonal block

$$\Delta_i = \delta_i \boldsymbol{I}_{m_i}, \quad \boldsymbol{I}_{m_i} \in \mathbb{R}^{m_i \times m_i}, \quad \delta_i \in \mathbb{R}, \quad |\delta_i| \leq 1 . \tag{3.70}$$

[MR97] states that a Δ_i in this form satisfies all IQC multipliers of the form

$$\boldsymbol{\Pi}(j\omega) = \begin{bmatrix} \boldsymbol{X}(j\omega) & \boldsymbol{Y}(j\omega) \\ \boldsymbol{Y}(j\omega)^* & -\boldsymbol{X}(j\omega) \end{bmatrix} . \tag{3.71}$$

An asymptotically exact factorisation of the multiplier is given by $\boldsymbol{\Pi}_i = \boldsymbol{\Psi}_i^* \boldsymbol{M}_i \boldsymbol{\Psi}_i$ [SK08], where

$$\boldsymbol{\Psi}_i = \begin{bmatrix} \boldsymbol{\psi}_i & \boldsymbol{0} \\ \boldsymbol{0} & \boldsymbol{\psi}_i \end{bmatrix} \tag{3.72}$$

with $\boldsymbol{\psi}_i \in \mathbb{C}^{[(n_\psi+1)m_i] \times m_i}$ of the form

$$\boldsymbol{\psi}_i = \begin{bmatrix} \boldsymbol{I}_{m_i} & \left(\frac{j\omega - \alpha}{j\omega + \alpha}\right) \boldsymbol{I}_{m_i} & \cdots & \left(\frac{j\omega - \alpha}{j\omega + \alpha}\right)^{n_\psi} \boldsymbol{I}_{m_i} \end{bmatrix}^T \tag{3.73}$$

and

$$\boldsymbol{M}_i = \begin{bmatrix} \boldsymbol{P}_i & \boldsymbol{Q}_i \\ \boldsymbol{Q}_i^T & -\boldsymbol{P}_i \end{bmatrix} \tag{3.74}$$

with

$$\boldsymbol{P}_i > 0 , \qquad \boldsymbol{P}_i \in \mathbb{S}^{[(n_\psi+1)m_i]} \tag{3.75}$$

$$\boldsymbol{Q}_i = -\boldsymbol{Q}_i^T , \qquad \boldsymbol{Q}_i \in \mathbb{R}^{[(n_\psi+1)m_i] \times [(n_\psi+1)m_i]} . \tag{3.76}$$

The order n_ψ and constant α are user-selectable parameters, with conservatism reducing with higher n_ψ. In the particular example shown in [SK08], setting $n_\psi > 2$ produced no significant reduction in conservatism for all chosen test values of α compared to $n_\psi = 2$.

By suitably stacking the $\boldsymbol{\Psi}_i$ and $\boldsymbol{M}_i$ corresponding to all n_δ of the Δ_i blocks, the full Δ block consisting of n_δ diagonal blocks as in (3.69) satisfies an IQC $(\boldsymbol{\Psi}, \boldsymbol{M})$, where

$$\boldsymbol{\Psi} = \begin{bmatrix} \operatorname{diag}(\boldsymbol{\psi}_i) & \boldsymbol{0} \\ \boldsymbol{0} & \operatorname{diag}(\boldsymbol{\psi}_i) \end{bmatrix} \tag{3.77}$$

$$\boldsymbol{M} = \begin{bmatrix} \operatorname{diag}(\boldsymbol{P}_i) & \operatorname{diag}(\boldsymbol{Q}_i) \\ \operatorname{diag}(\boldsymbol{Q}_i^T) & \operatorname{diag}(-\boldsymbol{P}_i) \end{bmatrix} \tag{3.78}$$

where $\operatorname{diag}(\boldsymbol{A}_i)$ denotes $\operatorname{diag}(\boldsymbol{A}_1, \ldots, \boldsymbol{A}_{n_\delta})$. The variables $\boldsymbol{P}_i$, $\boldsymbol{Q}_i$, $i = 1, \ldots, k$ are treated as optimisation variables in the SDP (3.37).

The state-space realisation shown below is based on [PFH12]. $\boldsymbol{\Psi}$ is given by

$$\dot{\boldsymbol{x}}_\Psi = \boldsymbol{A}_\Psi \boldsymbol{x}_\Psi + \boldsymbol{B}_\Psi \begin{bmatrix} \boldsymbol{v} \\ \boldsymbol{w} \end{bmatrix} \tag{3.79a}$$

$$\boldsymbol{q} = \boldsymbol{C}_\Psi \boldsymbol{x}_\Psi + \boldsymbol{D}_\Psi \begin{bmatrix} \boldsymbol{v} \\ \boldsymbol{w} \end{bmatrix} \tag{3.79b}$$

where

$$\boldsymbol{A}_\Psi = \begin{bmatrix} \operatorname{diag}(\boldsymbol{A}_{\psi_i}) & \boldsymbol{0} \\ \boldsymbol{0} & \operatorname{diag}(\boldsymbol{A}_{\psi_i}) \end{bmatrix}, \qquad \boldsymbol{B}_\Psi = \begin{bmatrix} \operatorname{diag}(\boldsymbol{B}_{\psi_i}) & \boldsymbol{0} \\ \boldsymbol{0} & \operatorname{diag}(\boldsymbol{B}_{\psi_i}) \end{bmatrix}$$

$$\boldsymbol{C}_\Psi = \begin{bmatrix} \operatorname{diag}(\boldsymbol{C}_{\psi_i}) & \boldsymbol{0} \\ \boldsymbol{0} & \operatorname{diag}(\boldsymbol{C}_{\psi_i}) \end{bmatrix}, \qquad \boldsymbol{D}_\Psi = \begin{bmatrix} \operatorname{diag}(\boldsymbol{D}_{\psi_i}) & \boldsymbol{0} \\ \boldsymbol{0} & \operatorname{diag}(\boldsymbol{D}_{\psi_i}) \end{bmatrix}.$$

The state space matrices of $\boldsymbol{\psi}_i$ are $\boldsymbol{A}_{\psi_i} \in \mathbb{R}^{n_{\psi_i} m_i \times n_{\psi_i} m_i}$, $\boldsymbol{B}_{\psi_i} \in \mathbb{R}^{n_{\psi_i} m_i \times m_i}$, $\boldsymbol{C}_{\psi_i} \in \mathbb{R}^{(n_{\psi_i}+1) m_i \times n_{\psi_i} m_i}$ and $\boldsymbol{D}_{\psi_i} \in \mathbb{R}^{(n_{\psi_i}+1) m_i \times m_i}$:

$$\boldsymbol{A}_{\psi_i} = \begin{bmatrix} -\alpha \boldsymbol{I}_{m_i} & \boldsymbol{0} & \cdots & \cdots & \boldsymbol{0} \\ -2\alpha \boldsymbol{I}_{m_i} & -\alpha \boldsymbol{I}_{m_i} & \cdots & \cdots & \boldsymbol{0} \\ \vdots & \vdots & & \ddots & \vdots \\ -2\alpha \boldsymbol{I}_{m_i} & -2\alpha \boldsymbol{I}_{m_i} & \cdots & -2\alpha \boldsymbol{I}_{m_i} & -2\alpha \boldsymbol{I}_{m_i} \end{bmatrix}, \qquad \boldsymbol{B}_{\psi_i} = \begin{bmatrix} -2\alpha \boldsymbol{I}_{m_i} \\ -2\alpha \boldsymbol{I}_{m_i} \\ \vdots \\ -2\alpha \boldsymbol{I}_{m_i} \end{bmatrix}$$

$$\boldsymbol{C}_{\psi_i} = \begin{bmatrix} \boldsymbol{0} & \boldsymbol{0} & \cdots & \boldsymbol{0} \\ \boldsymbol{I}_{m_i} & \boldsymbol{0} & \cdots & \boldsymbol{0} \\ \boldsymbol{I}_{m_i} & \boldsymbol{I}_{m_i} & \ddots & \cdots \\ \vdots & \vdots & & \cdots \\ \boldsymbol{I}_{m_i} & \boldsymbol{I}_{m_i} & \cdots & \boldsymbol{I}_{m_i} \end{bmatrix}, \qquad \boldsymbol{D}_{\psi_i} = \begin{bmatrix} \boldsymbol{I}_{m_i} \\ \boldsymbol{I}_{m_i} \\ \vdots \\ \boldsymbol{I}_{m_i} \\ \boldsymbol{I}_{m_i} \end{bmatrix}.$$

Chapter 4

Robust LPV Residual Generator Design

4.1 Overview

Model-based FDI methods exploit the analytical redundancy in a system to detect faults by checking the consistency of the measured variables against the known system model. A sub-class of these methods is residual-based FDI. As discussed in Chapter 2, a residual can be viewed as the difference between measured process variables and their estimates, and is calculated by a *residual generator*. A residual that deviates significantly from zero indicates the presence of a fault. Since residuals are generally affected by disturbances, uncertainties and noise, they are first post-processed by signal-processing measures before they are further evaluated to extract useful fault information. This takes place in the residual evaluation module. The subsequent decision making stage determines the diagnosis result (presence and location of a fault) on the basis of the outputs computed by a bank of residual generators and evaluators.

In the structured residual method, each post-processed residual is first converted into a binary feature by means of threshold comparison. Then, based on the observed pattern in the resulting array of binary features from the residual array, the pattern evaluation module isolates the fault, i.e. determines its location. This residual-based FDI architecture with the two-staged decision making is illustrated in Figure 4.1.

This chapter is concerned with the residual generation component, which represents the main focus in Part-I of the thesis. Residual evaluation, threshold comparison and signature processing are handled in the next chapter. The residual generator design task shares with estimator design the objective of attenuating the effects of disturbances and uncertainties, and it adds the requirement that the residuals must be sufficiently sensitive to faults. This chapter applies an approach in which this is achieved by demanding that the fault-to-residual response matches a reference model.

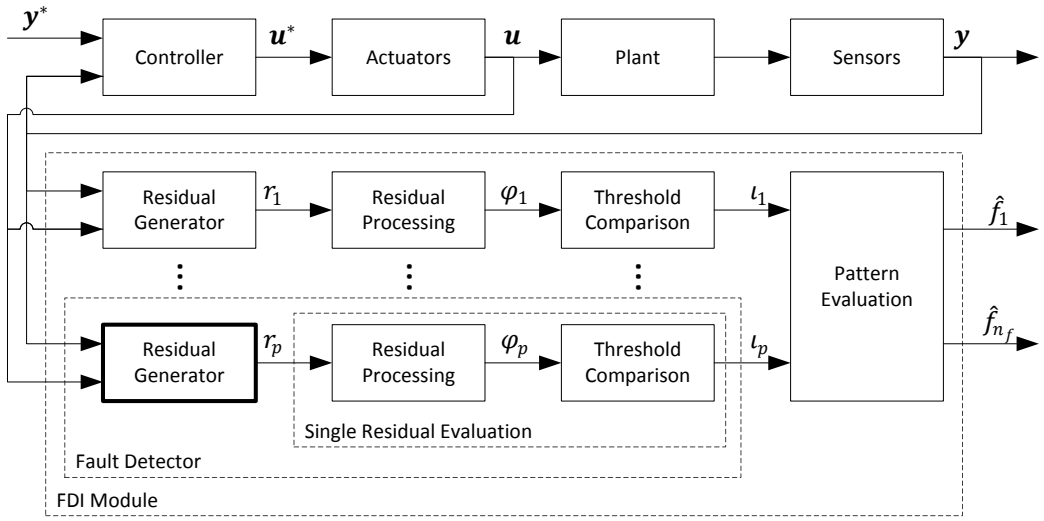

Figure 4.1: Residual-based FDI architecture. The residual generator component is highlighted.

The key contribution of this chapter is the improvement of scalar output residual generators with sensitivity requirements for multiple faults through the inclusion of optimisation degrees of freedom in the reference models for the fault-to-residual response. With some adaptations, these can be optimised in the same semi-definite program (SDP) solved for the estimator synthesis problem that the residual generator synthesis is recast into. It will be shown that this approach is also applicable to uncertain polytopic LPV plants by employing the tools presented in Chapter 3 for the synthesis. The use of IQCs to handle uncertain LPV plants in this context represents a novel feature of this work.

Since the ability to handle residuals with sensitivity to multiple faults is improved by the proposed adaptation, it is particularly relevant for the structured residuals approach where each residual is generally specified to have multiple fault sensitivity, for reasons that will be explained in Chapter 5.

The content of this chapter is based on the publications [Ho16; Ho17].

4.2 Brief Review of Model-Based Residual Generation

4.2.1 Fundamental Problem of Residual Generation

Consider the LPV plant $\boldsymbol{G}(\boldsymbol{\rho})$ given in state space form as

$$\dot{\boldsymbol{x}} = \boldsymbol{A}(\boldsymbol{\rho})\boldsymbol{x} + \boldsymbol{B}_u(\boldsymbol{\rho})\boldsymbol{u} + \boldsymbol{B}_d(\boldsymbol{\rho})\boldsymbol{d} + \boldsymbol{B}_f(\boldsymbol{\rho})\boldsymbol{f} \tag{4.1}$$

$$\boldsymbol{y} = \boldsymbol{C}(\boldsymbol{\rho})\boldsymbol{x} + \boldsymbol{D}_u(\boldsymbol{\rho})\boldsymbol{u} + \boldsymbol{D}_d(\boldsymbol{\rho})\boldsymbol{d} + \boldsymbol{D}_f(\boldsymbol{\rho})\boldsymbol{f} \tag{4.2}$$

where $\boldsymbol{x} \in \mathbb{R}^{n_x}$ is the plant state, $\boldsymbol{y} \in \mathbb{R}^{n_y}$ is the measured output, $\boldsymbol{u} \in \mathbb{R}^{n_u}$ is the input, $\boldsymbol{d} \in \mathbb{R}^{n_d}$ is the disturbance, and $\boldsymbol{f} \in \mathbb{R}^{n_f}$ contains the faults to be detected.

It can be equivalently expressed in transfer function form as

$$\boldsymbol{y} = \boldsymbol{G}_{yu}(\boldsymbol{\rho})\boldsymbol{u} + \boldsymbol{G}_{yd}(\boldsymbol{\rho})\boldsymbol{d} + \boldsymbol{G}_{yf}(\boldsymbol{\rho})\boldsymbol{f} \tag{4.3}$$

where $\boldsymbol{G}_{yu}(\boldsymbol{\rho})$, $\boldsymbol{G}_{yd}(\boldsymbol{\rho})$ and $\boldsymbol{G}_{yf}(\boldsymbol{\rho})$ are the parameter-dependent transfer function matrices from $\boldsymbol{u}$, $\boldsymbol{d}$ and $\boldsymbol{f}$ respectively to $\boldsymbol{y}$.

The *fundamental problem of residual generation* (FPRG) concerns the search for a stable filter $\boldsymbol{F}(\boldsymbol{\rho})$ whose output is sensitive to the occurrence of specified faults, while remaining insensitive to the disturbances. $\boldsymbol{F}(\boldsymbol{\rho})$ takes $\bar{\boldsymbol{y}} = [\boldsymbol{y}^T \ \boldsymbol{u}^T]^T$ as input and computes the residual $\boldsymbol{r}$, that is

$$\boldsymbol{r} = \boldsymbol{F}(\boldsymbol{\rho}) \begin{bmatrix} \boldsymbol{y} \\ \boldsymbol{u} \end{bmatrix} . \tag{4.4}$$

The residual signal $\boldsymbol{r}$ has the following properties:

i) $\boldsymbol{r}(t) = \boldsymbol{0}$ if $\boldsymbol{f}(t) = 0$ for all $\boldsymbol{u}(t)$ and $\boldsymbol{d}(t)$
ii) $\boldsymbol{r}(t) \neq \boldsymbol{0}$ if $f_j(t) \neq 0$ for any $j = 1, \ldots, n_f$

where f_j denotes the j-th element of the fault vector, also referred to as the j-th fault.

From (4.3) and (4.4), $\boldsymbol{r}$ can be written as

$$\boldsymbol{r} = \boldsymbol{G}_{ru}(\boldsymbol{\rho})\boldsymbol{u} + \boldsymbol{G}_{rd}(\boldsymbol{\rho})\boldsymbol{d} + \boldsymbol{G}_{rf}(\boldsymbol{\rho})\boldsymbol{f} \tag{4.5}$$

where

$$\boldsymbol{G}_{ru}(\boldsymbol{\rho}) = \boldsymbol{F}(\boldsymbol{\rho}) \begin{bmatrix} \boldsymbol{G}_{yu}(\boldsymbol{\rho}) \\ \boldsymbol{I} \end{bmatrix}, \quad \boldsymbol{G}_{rd}(\boldsymbol{\rho}) = \boldsymbol{F}(\boldsymbol{\rho}) \begin{bmatrix} \boldsymbol{G}_{yd}(\boldsymbol{\rho}) \\ \boldsymbol{0} \end{bmatrix}, \quad \boldsymbol{G}_{rf}(\boldsymbol{\rho}) = \boldsymbol{F}(\boldsymbol{\rho}) \begin{bmatrix} \boldsymbol{G}_{yf}(\boldsymbol{\rho}) \\ \boldsymbol{0} \end{bmatrix} .$$

The j-th column of $\boldsymbol{G}_{rf}$, i.e. the transfer function column vector from f_j to $\boldsymbol{r}$ is denoted $\boldsymbol{G}_{rf[j]}$. Condition ii) requires that this is non-zero for all $j = 1, \ldots, n_f$ while condition i) requires $\boldsymbol{G}_{ru} = 0$ and $\boldsymbol{G}_{rd} = 0$. [Var07] defines a stronger condition which requires that persistent (constant) faults produces asymptotically persistent (constant) residuals. This is referred to as *strong detectability* and requires $\|\boldsymbol{G}_{rf[j]}(0)\| > 0$. A detectable fault that does not fulfil this condition is known as *weakly detectable*.

4.2.2 Perfect and Approximate Decoupling

The problem formulation described in the previous section refers to *perfect decoupling*, in which the residual is completely insensitive to disturbances. The existence of such a solution is conditional on the subspace of the fault direction(s) lying outside of the minimal unobservability subspace containing the disturbance directions. This is shown by [MVW89] for LTI systems, [BB04] for LPV systems, and [PI01] for nonlinear systems. Geometric methods for residual generator synthesis based on these subspaces are proposed

in the respective works. Further approaches are available for solving the perfect decoupling problem, including unknown input observers and parametric eigenvalue assignments [CP99]. By approximating the effects of model uncertainties by appropriate disturbance inputs, robust residual generation may also be tackled using these methods [CP99].

When the condition for perfect decoupling is not satisfied, or it is desirable to handle model uncertainties directly, then approximate decoupling approaches for residual generation can be applied. In this formulation, the decoupling constraint is relaxed to an attenuation of the disturbance effects. The fault sensitivity constraint is also modified to ensure that the effect of the fault on the residual is not merely non-zero, but sufficiently large to be distinguishable from the effect caused by disturbances and uncertainties. To facilitate the discussion, let the function $\mathcal{R}(\cdot)$ be a suitable measure of system input-to-output gain, with $\mathcal{S}(\cdot)$ a compatible sensitivity measure. Considering only the case without uncertainty for now, conditions i) and ii) from the previous section are modified into

$$i)\ \mathcal{R}(\boldsymbol{G}_{rd}) < \gamma_d,\ \mathcal{R}(\boldsymbol{G}_{ru}) < \gamma_u \tag{4.6a}$$

$$ii)\ \mathcal{S}(\boldsymbol{G}_{rf}) > \gamma_f,\ \text{with } \gamma_f > \max(\gamma_d, \gamma_u) \tag{4.6b}$$

For uncertain systems, the above conditions need to hold for all permissible uncertainties. These conditions guarantee that for $\boldsymbol{d}$ and $\boldsymbol{u}$ with upper bounded sizes, one can find a lower-bound for $\boldsymbol{f}$ such that faults with sizes exceeding this lower bound have effects on $\boldsymbol{r}$ that are distinguishable from those due to the bounded disturbance and inputs.

The design objectives i) and ii) are generally conflicting, leading to a multi-objective optimisation for residual generation synthesis, i.e., minimising the influence of the disturbances and inputs on the residual while simultaneously maximising the effects of the possible faults. Some approaches fuse $\mathcal{R}(\cdot)$ and $\mathcal{S}(\cdot)$ into a single metric by means of subtractions or a quotient to reduce the multi-objective optimisation problem into a single objective one. [Din13] provides examples of these metrics:

- $J_{S-R} = \alpha_f \mathcal{S}(\boldsymbol{G}_{rf}) - \alpha_d \mathcal{R}(\boldsymbol{G}_{rd}) - \alpha_u \mathcal{R}(\boldsymbol{G}_{ru})$
- $J_{S/R} = \dfrac{\alpha_f \mathcal{S}(\boldsymbol{G}_{rf})}{\alpha_d \mathcal{R}(\boldsymbol{G}_{rd}) + \alpha_u \mathcal{R}(\boldsymbol{G}_{ru})}$

where $\alpha_d, \alpha_u, \alpha_f \in \mathbb{R}^+$. These two metrics, which should be maximised, are shown to be equivalent to the multi-objective one in a certain sense in [Din13]. Instead of using either of these in this work, the trade-off between attenuation and sensitivity measures is kept explicit at this stage as motivated by the mixed H_∞ / H_- approaches in literature [JLM05; WYL07]. The measures will be combined later in the worst-case induced-$\mathcal{L}_2$ norm framework.

The abovementioned norm is used in this work directly as the $\mathcal{R}(\cdot)$ measure. It was defined for uncertain LPV systems in the previous chapter in (3.17), and for nominal LTI systems it is equivalent to the H_∞ norm. In the next sections, it will be shown that recasting the sensitivity measure $\mathcal{S}(\cdot)$ in terms of a reference model matching constraint

allows the $\mathcal{R}(\cdot)$ and $\mathcal{S}(\cdot)$ to be combined into a single worst-case induced-$\mathcal{L}_2$ norm for the purpose of the synthesis optimisation.

4.3 Fault Sensitivity

To simplify the notation and focus on the fundamental ideas, fault sensitivity will first be discussed with respect to LTI systems. Later the chosen sensitivity metric is extended to uncertain LPV systems. Fault sensitivity measures the sizes of the faults' effects on the residual. In the deterministic robust control framework, a measure of the smallest fault effects is required to establish the worst-case distinguishability from disturbance effects. This suggests a minimum size measure for a system $\boldsymbol{T}$ in the form of

$$\mathcal{S}(\boldsymbol{T}) = \inf_{\boldsymbol{f}\neq 0} \frac{\|\boldsymbol{T}\boldsymbol{f}\|_2}{\|\boldsymbol{f}\|_2} \ . \tag{4.7}$$

When $\boldsymbol{T}$ is an LTI system, then at a fixed frequency $\omega = \bar{\omega}$ the definition of the above index corresponds to the minimum singular value of $\boldsymbol{T}(j\bar{\omega})$. Taking the minimum of the minimum singular values over a finite frequency range gives the definition of the H_- index, which is introduced below.

Definition 4.1 (H_- index)**.** *The H_- index of an LTI transfer function matrix $\boldsymbol{T}(s)$ is defined as*

$$\|\boldsymbol{T}(j\omega)\|_- = \inf_{\omega\in\Omega} \underline{\sigma}[\boldsymbol{T}(j\omega)] \ . \tag{4.8}$$

where $\underline{\sigma}(\boldsymbol{A})$ denotes the smallest singular value of $\boldsymbol{A}$.

Note that H_- index is not a norm, but is denoted by $\|\cdot\|$ to conform to notation in literature. It violates the property that a norm only vanishes if its argument is zero. We observe that $\boldsymbol{T}(j\omega)\boldsymbol{f}(j\omega)$ may vanish for non-zero $\boldsymbol{f}(j\omega)$ even if $\boldsymbol{T}(j\omega) \neq 0$, as long as the matrix $\boldsymbol{T}(j\omega)$ does not have full column rank. This limits the utility of the index as a sensitivity measure when $\boldsymbol{T}$ has more inputs than outputs, e.g., when $\boldsymbol{T}$ is a MISO system. To circumvent this problem, one could define an index based on the minimum *non-zero* singular value [HP96; Din00]. However, using the case of a scalar residual as an example, there is only one non-zero singular value, thus making it both the maximum and minimum. Therefore this is also generally not an accurate reflection of the minimum fault sensitivity.

Unlike system norms, there is no single standard definition in literature for the H_- index, and several indices have been proposed. [HP96] suggests a definition as the minimum non-zero singular value for $\omega = 0$, while other works [RN99; HZ05; Din00] take similar definitions but evaluate the minimum over a finite frequency range. Since in general the fault to residual transfer function $\boldsymbol{G}_{rf}$ can be strictly proper, with $\lim_{\omega\to\infty} \boldsymbol{G}_{rf}(j\omega) = \boldsymbol{0}$, the restriction to a finite frequency range is necessary to prevent the index from vanishing and hence providing no useful information. Restriction to $\omega = 0$ or the low-frequency

range is rooted in the assumptions that typical applications are interested in persistent fault manifestations which contain substantial static or low frequency components, and that strong detectability is desirable. Satisfaction of a lower bound for both the infinite frequency as well as the finite frequency versions of the H_- index can be verified by LMIs [Din13].

To alleviate the issues associated with the H_- index, [Din13] proposes another generalisation of the sensitivity measure within the so-called *unified approach*, in which *all* the singular values of $\boldsymbol{T}$ are accounted for. This proposed measure lies in a sense between the H_∞ norm and the H_- index, which correspond to the maximum and minimum singular values respectively. This approach is not applied in this work and will not be described further.

The preceding difficulties with using the H_- index as a minimum sensitivity measure arise largely due to its assumptions of norm-bounded fault detectors with arbitrary structures. In most practical fault detection and isolation schemes, it is commonly assumed that at most one or two can occur simultaneously, or that the simultaneous faults will not persistently cancel each other out [Ger98; Bar13; Jun15]. In particular, in the structured residual approach for fault isolation (see Chapter 5), this restriction on the number of simultaneous faults is usually necessary to draw conclusions about the location of the occurred fault. The H_- index in the variations described so far are not consistent with this assumption. Under the single-fault assumption, a more suitable metric would be the minimum sensitivity over the individual faults, i.e.,

$$\mathcal{S}(\boldsymbol{T}) = \min_{j=1,\dots,n_f} \left[\inf_{f \neq 0} \frac{\|\boldsymbol{T}_{[j]} f_j\|_2}{\|f_j\|_2} \right] . \tag{4.9}$$

It is noted that this work only considers the case of scalar residual signals, which are commonly employed in structured residual schemes. This allows some simplifications to the notation and calculations. In order to capture the single-fault assumption for a scalar output residual generator, the alternative fault sensitivity metric $H_{-,-}$ is formulated for a $(1 \times k)$ transfer function matrix in row vector form.

Definition 4.2 ($H_{-,-}$ index for an LTI system [Ho16])**.** *The $H_{-,-}$ index for a $(1 \times k)$ LTI transfer function matrix is defined as:*

$$\|\boldsymbol{T}(j\omega)\|^{\Omega}_{-,-} := \min_{j=1\dots k} \left(\inf_{\omega \in \Omega} |T_j(j\omega)| \right) \tag{4.10}$$

where $T_{[j]}$ denotes the j-th SISO component of $\boldsymbol{T}$.

Based on this and Definition 4.1, the minimum fault sensitivity constraint of

$$\|\boldsymbol{G}_{rf}\|^{\Omega}_{-,-} > \gamma_f \tag{4.11}$$

is equivalent to

$$\|G_{rf[j]}\|_{-}^{\Omega} > \gamma_f \ , \quad j = 1, \ldots, n_f \ . \tag{4.12}$$

That is, satisfaction of the constraint (4.11) guarantees that the residual has a sensitivity of at least γ_f to the occurrence of any single fault, as defined by the H_- index. We now provide a performance criterion to indicate whether faults can be adequately distinguished from disturbances and inputs.

The performance of a residual generator can be evaluated by the ratio between the residual's worst-case sensitivity to disturbances and inputs, and its sensitivity to faults. This is given by the following performance index, which is motivated by the one from [RN99].

Definition 4.3 (Residual generator performance index)**.** *The performance of a residual generator is defined by the index*

$$\tilde{\eta} := 2 \left(\frac{\max(\mathcal{R}(\boldsymbol{G}_{ru}), \mathcal{R}(\boldsymbol{G}_{rd}))}{\mathcal{S}(\boldsymbol{G}_{rf})} \right) \ . \tag{4.13}$$

Remark 4.1. *The factor* 2 *accounts for cancellation between the effects from* $(\boldsymbol{u}, \boldsymbol{d})$ *and* $\boldsymbol{f}$ *on the residual in the worst case. This is treated more rigorously in the proof for Lemma 4.1.*

Remark 4.2. *With the performance bounds* γ_d*,* γ_u *and* γ_f *defined in* (4.6)*, it is straightforward to deduce that* $\tilde{\eta}$ *satisfies the inequality*

$$\tilde{\eta} \leq \eta := 2 \left(\frac{\gamma_{ud}}{\gamma_f} \right) \tag{4.14}$$

where $\gamma_{ud} = \max(\gamma_d, \gamma_u)$*.*

Under some assumptions, an upper bound constraint on η ensures that a fault can be detected irrespective of other inputs. In the following discussion, it will be assumed that a fault is deemed to be detected when $\|r\|_2 > J$, where $J > 0$ is a constant residual threshold. If $\boldsymbol{u}$ and $\boldsymbol{d}$ are norm-bounded, the following lemma presents a performance requirement for the residual generator in terms of η.

Lemma 4.1 (Performance requirement for residual generator)**.** *Let* $\boldsymbol{u}$ *and* $\boldsymbol{d}$ *be bounded by* $\|[\boldsymbol{u}^T \ \boldsymbol{d}^T]\|_2 \leq 1$*. Then* γ_{ud} *is the minimum detection threshold* J *on the residual norm* $\|r\|_2$ *to avoid false alarms. Assuming that* $J = \gamma_{ud}$ *is selected and the single-fault assumption holds, then* η *represents the lower bound on the fault size* $\|f_j\|_2$ *that can always be detected for each fault.*

It follows that if the plant model is scaled such that any individual fault with $\|f_j\|_2 > 1$*,* $j = 1, \ldots, n_f$ *is required to be detected, then the residual generator must satisfy* $\eta < 1$*.*

Proof. The residual is composed of the fault-free and fault-induced components, i.e., $r = r_{ud} + r_f$. In the fault-free condition $r_f = 0$, so $\|r\|_2 = \|r_{ud}\|_2 < \gamma_{ud}\|[\boldsymbol{u}^T \ \boldsymbol{d}^T]^T\|_2$. Since

$\|[\boldsymbol{u}^T\ \boldsymbol{d}^T]^T\|_2 \leq 1$, the minimum detection threshold to prevent false alarms on the residual norm is $J = \gamma_{ud}$.

Now let $\mathcal{F}$ be the set of $\boldsymbol{f}$ that satisfy that single fault assumption and have magnitude larger than η. This set can be written as

$$\mathcal{F} = \bigcup_{k=1}^{n_f} \mathcal{F}_k \tag{4.15}$$

where

$$\mathcal{F}_k = \left\{ \boldsymbol{f} = [f_1 \dots f_{n_f}]^T \;\middle|\; \begin{array}{ll} \|f_j\|_2 > \eta, & j = k \\ f_j = 0, & j \neq k \end{array} \right\} . \tag{4.16}$$

To find a lower bound on $\|r\|_2$ under the effect of $\boldsymbol{f} \in \mathcal{F}$, apply the triangle inequality to $r_f = r - r_{ud}$ to get

$$\|r_f\|_2 \leq \|r\|_2 + \|r_{ud}\|_2 \tag{4.17}$$

Rearrange to get a lower bound on the residual:

$$\begin{aligned} \|r\|_2 &\geq \|r_f\|_2 - \|r_{ud}\|_2 \\ &\geq \gamma_f \max_j \|f_j\|_2 - \gamma_{ud} \|[\boldsymbol{u}^T\ \boldsymbol{d}^T]^T\|_2 \\ &\geq \gamma_f \max_j \|f_j\|_2 - \gamma_{ud} \ . \end{aligned} \tag{4.18}$$

Since $\boldsymbol{f} \in \mathcal{F}$ implies that $\max_j \|f_j\|_2 > \eta$, it follows from (4.14) that

$$\|r\|_2 \geq \gamma_f \eta - \gamma_{ud} \tag{4.19}$$

$$= 2\gamma_{ud} - \gamma_{ud} \tag{4.20}$$

$$= J \ . \tag{4.21}$$

Since $\|r\|_2 > J$ whenever $\|[\boldsymbol{u}^T\ \boldsymbol{d}^T]^T\|_2 \leq 1$ and $\boldsymbol{f} \in \mathcal{F}$, we deduce that the faults $\boldsymbol{f} \in \mathcal{F}$ can be reliably detected. □

The concepts presented so far can be readily extended to uncertain LPV systems. We start with redefining the H_- index for the SISO components, and then the $H_{-,-}$ index for the MISO fault-to-residual system.

Definition 4.4. *The H_- index of an uncertain parameter dependent SISO transfer function $T(\boldsymbol{\rho}, \Delta)$ is defined as*

$$\|T(\boldsymbol{\rho}, \Delta)\|_-^{\Omega, \mathcal{P}, \mathcal{D}} := \inf_{\substack{\boldsymbol{\rho} \in \mathcal{P}, \Delta \in \mathcal{D} \\ f \neq 0, f \in \mathcal{F}^\Omega}} \frac{\|T(\boldsymbol{\rho}, \Delta) f\|_2}{\|f\|_2} \tag{4.22}$$

where $\mathcal{P}$ denotes here the set of permissible trajectories of the scheduling parameter $\boldsymbol{\rho}$, and $\mathcal{D}$ denotes the set of permissible uncertainties Δ. $\mathcal{F}^{\Omega}$ denotes the set of signals whose frequency spectrum lie within the frequency band Ω.

Remark 4.3. *For SISO systems with frozen parameters $\boldsymbol{\rho}$, the definition is related to the LTI one (4.8), but with the singular value reduced to just the magnitude.*

$$\|T(\boldsymbol{\rho},\Delta)\|_{-}^{\Omega,\mathcal{P},\mathcal{D}} = \inf_{\substack{\omega\in\Omega \\ \boldsymbol{\rho}\in\mathcal{P} \\ \Delta\in\mathcal{D}}} |T(j\omega,\boldsymbol{\rho},\Delta)| \tag{4.23}$$

Definition 4.5. *The $H_{-,-}$ index of an uncertain parameter dependent $(1\times k)$ transfer function matrix $\boldsymbol{T}(\boldsymbol{\rho},\Delta)$ is defined as*

$$\|\boldsymbol{T}(\boldsymbol{\rho},\Delta)\|_{-,-}^{\Omega,\mathcal{P},\mathcal{D}} := \min_{j=1,\ldots,k} \|T_{[j]}(\boldsymbol{\rho},\Delta)\|_{-}^{\Omega,\mathcal{P},\mathcal{D}} \ . \tag{4.24}$$

4.4 Reference Following Approach to Residual Generator Synthesis

4.4.1 Reference Model Matching for Fault Sensitivity Constraint

It has been shown in literature (see [Din13; CFF08; WYL07]) that the fulfilment of a lower bound for the H_{-} index can be directly enforced for MIMO systems by linear or nonlinear matrix inequality constraints. In contrast, the $H_{-,-}$ index for scalar residuals is handled differently by simultaneously enforcing the single-fault sensitivity constraint (4.12) for each fault index j. The scalar output structure of this problem permits an alternative solution method which is used in this work. The method recasts the multiple H_{-} index lower bounding constraint into an optimal H_{∞} model matching problem, where the objective is to track a reference model of the fault-to-residual transfer function with possessing the desired fault sensitivity. The set-up is illustrated in Figure 4.2 and this will be referenced throughout the rest of this chapter. This approach has been studied in literature for nominal LTI [RN99], uncertain LTI [CFF05; FN06], and LPV [HZ05] systems. As remarked in the chapter introduction, in the usual formulation the reference model must be chosen a priori. The model contains the desired magnitudes of the sensitivities and therefore the ratios between them are also chosen in advance. The feature developed in this work aims to offset some of its restrictive consequences by incorporating some magnitude parameters from the reference model as degrees of freedom in the optimisation within the residual generator synthesis process.

The recast fault sensitivity constraint can be readily combined with the disturbance attenuation constraint to form a synthesis problem in the induced-$\mathcal{L}_2$ robust control framework. For uncertain LPV systems, the synthesis can be solved by employing the tools introduced in Chapter 3 to produce a residual generator $\boldsymbol{F}$. A common technique in norm-based robust synthesis is the use of weighting filters on the inputs and outputs to incorporate frequency information into the synthesis. In particular, incorporating the

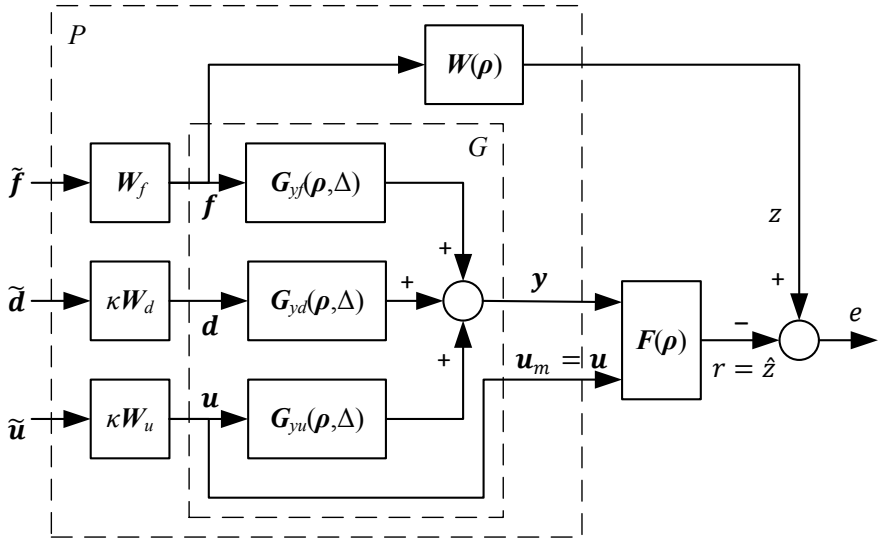

Figure 4.2: Set up for residual generator synthesis by specifying a reference model $\boldsymbol{W}(\boldsymbol{\rho})$ for fault-to-residual responses. $\tilde{\boldsymbol{f}}$, $\tilde{\boldsymbol{d}}$ and $\tilde{\boldsymbol{u}}$ represent norm-bounded inputs to allow the system inputs $\boldsymbol{f}$, $\boldsymbol{d}$ and $\boldsymbol{u}$ to be frequency weighted in the synthesis formulation.

weighting filter $\boldsymbol{W}_f$ in this framework allows the reference model matching requirement to be frequency weighted, thus providing an approximation to the finite-frequency fault sensitivity requirement.

Consider a $(1 \times n_f)$ parameter-dependent reference $\boldsymbol{W}(\boldsymbol{\rho})$ which matches the desired fault-to-residual response within $\omega \in \Omega$ for all fixed $\boldsymbol{\rho} \in \mathcal{P}$. $\boldsymbol{W}(\boldsymbol{\rho})$ and $\boldsymbol{W}_f$ have the forms

$$\begin{aligned} \boldsymbol{W}(\boldsymbol{\rho}) &= [W_{[1]}(\boldsymbol{\rho}) \ \ldots \ W_{[n_f]}(\boldsymbol{\rho})] \ , \\ \boldsymbol{W}_f &= diag([W_{f[1]} \ \ldots \ W_{f[n_f]}]) \ . \end{aligned}$$

For each SISO $G_{rf[j]}$, $j \in 1 \ldots n_f$, the sensitivity specification (4.12) is recast as an upper bound requirement on the norm of the difference between $G_{rf[j]}(\boldsymbol{\rho}, \Delta)$ and $W_{[j]}(\boldsymbol{\rho})$. The difference is weighted by a suitable SISO filter $W_{f,j}$ to relax the model-matching constraint at $\omega \notin \Omega$. The resulting constraint is

$$\sup_{\Delta \in \mathcal{D}} \|(W_{[j]}(\boldsymbol{\rho}) - G_{rf[j]}(\boldsymbol{\rho}, \Delta))W_{f[j]}\|_{i2} \leq \gamma, \quad j = 1, \ldots, n_f \ , \tag{4.25}$$

with the weighting filter $W_{f[j]}$ chosen such that

$$W_{f[j]}(j\omega) \begin{cases} \approx 1, & \omega \in \Omega \\ \ll 1, & \omega \notin \Omega \ . \end{cases} \tag{4.26}$$

The minimum $|W_{[j]}(\boldsymbol{\rho})|$ over $\omega \in \Omega$ has strong relevance to minimum fault sensitivity and is denoted as

$$\tilde{\lambda}_j(\boldsymbol{\rho}) = \inf_{\omega \in \Omega} |W_{[j]}(j\omega, \boldsymbol{\rho})| \ , \tag{4.27}$$

which will be later be related to a parametrisation of $\boldsymbol{W}(\boldsymbol{\rho})$. The relationship between $W_{[j]}$, $G_{rf[j]}$ and γ are visualised in Figure 4.3 for the LTI case.

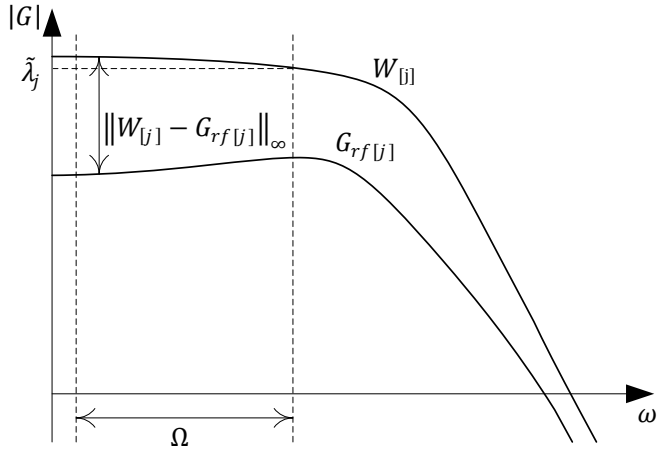

Figure 4.3: Illustration of the relationship between $W_{[j]}$, $G_{rf[j]}$ and the unweighted reference deviation $\|(W_{[j]} - G_{rf[j]})\|_\infty$ using an LTI example

Combining (4.25) for $j = 1, \ldots, n_f$ with a common γ yields

$$\sup_{\Delta \in \mathcal{D}} \|(\boldsymbol{W}(\boldsymbol{\rho}) - \boldsymbol{G}_{rf}(\boldsymbol{\rho}, \Delta))\boldsymbol{W}_f\|_{i2} < \gamma \ . \tag{4.28}$$

The constraints on $\boldsymbol{W}(\boldsymbol{\rho})$ and γ to satisfy the fault sensitivity constraint (4.12) will be treated in the next section. As already mentioned, the performance characteristics of the residual generator can be improved by allowing the reference model $\boldsymbol{W}(\boldsymbol{\rho})$ to be optimised. To see why this is the case, we introduced the concepts of a *consistent* optimisation criterion and an *attainable* reference model from [FN06] for problems in which a perfect decoupling solution exists. A reference model is said to be *attainable* if there exists a stable perfect decoupling residual generator which exhibits the specified response. An optimisation criterion J is *consistent* if any such perfect decoupling residual generator solutions result in the minimum value of J, that is, they are the optimal solutions. An attainable reference model is the prerequisite for a consistent optimisation criterion in synthesis using the model matching approach. This is because by definition, a perfect decoupling residual generator cannot exhibit the response of an unattainable model, and consequently a compromise solution with non-zero $\boldsymbol{G}_{rd}$ will minimise J. These concepts are particularly pertinent for residuals required to be sensitive to multiple faults.

For an arbitrary problem, the attainable reference is not known a priori. A possible approach is to first calculate a perfect decoupling solution to the nominal problem (without uncertainty) by other means such as the geometric method. The fault-to-residual response $\boldsymbol{G}_{rf}(\boldsymbol{\rho})$ of this perfect decoupling solution is then taken as the reference model for the synthesis problem with uncertainty. See [FN06; Van11] for more details on this approach. For problems where only approximate decoupling is possible on the nominal model, however, this approach for computing the residual reference is not applicable.

This work takes an alternative approach by simultaneously searching for an attainable model and synthesising the residual generator. For every $j = 1, \ldots, n_f$, the gain $\lambda_j(\boldsymbol{\rho})$ of the reference response $W_{[j]}(\boldsymbol{\rho})$, related to $\tilde{\lambda}_j(\boldsymbol{\rho})$ by $|\lambda_j(\boldsymbol{\rho})| = \tilde{\lambda}_j(\boldsymbol{\rho})$, is treated as an optimisation degree of freedom in the synthesis, rather than a fixed parameter. The parameter $\lambda_j(\boldsymbol{\rho})$ is defined more precisely later in (4.29). Although the frequency characteristics of the reference model must nevertheless be selected a priori, in many applications the designer is mainly interested in the fault-to-residual response in a small low frequency band, in which case a low-pass reference response is suitable. Relaxation of the reference matching requirement outside of this band the using weighting filter $\boldsymbol{W}_f$ serves to reduce the conservatism caused by the mismatch between the reference model with fixed frequency characteristics and that of the actual response at higher frequencies. This method provides the ability to handle requirements for a residual to be sensitive to multiple faults when the sensitivities are unspecified. Importantly, it permits the ratios between the sensitivities, i.e. $\frac{\|\boldsymbol{G}_{rf[j]}\|_-^\Omega}{\|\boldsymbol{G}_{rf[k]}\|_-^\Omega}$ for all pair $j, k = 1, \ldots, n_f$, to be optimised to best match the attainable ratios dictated by the system's structural constraints. In doing so, it provides a single step synthesis procedure that yields good fault sensitivity to disturbance attenuation performance, regardless of whether perfect decoupling is possible.

4.4.2 Conditions on the Fault-to-Residual Reference

We now describe the criteria on $W_{[j]}(\boldsymbol{\rho})$ in order to fulfil the sensitivity specification (4.12) for fault f_j. If $W_{[j]}(\boldsymbol{\rho})$ is chosen such that only its magnitude varies over $\boldsymbol{\rho} \in \mathcal{P}$, it can be written as

$$W_{[j]}(\boldsymbol{\rho}) = \lambda_j(\boldsymbol{\rho})\tilde{W}_{[j]} \ , \tag{4.29}$$

where the parameter-independent, normalised $\tilde{W}_{[j]}$ is an LTI filter that satisfies $\|\tilde{W}_{[j]}\|_-^\Omega = 1$. This restriction on $W_j(\boldsymbol{\rho})$ is reasonable since the frequency band of interest Ω usually does not vary significantly with $\boldsymbol{\rho}$. Now define

$$\underline{\lambda}_j := \min_{\boldsymbol{\rho}\in\mathcal{P}} |\lambda_j(\boldsymbol{\rho})| \tag{4.30a}$$

$$= \|W_{[j]}(\boldsymbol{\rho})\|_-^\Omega \qquad \text{due to (4.29).} \tag{4.30b}$$

Choosing $W_{f[j]}$ with roll-off behaviour according to (4.26) results in

$$\|W_j(\boldsymbol{\rho})W_{f[j]}\|_-^\Omega \approx \underline{\lambda}_j \ . \tag{4.31}$$

The next step in translating this H_- constraint to one on the induced-$\mathcal{L}_2$ norm is faciliated by the following Proposition.

Proposition 4.1. *For any two transfer function matrices H_1 and H_2,*

$$\|H_2\|_- \geq \|H_1\|_- - \|H_1 - H_2\|_{i2} \ . \tag{4.32}$$

Proof. The proof is given for the SISO case as only this case subsequently appears. In the following, $\mathcal{C}$ denotes the constraint set $\{\omega \in \Omega,\ \rho \in \mathcal{P},\ \Delta \in \mathcal{D}\}$.

$$\begin{aligned}\|H_1\|_- &= \inf_{\mathcal{C}} |H_1| \\ &= \inf_{\mathcal{C}} |H_2 + (H_1 - H_2)| \\ &\leq \inf_{\mathcal{C}} (|H_2| + |(H_1 - H_2)|) \\ &\leq \inf_{\mathcal{C}} |H_2| + \sup_{\mathcal{C}} |(H_1 - H_2)| \\ &= \|H_2\|_- + \sup_{\Delta} \in \mathcal{D} \|(H_1 - H_2)\|_{i2}\end{aligned} \tag{4.33}$$

□

Substituting $G_{rf[j]}(\boldsymbol{\rho})W_{f[j]} \to H_2$ and $W_{[j]}(\boldsymbol{\rho})W_{f[j]} \to H_1$ into (4.32) yields

$$\|G_{rf[j]}(\boldsymbol{\rho})W_{f[j]}\|_- \geq \|W_{[j]}(\boldsymbol{\rho})W_{f[j]}\|_- - \sup_{\Delta \in \mathcal{D}} \|(W_{[j]}(\boldsymbol{\rho}) - G_{rf[j]}(\boldsymbol{\rho}))W_{f[j]}\|_{i2}\ . \tag{4.34}$$

Using the bounds from (4.28) and (4.31) then gives

$$\|G_{rf[j]}(\boldsymbol{\rho})W_{f[j]}\|_-^{\Omega} \geq \underline{\lambda}_j - \gamma\ . \tag{4.35}$$

This results in the following sufficient constraint on $\underline{\lambda}_j$ to satisfy the sensitivity requirement (4.12). A similar result is also stated in [HZ05].

Lemma 4.2. *Consider $\underline{\lambda}_j$ and γ defined in (4.30a) and (4.28) respectively. Then,*

$$\|G_{rf[j]}(\boldsymbol{\rho})\|_-^{\Omega} > \gamma_f$$

holds if γ_f satisfies

$$\underline{\lambda}_j \geq \gamma + \gamma_f\ . \tag{4.36}$$

Proof. The result follows immediately from substituting $W_{f[j]}(j\omega) \approx 1$ for $\omega \in \Omega$ into (4.35). □

Corollary 4.1. *For given values of $\underline{\lambda}_j$ and γ,*

$$\gamma_f = \underline{\lambda}_j - \gamma \tag{4.37}$$

represents a lower bound for $\|\boldsymbol{G}_{rf[j]}(\boldsymbol{\rho})\|_-^{\Omega}$.

Recall that at the end of the last section, it was proposed that $\lambda_j(\boldsymbol{\rho}),\ j = 1, \ldots, n_f$ are treated as optimisation variables to allow an attainable residual reference to be approximated. (4.36) provides a magnitude lower bound on these optimisation variables. In the following, $\boldsymbol{\lambda}(\boldsymbol{\rho})$ denotes the vector of optimisation variables $[\lambda_1(\boldsymbol{\rho}) \ldots \lambda_{n_f}(\boldsymbol{\rho})]$. The "roll-off" behaviour of $W_{[j]}(\boldsymbol{\rho})$ for $\omega \notin \Omega$ is a design choice embedded in the frequency

behaviour of $\tilde{W}_{[j]}$. If steady state and low frequency fault manifestations are of primary interest, first-order low-pass filters can be chosen.

4.4.3 Residual Generation Problem Statement

With the fault sensitivity criterion treated, the input and disturbance suppression criteria (4.6) are now brought into a suitable form. As is common in robust control literature, frequency weights are used to focus the attenuation on particular frequency ranges. The choice of the worst-case induced-$\mathcal{L}_2$ norm as the system gain measure $\mathcal{R}(\cdot)$ and the definition of $\gamma_{ud} = \max(\gamma_u, \gamma_d)$ allow the conditions

$$\mathcal{R}(\boldsymbol{G}_{ru}) < \gamma_u, \quad \mathcal{R}(\boldsymbol{G}_{rd}) < \gamma_d \tag{4.38}$$

to be expressed as

$$\sup_{\Delta\in\mathcal{D}} \left\| \begin{bmatrix} \boldsymbol{G}_{rd}(\boldsymbol{\rho},\Delta)\boldsymbol{W}_d & \boldsymbol{G}_{ru}(\boldsymbol{\rho},\Delta)\boldsymbol{W}_u \end{bmatrix} \right\|_{i2} < \gamma_{ud} \ . \tag{4.39}$$

It is assumed that $\boldsymbol{W}_d$ and $\boldsymbol{W}_u$ are chosen to be parameter-independent. With (4.39) and the reference model matching criterion for fault sensitivity (4.28), the residual generator synthesis problem can now be stated.

Definition 4.6 (Residual Generator Synthesis Problem)**.** *Consider the set up in in Figure 4.2, in which $\boldsymbol{W}(\boldsymbol{\rho})$ is a function of $\boldsymbol{\lambda}(\boldsymbol{\rho})$. The residual generator synthesis problem searches for an LPV estimator $\boldsymbol{F}(\boldsymbol{\rho})$ and a gain vector $\boldsymbol{\lambda}(\boldsymbol{\rho})$ satisfying $\underline{\lambda}_j \geq \gamma + \gamma_f$, $j = 1, \ldots, n_f$ which simultaneously minimise the performance measures γ and γ_{ud} under the constraints that*

1. *$\boldsymbol{F}(\boldsymbol{\rho})$ is asymptotically stable*
2. $\sup\limits_{\Delta\in\mathcal{D}} \left\| \begin{bmatrix} \boldsymbol{G}_{rd}(\boldsymbol{\rho},\Delta)\boldsymbol{W}_d & \boldsymbol{G}_{ru}(\boldsymbol{\rho},\Delta)\boldsymbol{W}_u \end{bmatrix} \right\|_{i2} \leq \gamma_{ud}$
3. $\sup\limits_{\Delta\in\mathcal{D}} \|(\boldsymbol{W}(\boldsymbol{\rho}) - \boldsymbol{G}_{rf}(\boldsymbol{\rho},\Delta))\boldsymbol{W}_f\|_{i2} < \gamma \ .$

The method described in [RN99] pre-defines the tradeoff ratio

$$\kappa = \gamma/\gamma_{ud} \tag{4.40}$$

and merges conditions 2 and 3 into a single induced-$\mathcal{L}_2$ norm constraint

$$\sup_{\Delta\in\mathcal{D}} \left\| \begin{bmatrix} \kappa\boldsymbol{G}_{rd}(\boldsymbol{\rho},\Delta)\boldsymbol{W}_d & \kappa\boldsymbol{G}_{ru}(\boldsymbol{\rho},\Delta)\boldsymbol{W}_u & (\boldsymbol{W}(\boldsymbol{\rho}) - \boldsymbol{G}_{rf}(\boldsymbol{\rho},\Delta))\boldsymbol{W}_f \end{bmatrix} \right\|_{i2} < \gamma \ . \tag{4.41}$$

The performance indices $\tilde{\eta}$ and η are now given by

$$\tilde{\eta} = 2\left(\frac{\sup\limits_{\Delta\in\mathcal{D}} \| \begin{bmatrix} \boldsymbol{G}_{rd}(\boldsymbol{\rho},\Delta)\boldsymbol{W}_d & \boldsymbol{G}_{ru}(\boldsymbol{\rho},\Delta)\boldsymbol{W}_u \end{bmatrix} \|_{i2}}{\|\boldsymbol{G}_{rf}(\boldsymbol{\rho},\Delta)\|_{-,-}} \right) \leq \frac{\gamma_{ud}}{\gamma_f} = \eta \ . \tag{4.42}$$

By substituting (4.37) and (4.40) into the expression $\eta = \gamma_{ud}/\gamma_f$ from (4.42), we can write an upper bound $\bar{\eta}$ for η as a function of the solution parameters and variables to the problem defined in Definition 4.6. These are namely the parameter κ, the optimisation variable γ, and the minimum gain bounds $\underline{\lambda}_j,\ j = 1, \ldots, n_f$. The upper bound $\bar{\eta}$ is given by

$$\eta < \bar{\eta} = 2\frac{\gamma/\kappa}{\min_j \underline{\lambda}_j - \gamma}\ . \tag{4.43}$$

Note that this upper bound $\bar{\eta}$ is defined only for $\gamma < \min_j \underline{\lambda}_j$, which is consistent with Lemma 4.2. Note also that γ_f no longer appears in this expression. It will be seen later that it is convenient to constrain $\min_j \underline{\lambda}_j = 1$ in the optimisation. Then it is clear from the above expression that minimisation of γ also minimises $\bar{\eta}$, since the function $\gamma/(1-\gamma)$ is monotonically increasing for $\gamma > 0$.

[RN99] showed that the choice of κ can have a significant effect on the achievable performance η. The search for the optimal κ can be carried out using derivative-free one-dimensional search algorithms to minimise $\bar{\eta}$, in which the residual generator synthesis problem in Definition 4.6 is solved at every iteration. A possible search algorithm for this purpose is the Golden Section Search [Kie53]. Since this is not the focus of the work, it will not be discussed in more detail. The reader can find more on this and alternative search algorithms in [Pre07].

Remark 4.4. *For nominal LTI plants with a given residual generator $\boldsymbol{F}$, the $H_{-,-}$ index can be directly determined by evaluating (4.24) over a frequency grid, from which η can subsequently be computed. Due to the effect of $\dot{\boldsymbol{\rho}}$ on the induced-$\mathcal{L}_2$ norm, strictly speaking such an approach gridded over $\boldsymbol{\rho} \in \mathcal{P}$ and $\boldsymbol{\Delta} \in \mathcal{D}$ does not provide an upper bound on the $H_{-,-}$ index, but rather only on the frozen parameter values with $\dot{\boldsymbol{\rho}} = 0$. If it can be reasonably assumed that Δ is a time-invariant uncertainty and that $\boldsymbol{\rho}$ varies slowly, the η calculated from this gridding approach nonetheless provides a useful and often much less conservative indication of residual generator performance than the upper bound $\bar{\eta}$. However, with increasing grid dimensions this approach would quickly become intractable.*

4.5 Robust LPV Residual Generator Synthesis

Having now stated the residual generation problem, this section develops the algorithm for finding the optimal $\boldsymbol{F}(\boldsymbol{\rho})$ for a fixed value of κ, and concludes by summarising the steps for residual generator synthesis and design into respective procedures.

Recall the reference model following formulation of residual generator synthesis shown graphically in Figure 4.2. Connecting the uncertain plant $\boldsymbol{G}(\boldsymbol{\rho}, \Delta)$ with the reference model $\boldsymbol{W}(\boldsymbol{\rho})$ and the input weighting filters $\{\boldsymbol{W}_u, \boldsymbol{W}_d, \boldsymbol{W}_f\}$ produces the augmented plant $\boldsymbol{P}(\boldsymbol{\rho}, \Delta)$. This can be decomposed into an LFT interconnection of the nominal system

$\bar{\boldsymbol{P}}(\boldsymbol{\rho})$ and the uncertainty Δ. By defining augmented inputs and outputs as

$$\bar{\boldsymbol{d}} = \begin{bmatrix} \tilde{\boldsymbol{u}} \\ \tilde{\boldsymbol{d}} \\ \tilde{\boldsymbol{f}} \end{bmatrix}, \qquad \bar{\boldsymbol{y}} = \begin{bmatrix} \boldsymbol{y} \\ \boldsymbol{u} \end{bmatrix}, \tag{4.44}$$

the resulting system representation matches the standard form for an uncertain LPV system introduced at the beginning of Section 3.4.1. Then, for any specified value of the residual reference gains $\boldsymbol{\lambda}(\boldsymbol{\rho})$, the method from Section 3.4.1 can be directly applied, enabling us to synthesise an estimator for $\boldsymbol{P}(\boldsymbol{\rho}, \Delta)$ that outputs the residual $r = \hat{z}$. It will now be shown that the synthesis procedure can be adapted to accommodate the additional optimisation of $\boldsymbol{\lambda}(\boldsymbol{\rho})$ without compromising the convexity of the original optimisation. The polytopic LPV relaxation method will be used in the algorithm realisation.

4.5.1 Optimising the Residual Reference Gains

As suggested by its definition in (4.29), the optimisation variables $\lambda_j(\boldsymbol{\rho})$ for $j = 1, \ldots, n_f$ are each constrained by $|\lambda_j(\boldsymbol{\rho})| > 0$ for $\boldsymbol{\rho} \in \mathcal{P}$ to ensure non-zero sensitivity for all faults. An approach is now described for optimising these gains within the robust estimator synthesis SDP described in Section 3.4.1. To this end, we have to first handle the non-convex constraint $|\lambda_j(\boldsymbol{\rho})| > 0$, and then demonstrate that the modified LMI constraints of the SDP are affine in $\lambda_i(\boldsymbol{\rho})$ to preserve the convexity of the optimisation.

The strict inequality constraint $|\lambda_j(\boldsymbol{\rho})| > 0$ can be expressed as a non-strict inequality $|\lambda_j(\boldsymbol{\rho})| \geq \epsilon$ for some small non-zero positive ϵ. Its non-convexity can be attributed to the discontinuous permissible region of $\lambda_j(\boldsymbol{\rho})$. The constraint can be split into two convex ones, each representing a continuous sub-region:

$$\begin{aligned} &\lambda_j(\boldsymbol{\rho}) \geq \epsilon \quad \forall \boldsymbol{\rho} \in \mathcal{P}, \quad \text{and} \\ &\lambda_j(\boldsymbol{\rho}) \leq -\epsilon \quad \forall \boldsymbol{\rho} \in \mathcal{P} \, . \end{aligned}$$

This motivates the following change of variable to divide the original constraint on $\lambda_j(\boldsymbol{\rho})$ into the two above, which will be then be optimised in separate cases.

$$\lambda_j(\boldsymbol{\rho}) = l_j(\boldsymbol{\rho}) s_j, \quad s_j \in \{-1, 1\} \tag{4.45a}$$

$$l_j(\boldsymbol{\rho}) \geq \epsilon \quad \forall \boldsymbol{\rho} \in \mathcal{P} \, . \tag{4.45b}$$

The lower bound ϵ can be selected arbitrarily without affecting the performance of the synthesised residual generator. The following lemma demonstrates this.

Lemma 4.3 (freedom in choice of ϵ)**.** *Let the constraint (4.45b) for $j = 1, \ldots, n_f$ with $\epsilon = \epsilon_1$ correspond to an optimal $\boldsymbol{F}(\boldsymbol{\rho}) = \boldsymbol{F}_1(\boldsymbol{\rho})$ which gives the norm upper-bound $\gamma = \gamma_1$ as defined in (4.41). Then setting $\epsilon = a\epsilon_1$ for an arbitrary $a > 0$ results in the solution $\boldsymbol{F}(\boldsymbol{\rho}) = a\boldsymbol{F}_1(\boldsymbol{\rho})$ and $\gamma = a\gamma_1$.*

Moreover, the performance of the residual generator defined by η is the same for $\boldsymbol{F}_1(\boldsymbol{\rho})$ and $a\boldsymbol{F}_1(\boldsymbol{\rho})$.

Proof. Dependencies on $\boldsymbol{\rho}$ and Δ are omitted in this proof for compactness. $\|\boldsymbol{W}\|_{-,-} \geq \epsilon$ will be used below to denote the constraint $|\lambda_j(\boldsymbol{\rho})| \geq \epsilon$ for $j = 1, \ldots, n_f$. (4.41) can be rewritten as the following to explicitly show the influence of $\boldsymbol{F}$:

$$\sup_{\Delta \in \mathcal{D}} \left\| \left[\kappa \boldsymbol{F} \begin{bmatrix} \boldsymbol{G}_{yd} \\ \boldsymbol{0} \end{bmatrix} \boldsymbol{W}_d \quad \kappa \boldsymbol{F} \begin{bmatrix} \boldsymbol{G}_{yu} \\ \boldsymbol{I} \end{bmatrix} \boldsymbol{W}_u \quad \left(\boldsymbol{W} - \boldsymbol{F} \begin{bmatrix} \boldsymbol{G}_{yf} \\ \boldsymbol{0} \end{bmatrix} \right) \boldsymbol{W}_f \right] \right\|_{i2} < \gamma \ .$$

By the positive homogeneity of norms, the above holds for $\boldsymbol{F} = \boldsymbol{F}_1$, $\gamma = \gamma_1$, and $\boldsymbol{W} = \boldsymbol{W}_1$ satisfying $\|\boldsymbol{W}_1\|_{-,-} \geq \epsilon_1$ if and only if it also holds for $\boldsymbol{F} = a\boldsymbol{F}_1$, $\gamma = a\gamma_1$, and $\boldsymbol{W} = a\boldsymbol{W}_1$ for $a > 0$. Clearly, $a\boldsymbol{W}_1$ satisfies $\|a\boldsymbol{W}_1\|_{-,-} \geq a\epsilon_1$.

Thus if the optimal solution for $\epsilon = \epsilon_1$ corresponds to $\boldsymbol{F} = \boldsymbol{F}_1$ and $\gamma = \gamma_1$, then the optimal solution for $\epsilon = a\epsilon_1$ corresponds to $\boldsymbol{F} = a\boldsymbol{F}_1$ and $\gamma = a\gamma_1$, and the first part of the lemma is proven.

The definition (4.42) of η is rewritten to explicitly show $\boldsymbol{F}$:

$$\eta = 2 \left(\frac{\sup_{\Delta \in \mathcal{D}} \left\| \left[\boldsymbol{F} \begin{bmatrix} \boldsymbol{G}_{yd} \\ \boldsymbol{0} \end{bmatrix} \boldsymbol{W}_d \quad \boldsymbol{F} \begin{bmatrix} \boldsymbol{G}_{yu} \\ \boldsymbol{I} \end{bmatrix} \boldsymbol{W}_u \right] \right\|_{i2}}{\left\| \boldsymbol{F} \begin{bmatrix} \boldsymbol{G}_{yf} \\ \boldsymbol{0} \end{bmatrix} \right\|_{-,-}} \right) \tag{4.46}$$

From the first part of the proof, choosing $\epsilon = a\epsilon_1$ gives $\boldsymbol{F} = a\boldsymbol{F}_1$ as the solution. Since a is cancelled out between the numerator and denominator, η does not depend on a. Furthermore, for this case the upper bound defined in (4.43) can be written as

$$\bar{\eta} = 2 \frac{a\gamma/\kappa}{a\epsilon - a\gamma}$$

which is also independent from a. This proves that the second part of the lemma for both η and $\bar{\eta}$. □

It is convenient to set $\epsilon = 1$ for the remainder of this work. The minimisation of γ with constraints (4.41) and $l_j(\boldsymbol{\rho}) \geq 1,\ j = 1, \ldots, n_f,\ \boldsymbol{\rho} \in \mathcal{P}$ is then solved for all permutations of $s_j \in \{-1, 1\},\ j = 1, \ldots, n_f$, and the solution with the lowest optimum γ (denoted γ^*) is taken.

The computational load can be reduced by noticing that negating all $\lambda_j(\boldsymbol{\rho})$ is equivalent to negating $\boldsymbol{W}(\boldsymbol{\rho})$ and yields the negated residual generator $-\boldsymbol{F}(\boldsymbol{\rho})$ as the optimal solution with unchanged γ^*. This arises since the estimator synthesis set up minimises the norm of $e = z - \hat{z}$ (see Figure 4.2), thus negating the reference results in a negated estimator. Since fault sensitivity only concerns the magnitude of the residual, the two solutions $\boldsymbol{F}(\boldsymbol{\rho})$ and $-\boldsymbol{F}(\boldsymbol{\rho})$ are equivalent. Taking advantage of this insight, s_1 is fixed to $+1$ to avoid processing negated permutations of $\{s_1 \ldots s_{n_f}\}$. This halves the number of sign

permutations and results in solving the estimator synthesis SDP $2^{(n_f-1)}$ times in total, once for each permutation.

In order to demonstrate that the LMIs of each SDP are affine in $\lambda_j(\boldsymbol{\rho})$, we first examine how they enter $\bar{\boldsymbol{P}}(\boldsymbol{\rho})\boldsymbol{\Psi}$ (defined in (3.39)), whose state space matrices appear in the LMIs. Assume that $\boldsymbol{W}(\boldsymbol{\rho})$ is implemented in the form

$$\boldsymbol{W}(\boldsymbol{\rho}) = \begin{bmatrix} \lambda_1(\boldsymbol{\rho})\boldsymbol{C}_{\tilde{W}_{[1]}}(s\boldsymbol{I} - \boldsymbol{A}_{\tilde{W}_{[1]}})^{-1}\boldsymbol{B}_{\tilde{W}_{[1]}} \\ \vdots \\ \lambda_{n_f}(\boldsymbol{\rho})\boldsymbol{C}_{\tilde{W}_{[n_f]}}(s\boldsymbol{I} - \boldsymbol{A}_{\tilde{W}_{[n_f]}})^{-1}\boldsymbol{B}_{\tilde{W}_{[n_f]}} \end{bmatrix}^T \tag{4.47}$$

where $\boldsymbol{A}_{\tilde{W}_{[j]}}, \boldsymbol{B}_{\tilde{W}_{[j]}}, \boldsymbol{C}_{\tilde{W}_{[j]}}, \boldsymbol{D}_{\tilde{W}_{[j]}}$ are the state-space matrices of the normalised, parameter-independent residual reference filter $\tilde{W}_{[j]}$ with direct feed-through terms $\boldsymbol{D}_{\tilde{W}_{[j]}} = \boldsymbol{0}$. We note that the output of $\boldsymbol{W}(\boldsymbol{\rho})$ is to be estimated and hence corresponds to the auxiliary output z, which is given by the equation

$$z = \boldsymbol{C}_3(\boldsymbol{\rho})\boldsymbol{x} + \boldsymbol{D}_{31}(\boldsymbol{\rho})\boldsymbol{w} + \boldsymbol{D}_{32}(\boldsymbol{\rho})\bar{\boldsymbol{d}} \,. \tag{4.48}$$

The system can be easily formulated such that of all the state space matrices, only $\boldsymbol{C}_3(\boldsymbol{\rho})$ is a function of $\lambda_j(\boldsymbol{\rho})$, $j = 1, \ldots, n_f$. To simplify the explanations, it is assumed that the state space representation of each $\tilde{W}_{[j]}$ is in the observability canonical form, such that only the first state maps to its output. Then $\boldsymbol{W}(\boldsymbol{\rho})$ has state vector $\boldsymbol{x}_W$ and output matrix $\boldsymbol{C}_W$ in the form

$$\begin{aligned} \boldsymbol{x}_W &= \begin{bmatrix} x_{W_{[1]},1} & x_{W_{[1]},2} & \ldots & x_{W_{[1]},n_W} & x_{W_{[2]},1} & x_{W_{[2]},2} & \ldots & x_{W_{[n_f]},n_W} \end{bmatrix}^T \\ \boldsymbol{C}_W &= \begin{bmatrix} \lambda_1(\boldsymbol{\rho}) & 0 & \ldots & 0 & \lambda_2(\boldsymbol{\rho}) & 0 & \ldots & 0 \end{bmatrix} \,. \end{aligned}$$

To extract the $\lambda_j(\boldsymbol{\rho})$ from the state space matrices, the columns of $\boldsymbol{C}_3(\boldsymbol{\rho})$ are first partitioned into those that correspond to these non-zero output states in $\boldsymbol{W}(\boldsymbol{\rho})$ and the rest which are 0 since z is only a function of $\boldsymbol{x}_W$:

$$\boldsymbol{C}_3(\boldsymbol{\rho}) = \begin{bmatrix} \tilde{\boldsymbol{C}}_3(\boldsymbol{\rho}) & \boldsymbol{0} \end{bmatrix} \tag{4.49}$$

where $\tilde{\boldsymbol{C}}_3(\boldsymbol{\rho})$ can be decomposed as

$$\begin{aligned}\tilde{\boldsymbol{C}}_3(\boldsymbol{\rho}) &= \begin{bmatrix}\lambda_1(\boldsymbol{\rho}) & \dots & \lambda_{n_f}(\boldsymbol{\rho})\end{bmatrix} \\ &= \begin{bmatrix}1 & \dots & 1\end{bmatrix} \underbrace{\begin{bmatrix}\lambda_1(\boldsymbol{\rho}) & & \boldsymbol{0} \\ & \ddots & \\ \boldsymbol{0} & & \lambda_{n_f}(\boldsymbol{\rho})\end{bmatrix}}_{\boldsymbol{\Lambda}(\boldsymbol{\rho})} \\ &= \underbrace{\begin{bmatrix}1 & \dots & 1\end{bmatrix}}_{\boldsymbol{C}_{3c}} \underbrace{\begin{bmatrix}l_1(\boldsymbol{\rho}) & & \boldsymbol{0} \\ & \ddots & \\ \boldsymbol{0} & & l_{n_f}(\boldsymbol{\rho})\end{bmatrix}}_{\boldsymbol{L}(\boldsymbol{\rho})} \underbrace{\begin{bmatrix}s_1 & & \boldsymbol{0} \\ & \ddots & \\ \boldsymbol{0} & & s_{n_f}\end{bmatrix}}_{\tilde{\boldsymbol{S}}} .\end{aligned} \tag{4.50}$$

Inserting this back into $\boldsymbol{C}_3(\boldsymbol{\rho})$ yields

$$\boldsymbol{C}_3(\boldsymbol{\rho}) = \boldsymbol{C}_{3c}\boldsymbol{L}(\boldsymbol{\rho})\boldsymbol{S} \tag{4.51}$$

where

$$\boldsymbol{S} = \begin{bmatrix}\tilde{\boldsymbol{S}} & \boldsymbol{0}\end{bmatrix} .$$

The permissible values of $\tilde{\boldsymbol{S}}$ lie in the set $\tilde{\mathcal{S}} = diag([1, \pm 1, \pm 1, ..., \pm 1])$.

Substituting the above expression for $\boldsymbol{C}_3(\boldsymbol{\rho})$ into (3.50), which is the LMI constraint in the estimator synthesis SDP stemming from the transformed generalised Bounded Real Lemma, gives

$$\begin{bmatrix} \boldsymbol{A}^T\boldsymbol{Y} + \boldsymbol{Y}\boldsymbol{A} & \star & \star & \star & \star \\ \boldsymbol{A}^T\boldsymbol{Y} + \boldsymbol{X}_1\boldsymbol{A} + \bar{\boldsymbol{A}} & (\boldsymbol{A}^T\boldsymbol{X}_1 + \bar{\boldsymbol{B}}\boldsymbol{C}_2) + (\star) & \star & \star & \star \\ \boldsymbol{B}_1^T\boldsymbol{Y} & \boldsymbol{B}_1^T\boldsymbol{X}_1 + \boldsymbol{D}_{21}^T\bar{\boldsymbol{B}}^T & \boldsymbol{0} & \star & \star \\ \boldsymbol{B}_2^T\boldsymbol{Y} & \boldsymbol{B}_2^T\boldsymbol{X}_1 + \boldsymbol{D}_{22}^T\bar{\boldsymbol{B}}^T & \boldsymbol{0} & -\gamma\boldsymbol{I}_{n_{\bar{d}}} & \star \\ \boldsymbol{C}_{3c}\boldsymbol{L}\boldsymbol{S} - \boldsymbol{D}_F\boldsymbol{C}_2 - \bar{\boldsymbol{C}} & \boldsymbol{C}_{3c}\boldsymbol{L}\boldsymbol{S} - \boldsymbol{D}_F\boldsymbol{C}_2 & \boldsymbol{D}_{31} - \boldsymbol{D}_F\boldsymbol{D}_{21} & \boldsymbol{D}_{32} - \boldsymbol{D}_F\boldsymbol{D}_{22} & -\gamma\boldsymbol{I}_{n_z} \end{bmatrix} \\ + (\star)\boldsymbol{M}(\boldsymbol{\zeta}) \begin{bmatrix}\boldsymbol{C}_1 & \boldsymbol{C}_1 & \boldsymbol{D}_{11} & \boldsymbol{D}_{12} & \boldsymbol{0}\end{bmatrix} < 0 . \tag{4.52}$$

It can be seen that $\boldsymbol{\Lambda}(\boldsymbol{\rho})$ enters affinely into the LMI with respect to the set of other decision variables $\{\boldsymbol{X}_1, \boldsymbol{Y}, \bar{\boldsymbol{A}}, \bar{\boldsymbol{B}}, \bar{\boldsymbol{C}}, \boldsymbol{D}_F, \boldsymbol{M}(\boldsymbol{\zeta}), \gamma\}$. Hence the addition of $\boldsymbol{\Lambda}(\boldsymbol{\rho})$ to the set of decision variables does not contravene the convexity of the original optimisation problem. Moreover, $\boldsymbol{L}(\boldsymbol{\rho})$ is not multiplied with any parameter-dependent terms. This meets the conditions for a decision variable to be parameter-dependent when using the polytopic relaxation, which is stated in the following.

Proposition 4.2. *Let $\mathcal{L}(\boldsymbol{\rho}) > 0,\ \boldsymbol{\rho} \in \mathcal{P}$ be a parameter-dependent LMI, where the polytopic parameter region $\mathcal{P}$ has vertices $\boldsymbol{\rho}_1 \dots \boldsymbol{\rho}_m$. Let $\mathcal{Z}(\boldsymbol{\rho})$ denote the set of affinely*

parameter-dependent decision variables. Then the vertex property *holds if and only if each variable in* $\mathcal{Z}(\boldsymbol{\rho})$ *is affine with respect to the other parameter-dependent terms in* $\mathcal{L}(\boldsymbol{\rho})$.

Proof. The vertex property holds when $\mathcal{L}(\boldsymbol{\rho})$ is affine in $\boldsymbol{\rho}$. This is true if and only if $\mathcal{L}(\boldsymbol{\rho})$ is affine in the affinely parameter-dependent terms, which includes the decision varaibles $\mathcal{Z}(\boldsymbol{\rho})$. □

Remark 4.5. *The vertex variables* $\mathcal{Z}(\boldsymbol{\rho}_i),\ i = 1, \ldots, m$ *are decision variables in the polytopically relaxed LMIs.*

It follows that the polytopic vertex property is maintained when $\boldsymbol{L}(\boldsymbol{\rho})$ varies polytopically with $\boldsymbol{\rho}$. That is, $\boldsymbol{L}(\boldsymbol{\rho}) = \sum_{i=1}^{m} \vartheta_i(\boldsymbol{\rho})\boldsymbol{L}_i$ where $\boldsymbol{L}_i = \boldsymbol{L}(\boldsymbol{\rho}_i)$ and the interpolation coefficients $\vartheta_i(\boldsymbol{\rho})$ are defined in (3.57). This degree of freedom proves to be advantageous for better approximating an attainable reference model, which will in general be parameter-dependent.

In summary, the key result from this section is that when the residual reference multipliers $\lambda_j(\boldsymbol{\rho}),\ j = 1, \ldots, n_f$ are treated as parameter-dependent decision variables, the residual generator synthesis corresponding to the optimisation (3.68) can be solved through an array of SDPs by applying the following measures:

- the state space realisation of the residual reference model (4.47) integrates the $\lambda_j(\boldsymbol{\rho})$ terms only into the $\boldsymbol{C}_3(\boldsymbol{\rho})$ matrix, and
- the non-convex minimum magnitude constraints $|\lambda_j(\boldsymbol{\rho})| \geq 1,\ j = 1, \ldots, n_f,\ \boldsymbol{\rho} \in \mathcal{P}$ are split into $2^{(n_f-1)}$ convex cases, each corresponding to a permutation of the sign modifier $\tilde{\boldsymbol{S}} \in \tilde{\mathcal{S}}$ and under the same convex constraints $l_j(\boldsymbol{\rho}) \geq 1,\ j = 1, \ldots, n_f$. In the case of polytopic relaxation, the constraint $l_j(\boldsymbol{\rho}) \geq 1$ is replaced by the vertex constraints $l_{j,i} \geq 1$ for vertices $i = 1, \ldots, m$, where $l_{j,i}$ denotes the j-the diagonal element in $\boldsymbol{L}_i$.

4.5.2 Design Procedure

The results from the previous sections are summarised by the following theorem regarding the existence of a residual generator satisfying a specified performance. This then forms the basis for the residual generator synthesis and design procedures.

Theorem 4.1. *Let* $\boldsymbol{G}(\boldsymbol{\rho}, \Delta) = [\boldsymbol{G}_{yu}\ \boldsymbol{G}_{yd}\ \boldsymbol{G}_{yf}]$ *be an uncertain LPV plant, and let* $\boldsymbol{W}_d \in \mathbb{RH}_\infty^{n_d \times n_d}$, $\boldsymbol{W}_u \in \mathbb{RH}_\infty^{n_u \times n_u}$ *and* $\boldsymbol{W}_f \in \mathbb{RH}_\infty^{n_f \times n_f}$ *be diagonal transfer functions matrices. In addition, let* $\boldsymbol{W} : \boldsymbol{\rho} \to \mathbb{RH}_\infty^{1 \times n_f}$ *be a strictly proper stable parameter-dependent transfer function matrix of the form* (4.47)*, and* $\kappa, \bar{\eta} \in \mathbb{R}^+$. *Let* $\boldsymbol{P}(\boldsymbol{\rho}, \Delta)$ *be the augmented LPV system formed by the interconnection shown in Figure 4.2, decomposed by a LFT into the nominal plant* $\bar{\boldsymbol{P}}(\boldsymbol{\rho})$ *and a bounded casual perturbation operator* Δ. *Let* $(\boldsymbol{\Psi}, \boldsymbol{M}(\boldsymbol{\zeta}))$ *define IQC multipliers such that* $\Delta \in IQC(\boldsymbol{\Psi}, \boldsymbol{M}(\boldsymbol{\zeta}))\ \forall \Delta \in \mathcal{D}$, *where* $\boldsymbol{\zeta}$ *parametrises the valid*

set of $\boldsymbol{M}$. *Let the interconnection of* $\bar{\boldsymbol{P}}(\boldsymbol{\rho})$ *and* $\boldsymbol{\Psi}$ *have the state-space representation in* (3.39).

There exists a scalar output polytopic LPV residual generator

$$\boldsymbol{F}(\boldsymbol{\rho}) = \sum_{i=1}^{m} \vartheta_i(\boldsymbol{\rho}) \boldsymbol{F}_i \tag{4.53}$$

$$= \sum_{i=1}^{m} \vartheta_i(\boldsymbol{\rho}) \left[\begin{array}{c|c} \boldsymbol{A}_{F,i} & \boldsymbol{B}_{F,i} \\ \hline \boldsymbol{C}_{F,i} & \boldsymbol{D}_{F,i} \end{array}\right] \tag{4.54}$$

that is stable and whose performance metric

$$\tilde{\eta} = 2 \left(\frac{\sup\limits_{\Delta \in \mathcal{D}} \left\| \left[\boldsymbol{F}(\boldsymbol{\rho}) \begin{bmatrix} \boldsymbol{G}_{yd}(\boldsymbol{\rho}, \Delta) \\ \boldsymbol{0} \end{bmatrix} \boldsymbol{W}_d \quad \boldsymbol{F}(\boldsymbol{\rho}) \begin{bmatrix} \boldsymbol{G}_{yu}(\boldsymbol{\rho}, \Delta) \\ \boldsymbol{I} \end{bmatrix} \boldsymbol{W}_u \right] \right\|_{i2}}{\left\| \boldsymbol{F}(\boldsymbol{\rho}) \begin{bmatrix} \boldsymbol{G}_{yf}(\boldsymbol{\rho}, \Delta) \\ \boldsymbol{0} \end{bmatrix} \right\|_{-,-}} \right) \tag{4.55}$$

satisfies $\tilde{\eta} \leq \bar{\eta}$ *if there exist*

1. $0 < \gamma \leq (1 - {}^{2}/_{(2+\kappa\bar{\eta})})$
2. $\boldsymbol{L}_i = diag([l_{1,i} \ \ldots \ l_{n_f,i}])$ *with* $l_{j,i} \geq 1, \ j = 1, \ldots, n_f$ *for each* $i \in [1 \ldots m]$
3. $\tilde{\boldsymbol{S}} \in \tilde{\mathcal{S}}$
4. $\boldsymbol{M}(\boldsymbol{\zeta})$
5. $\boldsymbol{X}_1, \boldsymbol{Y}$
6. $\{\bar{\boldsymbol{A}}_i, \bar{\boldsymbol{B}}_i, \bar{\boldsymbol{C}}_i, \boldsymbol{D}_{F,i}\}, \ i = 1, \ldots, m$

such that at each polytope vertex, the LMI (4.52) *and* (3.55b) *are satisfied. Moreover,* $\{\boldsymbol{A}_{F,i}, \boldsymbol{B}_{F,i}, \boldsymbol{C}_{F,i}\}$ *can be computed using the transformations* (3.64), (3.65) *and* (3.66).

Theorem 4.1 leads to Procedure 4.1 to synthesise a residual generator for a fixed κ. Based on this, Procedure 4.2 describes the steps for designing a residual generator $\boldsymbol{F}^*(\boldsymbol{\rho})$ that minimises $\bar{\eta}$ for an uncertain LPV plant $\boldsymbol{G}(\boldsymbol{\rho}, \Delta)$ by iterating Procedure 4.1 over κ. At runtime, the residual generator state space matrices are calculated by interpolating between the vertex matrices using (3.56).

Procedure 4.1 Residual Generator Synthesis

Input: $\boldsymbol{G}(\boldsymbol{\rho}, \Delta)$, $\boldsymbol{W}_u$, $\boldsymbol{W}_d$, $\boldsymbol{W}_f$, $\tilde{\boldsymbol{W}}$, Ω, κ

Output: $\bar{\eta}$, $\boldsymbol{F}(\boldsymbol{\rho})$, $\boldsymbol{\Lambda}(\boldsymbol{\rho})$

1: Solve the following minimisation problem containing $2^{(n_f-1)}$ SDPs to obtain the vertex residual generators $\boldsymbol{F}_i$, $i = 1, \ldots, m$:

$$\min_{\tilde{\boldsymbol{S}} \in \tilde{\mathcal{S}}} \underbrace{\left(\min_{\substack{\boldsymbol{X}_1, \boldsymbol{Y}, \boldsymbol{M}(\boldsymbol{\zeta}) \\ \{\bar{\boldsymbol{A}}_i, \bar{\boldsymbol{B}}_i, \bar{\boldsymbol{C}}_i, \boldsymbol{D}_{F,i}, \boldsymbol{L}_i\}\ i=1,\ldots,m}} \gamma \right)}_{SDP} \tag{4.56}$$

subject to

a) the LMI (4.52) evaluated at each polytope vertex $\boldsymbol{\rho}_i$

b) $\gamma > 0$

c) 2) and 3) from Theorem 4.1

d) (optional) LMI region constraints for the estimator eigenvalues, evaluated at each polytope vertex, such as (3.60) - (3.62)

2: Reconstruct $\boldsymbol{F}_i = \{\boldsymbol{A}_{F,i}, \boldsymbol{B}_{F,i}, \boldsymbol{C}_{F,i}, \boldsymbol{D}_{F,i}\}$ using (3.64) - (3.66).

3: $\boldsymbol{F}(\boldsymbol{\rho}_i) \leftarrow \boldsymbol{F}_i, \quad i = 1, \ldots, m$

4: $\boldsymbol{\Lambda}(\boldsymbol{\rho}_i) \leftarrow \boldsymbol{\Lambda}_i, \quad i = 1, \ldots, m$

5: Compute $\bar{\eta}$ using (4.43)

Procedure 4.2 Residual Generator Design

Input: $\boldsymbol{G}(\boldsymbol{\rho}, \Delta)$

Output: $\bar{\eta}^*$, $\boldsymbol{F}^*(\rho)$

1: Choose weighting filters $\boldsymbol{W}_u$, $\boldsymbol{W}_d$ according to the expected bandwith of $\boldsymbol{u}$ and $\boldsymbol{d}$

2: Set $\boldsymbol{W}_f$, $\tilde{\boldsymbol{W}}$ according to the frequency range Ω in which the faults should be detected

3: Choose start value of κ

4: Set $\bar{\eta}^* = \infty$

5: **repeat**

6: Apply Procedure 4.1 to synthesise a residual generator $\boldsymbol{F}(\boldsymbol{\rho})$ and compute its $\bar{\eta}$

7: **if** $\bar{\eta} < \bar{\eta}^*$ **then**

8: $\bar{\eta}^* \leftarrow \bar{\eta}$

9: $\boldsymbol{F}^*(\boldsymbol{\rho}) \leftarrow \boldsymbol{F}(\boldsymbol{\rho})$

10: **end if**

11: Select next κ according to scalar search algorithm

12: **until** minimisation of $\bar{\eta}$ converges

4.6 Numerical Example

To demonstrate the ability of the proposed method to converge on an *attainable* residual reference, we study an example where perfect decoupling is possible. It is an extension of the illustrative example in [BB04], in which isolation of actuator and sensor faults in an LPV flight dynamics model was achieved using the geometric (subspace-based) approach. Consider the following linearised parameter varying model of an aircraft:

$$\dot{\boldsymbol{x}} = \boldsymbol{A}(\boldsymbol{\rho})\boldsymbol{x} + \boldsymbol{B}_u u + \boldsymbol{B}_f \boldsymbol{f} \tag{4.57}$$

$$\boldsymbol{y} = \boldsymbol{C}\boldsymbol{x} \tag{4.58}$$

where $\boldsymbol{\rho} = [\rho_1\ \rho_2]$ and $\boldsymbol{A}(\boldsymbol{\rho}) = \boldsymbol{A}_0 + \rho_1 \boldsymbol{A}_1 + \rho_2 \boldsymbol{A}_2$. It is assumed that the parameters ρ_1 and ρ_2 vary in the intervals $[-0.3, 0.3]$ and $[-0.6, 0.6]$ respectively. u contains the actuation input and $\boldsymbol{f} = [f_1 \dots f_4]^T$ denote the physical faults.

$$\boldsymbol{A}_0 = \begin{bmatrix} -1.05 & -2.55 & 0 & 0 & -170 & -0.0091 \\ 2.55 & -1.05 & 0 & 0 & 57.1 & 0.0017 \\ 0 & 0 & -77.5 & 39.6 & 0 & 0 \\ 0 & 0 & 0 & -20.2 & 0 & 0 \\ 0 & 0 & -8.8 & 0 & -20.2 & 0 \\ 0 & 0 & 0 & 0 & 0 & -0.1 \end{bmatrix}$$

$$\boldsymbol{A}_1 = \begin{bmatrix} 0 & 1 & 0 & 0 & 1 & 0 \\ 1 & 0 & 0 & 0 & 1 & 0 \\ 0 & 0 & 0 & 0 & 0 & 0 \\ 0 & 0 & 0 & 0 & 0 & 0 \\ 0 & 0 & 0 & 0 & 0 & 0 \\ 0 & 0 & 0 & 0 & 0 & 0 \end{bmatrix}, \quad \boldsymbol{A}_2 = \begin{bmatrix} 1 & 0 & 0 & 0 & 0 & 0 \\ 0 & 1 & 0 & 0 & 0 & 0 \\ 0 & 0 & 0 & 0 & 0 & 0 \\ 0 & 0 & 0 & 0 & 0 & 0 \\ 0 & 0 & 0 & 0 & 0 & 0 \\ 0 & 0 & 0 & 0 & 0 & 0 \end{bmatrix}$$

$$\boldsymbol{B}_u = \begin{bmatrix} 0 \\ 0 \\ 0 \\ -4.49 \\ 0 \\ 0 \end{bmatrix}, \quad \boldsymbol{B}_f = \begin{bmatrix} 0 & 3.55 & 2.41 & 7.1 \\ 0 & -0.55 & 8.04 & -1.1 \\ 0 & 0 & 0 & 0 \\ 0 & 0 & 0 & 0 \\ 1 & -0.02 & 0.56 & 2.96 \\ 0 & 0 & 0 & 0 \end{bmatrix}$$

$$\boldsymbol{C} = \begin{bmatrix} -0.01 & 0.09 & 0.07 & 0 & 0 & -0 \\ -0.48 & -0.59 & 0 & 0 & -49.5 & -0.0026 \\ 0.03 & 0.09 & -0.06 & 0 & -0 & 0 \\ 0.26 & -0.07 & 0.01 & 0 & 0 & -0 \end{bmatrix}$$

In order to demonstrate the ability of the proposed approach to determine structurally consistent fault-to-residual reference gains, the original three-fault model is augmented by a fourth fault. Its corresponding fourth column in $\boldsymbol{B}_f$ is a linear combination of the first

to third columns, i.e.,

$$\boldsymbol{B}_f = \begin{bmatrix} \boldsymbol{B}_{f[1]} & \boldsymbol{B}_{f[2]} & \boldsymbol{B}_{f[3]} & (k_1\boldsymbol{B}_{f[1]} + k_2\boldsymbol{B}_{f[2]} + k_3\boldsymbol{B}_{f[3]}) \end{bmatrix} ,$$

where $k_1,\ k_2,\ k_3 \in \mathbb{R}$ with $|k_1| > 0$. Our task is to detect f_1 and f_4 while rejecting f_2 and f_3. In the terminology used in this chapter, $[f_1\ f_4]$ corresponds to the "fault" vector since they should be detected, while $[f_2\ f_3]$ corresponds to the "disturbance" vector since they should be rejected.

The results in [BB04] shows that it is possible to detect fault f_1 while rejecting f_2 and f_3. By the construction of f_4 and the principle of superposition, any residual generator sensitive to f_1 will also be sensitive to f_4. Furthermore, the residual response to f_4 will be k_1 times that of f_1. To see this, consider the following with a slight abuse of notation, where $\boldsymbol{G}_{rf[j]}$ is the parameter-dependent transfer function between f_j and the residual r:

$$\begin{aligned} \boldsymbol{G}_{rf} \begin{bmatrix} 0 \\ 0 \\ 0 \\ 1 \end{bmatrix} f_4 &= \begin{bmatrix} G_{rf[1]} & G_{rf[2]} & G_{rf[3]} & G_{rf[4]} \end{bmatrix} \begin{bmatrix} k_1 \\ k_2 \\ k_3 \\ 0 \end{bmatrix} f_4 \\ &= k_1 G_{rf[1]} f_4 \ , \end{aligned} \tag{4.59}$$

since $G_{rf[2]} = G_{rf[3]} = 0$ due to the perfect decoupling of f_2 and f_3. This relationship holds for all values of $\boldsymbol{\rho}$ since the matrix $\boldsymbol{B}_f$ is independent of $\boldsymbol{\rho}$.

Using Procedure 4.2, the residual generator is synthesised for a plant with $[k_1\ k_2\ k_3] = [3\ 2\ 0]$, using the design parameters $\Omega = [0, 1.0]$ rad/s, $\tilde{\boldsymbol{W}} = \frac{1}{0.1s+1}[1\ 1]$, $\boldsymbol{W}_f = \frac{1}{0.33s+1}\boldsymbol{I}_2$. The desired residual generator eigenvalues are constrained to have $Re(s) \in [-300, -5]$. The synthesised 9-th order residual generator has the same relative gains of $[\lambda_1\ \lambda_4] = [1\ 2.96]$ at all four polytope vertices, which is close to the theoretical 1:3 ratio according to (4.59). The synthesis achieved $\bar{\eta}^* = 0.0038$ and frozen parameter eigenvalues with real components in the range $[-298.7, -8.5]$, which lie within the specified range. For comparison, the synthesis procedure is also carried out with fixed gains of $[\lambda_1\ \lambda_4] = [1\ 1]$. The achieved value of $\bar{\eta}^* = 0.4$ indicates a significantly poorer sensitivity to attenuation ratio, demonstrating the advantage of allowing $\boldsymbol{\Lambda}(\boldsymbol{\rho})$ to be optimised in the synthesis. For both cases of the optimised (denoted "variable") and pre-determined (denoted "fixed") $\boldsymbol{\Lambda}(\boldsymbol{\rho})$, the frequency responses of the residual to both u and $\boldsymbol{f}$ are displayed in Figure 4.4 for several frozen values of $\boldsymbol{\rho}$ in the permissible parameter region.

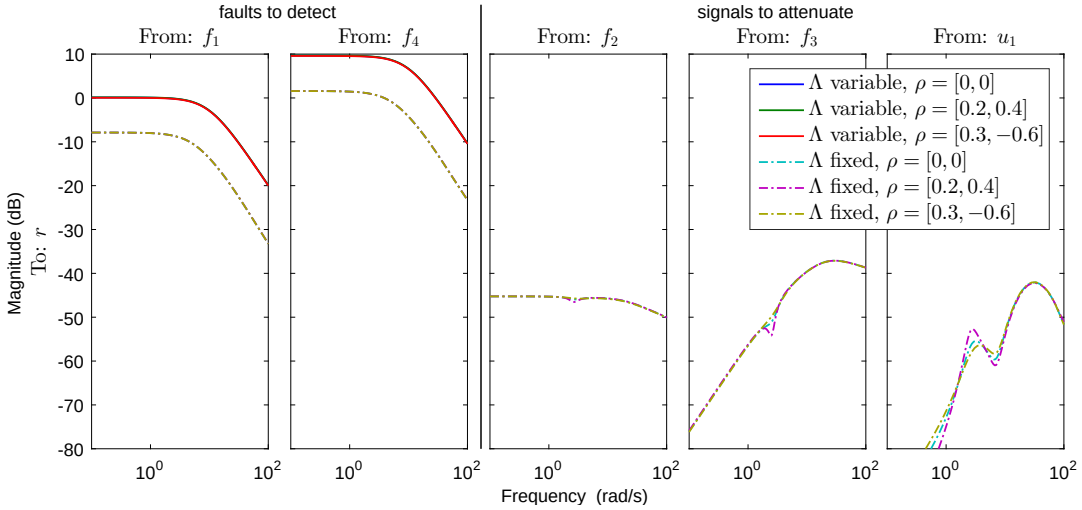

Figure 4.4: Bode plots of the example plant connected to the residual generator evaluated at selected frozen values of scheduling parameters $\boldsymbol{\rho}$. The cases with optimised (labelled "variable") and pre-determined (labelled "fixed") $\boldsymbol{\Lambda}(\boldsymbol{\rho})$ are both plotted.

Chapter 5

Residual Evaluation

After residual generators compute residual signals describing the degree of inconsistency between plant and model-behaviours, the signals are evaluated in order to detect and potentially isolate and identify faults. The necessary level of detail in the fault information to be extracted depends on the fault handling strategy. For example, a basic safety system may require only *detection* of the presence of a fault, so that the system can be brought into a pre-defined safe state. More advanced safety systems require knowledge of the location of a fault, known as *fault isolation*, in order to select an appropriate safety procedure specialised for that fault type. This level of fault information could be sufficient for certain fault-tolerant control algorithms, but it is often necessary to additionally *identify* the nature and magnitude of the fault so that a model of the faulty system can be configured and used in controller redesign. In the application treated in this work, only detection and isolation are considered.

To achieve these objectives, residual evaluation is conceptually divided into two parts. The first involves the evaluation of a single residual into an alarm to indicate whether faults belonging to its sensitive subset have occurred. After that, the pattern of alarms generated by a bank of fault detectors is evaluated logically to narrow down the diagnosis by isolating the present fault. These two parts fit into the overall FDI scheme as shown in Figure 5.1. This chapter is divided into two sections to address these parts separately.

It should be noted that residual evaluation development is not one of the main contributions in this thesis. State-of-the-art approaches are selected and adapted based on their compatibility with the presented residual generator design method and their suitability for the vehicle dynamics application in Chapter 8. The choice of the truncated 2-norm as the evaluation function permits the computation of a dynamic threshold by exploiting the analytical properties of the interconnection between the plant and the residual generator [Din13], thereby providing a sound starting point for further optimisation. For residual structure design, the applied method is based on an approach from structural analysis literature [KN02] which computes a suitable structure based on specified criteria. This approach remains efficient even for larger dimensional problems. This chapter is presented from a predominantly practical perspective and some of the discussions will not

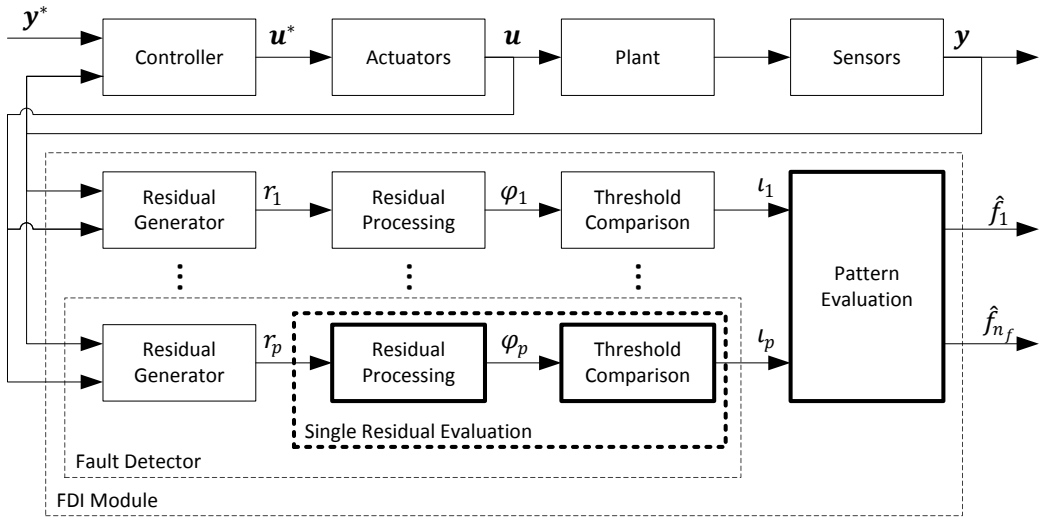

Figure 5.1: Residual-based FDI architecture. The components with bold outlines are addressed in this chapter. Inputs for threshold computation in the threshold comparison block are not shown.

be treated as rigorously. References to more in-depth treatments are provided for the interested reader.

5.1 Single Residual Evaluation

Given the output of a single residual generator in the deterministic framework, denoted $r(t)$, residual evaluation seeks to make the binary decision of whether a fault is present. The available methods can be broadly classified into stochastic and deterministic categories. Stochastic approaches are not considered here since they require knowledge of the probabilistic properties of the residual and model, and are therefore not compatible with the deterministic residual generator presented in the previous chapter. Due to uncertainties and mismatches in the model, initial conditions, actuation inputs, measurement noise, and disturbances, residual generators can produce (bounded) non-zero outputs in fault-free scenarios. In the case of approximate decoupling, residuals are by definition non-zero in the fault-free case and upper bounds on fault-free residual norms can be readily computed under the design assumptions on input signal norms. Hence it is reasonable to detect the presence of a fault by comparing an evaluation function $\varphi(r(t))$ of the scalar residual against a threshold function $\Phi(t)$ associated with the aforementioned bounds, with the no-fault and faulty hypotheses given by the conditions:

$$\begin{aligned} \text{no fault:} \quad & \varphi(r(t)) \leq \Phi(t) \quad \forall t \leq t_0 \\ \text{fault present at } t \geq t_0\text{:} \quad & \varphi(r(t)) > \Phi(t) \quad \forall t > t_0 \ . \end{aligned}$$

Clearly, the choice of an appropriate threshold function $\Phi(t)$ is closely tied to the choice of evaluation function $\varphi(\cdot)$. According to [Din13], it is the state of the art in practice that the evaluation function is first defined, and the threshold is established based on it.

However, an evaluation function may also be chosen due to the potential to favourably exploit available system and environment information to set a threshold function. In this work, the latter approach is chosen. The resulting threshold function can be used as is, or as a starting point for further data-driven optimisation.

5.1.1 Residual Evaluation for the Deterministic Framework

The robust LPV residual generation approach presented in the previous chapter is designed to minimise the upper-bound on the signal 2-norm of the residual, under the condition that the actuation and disturbance inputs are bounded. The $\bar{\eta}$ metric of residual generator performance relates to the ability to distinguish between the influence of faults and non-fault inputs on the 2-norm of the residual signal. Therefore, the validity of those performance claims are predicated on the use of the 2-norm as the evaluation function. However, if the $\bar{\eta}$-minimisation in the residual generator synthesis is viewed as a means of optimising its general performance, without using the achieved $\bar{\eta}$ to draw hard conclusions about the feasibility of reliable and robust fault detection, then other evaluation functions can be considered. We will see that this concession is necessary for online implementation.

Evaluation functions usually convert the residual into some measure of magnitude. One based on the filtered absolute value is used in [Oss14], while another similar function is suggested in [Bla06]. Both trade proximity to an ideal norm for their efficient state-space implementations. In [Oss14], the evaluated residual φ is computed by

$$\begin{aligned} \dot{\xi}(t) &= -\alpha_1 \xi(t) + \alpha_2 |r(t)| \\ \varphi(t) &= \xi(t) + \alpha_3 |r(t)| \ . \end{aligned} \tag{5.1}$$

where ξ is an auxiliary variable. The filter parameter α_1 represents the forgetting factor, while α_2 and α_3 represent the weights for the long-term and instantaneous residual norm values respectively. The absolute value $|\cdot|$ is shown here as it is equal to the vector norm $\|\cdot\|_2$ when the residual is scalar.

Using this approach forfeits the possibility of directly using analytical upper-bounds on $\|\boldsymbol{G}_{ru}\|$ and $\|\boldsymbol{G}_{rd}\|$ to set residual thresholds. [Oss14] takes an optimisation-based approach whereby the filter parameters, the threshold and selected residual generator parameters are automatically tuned over a large number of representative operation scenarios. The multi-objective optimisation aims to achieve a compromise between robustness to disturbances (i.e. eliminate or minimise false alarms), minimum detectable fault size, and low detection time. This method is not pursued in this thesis and it will not be discussed further. Interested readers are referred to [Oss14; Oss13] for details.

Under the deterministic assumption of norm-bounded inputs, using a norm to evaluate the residual permits the exploitation of the analytical induced-norm of the input-to-residual system for threshold calculation. The 2-norm is commonly used for this purpose, while [Din13] suggests alternative functions with peak, average or RMS norms. In fact, any combination of inputs bounded by a p-norm and residual evaluated with a q-norm

may be used as long as the induced norm

$$\sup_{\bar{\boldsymbol{d}}\neq 0} \frac{\|\boldsymbol{r}\|_q}{\|\bar{\boldsymbol{d}}\|_p}$$

can be computed, where $\bar{\boldsymbol{d}}$ denotes here a generic system input. For example, [Din13] demonstrates how the peak-to-peak norm can be calculated by means of LMIs. To keep the assumptions consistent with the residual generation chapter, we will consider an evaluation function based on the 2-norm and also assume inputs with bounded 2-norms. The resulting induced-$\mathcal{L}_2$ norm of the input-to-residual system can be calculated using the LMI-based methods presented in Chapter 3.

We begin by considering the 2-norm as a candidate evaluation function. The 2-norm of a vector-valued signal $\boldsymbol{v}(t)$ is calculated in the time domain by

$$\|\boldsymbol{v}(t)\|_2 = \left(\int_0^\infty \boldsymbol{v}^T(\tau)\boldsymbol{v}(\tau)d\tau\right)^{\frac{1}{2}} . \tag{5.2}$$

This is not realisable in practice since the residual signal needs to be known in the interval $t \in [0, \infty)$, and therefore for online evaluation an approximation is necessary. Commonly found in literature is the truncated 2-norm

$$\|\boldsymbol{v}(t)\|_{2,(t-T,t)} = \left(\int_{t-T}^{t} \boldsymbol{v}^T(\tau)\boldsymbol{v}(\tau)d\tau\right)^{\frac{1}{2}} , \tag{5.3}$$

where t denotes the current time and T is the window length. The choice of window length is a compromise affecting approximation quality, detection time, and computation resources. A longer window length provides a more accurate approximation of the actual norm but also damps changes in the output signal, reducing its rate of change in response to abrupt changes in the fault input and thereby increasing the time before the threshold is exceeded. A further consideration is that since the contained integral (or summation in discrete-time) represents a non-recursive, rectangular windowed filter, all residual values within the window must be stored. As a consequence, the memory requirement and computation load are directly proportional to the window length. The truncated 2-norm will be treated in more depth in Section 5.1.3. Before that, we address the basic concepts of analytical threshold calculation with respect to evaluation using ideal signal norms.

5.1.2 Ideal Norm-Based Residual Evaluation

Once an LPV residual generator $\boldsymbol{F}(\boldsymbol{\rho})$ has been synthesised, the input-output relations of $\boldsymbol{G}_{rd}(\boldsymbol{\rho}, \Delta)$ and $\boldsymbol{G}_{ru}(\boldsymbol{\rho}, \Delta)$ can be derived by connecting it to the plant. Expressions for them are given in (4.5). The corresponding upper-bounds on their worst-case induced-$\mathcal{L}_2$-norms can subsequently be computed. To keep the notation compact, the following

shorthand is introduced for the worst-case value of the norm over all permissible uncertainties:

$$\|\cdot\|_\Delta := \sup_{\Delta\in\mathcal{D}} \|\cdot\|_{i2} \ .$$

Define the upper bounds γ_d and γ_u such that

$$\|\boldsymbol{G}_{rd}(\boldsymbol{\rho},\Delta)\boldsymbol{W}_d\|_\Delta < \gamma_d \tag{5.4}$$
$$\|\boldsymbol{G}_{ru}(\boldsymbol{\rho},\Delta)\boldsymbol{W}_u\|_\Delta < \gamma_u \ , \tag{5.5}$$

where $\boldsymbol{W}_d$ and $\boldsymbol{W}_u$ are diagonal weighting transfer function matrices such that

$$\boldsymbol{d} = \boldsymbol{W}_d\tilde{\boldsymbol{d}} \ , \quad \|\tilde{\boldsymbol{d}}\|_2 \le \varepsilon_d \tag{5.6}$$
$$\boldsymbol{u} = \boldsymbol{W}_u\tilde{\boldsymbol{u}} \ , \quad \|\tilde{\boldsymbol{u}}\|_2 \le \varepsilon_u \ , \tag{5.7}$$

where $\tilde{\boldsymbol{d}}$ and $\tilde{\boldsymbol{u}}$ are norm bounded signals and $\varepsilon_d, \varepsilon_u > 0$. It should be noted that although these instances of $\boldsymbol{W}_u$ and $\boldsymbol{W}_d$ have the same definition as those used in the residual generator synthesis in Chapter 4, they can take on different values here since the design of residual evaluation is treated as an independent downstream process. The choice of these matrices will be discussed later.

From this point onwards, parameter dependencies are not shown for notational brevity. We now seek to find a bound on $\|r\|_2$ when no fault is present. Recall from (4.5) that

$$r = \boldsymbol{G}_{ru}\boldsymbol{u} + \boldsymbol{G}_{rd}\boldsymbol{d} + \boldsymbol{G}_{rf}\boldsymbol{f} \ .$$

Defining the components as

$$\begin{aligned} r_u &= \boldsymbol{G}_{ru}\boldsymbol{u} = \boldsymbol{G}_{ru}\boldsymbol{W}_u\tilde{\boldsymbol{u}} \\ r_d &= \boldsymbol{G}_{rd}\boldsymbol{d} = \boldsymbol{G}_{rd}\boldsymbol{W}_d\tilde{\boldsymbol{d}} \\ r_f &= \boldsymbol{G}_{rf}\boldsymbol{f} \ , \end{aligned}$$

the residual can be written as a sum of its components due to the inputs:

$$r = r_u + r_d + r_f \ . \tag{5.8}$$

When no fault is present, $r_f = 0$. The definition of the worst-case induced-$\mathcal{L}_2$ norm relates the 2-norms of the inputs and outputs by

$$\|r_u\|_2 \le \|\boldsymbol{G}_{ru}\boldsymbol{W}_u\|_\Delta\|\tilde{\boldsymbol{u}}\|_2 \tag{5.9}$$
$$\|r_d\|_2 \le \|\boldsymbol{G}_{rd}\boldsymbol{W}_d\|_\Delta\|\tilde{\boldsymbol{d}}\|_2 \ . \tag{5.10}$$

Combining the above and applying the triangle inequality on $r = r_u + r_d$ gives the following bound on the fault-free residual:

$$\begin{aligned} \|r\|_2 &\leq \|r_u\|_2 + \|r_d\|_2 && \text{(5.11a)} \\ &\leq \|\boldsymbol{G}_{ru}\boldsymbol{W}_u\|_\Delta \|\tilde{\boldsymbol{u}}\|_2 + \|\boldsymbol{G}_{rd}\boldsymbol{W}_d\|_\Delta \|\tilde{\boldsymbol{d}}\|_2 && \text{(5.11b)} \\ &\leq \gamma_u \|\tilde{\boldsymbol{u}}\|_2 + \gamma_d \|\tilde{\boldsymbol{d}}\|_2 && \text{(5.11c)} \\ &\leq \gamma_u \varepsilon_u + \gamma_d \varepsilon_d \ . && \text{(5.11d)} \end{aligned}$$

Since the actuation input $\boldsymbol{u}$ is a known signal, it is reasonable to use this information to compute ε_u rather than setting a conservative upper bound. Assume that the diagonal $\boldsymbol{W}_u$ is biproper (i.e., has relative degree zero) such that $\boldsymbol{W}_u^{-1}$ exists. Then $\tilde{\boldsymbol{u}} = \boldsymbol{W}_u^{-1}\boldsymbol{u}$ and in (5.11d) the constant ε_u can be replaced by the *dynamic* $\boldsymbol{u}$-dependent term

$$\varepsilon_u(\boldsymbol{u}) = \|\boldsymbol{W}_u^{-1}\boldsymbol{u}\|_2 \ .$$

This form of the dynamic threshold is commonly presented in literature, such as [FD97; Bla06; Din13]. The next section examines the implications of the truncated norm on the constant and dynamic components of the threshold (5.11d).

A brief discussion on the choices of $\boldsymbol{W}_d$ and $\boldsymbol{W}_u$ will now be presented, now that their roles in the threshold calculation have been defined. First consider $\boldsymbol{W}_d$. In the residual generation set up, this weighting matrix is used to focus the disturbance attenuation on frequencies where $\boldsymbol{d}$ has higher input energy. Since $\boldsymbol{G}_{rd}$ is now fixed for residual evaluation design, $\boldsymbol{W}_d$ is instead used to reduce the conservatism of the $\|\cdot\|_\Delta$ by "flattening" the spectrum of $\boldsymbol{G}_{rd}\boldsymbol{W}_d$. To do this, choose $\boldsymbol{W}_d$ such that $\|\boldsymbol{G}_{rd}\boldsymbol{W}_d\|_\Delta = \|\boldsymbol{G}_{rd}\|_\Delta$ and it satisfies

$$W_{d[i]}(j\omega) \geq 1 \quad \forall \omega, \ i = 1, \ldots, n_d$$

where $W_{d[i]}$ denotes the i-th diagonal element of the diagonal matrix $\boldsymbol{W}_d$. Then it can be deduced that $\|\tilde{\boldsymbol{d}}\|_2 = \|\boldsymbol{W}_d^{-1}\boldsymbol{d}\|_2 \leq \|\boldsymbol{d}\|_2$, resulting in a reduction of the threshold according to (5.11b). Therefore a $\boldsymbol{W}_d$ with the above properties should be chosen to minimise ε_d. An analogous argument can be applied for $\boldsymbol{W}_u$.

5.1.3 Using the Truncated Norm

The truncated 2-norm is frequently treated as a direct replacement for the ideal 2-norm in literature. This section reveals some issues with this approach and proposes a modification to address them. A core assumption in the following derivations is that the impulse responses of $\boldsymbol{G}_{ru}$ and $\boldsymbol{G}_{rd}$ *completely* decay within finite periods ζ_u and ζ_d respectively. Although in the general case this is not strictly correct due to the asymptotic decay of the response of many continuous system classes, in many cases it is a close approximation that significantly simplifies the arguments. A more rigorous derivation would involve bounding the energy integral of the "tail" of the impulse response. Taking a LTI SISO G_{rd} as an

example, this involves finding a small ϵ_1 such that

$$\int_{\zeta_d}^{\infty} g_{rd}(t)^2 < \epsilon_1 \ , \tag{5.12}$$

where $g_{rd}(t)$ is the impulse response of G_{rd}. A function of ϵ_1 is then added to the derived upper bounds as a constant offset. However, this term is neglected here and it is assumed that ζ_u and ζ_d are chosen large enough such that the complete decay assumption is reasonable.

The truncated 2-norm defined in (5.3) can be alternatively expressed as the ideal 2-norm of a truncated signal, since

$$\begin{aligned} \|\boldsymbol{v}\|_{2,(t-T,t)} &= \left(\int_{t-T}^{t} \boldsymbol{v}^T(\tau)\boldsymbol{v}(\tau)d\tau \right)^{\frac{1}{2}} \\ &= \left(\int_{0}^{\infty} \boldsymbol{v}_{(t-T,T)}^T(\tau)\boldsymbol{v}_{(t-T,T)}(\tau)d\tau \right)^{\frac{1}{2}} \\ &= \|\boldsymbol{v}_{(t-T,T)}\|_2 \end{aligned} \tag{5.13}$$

where $\boldsymbol{v}_{(t_1,t_2)}(\tau)$ denotes the signal $\boldsymbol{v}$ truncated to the time window $[t_1, t_2]$ as

$$\boldsymbol{v}_{(t_1,t_2)}(\tau) = \begin{cases} \mathbf{0}, & \tau < t_1 \\ \boldsymbol{v}(\tau), & t_1 \le \tau \le t_2 \\ \mathbf{0}, & \tau > t_2 \end{cases} \ . \tag{5.14}$$

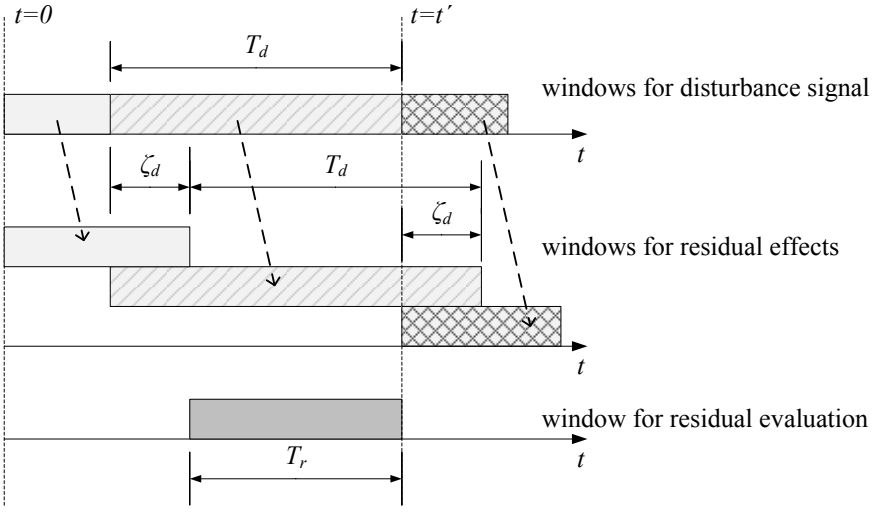

Figure 5.2: Illustration of the time windows of the effects from $\boldsymbol{d}$ to r_d, under the assumption of finite decay time ζ_d

Based on the truncated signal representation, we now present a conceptual derivation of the threshold on the truncated norm of the residual. Consider Figure 5.2 where t' denotes the reference time instant. Divide the disturbance $\boldsymbol{d}$ into two truncated signal (vectors) in the intervals $[0, t' - T_d]$ and $[t' - T_d, t']$, denoted by $\boldsymbol{d}_{(0,t'-T_d)}$ and $\boldsymbol{d}_{(t'-T_d,t')}$

respectively. The time intervals of influence of $\boldsymbol{d}$ on r_d can be established by applying the causality of $\boldsymbol{G}_{rd}$ and the decay time assumption:

$$\begin{array}{rcl} \boldsymbol{d} & & r_d \\ [0, t' - T_d] & \rightarrow & [0, t' - T_d + \zeta_d] \\ [t' - T_d, t'] & \rightarrow & [t' - T_d, t' + \zeta_d] \\ [t', \infty) & \rightarrow & [t', \infty) \ . \end{array} \tag{5.15}$$

If $\boldsymbol{d} = 0$ on the intervals $[0, t' - T_d]$ and $[t', t' + \zeta_d]$, then the ideal 2-norm condition $\|r_d\|_2 < \|\boldsymbol{G}_{rd}\boldsymbol{W}_d\|_\Delta \|\tilde{\boldsymbol{d}}\|_2$ is equivalent to

$$\|r_{d(t'-T_d,t'+\zeta_d)}\|_2 \leq \|\boldsymbol{G}_{rd}\boldsymbol{W}_d\|_\Delta \|\tilde{\boldsymbol{d}}_{(t'-T_d,t')}\|_2 \ . \tag{5.16}$$

However, in the general case, (5.15) shows that $[t' - T_d + \zeta_d, t']$ is the largest interval where r_d is only affected by $\boldsymbol{d}_{(t'-T_d,t')}$. The implication is that only a more conservative inequality holds, in which r_d is evaluated over this shorter interval:

$$\|r_{d(t'-T_d+\zeta_d,t')}\|_2 \leq \|\boldsymbol{G}_{rd}\boldsymbol{W}_d\|_\Delta \|\tilde{\boldsymbol{d}}_{(t'-T_d,t')}\|_2 \ . \tag{5.17}$$

It is assumed that $\tilde{\boldsymbol{d}}$ is characterised by its root-mean-square (RMS) value, which measures the average energy of a signal over a time interval. The RMS of a signal $\boldsymbol{v}$ evaluated over a time interval of length T is given by

$$\|\boldsymbol{v}\|_{RMS} = \left(\frac{1}{T} \int_{t-T}^{t} \boldsymbol{v}^T(\tau)\boldsymbol{v}(\tau) d\tau \right)^{\frac{1}{2}} \ . \tag{5.18}$$

It is related to the truncated 2-norm over the same time window by

$$\|\boldsymbol{v}\|_{2,(t-T,T)} = \sqrt{T}\|\boldsymbol{v}\|_{RMS} \ . \tag{5.19}$$

If $\tilde{\boldsymbol{d}}$ has a maximum RMS value of $\tilde{d}_{max}$ over any time window of length T_d, then $\|\tilde{\boldsymbol{d}}_{(t'-T_d,t')}\|_2 < \tilde{d}_{max}\sqrt{T_d}$, giving

$$\|r_{d(t'-T_d+\zeta_d,t')}\|_2 \leq \gamma_d \ \tilde{d}_{max}\sqrt{T_d} \ . \tag{5.20}$$

Applying the same argument to r_u results in the analogous expression

$$\|r_{u(t'-T_u+\zeta_u,t')}\|_2 \leq \gamma_u \|\tilde{\boldsymbol{u}}_{(t'-T_u,t')}\|_2 \ . \tag{5.21}$$

However, since the value of $\boldsymbol{u}$ is known, its truncated norm may be directly computed using (5.13) and setting an upper bound is not necessary. Inequality (5.21) then represents a dynamic input-dependent upper-bound on the r_u component of the evaluated residual.

The residual evaluation window length can be defined as $T_r = T_d - \zeta_d = T_u - \zeta_u$, where T_u, T_d are chosen such that the equality holds. Then by the triangle inequality, the

fault-free upper bound on the truncated norm of r is

$$\|r\|_{2,(t'-T_r,t')} \leq \gamma_d \ \tilde{d}_{max}\sqrt{T_r+\zeta_d} + \gamma_u \|\tilde{\boldsymbol{u}}\|_{2,(t'-(T_r+\zeta_u),t')} \ . \tag{5.22}$$

Using the terminology introduced earlier, the evaluation function $\varphi(r(t))$ and threshold function $\Phi(t)$ are

$$\varphi(r(t)) = \|r(t)\|_{2,(t'-T_r,t')} \tag{5.23}$$

$$\Phi(t) = \gamma_d \ \tilde{d}_{max}\sqrt{T_r+\zeta_d} + \gamma_u \|\tilde{\boldsymbol{u}}(t)\|_{2,(t'-(T_r+\zeta_u),t')} \ . \tag{5.24}$$

Comparing these to (5.11d) yields expressions for ε_u and ε_d:

$$\varepsilon_u(\boldsymbol{u}(t)) = \|\boldsymbol{W}_u^{-1}\boldsymbol{u}(t)\|_{2,(t'-(T_r+\zeta_u),t')} \tag{5.25}$$

$$\varepsilon_d = \tilde{d}_{max}\sqrt{T_r+\zeta_d} \ . \tag{5.26}$$

As already mentioned earlier, the usual solutions in literature use the same window length for the r, $\boldsymbol{u}$ and $\boldsymbol{d}$ components in the evaluation function and the threshold function. According to the presented argument, this results in a threshold that is lower than the theoretical upper bound and may contribute to false alarms. However, this gap recedes as the window length increases.

In the presented version of the residual evaluation, a longer window length reduces the conservatism attributed to the gap between the start of the window for r and the windows for $\boldsymbol{u}$ and $\boldsymbol{d}$. However, this benefit is offset by the disadvantages of longer detection time and more memory intensive computation.

5.1.4 Illustrative Example

The numerical example from Section 4.6 will be used as the basis for demonstrating the proposed residual evaluation design procedure. To obtain an uncertain plant, the parameter ρ_1 is changed from a scheduling parameter into an uncertain parameter with a permissible range of $[-0.1, 0.1]$, while the other parameter ρ_2 remains a scheduling parameter with a permissible range of $[-0.6, 0.6]$. The residual generation design procedure (Procedure 4.2) is performed to obtain a residual generator $\boldsymbol{F}$ with $\bar{\eta} = 0.33$. Design of the residual evaluation and threshold functions involves establishing the following parameters:

1. decay times ζ_d and ζ_u
2. window length T_r
3. weighting functions $\boldsymbol{W}_d$ and $\boldsymbol{W}_u$
4. the bound ϵ_d on the RMS weighted disturbance
5. the worst-case gains γ_d and γ_u.

We begin by inspecting the frequency and impulse responses of the $\boldsymbol{G}_{rd}$ and $\boldsymbol{G}_{ru}$ transfer functions to guide the choice of parameter groups 1-3. The reader is reminded that in this example, the disturbance vector consists solely of rejected faults, i.e. $\boldsymbol{d} = [f_2 \ f_3]^T$.

$\boldsymbol{G}_{rd}$ and $\boldsymbol{G}_{ru}$ are formed by connecting the plant $\boldsymbol{G}$ with the residual generator $\boldsymbol{F}$ and extracting the subsystem corresponding to inputs r and $\boldsymbol{d}$ respectively. In order to gauge the frequency ranges in which it may be possible to raise the LTI weighting matrices $\boldsymbol{W}_d(j\omega)$ or $\boldsymbol{W}_u(j\omega)$ without increasing $\|\boldsymbol{G}_{rd}\boldsymbol{W}_d\|_{i2}$ and $\|\boldsymbol{G}_{ru}\boldsymbol{W}_u\|_{i2}$, the bode magnitude plot of the SISO transfer functions from each input to the residual is illustrated in Figure 5.3 for a grid of scheduling parameters $\boldsymbol{\rho}$ and uncertain parameters Δ within their respective parameter regions.

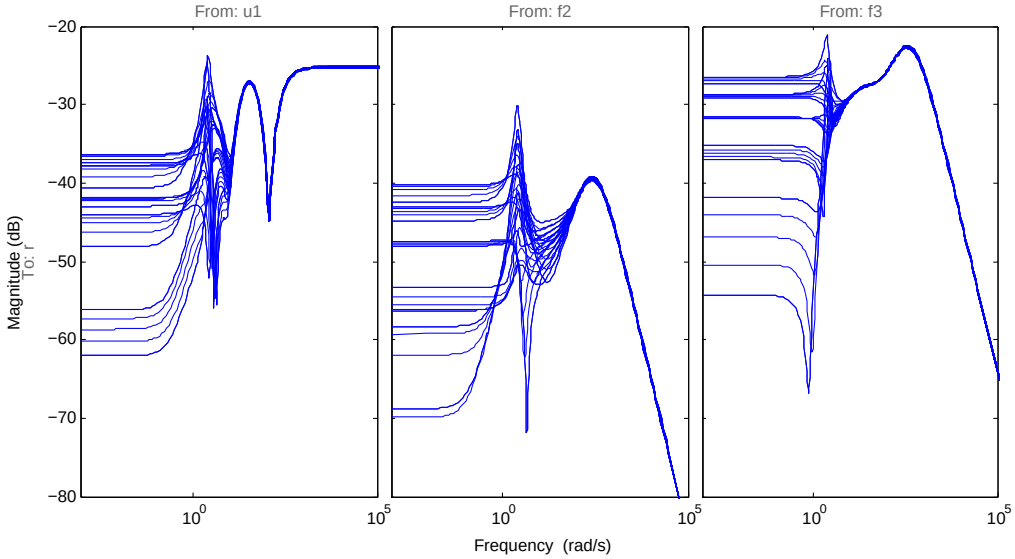

Figure 5.3: Bode magnitude plots from the actuation and rejected fault inputs to the residual on a parameter grid over $\rho_1 \in [-0.1,\ 0.1]$ and $\rho_2 \in [-0.6,\ 0.6]$

Iterative trials showed that we can choose

$$\boldsymbol{W}_d = diag\,(W_{f2},\ W_{f3})$$

where

$$W_{f2} = \frac{30s + 300}{s + 300}, \quad W_{f3} = \frac{10s + 600}{s + 600}\ ,$$

and

$$W_u = \frac{2s + 150}{s + 150}\ .$$

Then their diagonal elements satisfy $|W_{d[i]}(j\omega)| \geq 1$ and $|W_u(j\omega)| \geq 1$ for all ω without increasing the weighted worst-case induced-$\mathcal{L}_2$ norms, which are:

$$\gamma_{f2} = \|\boldsymbol{G}_{rd}\boldsymbol{W}_{f2}\|_\Delta = 0.031 \tag{5.27}$$

$$\gamma_{f3} = \|\boldsymbol{G}_{rd}\boldsymbol{W}_{f3}\|_\Delta = 0.087 \tag{5.28}$$

$$\gamma_u = \|\boldsymbol{G}_{ru}\boldsymbol{W}_u\|_\Delta = 0.067\ . \tag{5.29}$$

Due to the single fault assumption, only one of the faults f_2 and f_3 can occur at any given time and therefore we can set $\gamma_d = \max(\gamma_{f2},\ \gamma_{f3}) = 0.087$.

Next the decay times of the weighted functions are determined by inspecting the impulse responses of $\boldsymbol{G}_{rd}\boldsymbol{W}_d$ and $\boldsymbol{G}_{ru}\boldsymbol{W}_u$ in Figure 5.4, again over a grid of $\boldsymbol{\rho}$ and Δ. It is decided that the choices of $\zeta_d = 0.15$s and $\zeta_u = 0.12$s is adequate. Then T_r is chosen such that the ratios between the residual evaluation window length T_r and the ones for disturbances and actuation inputs ($T_r + \zeta_d$ and $T_r + \zeta_u$) are not too far below unity to avoid excessively conservative thresholds. It should also be kept sufficiently short to limit detection time and the necessary buffer sizes. In this case study, $T_r = 0.5$s is deemed a reasonable balance.

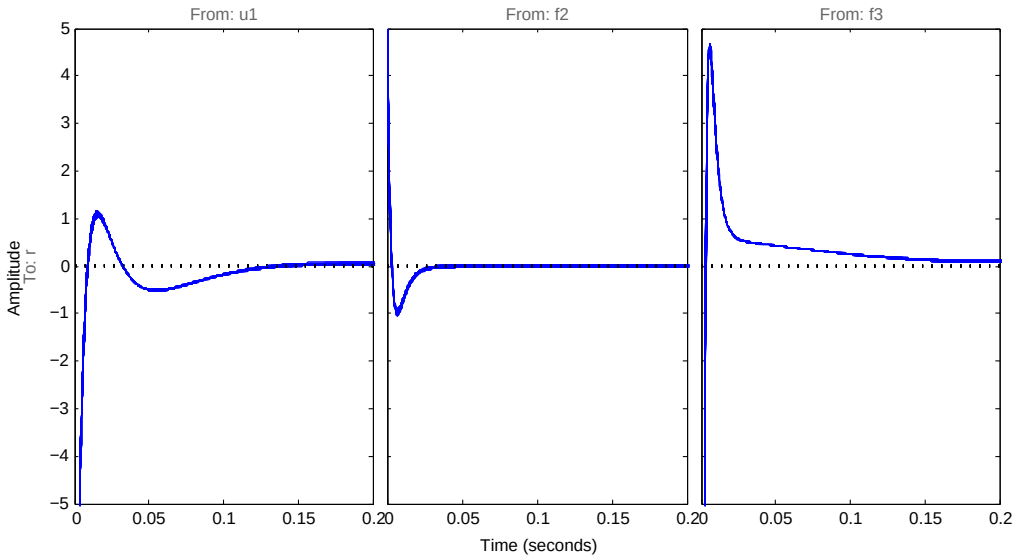

Figure 5.4: Impulse responses from the actuation and rejected fault inputs to the residual on a parameter grid over $\rho_1 \in [-0.1,\ 0.1]$ and $\rho_2 \in [-0.6,\ 0.6]$

The parameter $\tilde{d}_{max} = 1$ is set to comply with the signal size of the rejected faults in this example, which then allows ϵ_d to be computed. The u-dependent residual threshold $\Phi(t) = \epsilon_d + \epsilon_u(u(t))$ is computed online. A simulation was performed with the selected residual evaluation parameters with $[\rho_1, \rho_2]$ set to vary sinusoidally within their permissible ranges. The results are displayed in Figure 5.5.

The faults f_1 and f_4 occur at $t = 1.0$s and $t = 7.0$s respectively, and the residuals fire (i.e., $\varphi(t) > \Phi(t)$) in response to these faults at $t = 1.21$s and $t = 7.08$s. Without further post-processing measures on this logical signal, these correspond to detection delays of 0.21s and 0.08s. We also observe that large activity of input u in the period $[3, 6]$s causes the threshold to increase as expected, which accommodates the resultant rise in the evaluated residual. The dotted black line in the bottom plot represents a constant threshold, set here for illustrative purposes to the maximum value of the input-dependent threshold in order to ensure that no false alarm occurs under the same evolution of u. It is clearly more conservative and would have resulted in missing the detection of f_1 in this example.

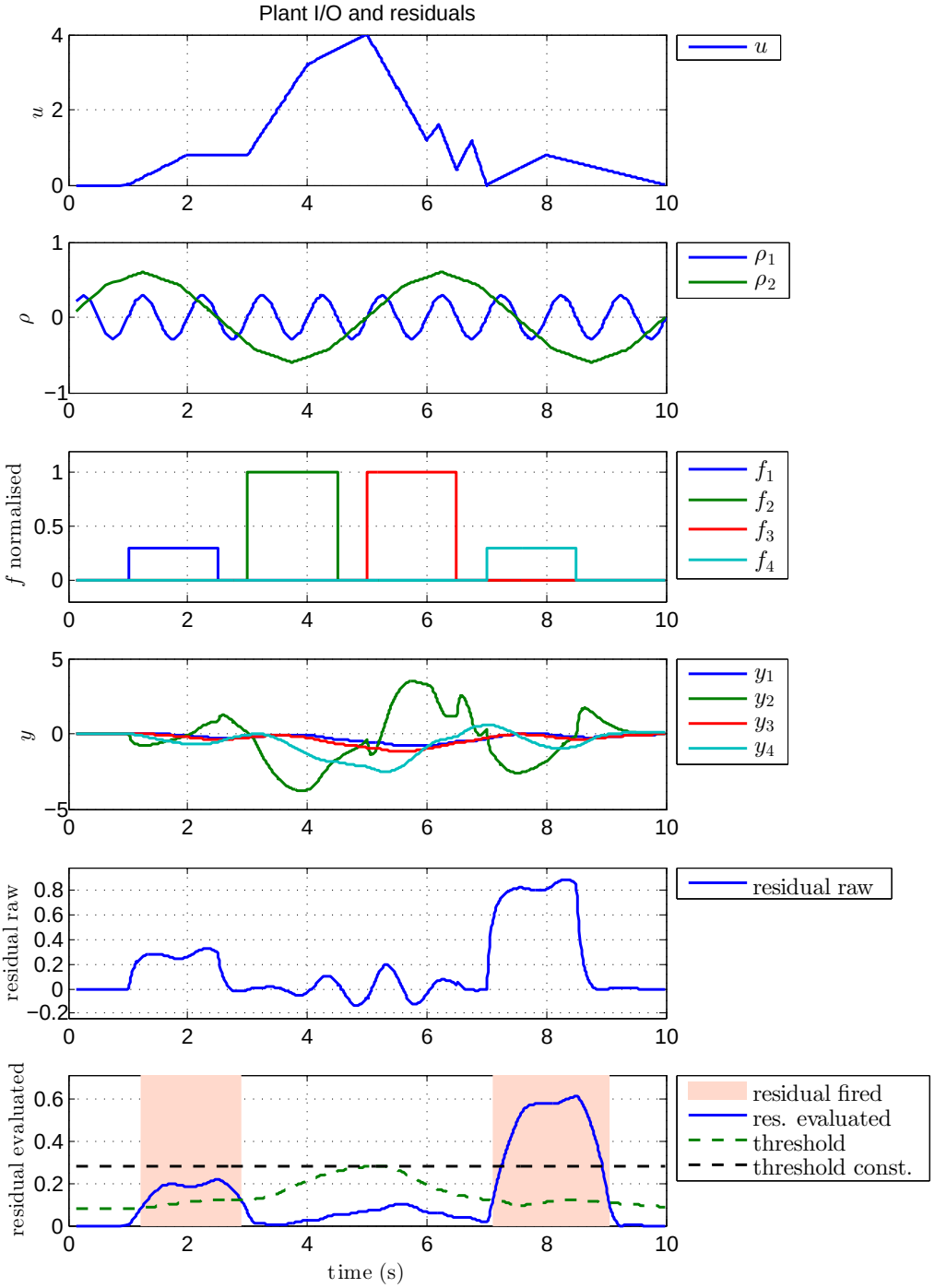

Figure 5.5: Simulation inputs and outputs demonstrating that the evaluated residual lies below the threshold when the nominal sized, rejected f_2 and f_3 are present. The threshold is exceeded when the sensitive f_1 and f_4 are present. Magnitudes of f_1 and f_4 smaller than their nominal values are simulated to improve the visibility of the threshold and fault-free residual by restricting maximum signal values in the plot.

5.2 Fault Isolation Using Structured Residuals

5.2.1 Basic Concepts

Fault isolation is the task of distinguishing between multiple faults of interest once the presence of a fault has been detected. In residual-based diagnosis this can be achieved by such methods as structured residuals [Ger98] and directional residuals [Bea71]. The structured residuals approach is used in this work. This section provides an overview of the approach and discusses some issues that are relevant to the application in Chapter 8. For a more detailed treatment, the reader is referred to [Ger98] and also literature on structural analysis in the fault diagnosis context such as [KN02; Bla06].

A residual is said to have *fired* if the evaluated value exceeds the threshold, i.e. $\varphi(r(t)) > \Phi(t)$, mapping the residual into the *alarm* state. Faults can be distinguished from each other through the different patterns of fired residuals that they trigger from a residual set. The expected pattern of fired residuals in the presence of a particular fault is called the *residual signature* of that fault. Conversely, the firing pattern of an individual residual in response to all faults of interest is called its *fault signature*. Extending the notation from [Var07], a signature entry is labelled as:

-1: *weakly detectable*, if the residual always fires when the corresponding fault fulfils the specified manifestation requirement (common: above a minimum size);

1: *strongly detectable*, if the fault is weakly detectable and satisfies the additional requirement that a persistent fault produces an asymptotically persistent residual response;

0: *undetectable*, if the residual never fires as long as the corresponding fault fulfils the specified manifestation requirement (common: below a maximum size);

$\times$: *indeterminate*, if it is uncertain whether the residual will fire in response to that fault.

An indeterminate entry can arise when the fault is disregarded in the synthesis of a residual, so that its response to the fault is unknown. Such an entry can be intentionally specified in the desired fault signature to improve solution feasibility and will be handled in the following treatment. On the other hand, the weakly detectable case will not be treated further. This is because when using the model-matching residual generator design approach in Chapter 4, choosing a reference frequency range Ω with $0 \in \Omega$ ensures that any residual deemed feasible will have an asymptotically persistent response to the sensitive faults, thus making those entries strongly detectable.

Stacking the fault signature row vectors together for a set of residuals produces the *incidence matrix*. Here is an example:

$$\begin{array}{c} \\ r_1 \\ r_2 \\ r_3 \\ r_4 \end{array} \begin{array}{c} \begin{array}{ccc} f_1 & f_2 & f_3 \end{array} \\ \begin{pmatrix} 1 & \times & 0 \\ 1 & 1 & 1 \\ 1 & 0 & 1 \\ 0 & 1 & 1 \end{pmatrix} \end{array} .$$

The residual signature of a fault can be determined simply by extracting its corresponding column from the incidence matrix. Fault isolation using structured residuals involves distinguishing one fault from another on the basis of their distinct residual signatures.

The ability to determine the presence of a particular fault from a residual pattern is dependent on several assumptions. The ones commonly found in literature are [Jun15]:

1. closed world: no unknown fault can occur besides the defined set of fault modes
2. single fault: only one fault can be present at any given time
3. exoneration: a fault will always cause a sensitive residual to fire
4. fault manifestation: magnitudes and manifestations (e.g. ramp, step) of a fault are specified

This work makes use of assumptions 1 and 2, as well as 4 partially. The closed world assumption is essential for drawing conclusions from a residual pattern, otherwise a possibility always exists that an observed residual pattern is due to an unknown fault. The single fault assumption is reasonable if it can be accepted that the faults in generally do not occur frequently, and that there will always be sufficient temporal separation between their occurrences. The latter provides enough time to isolate the first fault before the second one occurs, whose detection and isolation may necessitate a reconfigured FDI function. The single fault assumption is used throughout this work, both in residual generation and now in fault isolation. The isolation of multiple simultaneous faults is possible using the structured residuals approach but not handled here; the more complex and restrictive conditions on the necessary structures to achieve this are treated in [Ger98].

It was assumed in Chapter 4 that the faults to be detected are persistent and have a minimum magnitude. This can be considered a loose form of the fault manifestation assumption. On the other hand, the exoneration assumption is considered unrealistic for the presented residual generation and evaluation scheme since the non-zero residual threshold, necessary to avoid false alarms, will mask the effects of faults with smaller magnitudes. This leads to the *partial firing* phenomenon and its robustness implications are treated next.

5.2.2 Robust Isolation

For the fault isolation scheme to function reliably in a practical application, some robustness issues need to be considered. These include the phenomenon of partial firing due to small faults, and also that of erroneous firing due to uncertainty and disturbances. Once these have been addressed, procedures are presented to determine the isolation capability of a given set of residuals, and on the basis of this information, select an appropriate residual subset to be implemented.

The evaluation of fault isolation capabilities first requires elaboration on the topic of desirable fault signatures, which has been discussed in [Ger98; KN02; Oss13]. The basic premise is that robustness is improved when any two fault signatures are as 'far' apart from each other as possible, in the sense where the distance is measured by the number and type of entries which would have to be changed in one signature to transform it into the other.

The following discussion uses the terminology from [Ger98]. A fault is said to be *undetectable* if its signature is identically zero. Two faults are said to be *indistinguishable* if their signatures are identical. A structure is referred to as *weakly isolating* if all columns in the incidence matrix (i.e. all residual signatures) are different and nonzero. In this case, all faults are detectable and all pairs of single faults are mutually distinguishable. A *bidirectional strong isolating* structure of *degree* k is weakly isolating and no signature can be obtained from another by changing k or less arbitrary elements. A *unidirectional strongly isolating* structure is one that is weakly isolating, and additionally no signature can be obtained from another by changing only '1's into '0's or '0's into '1's. To quantify the robustness, we extend this terminology with the 'degree' designation, such that a *unidirectional strongly isolating structure of degree* k means that no signature can be obtained from another by changing only k '1's into '0's or k '0's into '1's.

The choice of desired structure type depends on the robustness requirements. Clearly, a structure where no signature is identical zero is required for fault detection, while the minimum requirement for fault isolation is a weakly isolating structure of degree 1. More stringent requirements can be imposed to increase robustness. For robustness against $k-1$ erroneous firing of k residuals, a bidirectional strong isolating structure of degree k is necessary. Robustness to the phenomenon of partial firing, explained in more detail below, requires a unidirectional strong isolating structure, with higher degrees providing improved robustness.

As already explained, non-zero residual thresholds have to be used in any practical application. Small values of a fault can therefore result in small residual values that do not exceed their respective thresholds, so that only a subset of the sensitive residuals fires. This phenomenon is known as partial firing, which can also arise during fault transients due to differing transient responses between residuals. The effect of partial firing upon the occurrence of a fault is that a residual pattern is obtained in which some '1's in its residual signature are replaced by '0's.

For robust fault diagnosis it is paramount that a fault is not mistaken for another due to partial firing. To avoid this it must be ensured that changing only '1's to '0's in a residual's signature cannot arrive at the signature of another fault. This is the definition of the necessary unidirectional strongly isolating structure. In cases where only a weakly isolating but not a unidirectionally strong isolating structure is achievable, additional logic must be integrated to reduce the chance of erroneous isolation.

Rather than considering the requirement on global residual structure, fault isolation can also be analysed locally between any pair of faults. Using the terminology from [KN02], a fault f_a is said to *explain* another fault f_b if the occurrence of f_a may lead to a residual pattern that matches the signature of f_b. This relationship is symmetrical only if partial firing is neglected. Otherwise, the behaviour is asymmetric and f_a explains f_b if all the '1' entries in f_b's signature correspond to '1' entries in f_a. For example, consider two faults f_2 and f_3 from the earlier example and only the residuals $\{r_2, r_3, r_4\}$. Its incidence matrix is given by

$$\begin{array}{c} \\ r_2 \\ r_3 \\ r_4 \end{array} \begin{array}{c} \begin{array}{cc} f_2 & f_3 \end{array} \\ \begin{pmatrix} 1 & 1 \\ 0 & 1 \\ 1 & 1 \end{pmatrix} \end{array}.$$

The signature of f_2 can be reached by changing one '1'-entry in the signature of f_3 to '0'. Then,

- f_2 does not explain f_3: when the signature of f_3 appears, this could not be caused by the partial firing of f_2;
- f_3 explains f_2. When the signature of f_2 appears, this may be caused by the partial firing of f_3.

When this asymmetric isolation is taken into account in further analysis below, the method is referred to in this work as *conservative*. When partial firing is ignored, then f_2 and f_3 from the previous example are considered isolable from each other. The method is then termed *non-conservative*. If either of their residual signatures contain indeterminate entries, those residuals are removed from the residual signatures of both faults before conducting the above analysis.

5.2.3 The Fault Matrix

A convenient method to visualise and process the pair-wise fault isolation capability of a set of residuals is to use the *fault matrix* [KN02]. Each column of the square matrix corresponds to a present fault, while each row corresponds to an interpreted fault, so that fault f_k corresponds to the k-th row and column. A '1' in the ij-th entry in the matrix (i-th row, j-th column) indicates that the residual firing pattern due to the presence of f_j may be explained by f_i under the specified robustness assumptions. The fault isolation matrix may be asymmetrical if these assumptions account for partial firing. The diagonal

elements are always filled because every fault can be explained by itself. Maximum fault isolation is achieved when only the diagonal elements are filled, meaning that each fault can be uniquely isolated.

The fault matrix is derived below using the conservative method (with partial firing) for the incidence matrix in Section 5.2.1, which is repeated below on the left hand side. If f_1 is present, its full residual pattern $[1\ 1\ 1\ 0]^T$ can be explained by itself, which is trivial. However, it cannot be explained by f_3, and its partial pattern $[r_2\ r_3\ r_4]^T = [1\ 1\ 0]^T$ cannot be explained by f_2 either. In the latter situation, r_1 is neglected because it is indeterminate for f_2. From these observations, the first column of the fault matrix is $[1\ 0\ 0]^T$. Following the same logic, we arrive at the remaining two columns of the fault matrix. It shows that full isolation is not possible since the presence of f_2 may be interpreted as f_3 due to the partial firing assumption. If the effects of partial firing is neglected, a diagonal fault matrix is obtained.

$$\begin{array}{c} \\ r_1 \\ r_2 \\ r_3 \\ r_4 \end{array} \begin{array}{c} \begin{array}{ccc} f_1 & f_2 & f_3 \end{array} \\ \begin{pmatrix} 1 & \times & 0 \\ 1 & 1 & 1 \\ 1 & 0 & 1 \\ 0 & 1 & 1 \end{pmatrix} \end{array} \qquad \begin{array}{c} \text{interpreted} \\ \text{fault} \end{array} \begin{array}{c} \\ f_1 \\ f_2 \\ f_3 \end{array} \begin{array}{c} \text{present fault} \\ \begin{array}{ccc} f_1 & f_2 & f_3 \end{array} \\ \begin{pmatrix} 1 & 0 & 0 \\ 0 & 1 & 0 \\ 0 & 1 & 1 \end{pmatrix} \end{array}$$

5.2.4 Residual Selection

A residual signature is referred to as feasible if there exists a residual generator that is a solution to the corresponding residual generation problem, satisfying the decoupling and fault sensitivity constraints. In general, the set of feasible residual signatures in an FDI problem exhibits redundancy for fault isolation, in that some residuals could be removed without reducing the fault isolating capability of the whole set. The selection of a non-redundant set of residuals depends on the cost-function that should be optimised. These cost functions indicate the preference for using each residual generator and can be divided into the groups 'cumulative' and 'worst-case'. Cumulative cost functions represent the sum of the cost over all residuals in the set. An example of this is the size of the set, which is considered in the *greedy method* in [SNF11]. In contrast, worst-case cost functions simply consider the worst value over all residuals in the set. An example of this is the worst-case fault-vs-disturbance sensitivity ratio.

A simple selection algorithm to optimise a worst-case criteria is now described by Procedure 5.1. This procedure is similar to the one presented in [KN02].

Procedure 5.1 Residual Selection for Worst-Case Cost Function

Input: feasible residuals $\mathcal{R}$, their signatures $\mathcal{S}$, associated costs $\boldsymbol{c}$

Output: residual subset $\tilde{\mathcal{R}}$, fault matrix $\tilde{\boldsymbol{M}}$, maximum cost $\bar{c}$

```
1: R̃ ← R
2: sort residuals and signatures in descending order of cost c
3: calculate fault matrix of R, assign to M
4: for all i ∈ [1, number of residuals in R] do
5:     R̃_tmp ← R̃ \ r_i
6:     calculate fault matrix of R̃_tmp, assign to M̃
7:     if M̃ = M then
8:         R̃ ← R̃_tmp
9:     end if
10: end for
11: c̄ ← c(R̃(1))                    ▷ store the cost of the first element in R̃
```

The residual generator design procedure presented in Chapter 4 provides the fault-to-disturbance sensitivity ratio $\bar{\eta}$ as a performance measure of the residual generator. A lower $\bar{\eta}$ indicates a preferred residual generator in that sense and can be used as the cost function. The procedure also provides a theoretical upper bound of $\bar{\eta} < 1$ in order to guarantee reliable fault detection, under the assumptions for input and uncertainty bounds. As discussed in Section 5.1 on single residual evaluation, this condition can be relaxed somewhat due to the conservatism of the $\bar{\eta}$ metric (see Chapter 4), the use of a non-ideal truncated norm for residual evaluation, and the fault sensitivity benefits of the $\boldsymbol{u}$-dependent dynamic threshold.

In the application in Chapter 8, the residual generator design procedure is first carried out for every possible fault signature permutation. Those residuals with $\bar{\eta} < \bar{\eta}_{max}$, where the chosen threshold $\bar{\eta}_{max}$ satisfies $\bar{\eta}_{max} > 1$, are then designated as the feasible set. This set is then sorted with respect to the cost function $\bar{\eta}$ before the residual selection algorithm of Procedure 5.1 is applied.

5.2.5 Residual Pattern Evaluation Procedure

Now that a set of residuals has been selected, we shift our attention to the pattern evaluation function in Figure 5.1, which is to be executed online. Given a pattern of fired residuals, the following logic determines the set of faults that could have induced the observed pattern. Let $\boldsymbol{\theta}$ denote the observed residual pattern, and $\boldsymbol{S}$ the incidence matrix. To evaluate whether f_i is a fault candidate, the i-th column of $\boldsymbol{S}$, denoted $\boldsymbol{s}_i$, is considered. The residuals corresponding to indeterminate entries in $\boldsymbol{s}_i$ are first removed from both $\boldsymbol{\theta}$ and $\boldsymbol{s}_i$ to give $\tilde{\boldsymbol{\theta}}$ and $\tilde{\boldsymbol{s}}_i$ respectively. Then the outcome depends on the robustness assumptions:

A) partial firing considered: f_i explains the observation $\tilde{\boldsymbol{\theta}}$ and is therefore a fault candidate, if the observed set of fired residuals is a subset of the '1' entries in $\tilde{\boldsymbol{s}}_i$. That is, $\tilde{\boldsymbol{\theta}} \wedge \tilde{\boldsymbol{s}}_i = \tilde{\boldsymbol{\theta}}$.

B) partial firing neglected: f_i explains the observation $\tilde{\boldsymbol{\theta}}$ only if the residual pattern is an exact match with $\tilde{\boldsymbol{s}}_i$. That is $\tilde{\boldsymbol{\theta}} = \tilde{\boldsymbol{s}}_i$.

The use of the partial firing variant actually permits residuals with any $\bar{\eta}$ value to be added to the selected residual set $\tilde{\mathcal{R}}$, as long as their evaluation threshold is set robustly to prevent false alarms. A fault with a larger magnitude will cause the firing of more residuals, thus improving the isolation by ruling out more faults, while smaller faults may only set off a smaller subset and thus deliver a hypothesis with more fault candidates.

In the case that some robustness against erroneous firing (i.e. false alarms) is desired, the above evaluation logic can be extended according to the principle behind *bidirectionally strong isolating* structures of higher degrees. A fault remains in the candidate set as long as only k of the fired residuals correspond to '0's in its residual signature, with higher k improving robustness against false alarms but also potentially increasing the size of the candidate set. This extension is not used in the application in Chapter 8 and is therefore not described further. The pattern evaluation procedure is summarised in Procedure 5.2.

Procedure 5.2 Residual Pattern Evaluation

Input: incidence matrix $\boldsymbol{S}$, observed residual pattern $\boldsymbol{\theta}$

Output: fault candidate set $\mathcal{C}$

1: $\mathcal{C} = \emptyset$
2: **for** $i = 1 \ldots$ number of faults **do**
3: find index vector $\boldsymbol{a}$ of indeterminate ($\times$) entries in $\boldsymbol{s}_i$
4: remove elements in positions $\boldsymbol{a}$ from $\boldsymbol{s}_i$ to give $\tilde{\boldsymbol{s}}_i$
5: remove elements in positions $\boldsymbol{a}$ from $\boldsymbol{\theta}$ to give $\tilde{\boldsymbol{\theta}}$
6: **if** consider partial firing **then**
7: **if** $\tilde{\boldsymbol{\theta}} \wedge \tilde{\boldsymbol{s}}_i = \tilde{\boldsymbol{\theta}}$ **then** $i \rightarrow \mathcal{C}$
8: **end if**
9: **else**
10: **if** $\tilde{\boldsymbol{s}}_i = \tilde{\boldsymbol{\theta}}$ **then** $i \rightarrow \mathcal{C}$
11: **end if**
12: **end if**
13: **end for**

Part II

Model-Based Diagnosis of Vehicle Dynamics Control Systems

Chapter 6

Fault Diagnosis on the ROboMObil Test Platform

This chapter introduces the ROboMObil, the application subject of this thesis on which the model-based FDI methods introduced in Part I are applied, and investigates the role of vehicle dynamics based diagnosis in its fault management framework. The German Aerospace Center's (DLR's) ROboMObil is a test platform of automotive technologies, which has a novel X-by-Wire architecture with electric propulsion and is equipped with a wide array of sensing and actuation. Through its in-wheel motors and individual wheel steering capable of large angles, as well as sensors measuring the complete body velocity and acceleration vectors, new opportunities are opened for enhancing manoeuvrability, control and estimation. However, detecting and distinguishing between the influences of the increased number of potential faults represents a significant challenge which must be met to ensure fault tolerance and safety in such an architecture.

Although the robotics inspired, centralised and hierarchical architecture for control, sensing and actuation (see Figure 6.3) of this X-by-Wire research platform represents a departure from the road vehicles in series production today, it coincides with concepts that are being pursued in the automotive industry where intelligent control and assistance functions are being increasingly integrated. The architecture permits higher level fault diagnosis functions to access information from all relevant systems, thus providing a powerful platform for enhanced fault diagnosis through advanced algorithms observing the vehicle holistically.

The rest of the chapter begins by describing the ROboMObil including its system and controller architectures in Section 6.1, focussing on the vehicle dynamics systems. The system is then broken down into its constituent subsystems. Each of these is analysed from a functional perspective, and the potential faults and common diagnostic solutions for the system classes are presented in Section 6.2. Following this, the fault diagnosis software module on the ROboMObil and its hierarchical modular concept are introduced in Section 6.3. Lastly, Section 6.4 describes the requirements and design of the sub-module

Figure 6.1: The DLR's ROboMObil

for vehicle dynamics fault diagnosis, and presents the specifications for the model-based fault diagnosis functions that are the subjects of Chapters 8 and 9.

6.1 Description of the ROboMObil

6.1.1 Vehicle Concept

The ROboMObil was conceived as a test platform for vehicle dynamics control, electric propulsion, vision-based autonomous driving functions, and driver interaction concepts [Bre11]. The modular construction concept integrates the vehicle dynamics and propulsion components into the lower modules of the vehicle, whereas the useable space and interaction elements for the driver and passenger are contained in an upper cabin module (see Figure 6.2). Propulsion is realised by means of four permanent magnet synchronous machines (PMSM) serving as wheel-hub electric motors, powered by a 350V Lithium-Ion battery. The driver commands the vehicle's motion using a force feedback sidestick, the inputs from which are subsequently combined with perception data and decisions from the autonomy modules to form motion demands that are passed to the vehicle. These functionalities form the vehicle-level application (VLA) layer in the control architecture shown in Figure 6.3.

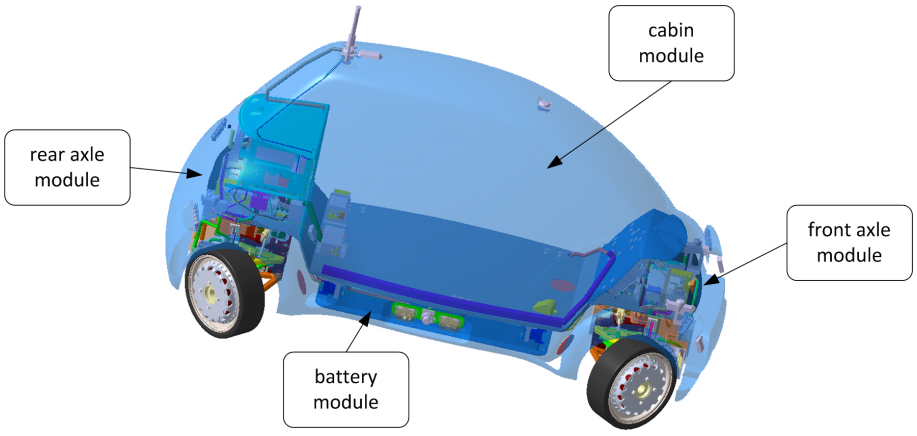

Figure 6.2: CAD image of the ROboMObil revealing its main modules of front and rear axles, main battery and cabin

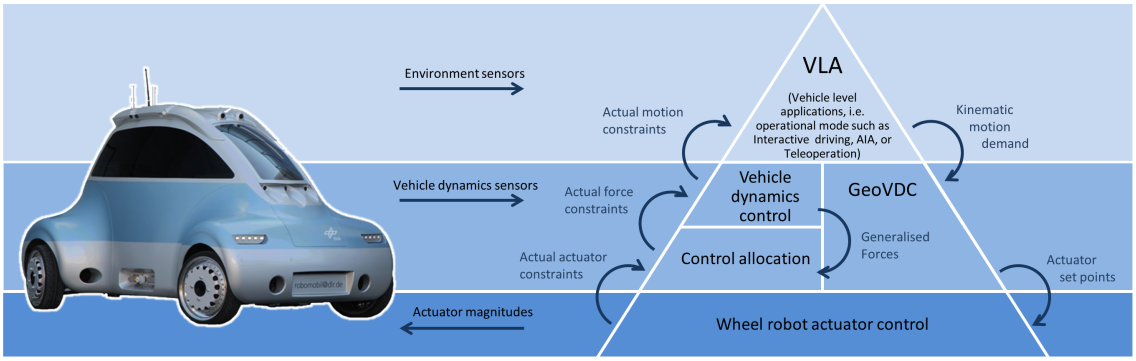

Figure 6.3: Scalable vehicle dynamics control architecture (reproduced from [Bün14])

Since the FDI functions proposed in this thesis are concerned with the vehicle dynamics subsystems, the hardware components together with the associated controllers will be described in more depth. The vehicle dynamics actuators are packaged into four so-called *Wheel-Robot* modules, each containing the aforementioned wheel hub propulsion motor, independent high angle range steering, electro-hydraulic disc brake and suspension with semi-active dampers. The hydraulic systems of the two disc brakes on each axle are interlinked, such that one electromechanical actuator controls the pressure in both brakes. The steering system on each wheel module contains a wheel-carrier mounted motor-gearbox unit, whose output pinion gear drives a large spur gear rotationally fixed to the control arm. The actuators in the Wheel-Robot module can be seen in Figure 6.4, while key characteristics of the wheel robot modules are listed in Table 6.1.

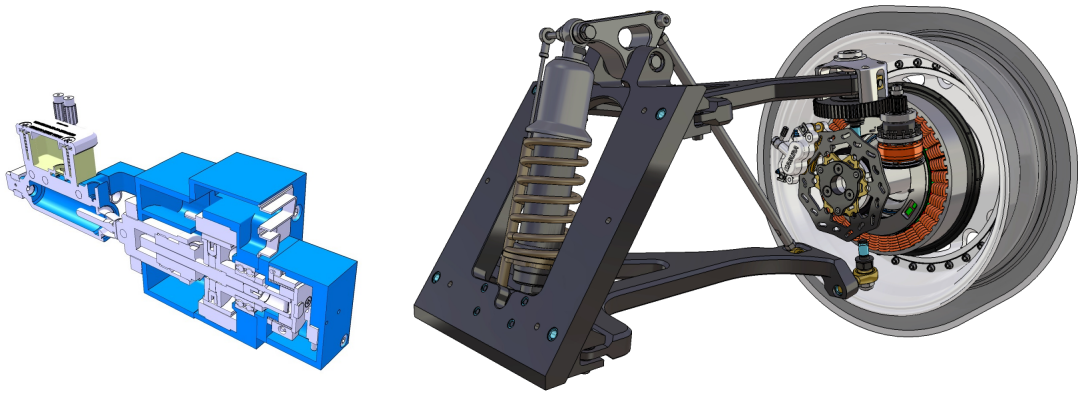

Figure 6.4: Left: The electromechanical brake pressure actuator. The motor-spindle actuator on the right part drives the shaft of the brake master cylinder in the left part. Right: The "Wheel Robot" with integrated vehicle dynamics actuators

The independently controllable wheel torques and steering angles provide additional degrees of actuation freedom which offer new opportunities for vehicle motion control. The large steering angle ranges permit unique manoeuvring capabilities of sidewards motion and rotation about axes within and close to the vehicle bounds, offering advantages for parking and driving in tight spaces. Similar steering concepts are used by some concept and research vehicles, including ZF Advanced Urban Vehicle [ZF16], Project OmniSteer [KIT16], and SpeedE by IKA [RWT16]. The NASA MLV [RS14] employs a similar integrated wheel actuation design.

Table 6.1: Key data related to the wheel robot modules

Property	**Value**
outermost steering angle (FL,FR,RL,RR)	$-95°, 95°, 95°, -95°$
innermost steering angle (FL,FR,RL,RR)	$34°, -34°, -25°, 25°$
wheel hub motor peak torque	160 Nm
wheel hub motor top speed	1000 rpm
wheel hub motor peak power	16 kW
maximum brake pressure	120 bar
equivalent maximum braking moment per wheel	445 Nm

Besides its flexible actuation, the ROboMObil is also extensively equipped with sensors to measure chassis and vehicle states. The wheel robots are intelligent actuators under closed-loop control, and their sensor measurements are transmitted to the central control units. Furthermore, motion sensors are installed on the vehicle body for control and data acquisition in the area of horizontal and vertical dynamics. Only those relevant to horizontal dynamics will be described here, as vertical dynamics is beyond the scope of this work. The body-mounted sensors comprise:

- OxTS RT4003 inertial navigation system (INS) [Oxf15] - 3-axis acceleration and rotational velocity measurements, velocity and position estimations using GPS-assisted bootstrap estimators.
- Correvit S-HR optical sensor (OS) [Kis16] - 2-axis horizontal velocity measurement.

The sensors are mounted at the locations shown in Figure 6.5. The OxTS INS is mounted as close to the vehicle centre of mass as practically possible, while mounting the Correvit sensor behind the rear axle permits it to be located closer to the vehicle longitudinal centre plane. Although the configuration and quality of these motion sensors are very much on the high level of those for data acquisition on development vehicles, one can still draw parallels with the set up from production vehicle concepts in the near future. The raw acceleration and rotation rate sensor outputs of the OxTS INS are already in the sensor clusters for horizontal and vertical dynamics control systems of today's cars. Meanwhile, the velocity measurements from the Correvit sensor can potentially be obtained by processing data from low-cost stereo cameras used in driver assistance functions [SB17].

The electronic hardware architecture follows the hierarchical control concept depicted in Figure 6.3. Lower-level control of the wheel robot modules are executed on local control units which communicate with the central controller via Control Area Network (CAN) bus. Besides the control functionalities, each local control unit also hosts basic diagnostic functions for mechatronic actuators, such as sensor limit checks and monitoring of temperatures and motor currents. The central controller is primarily responsible for vehicle dynamics control and energy management functionalities, which corresponds to the middle layer in the hierarchy in Figure 6.3. It also hosts some functions from the VLA layer such as driver input processing, and the fault management module including fault diagnosis functions reside here as well. Vehicle level applications running on separate processing

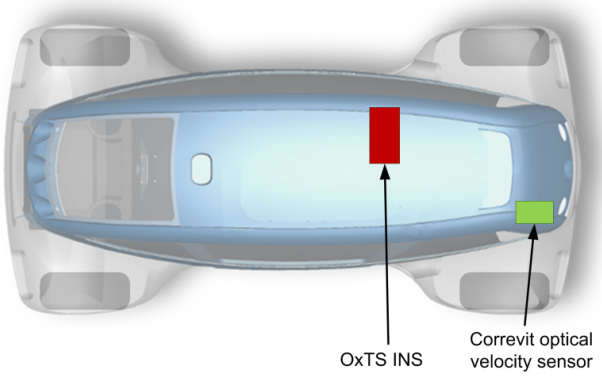

Figure 6.5: Mounting locations of the horizontal body motion sensors

units, such as vision-based control, path planning, and navigation, can exchange motion commands and feedback data with the central controller via data network connections such as an Ethernet link. This is illustrated in Figure 6.6.

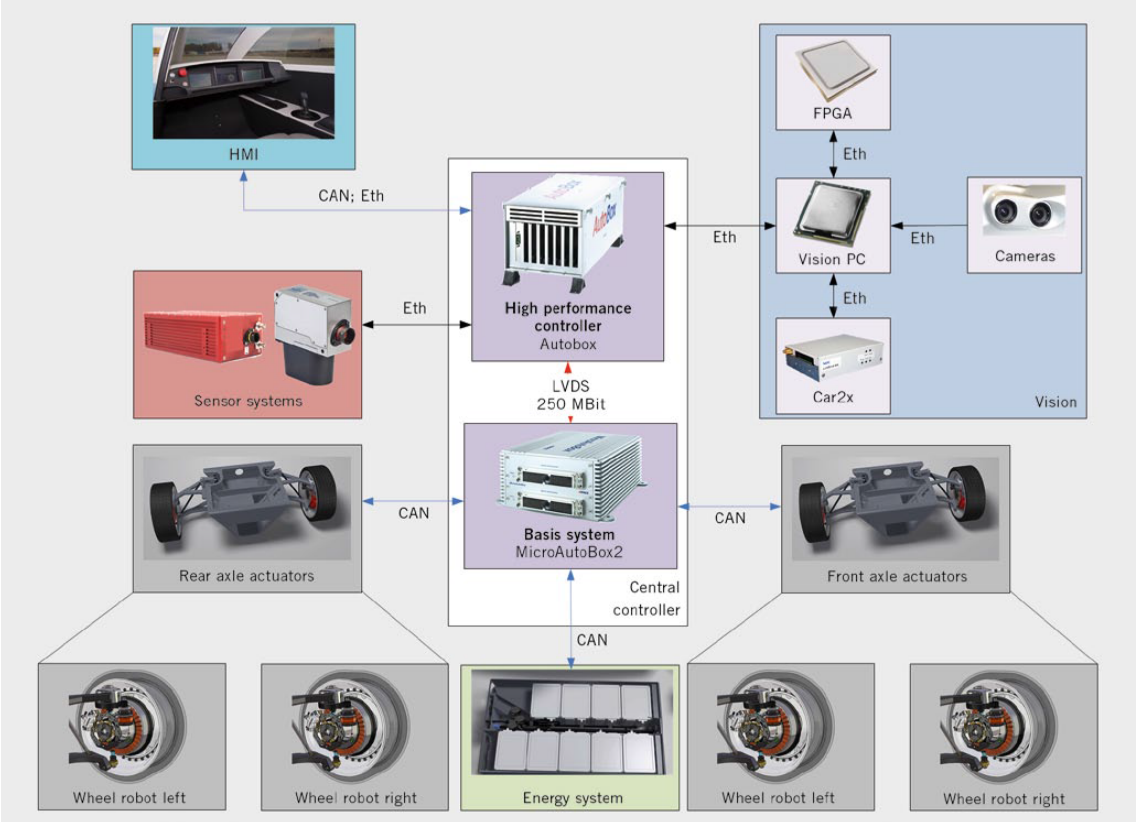

Figure 6.6: ROboMObil control unit architecture and communication network (source: [Bün14])

Functional Safety Concept

As a prototype aimed mainly at the development and evaluation of advanced vehicle functions in closed test arenas, the fault tolerance architecture is kept to the minimum

required to safely stop in the test area in case of a serious issue. This "emergency braking" action must be executed using redundant actuators and without the need for any body motion sensor feedback in order to guarantee its effectiveness in most conceivable, realistic cases of actuator and sensor failures. The selected concept takes inspiration from Brake-by-Wire solutions (see [ISS02] for an example) and is designed with simplicity rather than optimal availability in mind. It makes use of the redundancy inherent in the overactuated architecture, thus minimising the need for direct redundancies in the form of repeated components. The system consists of:

- redundant low voltage (LV) power supply - an LV battery and a DC/DC converter in each axle to supply the electrical and electronic systems
- redundant friction brake systems - one electromechanical pressure actuator in each axle
- automatic "safe" reactions when central-to-wheel controller communication is lost -
  - wheel unit reaction upon sensing a faulty / unavailable central controller: automatically apply friction brakes, deactivate traction motors and lock steering
  - central controller reaction upon sensing a faulty / unavailable wheel unit: command the above reaction from the remaining connected wheel units
  - operator controlled manual triggers for the above safety action

Control-oriented fault-tolerance solutions are described at the end of the next section.

6.1.2 Overview of Vehicle Dynamics Controller

In this section, a brief overview is presented of the implemented vehicle dynamics control functions for the horizontal degrees of freedom (DOFs). Although the vehicle dynamics control functions are not part of the plant to which the FDI is applied, they are relevant for understanding the fault management module, as they decisively influence the states that the vehicle "plant" can reach. Horizontal motion control of the vehicle body is divided into longitudinal and lateral DOFs. The longitudinal DOF corresponds to the speed v in the path direction, while the other two DOFs (yaw rate $\dot{\psi}$ and body side-slip angle β) are considered the lateral DOFs. These variables are depicted in Figure 6.7. On the ROboMObil, longitudinal dynamics can be controlled either in an open-loop mode, or by using velocity or acceleration feedback. For lateral dynamics, two control modes have been implemented, namely open-loop kinematic control and feedback control. These are underpinned by different assumptions and are designed to exploit the flexible actuation of the ROboMObil in different ways. The controllers are presented in [Bün14] and [CBB15] and a summary is provided below. Note that the actuation inputs available to the controllers are the in-wheel motor torques, steering angles, and disc brake pressures.

The first control mode is kinematic control, a feedforward control law which maps the motion demand to wheel robot actuator demands through a static (i.e. memoryless) model of the horizontal kinematics. Kinematic control covers all three motion modes of

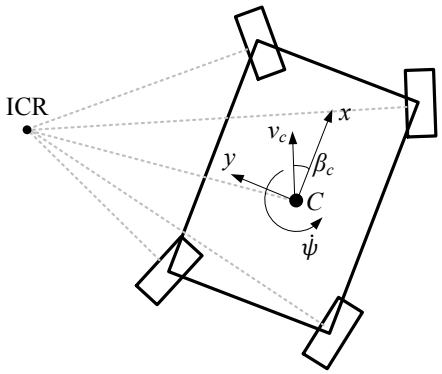

Figure 6.7: Horizontal degrees of freedom of a vehicle body

which the ROboMObil is capable, which are classified by the location of the instantaneous centre of rotation (ICR) in the three non-contiguous feasible regions (see Figure 6.8):

- **(0) longitudinal motion** - includes straight, curved and diagonal driving in which the longitudinal velocity is dominant. The motion possibilities of conventional road cars lie completely within this region.
- **(1) rotational motion** - the yaw velocity is dominant. An off-centre ICR as shown in the lower image of Figure 6.8 will contain small longitudinal and lateral velocity components.
- **(2) lateral motion** - sideways driving where the lateral velocity is dominant

The non-contiguity of the regions can be explained by the asymmetric and limited angle ranges on each wheel, resulting in the need for the vehicle to be stationary when changing between motion modes. Kinematic control is built on the assumption of negligible wheel slips and therefore low accelerations, but analyses and tests have shown that it may still be used at higher accelerations, albeit with larger control errors.

The second control mode is that of feedback control. As described in [CBB15], lateral dynamics feedback control has only been developed for longitudinal motion mode, the one which most closely resembles conventional vehicle motion. The reason for this is that the lateral and rotational modes are manoeuvring and parking modes, which are intended to run exclusively at low speeds. Feedback control is most beneficial when kinematic feed-forward control is no longer sufficient due to increased tyre slips when body accelerations and tyre forces are high. These conditions are typically encountered at medium to high speeds which have to be handled by the longitudinal motion mode.

Due to the overactuation of the ROboMObil including rear wheel steering, set points for the two lateral degrees of freedom, β and $\dot{\psi}$, can be independently generated and tracked. In [CBB15] this is achieved through approximately decoupled SISO control of these motion states, using the disturbance observer (DOB) controller structure (shown schematically in Figure 6.9). A further noteworthy aspect of the lateral dynamics control is the handling of the overactuation, referring to the existence of more actuation inputs than the two motion degrees of freedom β and $\dot{\psi}$. Indeed the lateral dynamics are influenced by the four steering angles as well as torque vectoring, which denotes the use of in-wheel

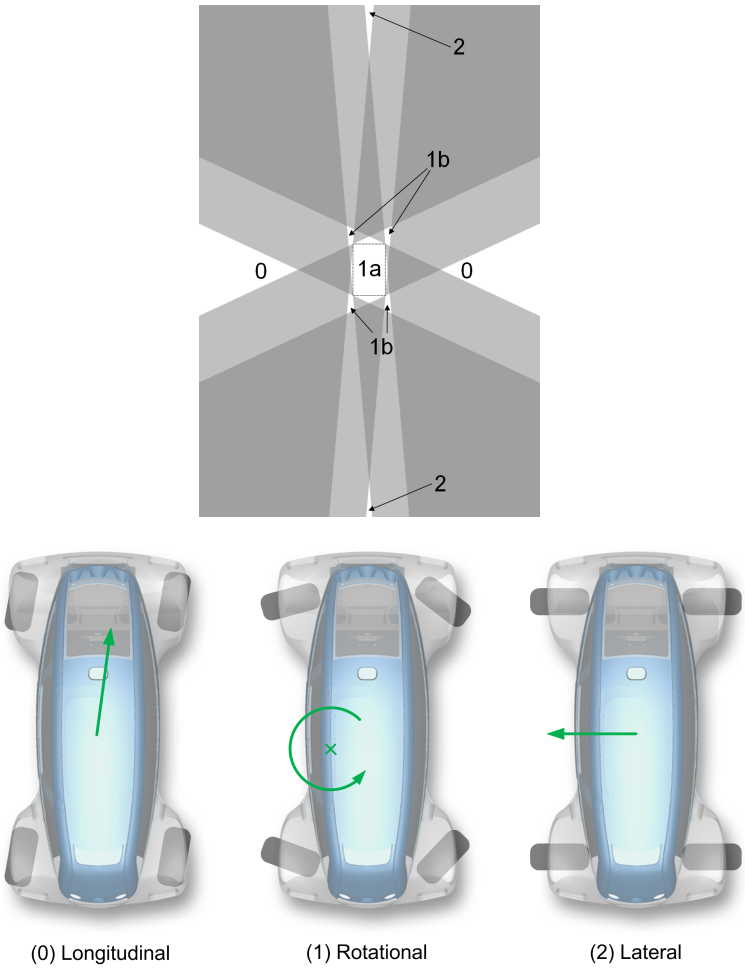

Figure 6.8: Instantaneous centre of rotations (without wheel slip) for the three motion modes. (top diagram sourced from [Bün14]) For the rotational mode, 1a/1b can be interpreted as ICR locations within/outside the vehicle envelope.

motor torques to produce a yaw moment. In the feedback control of the ROboMObil, this control allocation problem is handled by rules constraining the distribution of the actuation efforts between the variables [CBB15]. Alternative solution methods range from simple daisy-chain methods to dynamic allocation [Tjø08] and more computationally intensive online-optimisation-based approaches [Rit13].

Control-oriented fault-tolerance solutions are implemented to avoid uncontrolled behaviour in case of sensor failures. Particularly critical are failures of sensors that provide feedback for motion control. In case of reported faults or unavailability, a sensor fusion block is reconfigured to employ other sources to compute the signals necessary for control and operation. This is referred to as the virtual sensor approach in fault tolerant control literature [Bla06]. For example, lateral motion information can be sourced from the OxTS sensor, the Correvit sensor or estimation from wheel speeds and steering angles. When no reliable source is available, the next degradation stage is triggered, where the vehicle dynamics control switches to a backup open-loop control law. The described measures are shown schematically for lateral dynamics control in Figure 6.9. Fault tolerance through the

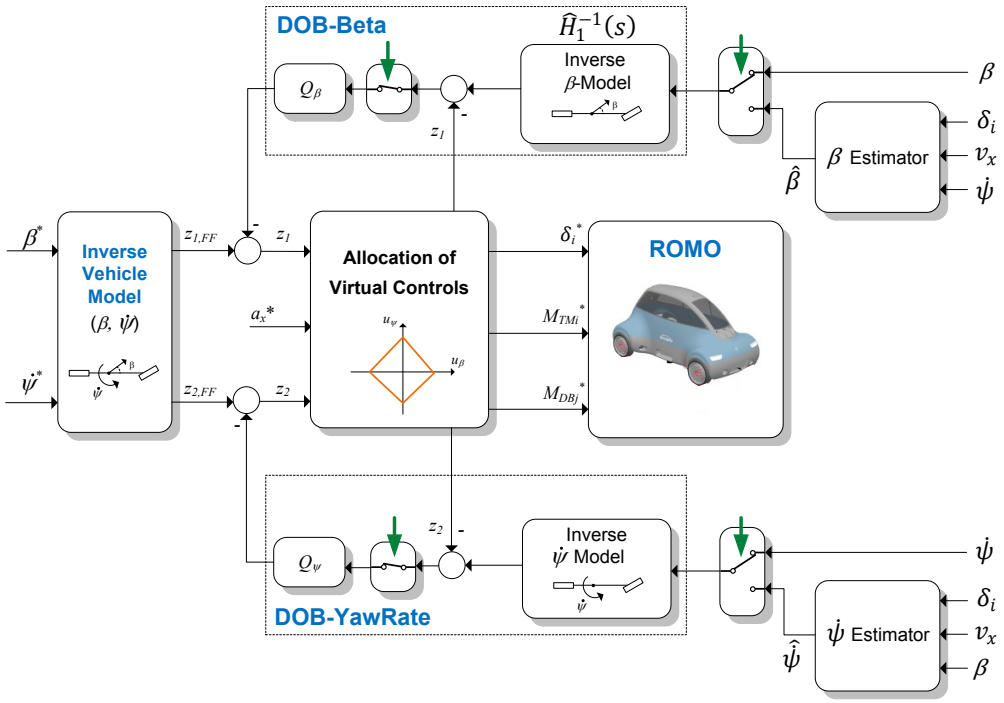

Figure 6.9: Schematic of the DOB-based fault-tolerant lateral dynamics feedback controller for longitudinal motion mode, adapted from [CBB15]. The green vertical arrows indicate the reconfiguration possibilities for fault tolerance.

multi-staged application of virtual sensors and then degraded control without the failed sensors has parallels in flight control FTC concepts, see e.g. [VOJ14].

6.2 System Analysis

In this section we analyse the vehicle dynamics system with the goal of establishing a concept for the fault diagnosis system. It would be desirable to split the global system level diagnosis task into smaller, more manageable independent tasks, whose outputs are aggregated into a final diagnosis. The pre-requisite for an effective division is that the diagnosed subsystems are either decoupled or only weakly coupled. This can be tackled in two ways, either using structural analysis or decomposition based on system hierarchy.

Structural analysis techniques involve analysing the model structure, represented by a bipartite graph with variables and equations as node sets, to find overconstrained systems [Bla06; KAN08]. Each of these overconstrained subsystems can subsequently be tested for inconsistencies to detect the presence of a fault. This is effective for larger systems that do not have a “natural” hierarchy or distributed structure, which is often found in process control applications [KN02] or automotive powertrains [SN10]. The structural analysis approach was applied to the vehicle dynamics system in [Ho13], but the standard methods are unable to take advantage of the weak couplings between subsystems to discover some potential decompositions. While the structural analysis approach offered helpful insights into this application, due to the manageable number of variables in the vehicle dynamics

system, decomposition according to the system's hierarchical design proved to be more effective and is used in this work.

6.2.1 Functional Description

The structure of the RObMObil's centrally controlled X-by-Wire vehicle dynamics system is shown in Figure 6.10. The states of the *wheel robot actuators* act on the *vehicle dynamics*, whose states are then measured by the *sensors* and made available for the control functions. The upper level denoted *actuator demand generation*, consisting of trajectory control and central vehicle dynamics motion controller, are outside the plant system containing the faults of interest. They are therefore not considered in this study. The following analysis treats the *Wheel Robot* actuator systems, the vehicle dynamics components, and the sensors.

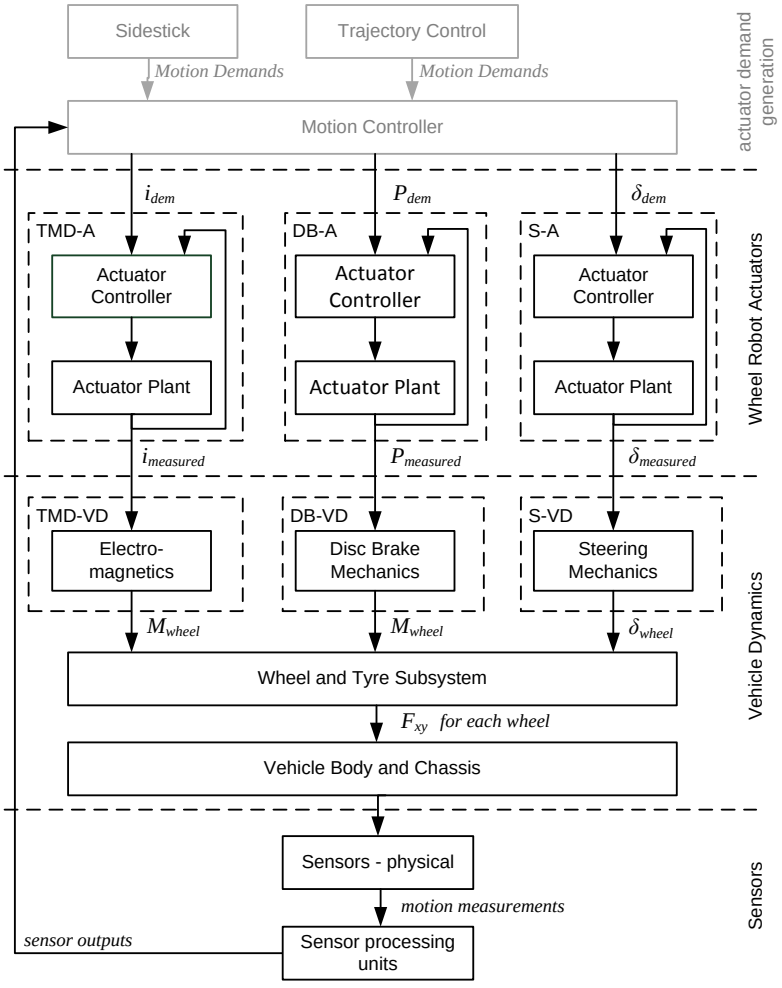

Figure 6.10: Structure of the RObMObil vehicle dynamics system

The task of each actuator subsystem is to regulate its respective controlled output to the demanded value. On the other hand, for vehicle dynamics control, the outputs of interest are actually those with direct influence on vehicle dynamics. From this perspective, ideally the traction motor drive system should generate the commanded torque at the

respective wheel, the steering subsystem should rotationally position the wheel in vehicle coordinates to track the steering angle demand, while the disc brake subsystem should produce a decelerating wheel torque.

However, these outputs are not directly measured, and instead the actuators control a related set of outputs. This insight divides each actuator subsystem into two components - the first being the closed-loop controlled actuator itself, and the second being the output translation component. This latter represents the physical relationship that translates the controlled output to the actual output of interest. This division of functions is summarised for the ROboMObil's three actuator types in Table 6.2.

Table 6.2: Controlled variables and related vehicle dynamics variables of the ROboMObil actuator types

Actuator Type	**Abbrev.**	**Controlled Variable**	**Vehicle Dynamics Variable**
Traction Motor Drive	TMD	motor current (i_m)	wheel drive torque ($M_{w,TM}$)
Disc Brakes	DB	brake pressure (P_b)	wheel brake torque ($M_{w,DB}$)
Steering	S	actuator angle (δ_A)	wheel steering angle (δ_U)

The functions and behaviours of the actuator as well as output translation components of each of the three actuator subsystems are described below. The actuator component is denoted with suffix 'A', while the output translation component is treated as part of the vehicle dynamics and denoted with the suffix 'VD' to represent its grouping with the vehicle dynamics subsystem later. The functions of the wheels, tyres, chassis and sensors are then briefly examined. Mathematical models of the subsystems' behaviours will be derived in Chapter 7.

Traction Motor Drives

The ROboMObil's in-wheel traction motor drives are wheel hub mounted direct drive Permanent Magnet Synchronous Motors (PMSMs) under field-oriented control. The actuator (TMD-A) has the following functions:

- closed-loop control of the motor current
- provide measurements of motor current and wheel speed

In the output translation component (TMD-VD), the wheel drive torque is related to motor current by the electromechanical properties of the motor. The gear ratio also comes into play, but the ROboMObil's wheel hub motors are direct-drive units and the ratio simplifies to unity.

Steering

The steering subsystem is mounted on the wheel carrier and directly actuates its rotation about the steering axis, which passes through the top and bottom control arm ball joints. This axis is marked 'A-A' in Figure 6.11. A resolver measures this angle output.

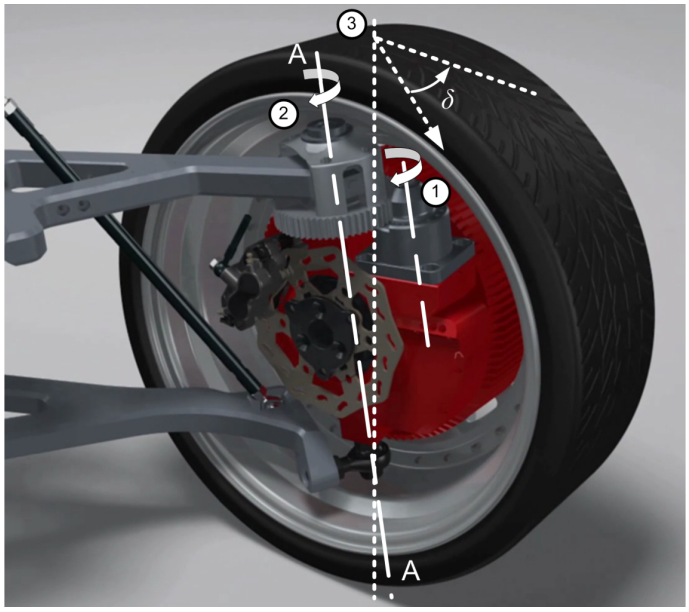

Figure 6.11: ROboMObil steering actuator. (1)-actuator output shaft axis, (2)-steering axis, (3)-wheel steering angle axis. δ is the steering angle in the vehicle coordinate system.

The actuator (S-A) has the following functions:

- closed-loop control of the actuator output shaft angle, including inner control loops of motor velocity and motor current
- provide measurement of the actuator output shaft angle

In the output translation component (S-VD), the steering actuator axis and the wheel vertical axes are not aligned, but are rather displaced and rotated relative to each other (see Figure 6.11). The output shaft angle and the wheel steering angle are therefore related by a kinematic transformation. Other types of actuated steering mechanisms may have different relationships between actuator and wheel angles that are possibly dependent on the steering angle and suspension position.

Disc Brakes

The electrohydraulic disc brake system consists of a motor actuating a ball screw, which is in turn connected to a hydraulic master cylinder. Through hydraulic pipes, the master cylinder is connected to the slave cylinders on the brake callipers, which apply force on the brake pads against the brake discs. The wheel braking torque is generated from the resulting pad-disc friction pairing. A schematic of the disc brake subsystem is shown in Figure 6.12.

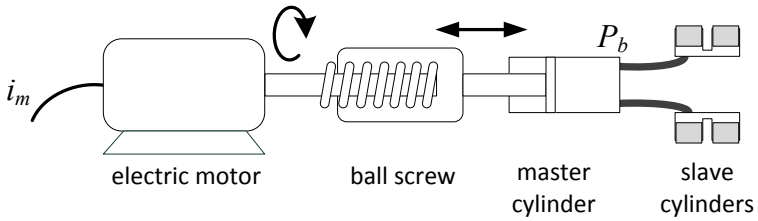

Figure 6.12: RObоMObil electrohydraulic disc brake actuator (brake pad and disc not shown)

The actuator (DB-A) has the following functions:

- closed-loop control of the hydraulic brake pressure, including inner control loops of motor velocity and motor current
- provide measurement of brake pressure

In the output translation component (DB-VD), the controlled hydraulic pressure measured at the master cylinder is a close estimate of the slave cylinder pressure, with equality at steady state. Slave cylinder pressure is transformed into wheel brake torque via the disc brake mechanism. Influencing factors on this transformation are piston number and areas, friction properties between pad and disc, and the effective brake disc radius.

Wheel, Tyre, Chassis and Sensors

The wheel and tyre, together with the vehicle body and chassis, translate the wheel variables of steering angle and total wheel torques into vehicle motion. Chapter 7 describes their behaviour in more detail and provides mathematical models with several levels of detail. The sensors relevant to vehicle dynamics measure motion of the vehicle body and other components. The body sensors measure body accelerations and its translational and rotational velocities. Vertical dynamics sensors measure suspension motion, but they are not considered in this study.

6.2.2 Fault Analysis

Faults can occur in actuators, sensors or within the plant itself. Since most of the changes from a conventional vehicle to an X-by-Wire one with an electrified powertrain are in the areas of actuation and sensing, these new challenges form the focus of this discussion. Here, each system described in the previous section is studied to determine relevant faults that may occur. Faults of the actuator subsystems are examined both within the closed-loop (i.e. the '-A' components), which can often be detected at the local actuator level, and those outside the loop (i.e. the '-VD' components). Vehicle sensor faults are then considered, before controller and communication faults are briefly addressed. Faults which cannot be reliably diagnosed on the local subsystem level are summarised at the end of

each sub-section, and these have to be handled at a higher level of the fault diagnosis hierarchy.

The following analysis is conducted with the help of guidelines from the failure modes and effects analysis (FMEA) method. In particular, the causes of faults and failures, as well as their detectability, are examined. They constitute elements for the construction of an FMEA, which itself is out of the scope of this work.

Traction Motor Drive Subsystem

This discussion is restricted to wheel hub motors since these are installed on the ROboMObil. It is claimed in [Nus13; WDT14] that the following effects may arise due to faults in the wheel hub motor actuator (TMD-A):

fault symptom	**possible causes**
negative electrical torque	single or multi phase short circuits, inverter shutdown in the field weakening region (for PMSM), transistor failure, and current sensor fault (misalignment)
uncontrolled electrical torque	failure in motor control, circuit failure
excessive torque ripples	open-phase fault, turn-to-turn short circuit or rotor related faults
reduced torque effectiveness	deviation of motor torque constant from calibrated value due to, e.g. overheating

Out of these, all but reduced torque effectiveness and some cases of current sensor misalignment are detectable locally by monitoring signal behaviour, the field oriented control (FOC) and the motor current control loop. Both signal-based [KM99; Ala15] and model-based [Liu06] approaches can be found in literature for this purpose.

Mechanical faults can also affect the behaviour of the drive actuator system:

fault symptom	**possible causes**
excessive mechanical torque loss	high friction, or oscillating torque due to bearing damage
jamming	bearing failure, gearbox jamming (in non-direct drive systems) - manifested as maximum negative torque defined by sliding friction of the tyre-road interface

Jamming of a traction motor drive is an extreme fault case that can be locally detected under most operating conditions. In contrast, excessive mechanical loss torque is difficult to detect locally, as the total wheel load torque is required for a consistency check but is unknown at the actuator level due to the dependency on global vehicle dynamics.

In summary, the TMD-A faults which cannot be locally detected, and therefore must be processed at the vehicle dynamics level are:

- reduced torque effectiveness
- current sensor fault (misalignment)
- excessive mechanical loss torque

Steering Subsystem

Faults in electromechanical actuators (EMAs) are well-documented and the detection of such faults has also been extensively studied in the past [MBI09; SK05; TB06; LDD16]. In addition, a failure modes and effects analysis (FMEA) has been performed specifically on the ROboMObil's steering mechanism in [Bau11]. From these sources, the following examples can be given for faults within the closed-loop position controlled actuator (S-A):

fault symptom	**possible causes**
motor electrical faults	see first table for TMD subsystem
jamming	bearing failure, gearbox jamming
backlash or disconnection between motor and output shaft	broken transmission shaft, broken or worn gear teeth
output shaft angle error	sensor fault

All of these faults, except for the constant offset case of the output shaft angle sensor fault, are detectable within the local subsystem either at the electrical motor control level or by observing the mechanical behaviour within the control loop. Faults may also occur beyond the closed-loop, in the steering mechanics which is denoted as the subsystem S-VD. These faults include:

fault symptom	**possible causes**
incorrect offset in the translation from actuator angle to steering angle	mounting, sensor calibration offset, or fault in the output shaft sensor, deformed linkage from actuator output to wheel carrier (on steering systems without direct mounting, e.g. those with a steering arm)
excessive backlash and elasticity	damaged actuator mounting and linkages

These faults in the steering mechanics and output shaft angle sensor offset cannot be reliably detected locally because their effects lie outside of the closed-loop. Thus they should be detected at the vehicle dynamics level diagnostics. To summarise, they are:

- incorrect offset in the translation from actuator angle to steering angle

- excessive backlash and elasticity

Disc Brake Subsystem

The electromechanical pressure actuators are affected by faults analogous to the EMA faults described in the steering section. According to the system analysis of the disc brake subsystem, the other components can be classified into pressure transmission to the slave cylinder, and wheel torque generation via the slave cylinders, brake pads and disc. According to [Len14], faults in the EMA and pressure transmission system include:

fault symptom	**possible causes**
motor electrical faults	see first table for TMD subsystem
jamming	bearing failure, gearbox jamming
backlash or disconnection between motor and output shaft	broken transmission shaft, broken or worn gear teeth, spindle wear
pressure sensor fault	sensor fault
failure to build pressure	hydraulic leakage
excessive motor motion to build pressure	pipe damage, excessive brake pad or disc wear, damaged calliper, boiling of brake fluid due to excessive temperature

Except for pressure sensor gain and offset faults of small-to-moderate magnitudes, the other faults can be monitored by a combination of signal- and model-based methods using measurements available within the pressure actuator, and thus do not need to be detected on the vehicle dynamics level. For example, [HH14] proposes an actuator-level, model-based FDI approach for motor current and speed sensor fault detection in a similarly configured electromechanical brake actuator.

Faults in the brake friction properties affect the relationship between the generated pressure and the brake torque acting on the wheel. This category includes [Puh87]:

fault symptom	**possible causes**
loss of effectiveness in friction force generation	wear, operation outside the permitted temperature range, incorrect installation
undesired brake torque	incorrect pad alignment, foreign bodies, or stuck slave cylinder

Since the brake friction abnormalities are outside the pressure control loop, they cannot be detected at the local actuator level. In summary, the faults that should be detected at the vehicle dynamics level diagnostics are:

1. pressure sensor gain and offset faults (up to moderate magnitudes)

2. loss of effectiveness in friction force generation
3. undesired brake torque

Vehicle Body and Chassis Sensors

The OxTS INS and Correvit optical sensors are intelligent sensor units that pre-process and verify the sensor measurements before outputting them via a data bus connection (e.g. CAN or Ethernet). This extent of self-diagnosis is usually not possible on a series production vehicle, and rather the raw measurements with minimal processing would be outputs of the sensor units. Without the GPS-assisted estimates and only the raw sensor measurements, it would be more accurate to refer to the OxTS as an *Inertial Measurement Unit (IMU)*. The rest of this analysis will consider this situation.

The failure modes of a sensor depend on its measuring principle. A review of fault modes and their physical causes for a selection of sensors is available in [Bal09]. The effects on the output signals can be summarised into scaling, bias, drift and hard faults [Mar12].

In the cases where multiple sensors are integrated within a sensor unit, faults to the processing unit such as power loss or processor failure would result in a common cause failure mode where all sensors signals handled by this unit are rendered faulty. However, this type of fault is adequately monitored by observing the communication with the sensor unit as well as the status signals, and can therefore be excluded from this work. As a result, only faults in the sensors themselves have to be detected in the vehicle dynamics level diagnostics.

Controllers and Communication of Intelligent Subsystems

Faulty behaviour in the communication channels hampers the transfer of actuator demands and sensor measurements between intelligent subsystems. There is a rich literature devoted to design, analysis and monitoring of communication in safety-critical systems, e.g. [Lea05; Wil05; Rei06]. It will be assumed that the protocols are designed such that each control unit is aware of any degradation or loss in communication with a connected device, or its complete outage. Therefore, there is no need to detect this class of faults at the vehicle diagnostics level.

6.3 Fault Diagnosis on the ROboMObil

Within the ROboMObil's control software, the Fault Management module handles the tasks of fault diagnosis, mitigation measures, fault data logging, and communication of diagnostic information (see Figure 6.13). This section concerns the fault diagnosis component, which contains the vehicle dynamics level fault diagnosis functions developed in

the next chapters. We touch on software related aspects and demonstrate why a hierarchical structure suits this application and how this can be implemented. The design of the sub-module for vehicle dynamics diagnosis is covered in depth in Section 6.4.

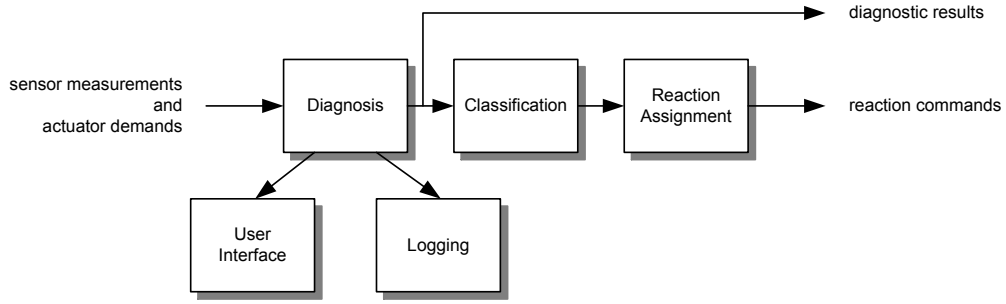

Figure 6.13: Functions of the Fault Management Module on the RObоMObil

6.3.1 Hierarchical Diagnosis Architecture

The design of the fault diagnosis module is inspired by the concept of the Generalised Diagnostic Component (GDC) [YJ04], a diagnostic structure for X-by-Wire systems with hierarchical and distributed controller architectures. Each GDC, illustrated schematically in Figure 6.14, has the same structure and interface regardless of its level in the hierarchy. Besides the control system it consists of three parts for diagnostics:

- Sub-GDCs: Lower level diagnostic blocks
- residual generator: diagnoses faults on the current level using available measurements and actuator demands
- diagnostic manager: draws conclusions based on diagnostic results from the Sub-GDCs and residual generators, controls execution and operation of the Sub-GDCs and residual generators

The bi-directional communications between the parents and children take place through standardised interfaces, with a topology strictly in the form of a tree. The diagnostic topology of the RObоMObil is shown in Figure 6.15. The standardised interface improves code reusability and allows consistent communication across all levels of this recursive structure. In the proposed concept in [YJ04], the interface consists of commands to the Sub-GDCs to select the diagnostic mode, as well as fault status feedback to the parent GDC, as shown in Figure 6.14. Furthermore, the modular concept simplifies the addition or removal of components and facilitates encapsulation of the diagnosis algorithms used in the lower levels, and thereby increasing flexibility for making changes.

In this architecture, a fault state is most frequently detected at the lowest hierarchical level on which sufficient information is available. Besides the resulting reduction in communication overhead, this has two significant robustness advantages for the consistency checks. In lower level diagnostics, the smaller and more localised signal sets result in lower uncertainties, and the functions often benefit from higher sample rates, signal

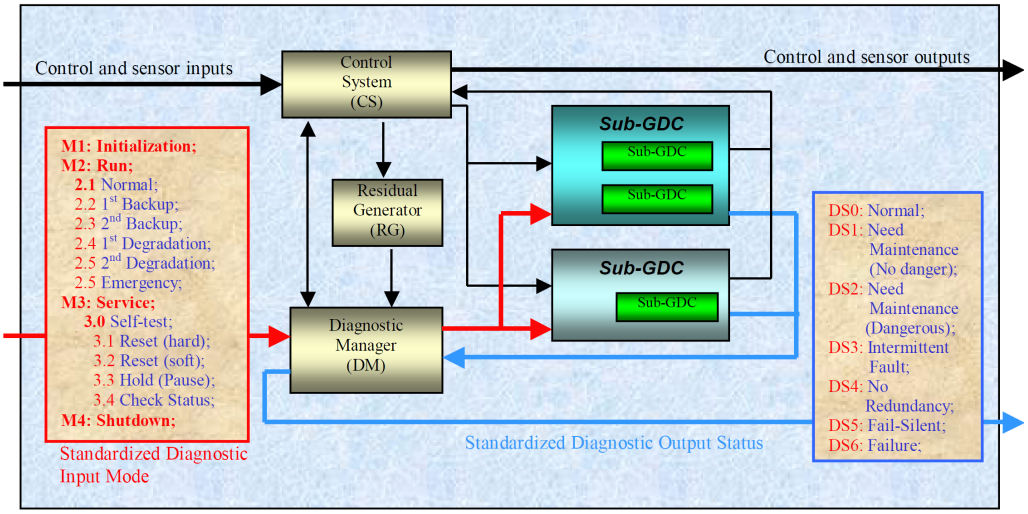

Figure 6.14: Generalised diagnostic component structure [YJ04]

resolution, and lower communication delays of the lower level controller hardware. Each GDC is only required to detect faults that are not already diagnosed to a sufficient quality in the connected lower-level Sub-GDCs. Furthermore, the upper-level GDC may assume that the lower-level component will have enacted the specified fault reaction, such that unmitigated fault behaviours do not need to be taken into consideration.

To illustrate this last property, consider a PMSM traction motor drive. Inverter failure during field-weakening operation can cause a sizeable negative torque to be generated [Wan13; JW07]. If the fault can be detected in the GDC of the TMD promptly, and a mitigation measure such as activation of a braking resistor in a gate driver (e.g. [Int07]) or a backup gate driver supply (e.g. [GGB09]) can be activated, then the faulty behaviour with negative torque may be excluded in the design of the upper-fault diagnosis levels.

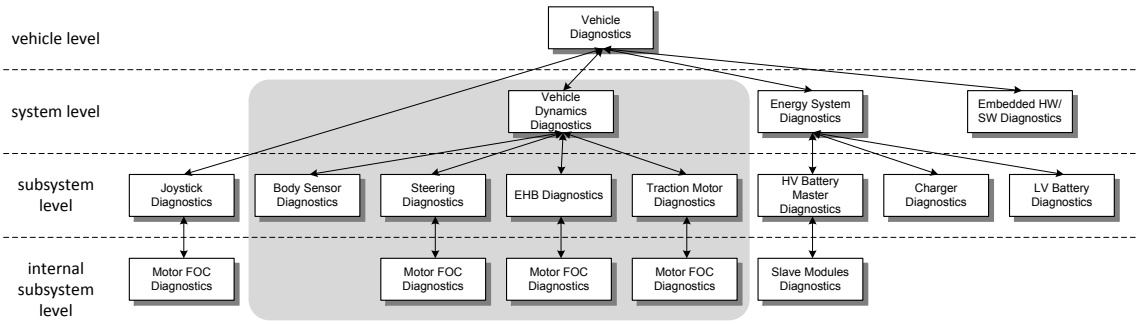

Figure 6.15: Diagnostic hierarchy of the ROboMObil (vehicle dynamics sub-tree highlighted in grey)

6.3.2 ROboMObil Diagnostic System

Having introduced the hierarchical concept, the attention will now focus on the specifics of the ROboMObil application, with generalisations to more realistic X-by-Wire vehicle

architectures of future production vehicles whenever possible. The vehicle dynamics diagnosis system can be decomposed hierarchically according to the system design described in Section 6.2 and the fault analysis in Section 6.2.2. The structure is shown in the region with grey background in Figure 6.15. The remainder of the tree in the figure depicts the diagnostic hierarchy for other vehicle systems that are outside the scope of this study.

As already mentioned in the previous sections, each wheel unit actuator (TMD-A, DB-A, S-A) is assigned a diagnostic component which is responsible for the handling the locally detectable faults described in Section 6.2.2. Each intelligent body sensor unit (the IMU and optical sensor) is also assigned a diagnostic component. Together, these comprise the Sub-GDCs within the higher level Vehicle Dynamics GDC. The remaining faults are diagnosed in this higher level GDC by its "residual generator" (in the terminology of [YJ04]), now referred to as the Vehicle Dynamics FDI. The diagnostic manager of the vehicle dynamics GDC consolidates the reported fault statuses from its Sub-GDCs with the diagnosis outputs from the Vehicle Dynamics FDI module. The scheme is illustrated in Figure 6.16.

It should be noted that on the RObоMObil, the diagnostic components corresponding to the wheel unit actuator are divided across two hardware control units, due to legacy controller and software design in the wheel actuators. Most of the detection functionalities are integrated within the local control unit, while the additional input-output monitoring of the closed-loop and the diagnostic manager reside in the central controller.

The problem definition and architecture design of the Vehicle Dynamics FDI are presented in the next section.

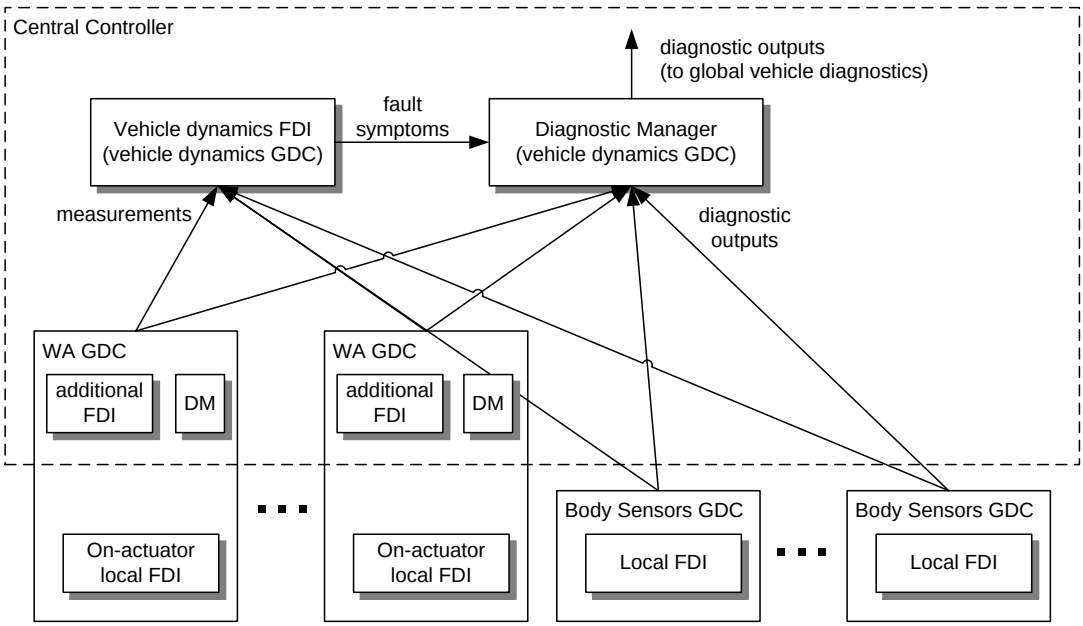

Figure 6.16: Vehicle dynamics GDC (generalised diagnostic component) as implemented on the RObоMObil fault diagnosis system. (DM = Diagnostic Manager, WA = Wheel Actuator)

6.4 Vehicle Dynamics FDI

The vehicle dynamics FDI operates as a component within a system responsible for mitigating faults and managing fault responses in the complete vehicle. In this section we provide a qualitative overview of fault mitigation requirements and their implications for the diagnosis functions. First, a discussion on requirements analysis for fault diagnosis on X-by-Wire vehicles is presented in Section 6.4.1. Subsequently the requirements on the Vehicle Dynamics FDI functions are analysed in Section 6.4.2. Based on these insights, a design is chosen and the structure of the Vehicle Dynamics FDI module is presented in Section 6.4.3. Design and analysis of the core functionalities of this module form the subject of investigation in the remaining chapters.

6.4.1 Influencing Factors for Diagnosis Requirements

To establish the requirements for the vehicle dynamics diagnosis module, the following questions are examined:

- Which faults need to be diagnosed?
- Under what conditions (of the system and the environment) do they need to be diagnosed?
- What are the performance requirements for the diagnosis?

Studies on XbW automotive chassis systems have shown that the minimum safety goal is, in case of a fault, to allow the vehicle to be brought to a safe state, defined in [ISS02] as a stop or low-speed in a non-hazardous place. This demands that the system shall be *short-time fail operational*, with at least fail-silent behaviour from the propulsion system, and degraded fail-operational behaviour from driver input, steering and brake systems. Based on these global system requirements, the designer can use safety analysis methods to determine the faults and abnormalities that must be treated online due to the severity of their effects. Safety analysis can be conducted using methods such as failure mode and effect analysis (FMEA), event tree analysis (ETA), fault tree analysis (FTA), and hazard and operability study (HAZOP). The further step of classifying faults into groups with similar effects and the same mitigation measures can relax the isolation requirements [WDT14].

The fault diagnosis component is intertwined with the remaining components of a reconfiguration-based fault-tolerant control (FTC) system. The timely introduction of suitable fault mitigation measures, whether implemented by an automatic control system, human operators or other agents, demand the availability of accurate and sensitive diagnosis results. The quantitative requirements can be derived from FTC requirements, which, within a deterministic framework, include these significant criteria:

- maximum tolerable fault size without mitigation measures
- maximum tolerable delay until mitigation measures

These parameters may be dependent on system states, fault type and size, and environmental conditions. They may be established through a combination of expert knowledge, experiments and simulations. These two criteria may be translated into performance requirements on the fault diagnosis system in the form of:

- worst-case detection time
- worst-case fault-size sensitivity

The conditions under which each fault has to be reliably diagnosed are outputs from many of the safety analysis methods mentioned above. Influencing factors considered include commonly encountered operating conditions and states of a road vehicle, as well as the danger and dissatisfaction caused by a particular fault in those conditions and states. The architectural, functional, performance, and operating condition constraints of the fault diagnosis design process is summarised in Figure 6.17.

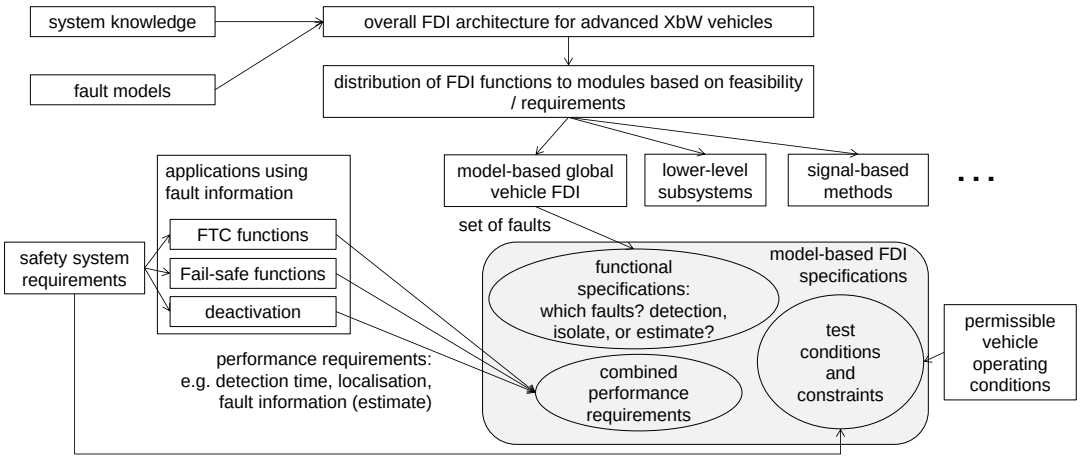

Figure 6.17: Fault diagnosis requirements and design process

6.4.2 Requirements on the Vehicle Dynamics FDI Module

Based on the above considerations, the fault diagnosis problem is now defined qualitatively, including the faults to be detected and isolated, the permitted operating conditions, the constraints and unknown perturbations. A summary of the faults to be diagnosed by each FDI module in the Vehicle Dynamics GDC is repeated in Table 6.3 for convenience. Note that wheel speed sensor faults are included although they are detectable at the in-wheel motor level on the RObоMObil. For vehicle architectures without individual wheel drives, wheel speed sensor faults may not be detectable from within the traction motor drive system, therefore their detection is also specified.

Figure 6.18 provides an abstracted view of Figure 6.10, to aid with visualising the parts of the complete vehicle dynamics system which the FDI functions in each diagnostic component monitor. In particular, the subsystem monitored by the Vehicle Dynamics FDI module is highlighted and its interfaces are displayed.

Table 6.3: Faults to be diagnosed in the FDI module of each GDC

GDC	Faults to be diagnosed in FDI module
TMD-A	electrical faults, inverter shutdown, motor control failure, torque ripples
DB-A	motor faults, hydraulic faults, elasticity, pad/disc thickness and stiffness error
S-A	motor faults, jamming, backlash within actuator, severe angle sensor faults
Body sensor units	processor fault, signal out-of-specification
Vehicle Dynamics FDI	TMD: loss of torque effectiveness, current sensor faults (some cases), excessive friction, wheel speed sensor faults DB: pressure sensor fault, loss of effectiveness in friction torque generation, undesired brake torque S: damaged linkage, incorrect angle sensor calibration, backlash downstream of the actuator angle sensor Body sensors: small to moderate measurement errors (sensors: IMU, optical velocity sensor)

Even though the ROboMObil is able to drive dynamically at highway speeds and manoeuvre in tight spaces, not all combinations between the spectrum of conditions need to be monitored. As explained in the overview of the implemented vehicle dynamics controller in Section 6.1.2, the ROboMObil operates over the full range of speed and dynamics only in the forward longitudinal motion mode. In the backwards direction and in the lateral / rotational motion modes intended for the purposes of manoeuvring and parking, high speed and highly dynamic driving are prevented by the control functions, so these combinations of conditions do not need to be handled.

For model-based FDI methods, further restrictions have to be placed on external disturbances and uncertainties. As will be explained later, the single-track model for lateral dynamics is sensitive to external lateral forces (such as crosswinds) and yaw moments, as well as road banking, while the force-based longitudinal dynamics model is affected by external longitudinal forces and road gradient. In this development, they are assumed to be bounded within value ranges realistic for the test operation of the ROboMObil. For vehicles with a broader range of operating conditions, it may be possible to estimate these values to compensate for their influences. This issue will be discussed in more detail in the Chapter 8.

Additionally, the model-based FDI functions are designed assuming only the presence of single-faults to enable more powerful conclusions to be drawn. As long as common cause failures can be excluded, this represents a realistic assumption due to the low probability of appearance of multiple faults within a short time window.

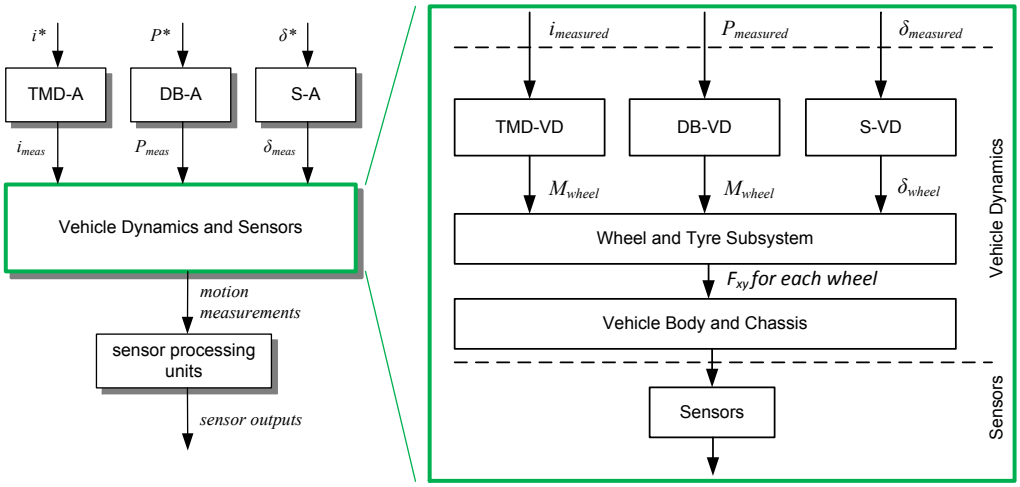

Figure 6.18: Boundaries and interfaces of the vehicle dynamics subsystem (outlined in green) handled by the Vehicle Dynamics FDI module

6.4.3 Module Structure

The Vehicle Dynamics FDI function module is divided into model-free and model-based components. This is shown schematically in the module structure in Figure 6.21. These components are introduced in more detail below. Besides the detection and evaluation functions, the vehicle dynamics FDI module also contains a supervisor and an arbitrator, which together correspond to the diagnostic manager of the GDC concept. The supervisor selectively activates diagnostic functions based on the validity status of their signal sources as well as environmental conditions and plant states. The arbitrator fuses outputs from the valid and active diagnostic functions into consolidated fault statuses. The supervisor and arbitrator functions are outside the scope of this thesis.

Model-Free Fault Diagnosis

The model-free diagnosis methods used in the Vehicle Dynamics FDI module are comprised of signal processing and hardware redundancy solutions. The former can diagnose sensor and plant faults by checking the sensor signal for violation of admissible characteristics, and the latter diagnoses sensor faults by checking for inconsistency between the sensor output and a redundant measurement of the same variable. As long as the sensor signals are available, these model-free methods are not affected by vehicle states, path curvature, as well as other vehicle states and environmental conditions. This is an advantage over model-based methods, as shown in Figure 6.19. The main drawback for signal processing approaches is the lack of fault sensitivity when the signal properties (e.g. value and derivative) lie within the normal range. For hardware redundancy solutions, the additional costs and installation challenges of redundant measurements are stumbling blocks.

Range and slew rate (where applicable) checks are performed for all sensor signals provided to the Vehicle Dynamics FDI module. Hardware redundancy is not available

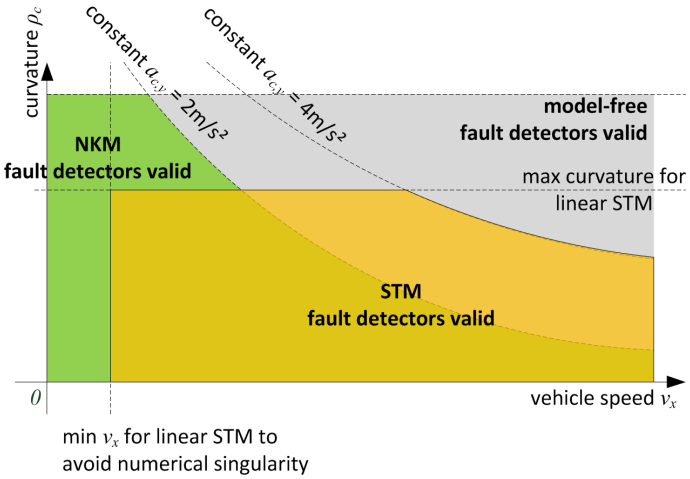

Figure 6.19: Illustration of the validity regions of the model-based fault detectors based on the Nonlinear Kinematic Model (NKM) and Single Track Model (STM), and the model-free detectors

for any sensors on the ROboMObil, but approximate plausibility checks are carried out between velocity variables when operating in the predominantly longitudinal driving region.

Model-based Fault Diagnosis

The schematic layout of the model-based FDI is illustrated in Figure 6.21. Simplified models of vehicle dynamics are used to facilitate development of diagnostic functions of manageable complexity. However, being simplifications, they are not universally valid and two different representations are used to augment the valid operating region for the FDI functions. The *nonlinear kinematic model* (NKM) assumes that the tyre slips are negligible and therefore wheel speeds, steering angles and body velocities are related kinematically. In constrast, the *single track model* (STM) accurate describes lateral dynamics behaviour for moderate tyre slips and lateral acceleration, but the motion must remain predominantly longitudinal. These models are described and derived in detail in Chapter 7. The validity of the model-based FDI functions are monitored by the module labelled *validity conditions*, which inspects the vehicle velocities, accelerations and related states. It should be noted that the fault detectors based on the NKM and STM cover different but overlapping subsets of the faults to be detected, and the fusion of the outputs is handled by the arbitrator block. This topic of combining diagnostic outputs is briefly discussed in Section 9.7.

Before introducing the diagnostic functions in more detail, we will review some experimental studies on lateral accelerations encountered in normal driving, in order to justify the choice of the STM to provide adequate diagnostic coverage. An accident reconstruction research from Germany [HN03] conducted one hour road tests with a range of volunteer drivers, on a combination of a round course, country roads, highway intersections and inner city route. It was found that even tighter curves were negotiated only with moderate

lateral accelerations, e.g. 90% of the curves with radii of $20-40$m were taken with 5.3m/s^2 or less. For larger curve radii the lateral accelerations decrease well below 4 m/s^2. A similar, more recent study on highways in Sichuan, China again demonstrated that the lateral acceleration lied below 4 m/s^2 on over 90% of the curves, and over half lied below 2 m/s^2 (see Figure 6.20). These studies confirm the utility of STM for fault diagnosis in real world driving, since it simulates the lateral dynamics adequately for lateral accelerations up to approximately 4 m/s^2 [Ise06a].

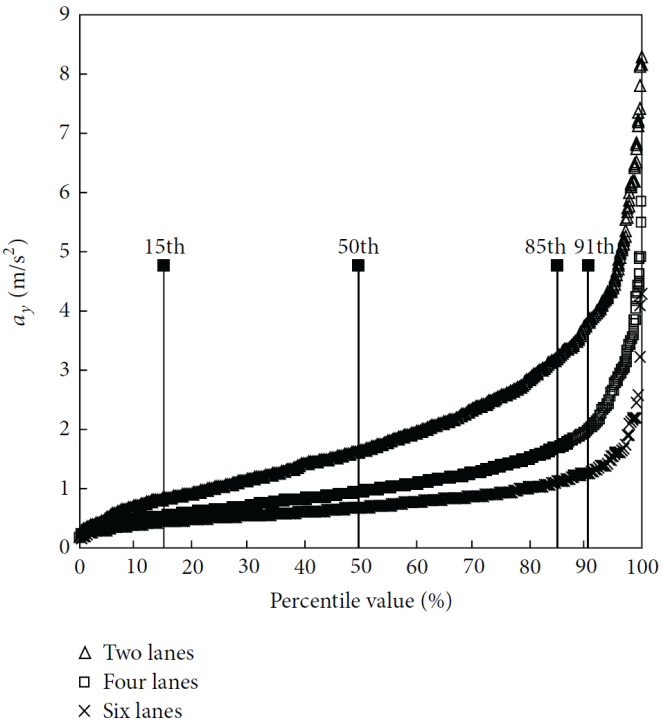

Figure 6.20: Distributions of lateral accelerations for highways with different lanes [Xu15]

Diagnosis for the moderate-to-high speed, predominantly longitudinal cruising region is achieved by the combination of separate longitudinal and lateral fault detectors. When a vehicle is driving with low-to-moderate accelerations (and therefore path curvatures), the cross-coupling between longitudinal and lateral dynamics is limited, permitting decoupled monitoring of the two DOFs. The development of the longitudinal fault detector is not covered in this study. However, as an example, it could be implemented using a parity relation based on the longitudinal force balance:

$$F_{traction} - F_{drag} - F_{gradient} = m \times a_x \tag{6.1}$$

where $F_{(.)}$ denotes longitudinal forces, m the vehicle mass, and a_x the body acceleration in the longitudinal direction.

When a vehicle is driven with time-varying velocity, its lateral dynamics behaviour is dependent on the longitudinal velocity v_x. The model for moderate-to-high speed operation is therefore represented by the Linear Parameter-Varying (LPV) STM, with v_x as the scheduling parameter. The solution presented in Chapter 8, denoted by *STMFDI*,

employs a bank of robust LPV fault detectors designed using a combination of the reference model-matching method presented in Chapter 4 and residual evaluation based on the norm-based approach in Chapter 5. Fault isolation is then achieved by structured residuals. Since the longitudinal vehicle velocity v_x schedules the STM, it is crucial that a reliable v_x signal is available. In the ROboMObil application, its verification is provided by plausibility checks between wheel and vehicle speeds in the longitudinal direction.

When manoeuvring at lower speeds, diagnostic functions based on the NKM are activated. The approach presented in Chapter 9, denoted by *NKMFDI*, examines the plausibilities of the measured wheel speeds, steering angles, and horizontal body velocities and accelerations with respect to the NKM. The effects of permissible tolerances due to measurement and modelling errors are systematically taken into account.

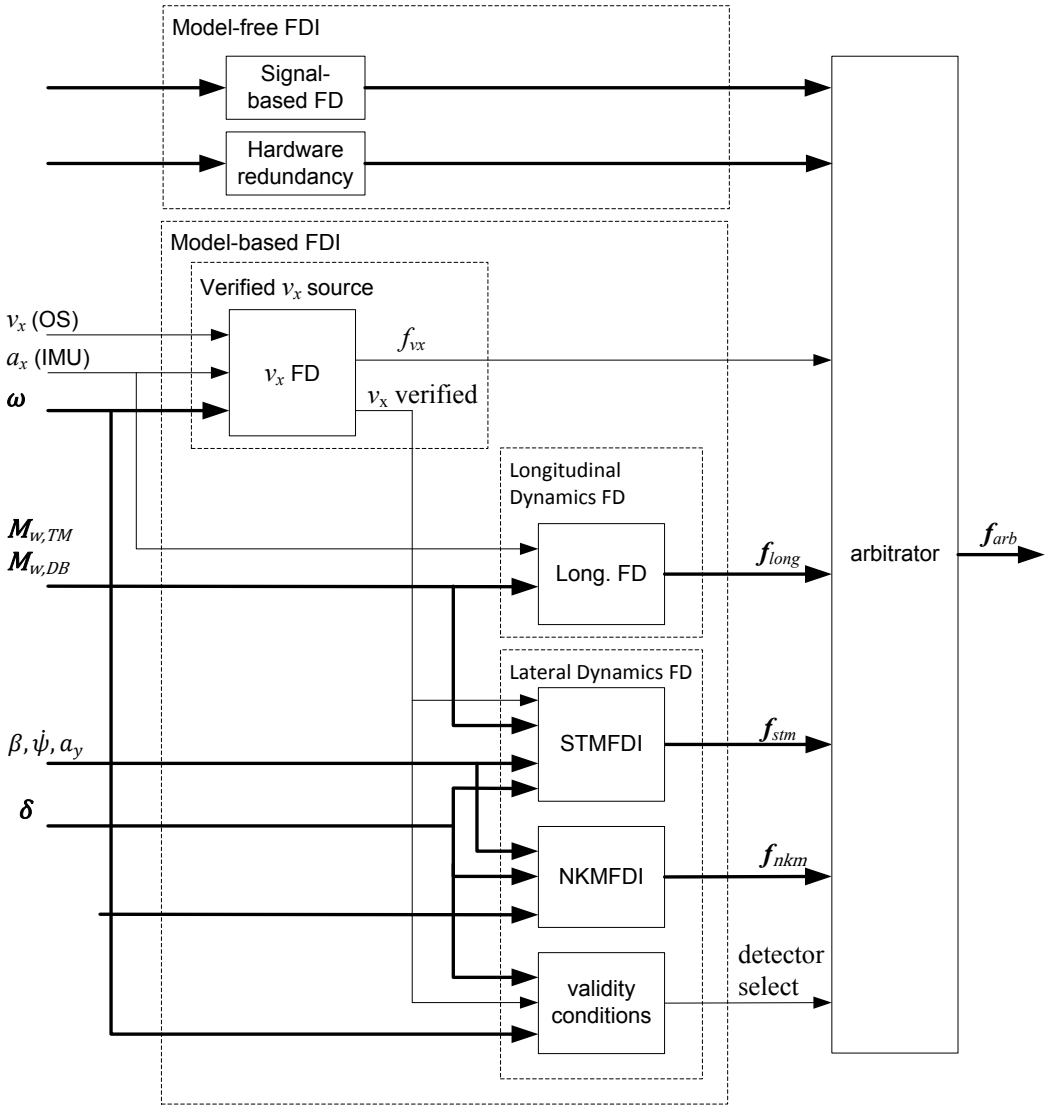

Figure 6.21: Structure of the Vehicle Dynamics FDI software module

Chapter 7

Vehicle Dynamics Modelling

In this chapter, we present the vehicle models that will be used for FDI design and simulative validation. For design, simplified control-oriented models are sought that captures only the most important effects under the assumed operating conditions. On the other hand, validation models should reproduce the real behaviour with higher fidelity over all the validation conditions. Figure 7.1 illustrates the system interconnections in an advanced X-by-Wire vehicle. The vehicle dynamics component with idealised inputs and outputs (I/O) is central to the model and simulates the relationship between the wheel variables (steering angles and wheel torques) and body motion. From a modelling perspective, the adjacent blocks representing the mapping from actuator outputs to wheel variables and that representing the mapping from body motion to measured outputs can be considered a wrapper to the vehicle dynamics model, transforming between the real and ideal I/O variables. Further components model the vehicle dynamics controller and the closed-loop controlled actuators, which are described in the preceding chapter.

For the vehicle dynamics component with idealised I/O, mathematical models for conventional vehicle architectures are adapted to represent overactuated X-by-Wire vehicles and parametrised for the ROboMObil. The first and major part of this chapter is devoted to the modelling of vehicle dynamics for the needs of identification, design and validation. Their derivation is covered in Section 7.1, while topics related to their parameterisation are discussed in Section 7.6. Section 7.2 describes the transformations in the wrapper components.

Actuator and sensor models are derived in Section 7.3, where it is argued that simple models are adequate for preliminary validations. The faults designated in Chapter 6 for diagnosis on the global vehicle dynamics level are modelled mathematically in Section 7.4. Subsequently, Section 7.5 describes the simulation model used in the validation of the *STMFDI* in Chapter 8, whose components are based on the previously described models.

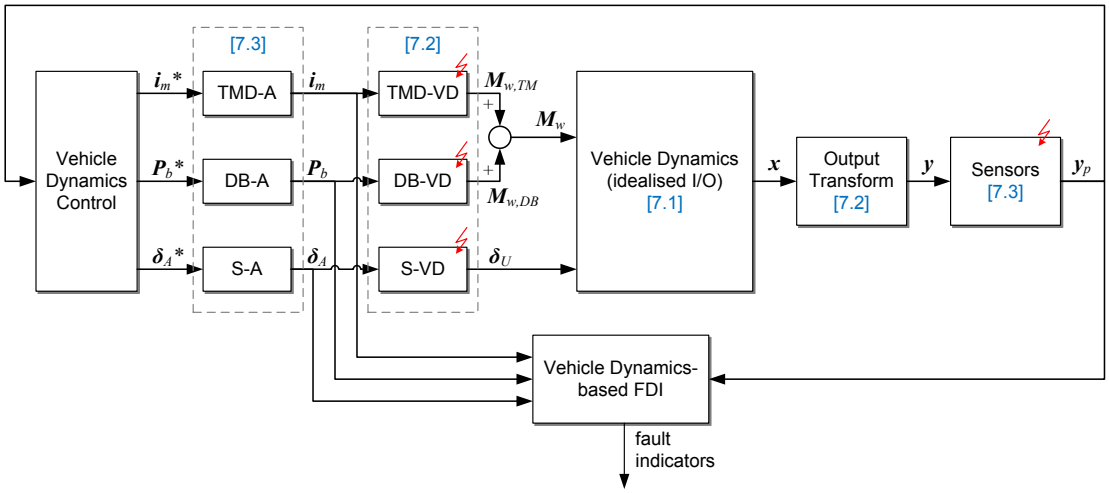

Figure 7.1: Block diagram of the vehicle dynamics system and its interconnection with the FDI module. *TMD*, *DB* and *S* denote the traction motor, disc brake and steering systems, while the *-A* and *-VD* suffixes denote the closed-loop actuator and open-loop parts of the above systems respectively. The superscript $*$ denotes the demand signal. $\boldsymbol{x}$, $\boldsymbol{y}$ and $\boldsymbol{y}_p$ denote the vehicle dynamics states, ideal outputs and processed outputs respectively. The systems and variables will be explained in more detail in this chapter. The blocks are treated in the section number in the blue square brackets, while those affected by the faults modelled in this chapter are each marked with a red lightning symbol.

7.1 Plant Model: Vehicle Dynamics

Vehicle dynamics models of varying levels of complexity are necessary for the various design and validation stages of fault diagnosis functions. The behaviour of a road vehicle is determined by the elastokinematic multi-body dynamics of the chassis, suspension and wheels, and includes the dynamics of the force generating components (i.e., springs, dampers and tyres). A lumped parameter multi-body model can accurately simulate the nonlinear effects of all these components. However, such a level of detail is computationally intensive to simulate, and for preliminary investigations a simpler model which reproduces the key vehicle dynamics behaviours is desirable. By making simplifying assumptions in the area of suspension kinematics, the Double Track Model (DTM) offers a suitable compromise between detail and complexity and is often used in proof-of-concept studies of vehicle dynamics control and estimation. This model is presented in Section 7.1.1.

For the design of model-based fault detectors, even simpler models are desirable in the synthesis process to reduce the complexity of the detectors and consequently their computational demands. Moreover, using models belonging to well-established system classes, such as static, LTI, or LPV, permits powerful design methods to be drawn from a mature literature. However, simplification of the models generally exploit approximations that are only acceptable under restricted operating conditions, so appropriate models must be carefully chosen. In this work, FDI synthesis for two vehicle operating regions is addressed, namely cruising and parking. Cruising operation refers to driving at moderate-to-high speeds on highways and arterial roads, which is characterised by low-to-moderate

lateral acceleration, small steering angles and a small body side-slip angle. Under these conditions, the linear parameter-varying (LPV) Single Track Model (STM) derived in Section 7.1.2 provides a close approximation of vehicle behaviour.

The second operating region of parking (also referred to as manoeuvring) is characterised by low-to-moderate speeds, low accelerations, and steering angles varying over large ranges. Large steering angles introduce significant trigonometric nonlinearities into the system equations. On the other hand, the low accelerations and the resulting tyre forces, and consequently tyre slips, permit the use of a kinematic model, which relies on the assumption of no tyre slip. This control-oriented representation is valid not limited to vehicle motion close to straight-ahead driving, but also describes other motion regions such as sideways driving or rotation dominated motion. Fault detectors that can operate over such a broad range of conditions are particularly interesting for highly manoeuvrable vehicles such as the ROboMObil. To improve content flow in the thesis, this nonlinear kinematic model (NKM) representation is described at the beginning of Chapter 9, just before the development of NKM-based fault detectors is presented.

7.1.1 Double Track Model (Simulation)

The nonlinear Double Track Model (DTM) is a vehicle model which describes the 6-DOF rigid body motion of the chassis, combined with vertical dynamics, rotational dynamics of the wheels and a nonlinear tyre-road friction model. The principal degrees of freedom of a vehicle are illustrated in Figure 7.3. The model introduced below is based on the formulation in [Ore06] and has the structure shown in Figure 7.2. This simplified model provides a sufficiently accurate description of vehicle dynamics behaviour for simulative investigations of control, estimation and diagnosis algorithms. This section provides a brief overview, and the reader is referred to [Ore06; KN05] for more detailed descriptions and analyses.

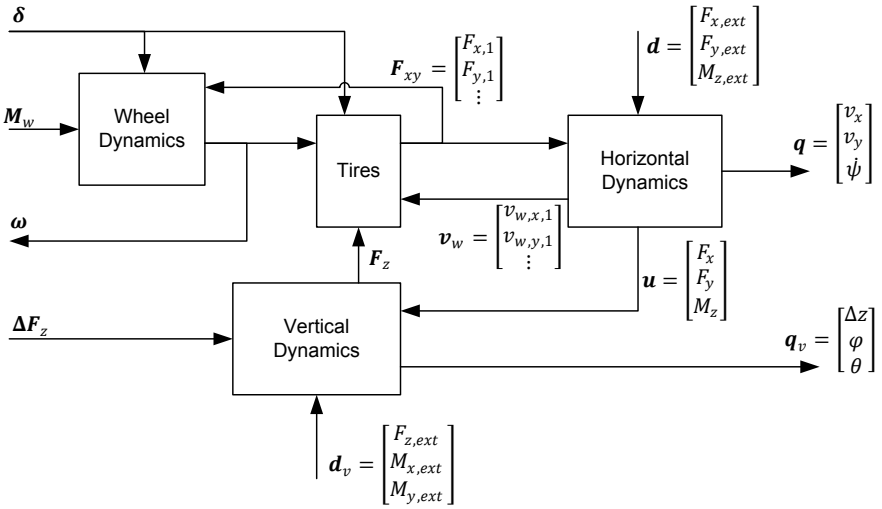

Figure 7.2: Model block diagram of the double track model (DTM)

Coordinate System and Indices

In order to describe the model, we first introduce four relevant coordinate systems using the nomenclature from [KN05]. They are:

B: body coordinate system
U: undercarriage system
W: wheel coordinate system
I: fixed inertial system.

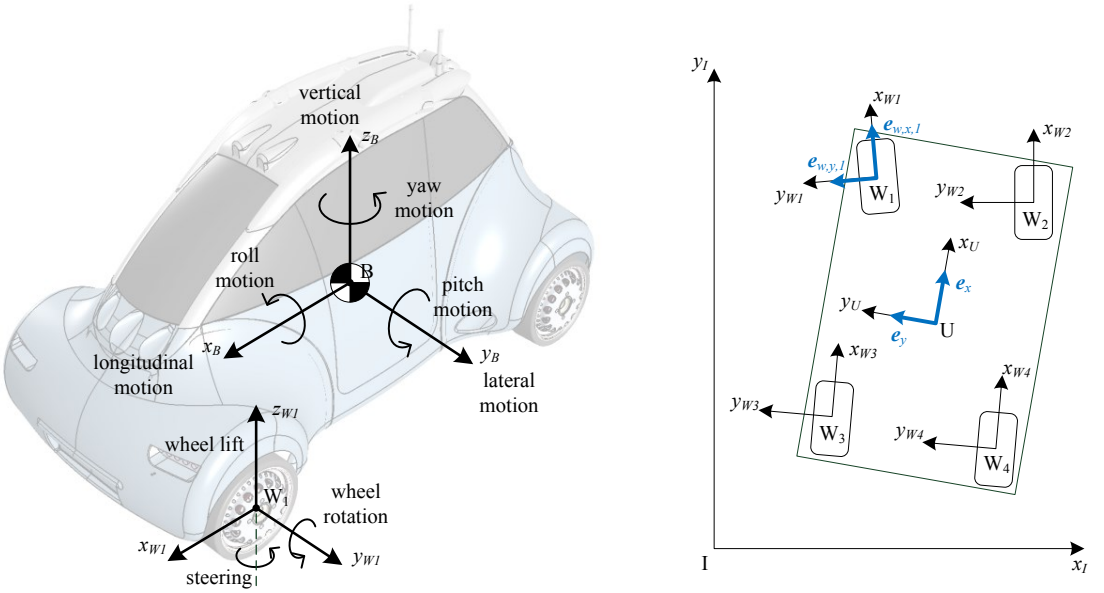

Figure 7.3: Left: degrees of freedom of a vehicle. Right: the horizontal coordinate systems U, W and I.

The body coordinate system (B) is fixed to the vehicle body at its centre of gravity (CoG). The undercarriage system (U) differs from the body coordinate system only in that it is projected onto the ground plane, and is not affected by roll or pitch motion. For each wheel, the wheel coordinate system (W) is fixed at the centre of the wheel and aligned with the wheel plane. The DTM assumes that the wheel plane is always vertical, thus the vertical direction of the wheel coordinate systems is aligned with those of the undercarriage system, and the forward directions rotate with the respective steering angles. The fixed inertial system (I) does not move with the vehicle.

In all coordinate systems, positive x corresponds to the forward direction, while positive z corresponds to the upward direction. Positive y represents the left direction looking down the positive x vector. The basis unit vectors point in these directions (the undercarriage coordinates is used here as an example) and satisfy

$$\boldsymbol{e}_z = \boldsymbol{e}_x \times \boldsymbol{e}_y \ . \tag{7.1}$$

Here the $\times$ symbol denotes the vector cross-product. For the i-th wheel, the unit vectors of the wheel coordinate system W are denoted $\boldsymbol{e}_{w,x,i}$, $\boldsymbol{e}_{w,y,i}$ and $\boldsymbol{e}_{w,z,i}$ respectively. In this work, the x_{W_i} and y_{W_i} directions are also referred to as the tangential and lateral directions of the i-th wheel. For a regular four wheeled vehicle as illustrated in Figure 7.3, the wheels are identified by numerical indices with 1: front left, 2: front right, 3: rear left, 4: rear right.

Besides the fixed vertical wheel directions, another key simplifying assumption of the DTM relates to the partial decoupling of the vertical from the horizontal kinematics, in that the horizontal positions of the wheels are not affected by vertical, roll or pitch motion. With these assumptions it is possible to divide the horizontal dynamics from the vertical dynamics, with coupling restricted to only the generalised horizontal force vector $\boldsymbol{u} = [F_x \; F_y \; M_z]^T$ and the wheel load input $\boldsymbol{F}_z$ to the tyre model, as illustrated in Figure 7.2. The horizontal and vertical dynamics components will now be described in more detail.

Horizontal Dynamics

The horizontal dynamics is described in the undercarriage (U) coordinate system. Velocity is represented by the vector $\boldsymbol{v} = [v_x \; v_y]^T$, or equivalently by velocity magnitude v and body side-slip angle β, where

$$\beta = \arctan \frac{v_y}{v_x} \; , \tag{7.2}$$

$$v = |\boldsymbol{v}| = \sqrt{v_x^2 + v_y^2} \; . \tag{7.3}$$

The longitudinal and lateral accelerations a_x and a_y are given by the kinematic relations:

$$a_x = \dot{v}_x - v_y \dot{\psi} \; , \tag{7.4}$$

$$a_y = \dot{v}_y + v_x \dot{\psi} \; . \tag{7.5}$$

The translational velocity of the wheel centre of the i-th wheel is given by

$$\boldsymbol{v}_{w,i} = [v_{w,x,i} \quad v_{w,y,i}]^T \; , \tag{7.6}$$

where

$$v_{w,x,i} = v_x - \dot{\psi} s_i \; , \tag{7.7}$$

$$v_{w,y,i} = v_y + \dot{\psi} l_i \; . \tag{7.8}$$

where s_i and l_i are the displacements from the vehicle CoG to the i-th wheel in the x and y directions respectively. For a "rectangular" vehicle with the same track dimensions s_l

and s_r on both front and rear axles as shown in Figure 7.4, the parameters simplify to

$$\begin{bmatrix} s_1 \\ s_2 \\ s_3 \\ s_4 \end{bmatrix} = \begin{bmatrix} s_l \\ -s_r \\ s_l \\ -s_r \end{bmatrix} , \qquad \begin{bmatrix} l_1 \\ l_2 \\ l_3 \\ l_4 \end{bmatrix} = \begin{bmatrix} l_f \\ l_f \\ -l_r \\ -l_r \end{bmatrix} . \tag{7.9}$$

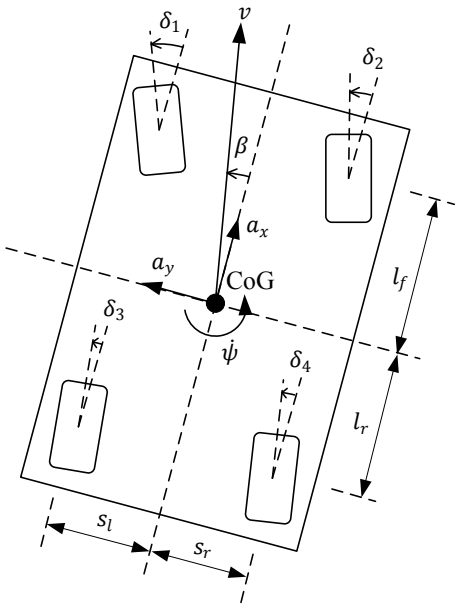

Figure 7.4: Horizontal vehicle dynamics of the DTM

The vehicle's horizontal dynamics are described by force balances in the x and y directions, and a moment balance about the z direction. Denote the tyre forces at the i-th wheel in the x, y directions as $F_{x,i}, F_{y,i}$. The disturbance forces due to road grade angle α_g and banking angle α_b are given by $-mg\sin\alpha_g$ and $mg\sin\alpha_b$ respectively, where m denotes the total vehicle mass and g the acceleration due to gravity. The remaining external forces and moments are combined into $F_{x,ext}$, $F_{y,ext}$ and $M_{z,ext}$. The force and moment balance then gives:

$$ma_x = F_x + F_{x,ext} - mg\sin\alpha_g \ , \tag{7.10}$$

$$ma_y = F_y + F_{y,ext} + mg\sin\alpha_b \ , \tag{7.11}$$

$$J_z\ddot{\psi} = M_z + M_{z,ext} \ , \tag{7.12}$$

where F_x, F_y and M_z denote the total force and moment contributions due to all tyre forces:

$$F_x = \sum_{i=1}^{4} F_{x,i} \ , \tag{7.13}$$

$$F_y = \sum_{i=1}^{4} F_{y,i} \ , \tag{7.14}$$

$$M_z = \sum_{i_1}^{4} -s_i F_{x,i} + l_i F_{y,i} \ . \tag{7.15}$$

The presented relationships between horizontal forces and velocities at the vehicle CoG and wheel centres can be summarised by the following vector equations:

$$\boldsymbol{u} = \boldsymbol{G}^T \boldsymbol{F}_{xy} \ , \tag{7.16}$$

$$\boldsymbol{v}_w = \boldsymbol{G}\boldsymbol{q} \ , \tag{7.17}$$

where

$$\boldsymbol{G} = \begin{bmatrix} 1 & 0 & 1 & 0 & 1 & 0 & 1 & 0 \\ 0 & 1 & 0 & 1 & 0 & 1 & 0 & 1 \\ -s_1 & l_1 & -s_2 & l_2 & -s_3 & l_3 & -s_4 & l_4 \end{bmatrix}^T \ ,$$

$$\boldsymbol{F}_{xy} = \begin{bmatrix} F_{x,1} & F_{y,1} & F_{x,2} & F_{y,2} & F_{x,3} & F_{y,3} & F_{x,4} & F_{y,4} \end{bmatrix}^T \ ,$$

$$\boldsymbol{v}_w = \begin{bmatrix} v_{w,x,1} & v_{w,y,1} & v_{w,x,2} & v_{w,y,2} & v_{w,x,3} & v_{w,y,3} & v_{w,x,4} & v_{w,y,4} \end{bmatrix}^T \ ,$$

$$\boldsymbol{u} = \begin{bmatrix} F_x & F_y & M_z \end{bmatrix}^T \ ,$$

$$\boldsymbol{q} = \begin{bmatrix} v_x & v_y & \dot{\psi} \end{bmatrix}^T \ .$$

Vertical Dynamics

In the DTM, each wheel is assumed to move perpendicularly relative to the ground (i.e. in the undercarriage z direction) and to be connected to the body via springs and dampers. In addition, the wheels of each axle are connected to each other via a spring representing the anti-roll bar. For simplicity, all springs and dampers are modelled as linear elements. The vertical springs and dampers at the i-th wheel have stiffness $c_{s,i}$ and damping $k_{d,i}$, while the anti-roll bars of the front and rear axles have stiffnesses $c_{a,f}$ and $c_{a,r}$. With the four wheels lying on a flat (but possibly sloped) road surface, the vertical degrees of freedom of the DTM can represent a combination of roll and pitch motions of the vehicle body.

Due to the small roll angle ϕ and pitch angle θ experienced in normal road driving, it is reasonable to apply the small angle approximation, as well as assume that the wheels remain in the same horizontal positions relative to the CoG. Consequently a linear kinematic

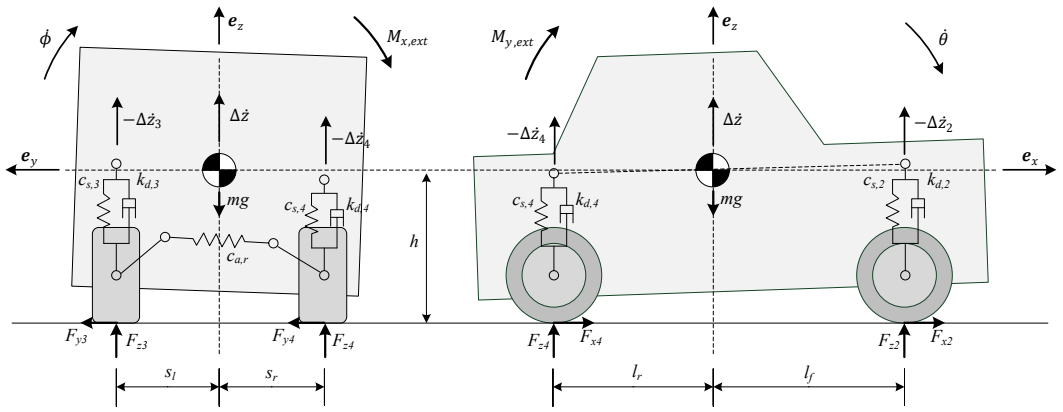

Figure 7.5: Vertical vehicle dynamics [Ore06]

model is obtained with the following relations for each wheel DOF:

$$-\Delta\dot{z}_i = \Delta\dot{z} + s_i\dot{\phi} - l_i\dot{\theta} \ , \tag{7.18}$$

$$-\Delta z_i = \Delta z + s_i\phi - l_i\theta \ , \tag{7.19}$$

where Δz and Δz_i are respectively the vertical displacements of the body and suspension travel of the i-th wheel from the resting position. Based on these relations, the load on the i-th wheel, denoted $F_{z,i}$, is given for the front axle ($i = 1, 2$) by

$$F_{z,i} = \underbrace{-c_{s,i}(\Delta z + s_i\phi + l_i\theta) + \frac{c_{a,f}\ \mathrm{sgn}(s_i)}{s_1 - s_2}\phi - k_{d,i}(\Delta\dot{z} + s_i\dot{\phi} + l_i\dot{\theta})}_{\Delta F_{z,i}} + F_{z,0,i} \tag{7.20}$$

where $F_{z,0,i}$ is the resting wheel load and $\Delta F_{z,i}$ is the wheel load's deviation from the resting value. The expressions for the rear axle ($i = 3, 4$) are obtained by replacing the terms $c_{a,f}$ and $(s_1 - s_2)$ by $c_{a,r}$ and $(s_3 - s_4)$ respectively.

The body dynamics are then given by force and moment balances:

$$m\Delta\ddot{z} = \sum_{i=1}^{4} \Delta F_{z,i} + F_{z,ext} \ , \tag{7.21}$$

$$J_x\ddot{\phi} = \sum_{i=1}^{4} \Delta F_{z,i}s_i + hF_y + M_{x,ext} \ , \tag{7.22}$$

$$J_y\ddot{\theta} = \sum_{i=1}^{4} -\Delta F_{z,i}l_i - hF_x + M_{y,ext} \ . \tag{7.23}$$

Wheel Dynamics

The wheel dynamics will be described here for the i-th wheel. Its $x_{W_i}z_{W_i}$ plane is rotated about the z_U-axis by the steering angle δ_i relative to the x_Uz_U-plane. The i-th wheel, the

unit vectors of the coordinate systems W and U are related to each other by:

$$\boldsymbol{e}_{w,x,i} = \cos(\delta_i)\boldsymbol{e}_x + \sin(\delta_i)\boldsymbol{e}_y \ , \tag{7.24}$$

$$\boldsymbol{e}_{w,y,i} = -\sin(\delta_i)\boldsymbol{e}_x + \cos(\delta_i)\boldsymbol{e}_y \ , \tag{7.25}$$

$$\boldsymbol{e}_{w,z,i} = \boldsymbol{e}_z \ . \tag{7.26}$$

The wheel coordinate system W will be used later in expressing the relationships in the next subsection "Tyre Model". Meanwhile, the absolute velocity of the wheel circumference at the ground contact point is

$$\boldsymbol{v}_{cp,i} = \boldsymbol{v}_{w,i} - \boldsymbol{e}_{w,x,i} r_w \omega_i \tag{7.27}$$

where ω_i denotes the wheel rotational velocity, and r_w the effective wheel radius.

The wheel's rotational dynamics can be obtained from a moment balance about the wheel rolling (y_{W_i}) axis:

$$J_w \dot{\omega}_i = M_{w,i} - r_w \left(\cos(\delta_i)F_{x,i} + \sin(\delta_i)F_{y,i}\right) \ . \tag{7.28}$$

Tyre Model

The tyre model describes horizontal tyre force generation from the influencing parameters and states. The model used here is a simplified variant of the semi-empirical Pacejka Magic Formula tyre model [Pac02]. The generated steady state force is dependent on the *slip* of the tyre, the wheel load, as well as parameters describing the effects of the tyre-road contact.

The slip of the tyre is defined as the relative velocity between the tyre's ground contact point and the road, normalised by the magnitude of the wheel centre velocity. The calculation of slip in and perpendicular to the wheel plane (tangential / lateral) are well defined individually, but there exist a variety of approaches for combining them and / or their effects [BR93; Pac02; Ril13; Ore06]. Here, the isotropic combined slip approach is taken, as used in [Ore06].

In this model, the behaviour from tyre slip to steady state force is assumed to be isotropic as defined by the friction circle [Pac02], such that the gain from slip to force is equal for the tangential and normal wheel directions. Thus the total steady state force vector on the tyre has the same direction as the combined slip vector. The combined slip $\boldsymbol{s}_i$ is defined as the vector velocity $\boldsymbol{v}_{cp,i}$ of the tyre at the contact point with the road

(defined in (7.27)) normalised by the magnitude of the wheel centre velocity $\boldsymbol{v}_{w,i}$:

$$\boldsymbol{s}_i = \frac{1}{|\boldsymbol{v}_{w,i}|}\boldsymbol{v}_{cp,i} \tag{7.29a}$$

$$= -\frac{1}{|\boldsymbol{v}_{w,i}|}\left(\boldsymbol{v}_{w,i} - \boldsymbol{e}_{w,x,i} r_w \omega_i\right) \tag{7.29b}$$

$$= \frac{1}{|\boldsymbol{v}_{w,i}|}\left(\left(r_w\omega_i \cos\delta_i - v_{w,x,i}\right)\boldsymbol{e}_x + \left(r_w\omega_i \sin\delta_i - v_{w,y,i}\right)\boldsymbol{e}_y\right) \ . \tag{7.29c}$$

The steady state tyre force is modelled by the simplified Pacejka Magic Formula (MF):

$$\boldsymbol{F}_i^{stat} = F_{max,i} \sin\left(C_i \arctan\left(B_i \frac{|\boldsymbol{s}_i|}{\mu_i}\right)\right)\frac{\boldsymbol{s}_i}{|\boldsymbol{s}_i|} \tag{7.30}$$

where μ is the "friction coefficient" of the tyre-road interface, B_i and C_i are curve shape parameters. The maximum tyre force $F_{max,i}$ is given by

$$F_{max,i} = \mu_i F_{zi}\left(1 + k_{Fz}\frac{F_{z0} - F_{zi}}{F_{z0}}\right) \tag{7.31}$$

with a positive degressivity factor k_{Fz} such that the slip-force gradient reduces with increasing wheel load. Characteristic curves of the tyre model are shown in Figure 7.6.

It is well known that in the normal direction of a pneumatic tyre, the generated force exhibits a dynamic behaviour with respect to tyre slip. Here, this effect is modelled by a first order behaviour with respect to the rolled distance, where the distance constant is termed the relaxation length σ_α [Pac02]. To compute the dynamic tyre force $\boldsymbol{F}_i = [F_{x,i}\ F_{y,i}]^T$, first transform $\boldsymbol{F}_i^{stat} = [F_{x,i}^{stat}\ F_{y,i}^{stat}]^T$ from the undercarriage (U) to the wheel (W) coordinate system:

$$\begin{bmatrix} F_{w,x,i}^{stat} \\ F_{w,y,i}^{stat} \end{bmatrix} = \begin{bmatrix} \cos\delta_i & \sin\delta_i \\ -\sin\delta_i & \cos\delta_i \end{bmatrix} \begin{bmatrix} F_{x,i}^{stat} \\ F_{y,i}^{stat} \end{bmatrix} \ . \tag{7.32}$$

In this model, the tangential tyre force $F_{w,x,i}$ will be assumed to be the same as its steady state value $F_{w,x,i}^{stat}$. Applying the relaxation length dynamics to the $F_{w,y,i}$ component results in the following velocity-dependent first order differential equation:

$$F_{w,y,i} + \frac{\sigma_\alpha}{|\boldsymbol{v}_{w,i}|}\dot{F}_{w,y,i} = F_{w,y,i}^{stat} \ . \tag{7.33}$$

The tyre force $\boldsymbol{F}_i$ is then given by a transformation back into the coordinate system U:

$$\boldsymbol{F}_i = \begin{bmatrix} \cos\delta_i & -\sin\delta_i \\ \sin\delta_i & \cos\delta_i \end{bmatrix} \begin{bmatrix} F_{w,x,i} \\ F_{w,y,i} \end{bmatrix} . \tag{7.34}$$

When tangential tyre slip is negligible, the lateral slip of a tyre is equal to the sine of the slip angle α_i, defined as the angle between the directions of $\boldsymbol{e}_{w,x,i}$ (given by the steering angle δ_i) and the wheel centre velocity $\boldsymbol{v}_{w,i}$ (defined in (7.6)-(7.8)). The slip angle

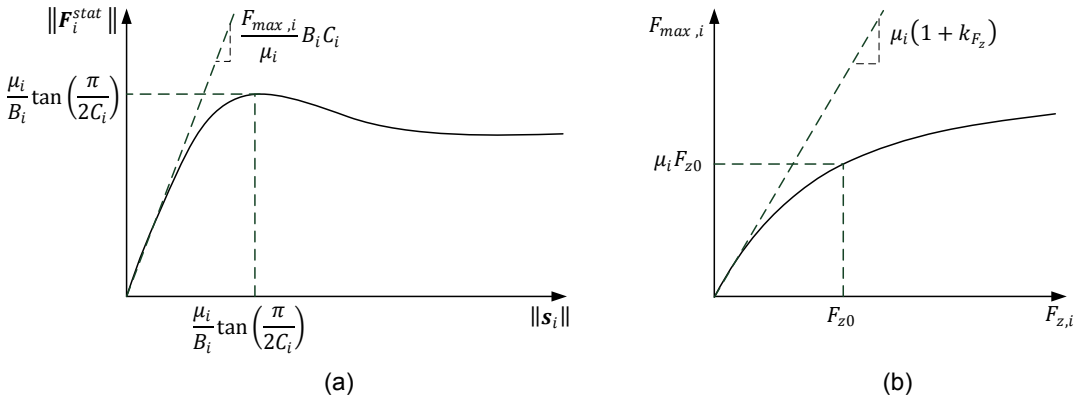

Figure 7.6: Simplified Pacejka Magic Formula tyre model: a) force-slip characteristics, b) degressive maximum force vs vertical tyre load (adapted from [Ore06, p.20])

α_i of the i-th wheel is given by

$$\alpha_i = \delta_i - \arctan\left(\frac{v_y + l_i\dot{\psi}}{v_x - s_i\dot{\psi}}\right) . \tag{7.35}$$

For zero tangential slip, the lateral slip calculated by $\sin\alpha_i$ is equivalent to the slip defined in (7.29c).

7.1.2 Single Track Model (Control-Oriented)

The Single Track Model (STM), also commonly known as the *bicycle model*, is a further simplified representation of vehicle dynamics for moderate values of steering angles, body side-slip angles, and lateral acceleration. It is suitable for representing motion with a velocity vector predominantly in the longitudinal direction, and is used mainly for control-oriented purposes related to lateral dynamics. Due to the lack of modelling of vertical dynamics and lateral load transfer effects, it only simulates the lateral dynamics adequately for lateral accelerations up to approximately 4 m/s^2 [Ise06a]. The basic variant consists of a lumped mass and rotational inertia about the vertical z-axis at the vehicle centre of mass. Only the horizontal degrees of freedom are considered, namely translation in x and y directions, and rotation about the z-axis. Pitch and roll dynamics of the body are neglected, thereby aligning the body and undercarriage coordinate systems. Wheel rotational dynamics are also neglected, and the forces from the two wheels on each of the front and rear axles are assumed to act at the respective axle midpoints. Figure 7.7 provides an depiction of the STM.

The tyre model is linearised about the low slip region where the slip-force curve approaches a straight line. With this approximation, steady state lateral tyre forces $F_{w,y,j}^{stat}$

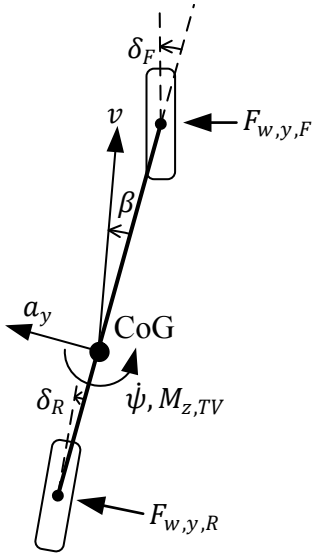

Figure 7.7: Degrees of freedom of the STM, and the forces and moment acting on it

are proportional to the slip angle α_j via the cornering stiffness $c_{\alpha,j}$ as given by:

$$F_{w,y,j}^{stat} = c_{\alpha,j}\alpha_j \tag{7.36}$$

$$= c_{\alpha,j}\left(\delta_j - \arctan\left(\frac{v_y + l_j\dot{\psi}}{v_x}\right)\right) , \tag{7.37}$$

where $j \in [F, R]$ denotes the front and rear axles when discussing the STM. The dynamic lateral tyre force acting on the wheel centre, $F_{w,y,j}$, is governed by a velocity-dependent first order system representing the relaxation length effect which is analogous to (7.33) for the DTM. Due to the small angle assumptions, the wheel centre velocity term $|\boldsymbol{v}_{w,i}|$ can be replaced by v_x to give:

$$F_{w,y,j} + \frac{\sigma_\alpha}{v_x}\dot{F}_{w,y,j} = F_{w,y,j}^{stat} . \tag{7.38}$$

Neglecting longitudinal tyre slip and wheel rotational dynamics is a reasonable approximation when wheel torques are low. This results in tangential tyre forces of the individual wheels, $F_{w,x,i}$, being proportional to motor torque:

$$F_{w,x,i} = \frac{M_{w,i}}{r_w} \quad i = 1, \ldots, 4 . \tag{7.39}$$

The forces on the left and right wheels are summed on each axle to give

$$F_{w,x,F} = F_{w,x,1} + F_{w,x,2} \tag{7.40}$$

$$F_{w,x,R} = F_{w,x,3} + F_{w,x,4} . \tag{7.41}$$

The torque vectoring moment $M_{z,TV}$ is the yaw moment generated by the tangential tyre forces. Its computation requires the lateral positions of the wheels to be taken into

account. It is given by:

$$M_{z,TV} = \sum_{i=1}^{4} F_{w,x,i} \left(l_i \sin \delta_i - s_i \cos \delta_i \right) \ . \tag{7.42}$$

External disturbances are injected as disturbance forces and moments in the three DOFs. In the following equations, the effect of road banking angle α_b is also modelled. The system can be described in the form of a standard nonlinear state space system:

$$\dot{\boldsymbol{x}} = f\left(\boldsymbol{x}, \boldsymbol{u}, \boldsymbol{d}\right) \tag{7.43}$$

$$\boldsymbol{y} = h\left(\boldsymbol{x}, \boldsymbol{u}, \boldsymbol{d}\right) \ , \tag{7.44}$$

where the input $\boldsymbol{u}$, state vector $\boldsymbol{x}$, measurement output $\boldsymbol{y}$, and disturbance $\boldsymbol{d}$ of the system are defined by

$$\boldsymbol{u} = \begin{bmatrix} \delta_F \\ \delta_R \\ M_{z,TV} \\ F_{w,x,F} \\ F_{w,y,F} \\ F_{w,x,R} \\ F_{w,y,R} \end{bmatrix} \ , \quad \boldsymbol{x} = \begin{bmatrix} v_x \\ v_y \\ \dot{\psi} \end{bmatrix} \ , \quad \boldsymbol{y} = \begin{bmatrix} v_x \\ v_y \\ \dot{\psi} \\ a_y \\ a_x \end{bmatrix} \ , \quad \boldsymbol{d} = \begin{bmatrix} F_{x,ext} \\ F_{y,ext} \\ M_{z,ext} \\ \alpha_b \end{bmatrix} \ . \tag{7.45}$$

The state equation $\dot{\boldsymbol{x}} = f\left(\boldsymbol{x}, \boldsymbol{u}, \boldsymbol{d}\right)$ is given by the following force and moment balance equations, which are analogous to those for DTM horizontal dynamics. The individual scalar equations represent the force balance in the vehicle x and y directions, as well as the moment balance about the z-axis:

$$\dot{v}_x = v_y \dot{\psi} + \frac{1}{m} \left[\sum_{j \in [F,R]} \left(F_{w,x,j} \cos \delta_j - F_{w,y,j} \sin \delta_j \right) - F_{drag} + F_{x,ext} \right] \tag{7.46}$$

$$\dot{v}_y = -v_x \dot{\psi} + \frac{1}{m} \left[\sum_{j \in [F,R]} \left(F_{w,x,j} \sin \delta_j + F_{w,y,j} \cos \delta_j \right) + mg \sin \alpha_b + F_{y,ext} \right] \tag{7.47}$$

$$\ddot{\psi} = \frac{1}{J_z} \left[\left(\sum_{j \in [F,R]} l_j \left(F_{w,x,j} \sin \delta_j + F_{w,y,j} \cos \delta_j \right) \right) + M_{z,TV} + M_{z,ext} \right] \tag{7.48}$$

where F_{drag} denotes aerodynamic drag. From the output equation $\boldsymbol{y} = h\left(\boldsymbol{x}, \boldsymbol{u}, \boldsymbol{d}\right)$, the first three outputs $\{v_x, v_y, \dot{\psi}\}$ correspond to components of $\boldsymbol{x}$, whereas the $\{a_y, a_x\}$ are

given by the following algebraic equations:

$$\begin{aligned} a_y &= \dot{v}_y + v_x\dot{\psi} - g\sin\alpha_b \\ &= \frac{1}{m}\left[\sum_{j\in[F,R]}(F_{w,x,j}\sin\delta_j + F_{w,y,j}\cos\delta_j) + mg\sin\alpha_b + F_{y,ext}\right] - g\sin\alpha_b \\ &= \frac{1}{m}\left[\sum_{j\in[F,R]}(F_{w,x,j}\sin\delta_j + F_{w,y,j}\cos\delta_j) + F_{y,ext}\right] \end{aligned} \tag{7.49}$$

$$\begin{aligned} a_x &= \dot{v}_x - v_y\dot{\psi} \\ &= \frac{1}{m}\left[\sum_{j\in[F,R]}(F_{w,x,j}\cos\delta_j - F_{w,y,j}\sin\delta_j) - F_{drag} + F_{x,ext}\right] . \end{aligned} \tag{7.50}$$

Observe that the output equation for a_y is insensitive to the disturbance α_b, due to the cancellation between its effects on the total force and the acceleration measurement in the y-direction. This property is useful for distinguishing its effects from the generic force disturbance $F_{y,ext}$.

Linearised STM for Lateral Dynamics

In order to be used in LTI or LPV methods for analysis and control design, the trigonometric functions in the STM are linearised about the undercarriage x-direction using the small angle approximations of $\sin\gamma \approx \gamma$ and $\cos\gamma \approx 1$. The resulting model is referred to as the linearised STM. In the version presented below, the relaxation length has also been neglected. Note that for the representation of lateral dynamics, we discard the inputs $\{F_{w,x,F}, F_{w,x,R}\}$ and the outputs $\{v_x, a_x\}$, and v_x is considered as a parameter instead of a state in the system equations. Furthermore, due to the small angle assumption, the absolute velocity v can be used in place of v_x because $v \approx v_x$. Another adaptation is the replacement of the state v_y by the body side slip angle β, which is related to v_y by $v_y = v_x\beta$ under the small angle assumption. This form of the STM is employed in the fault detector synthesis in Chapter 8. With these measures, the linearised STM is given by the state space equations:

$$\dot{\boldsymbol{x}} = \boldsymbol{A}\boldsymbol{x} + \boldsymbol{B}_u\boldsymbol{u} + \boldsymbol{B}_d\boldsymbol{d} \tag{7.51}$$

$$\boldsymbol{y} = \boldsymbol{C}\boldsymbol{x} + \boldsymbol{D}_u\boldsymbol{u} + \boldsymbol{D}_d\boldsymbol{d} \tag{7.52}$$

where

$$\boldsymbol{x} = \begin{bmatrix}\beta \\ \dot{\psi}\end{bmatrix} , \quad \boldsymbol{u} = \begin{bmatrix}\delta_F \\ \delta_R \\ M_{z,TV}\end{bmatrix} , \quad \boldsymbol{y} = \begin{bmatrix}\beta \\ \dot{\psi} \\ a_y\end{bmatrix} , \quad \boldsymbol{d} = \begin{bmatrix}d_{\alpha_b}\end{bmatrix} , \tag{7.53}$$

$$\boldsymbol{A} = \begin{bmatrix} -\dfrac{c_{\alpha F} + c_{\alpha R}}{mv} & \dfrac{c_{\alpha R} l_R - c_{\alpha F} l_F}{mv^2} - 1 \\ \dfrac{c_{\alpha R} l_R - c_{\alpha F} l_F}{J_z} & \dfrac{c_{\alpha R} l_R^2 + c_{\alpha F} l_F^2}{J_z v} \end{bmatrix}, \tag{7.54}$$

$$\boldsymbol{B}_u = \begin{bmatrix} \dfrac{c_{\alpha F}}{mv} & \dfrac{c_{\alpha R}}{mv} & 0 \\ \dfrac{c_{\alpha F} l_F}{J_z} & -\dfrac{c_{\alpha R} l_R}{J_z} & \dfrac{1}{J_z} \end{bmatrix}, \quad \boldsymbol{B}_d = \begin{bmatrix} \dfrac{1}{v} \\ 0 \end{bmatrix}, \tag{7.55}$$

$$\boldsymbol{C} = \begin{bmatrix} 1 & 0 \\ 0 & 1 \\ -\dfrac{c_{\alpha F} + c_{\alpha R}}{m} & \dfrac{c_{\alpha R} l_R - c_{\alpha F} l_F}{mv} \end{bmatrix}, \tag{7.56}$$

$$\boldsymbol{D}_u = \begin{bmatrix} 0 & 0 & 0 \\ 0 & 0 & 0 \\ \dfrac{c_{\alpha F}}{m} & \dfrac{c_{\alpha R}}{m} & 0 \end{bmatrix}, \quad \boldsymbol{D}_d = \begin{bmatrix} 0 \\ 0 \\ 0 \end{bmatrix}, \tag{7.57}$$

with $d_{\alpha_b} = g \sin \alpha_b$. The description corresponds to an LTI system if v is fixed, and represents and LPV system if v is a time-varying but measurable scheduling parameter.

7.2 Plant Model: Transformations between Real to Ideal Inputs and Outputs

As explained in the introduction to this chapter, the idealised input and output variables referenced by the classical vehicle dynamics plant models presented here do not in general correspond to the actuated and measured states on an X-by-Wire vehicle. On the ROboMObil, the transformations from real to ideal inputs of the vehicle dynamics plant are static and independent of the plant states, whereas the transformations from the ideal outputs to the real measured variables are static but state-dependent. These transformations are integrated into the model structure as wrapper functions of the vehicle dynamics model. The input transformations correspond to the TMD-VD, DB-VD and S-VD subsystems in the structure presented in Figure 6.10, while the output transformations reflect the location and mounting of the physical sensors. These transformations depend on the type and design of the actuators and sensors in a particular application.

7.2.1 Input Transformations

Steering (S-VD)

In a general steering actuator, the actuator output shaft position (δ_A) is mapped to the wheel orientation in the undercarriage system (δ_U) by $\delta_U = f_s(\delta_A)$, where $f_s(\cdot)$ is a nonlinear function that reflects steering and suspension kinematics. In the ROboMObil, the direct actuation of the steering axis on each wheel leads to an $f_s(\cdot)$ that is close to

unity in the fault-free case. The approximation

$$\delta_U = \delta_A \tag{7.58}$$

will be used in the later developments.

Traction Motor Drive (TMD-VD)

The transformation for the PMSM traction motor is modelled as a linear gain which relates the motor current into its torque $M_{w,TM}$ via the motor constant k_T:

$$M_{w,TM} = k_T i_m \ . \tag{7.59}$$

Disc Brake (DB-VD)

The transformation for the disc brake system relates brake pressure to the resultant braking wheel torque. The brake pressure P_b is related to clamp force F_{cl} via slave cylinder area A_b, while the clamp force produces a wheel torque via a friction coefficient μ_b and effective braking radius r_b. The result is a linear gain from P_b to $M_{w,DB}$:

$$M_{w,DB} = 2 r_b A_b \mu_b P_b \ . \tag{7.60}$$

7.2.2 Output Transformations

In most automotive applications, motion sensors measuring body accelerations and rotation rates are fixed to the body at a general location that may not match the vehicle CoG. That is, the measurements are made in the body coordinate system B. However, the idealised outputs in the DTM refer to the vehicle CoG location in the undercarriage coordinate system, and do not account for pitch or roll motion even though these DOFs are modelled. The transformation from the idealised outputs to the real sensor measurements in the body coordinate system is computed by first accounting for the position displacement, followed by the application of a rotation matrix [KN05, p.331].

Let horizontal location of a sensor σ be denoted by (x_σ, y_σ), where the vehicle CoG is considered the origin. Using the subscripts σ and cg to denote the sensor and CoG locations respectively, the velocities at the two locations are related by

$$\begin{bmatrix} v_{x,\sigma} \\ v_{y,\sigma} \\ \dot{\psi}_\sigma \end{bmatrix} = \begin{bmatrix} 1 & 0 & -y_\sigma \\ 0 & 1 & x_\sigma \\ 0 & 0 & 1 \end{bmatrix} \begin{bmatrix} v_{x,cg} \\ v_{y,cg} \\ \dot{\psi}_{cg} \end{bmatrix} \ . \tag{7.61}$$

From the above equation and its derivative, we can write the following expressions for the horizontal outputs at sensor location σ:

$$v_{x,\sigma} = v_{x,cg} - y_\sigma \dot{\psi} \tag{7.62}$$

$$\beta_\sigma = \arctan\left(\frac{v_{y,cg} + x_\sigma \dot{\psi}_{cg}}{v_{x,cg} - y_\sigma \dot{\psi}_{cg}}\right) \tag{7.63}$$

$$a_{x,\sigma} = a_{x,cg} - y_\sigma \ddot{\psi}_{cg} \tag{7.64}$$

$$a_{y,\sigma} = a_{y,cg} + x_\sigma \ddot{\psi}_{cg} \tag{7.65}$$

$$\dot{\psi}_\sigma = \dot{\psi}_{cg} \tag{7.66}$$

where $v_{y,cg} = v_{x,cg} \tan \beta_{cg}$ and $v_{y,\sigma} = v_{x,\sigma} \tan \beta_\sigma$.

The outputs at location σ can then be transformed into the body coordinate system. For the modest roll and pitch angles encountered during the normal operation of a road vehicle, this transformation is only important for the acceleration components due to the relatively high effect of gravity. The body coordinate acceleration outputs are given by

$$\begin{bmatrix} a_{x,\sigma} \\ a_{y,\sigma} \\ a_{z,\sigma} \end{bmatrix}_B = \boldsymbol{T}_{BU}^{-1} \begin{bmatrix} a_{x,\sigma} \\ a_{y,\sigma} \\ a_{z,\sigma} \end{bmatrix}_U \tag{7.67}$$

where ϕ is the roll angle and θ is the pitch angle, and

$$\boldsymbol{T}_{BU} = \begin{bmatrix} \cos\theta & \sin\theta\cos\phi & \sin\theta\cos\phi \\ 0 & \cos\phi & -\sin\phi \\ -\sin\theta & \cos\theta\sin\phi & \sin\theta\cos\phi \end{bmatrix}$$

is the rotation matrix from the body to the undercarriage coordinate system, formed by first pitching and then rolling.

This modelling is useful for replicating real sensor measurements in the validation models. Further effects, such as the dynamic effects of rolling and pitching due to the vertical displacement from the CoG to the sensor, have been neglected in this study. This is a reasonable assumption for the ROboMObil application due to its high roll stiffness, resulting in small roll and pitch displacements.

7.3 Actuator and Sensor Modelling

The response of the steering and disc brake actuator systems are governed by that of the electromechanical actuator under closed-loop servo control. In the ROboMObil application, both are controlled using the common cascaded control scheme, consisting of an innermost motor current loop, a middle motor velocity loop, and an outer loop controlling either the steering output shaft position or the brake pressure [LMG04]. Physical constraints are handled by saturation operators in the motor current, rate and outermost

loops. The demand to output response of each controlled actuator can be adequately represented by a rate-limited second order filter under the assumptions that

- the controlled system is tuned to have a pair of dominant poles,
- the controller is designed conservatively such that the motor current limits are seldom reached in normal operation,
- the controllers can adequately reject disturbances (e.g. external loads) and unmodelled dynamics such that the steady state error remains negligible,
- the demand is correctly limited to prevent unrealisable values.

On the other hand, the motor current of the traction motor drive on the ROboMObil is controlled with a PI-controller. The demand to output response is well approximated by a first-order filter.

The sensor model replicates the behaviour of the sensor system, which consists of the physical sensor, analog amplification, and digital sensor processing. In general, this processing of the measured physical state can be adequately modelled by a delay and a linear filter, parametrised depending on the specifications and behaviour of the sensor system.

7.4 Fault Modelling

The goal of this section is to model the faults which need to be diagnosed by the global vehicle level diagnosis system. This fault catalogue has already been created in Section 6.4 and is listed in Table 6.3 in the category "Vehicle Dynamics FDI". These faults are specific to X-by-Wire vehicle dynamics systems, and all of them lie in the modules of actuator output transformations (i.e. the '-VD' subsystems) and the vehicle motion sensors. The affected modules are marked in the block diagram of Figure 7.1 with lightning symbols.

The actuator faults from Table 6.3 in the category "Vehicle Dynamics FDI" can be classified into two types. The first, measurement fault, is denoted type-M and refers to an error in the sensor which is used for actuator feedback control. The second, plant faults, is denoted type-P refer to faults outside of the closed-loop. Both of them have the same steady state effect by causing a deviation between the true value of a variable and its nominal value calculated from measured signals, and only type-M faults are modelled in the later simulations. However, the distinction will be made in the upcoming fault listings.

In the mathematical expressions in the rest of this section, a symbol a denotes the true value of a parameter or variable, while a' denotes the fault-affected value. The difference $a' - a$ is denoted by Δ_a, which represents the effect of an individual physical fault mode.

There is some subtlety in how the Δ_a terms relate to an additive fault of the actuator, which is detected by many common FDI approaches including the one presented in Chapter 8. Let an actuator have the output b. Then it has a "measured" value $\hat{b}$ computed from measurements, and a true physical value $\tilde{b}$. Let $b = f(a_m, a_p)$ where a_m and

a_p denote variables affected by type-M and type-P faults respectively. When affected by faults, we can deduce that $\hat{b} = f(a'_m, a_p)$ and $\tilde{b} = f(a_m, a'_p)$. The additive fault of the actuator is given by $f_b = \tilde{b} - \hat{b}$. The following subsections derive this additive fault for each of the vehicle dynamics actuators. Although these derivations are not used further in the FDI developments, they are intended to provide insights into how the physical fault parameters contribute to the additive fault terms.

7.4.1 Electromechanical Steering

The steering system faults listed in Table 7.1 need to be detected on the vehicle dynamics FDI level:

Table 7.1: Steering (S-VD) faults

fault	**type**	**mathematical representation**
incorrect angle sensor calibration	M	$\delta'_A = \delta_A + \Delta_{\delta_A}$
damaged linkage	P	$\delta'_U = \delta_U + \Delta_{\delta_U}$
backlash outside actuator	P	same as above

All of these faults can be aggregated into an additive fault term f_{δ_U} in the steering angle transformation equation (7.58). It is composed of the individual faults as derived below:

$$\tilde{\delta}_U = \delta'_A \qquad = \delta_A + \Delta_{\delta_A} \tag{7.68a}$$

$$\hat{\delta}_U = \delta'_U \qquad = \delta_A + \Delta_{\delta_U} \tag{7.68b}$$

$$f_{\delta_U} = \tilde{\delta}_U - \hat{\delta}_U = \Delta_{\delta_A} - \Delta_{\delta_U} \ . \tag{7.68c}$$

7.4.2 Traction Motor Drive

The traction motor drive faults listed in Table 7.2 need to be detected on the vehicle dynamics FDI level. The wheel speed sensor fault is covered within the "sensor" section later.

Table 7.2: Traction motor drive (TMD-VD) faults

fault	**type**	**mathematical representation**
current sensor faults	M	$i'_m = i_m + \Delta_{i_m}$
loss of torque effectiveness	P	$k'_T = k_T + \Delta_{k_T}$
excessive friction	P	$M'_{w,TM} = M_{w,TM} + \Delta_{M_{w,TM}}$

All of these faults may be aggregated into an additive fault term $f_{M_{w,TM}}$ in the motor torque equation (7.59). It is composed of the individual faults as derived below:

$$\tilde{M}_{w,TM} = k'_T i_m + \Delta_{M_{w,TM}} = (k_T + \Delta_{k_T}) i_m + \Delta_{M_{w,TM}} \tag{7.69a}$$

$$\hat{M}_{w,TM} = k_T i'_m = k_T (i_m + \Delta_{i_m}) \tag{7.69b}$$

$$f_{M_{w,TM}} = \tilde{M}_{w,TM} - \hat{M}_{w,TM} = \Delta_{k_T} i_m - k_T \Delta_{i_m} + \Delta_{M_{w,TM}} \ . \tag{7.69c}$$

7.4.3 Electrohydraulic Disc Brake

The disc brake system faults listed in Table 7.3 need to be detected on the vehicle dynamics FDI level:

Table 7.3: Disc brake (DB-VD) faults

fault	**type**	**mathematical representation**
pressure sensor fault	M	$P'_b = P_b + \Delta_{P_b}$
loss of friction torque effectiveness	P	$\mu'_b = \mu_b + \Delta_{\mu_b}$
undesired brake torque	P	$M'_{w,DB} = M_{w,DB} + \Delta_{M_{w,DB}}$

All of these faults can be aggregated into an additive fault term $f_{M_{w,DB}}$ in the brake torque equation (7.60). It is composed of the individual faults as shown below:

$$\tilde{M}_{w,DB} = 2 r_b A_b \mu'_b P_b + \Delta_{M_{w,DB}} = 2 r_b A_b (\mu_b + \Delta_{\mu_b}) P_b + \Delta_{M_{w,DB}} \tag{7.70a}$$

$$\hat{M}_{w,DB} = 2 r_b A_b \mu_b P'_b = 2 r_b A_b \mu_b (P_b + \Delta_{P_b}) \tag{7.70b}$$

$$f_{M_{w,DB}} = \tilde{M}_{w,DB} - \hat{M}_{w,DB} = 2 r_b A_b (\Delta_{\mu_b} P_b - \mu_b \Delta_{P_b}) + \Delta_{M_{w,DB}} \ . \tag{7.70c}$$

7.4.4 Vehicle Body and Chassis Sensor Faults

For each sensor on the vehicle body and chassis, the fault manifestations in the forms of *scaling*, *bias*, *drift* and *hard fault* should be addressed. [Mar12] models these faults with the general model:

$$y' = \sigma_s (1 + \epsilon_s) y + y_f \tag{7.71}$$

where the parameters are set according to the fault type as shown in Table 7.4.

Table 7.4: Model parameters for sensor faults

	Bias	**Drift**	**Scaling**	**Hard fault**	**No fault**
ϵ_s	0	0	$\neq 0$	0	0
σ_s	1	1	1	0	1
y_f	$\neq 0$ (constant)	$\neq 0$ (time-varying)	0	constant	0

All of these can be represented with a time-varying, sensor state dependent additive fault term f_y, where

$$f_y = y' - y = (\sigma_s + \sigma_s \epsilon_s - 1)y + y_f \ . \tag{7.72}$$

7.5 Simulation Model

The model-based FDI functions *STMFDI* and *NKMFDI* developed in Chapters 8 and 9 respectively are virtually tested and validated using Simulink. The simulation environment for *NKMFDI* validation is more reliant on experimentally recorded signals in order to more realistically replicate the multiple motion modes of the ROboMObil (see Section 6.1.2), and this set up will be described in Chapter 9 in more detail. Here we briefly describe the simulation for validating the *STMFDI*. The structure of the simulation model is analogous to that of the system block diagram in Figure 7.1, consisting of the main components of:

- vehicle dynamics model,
- actuator and sensor models incorporating fault simulations,
- longitudinal and lateral dynamics controllers,
- motion reference generation, and
- the FDI module being evaluated.

The vehicle dynamics is modelled by the nonlinear DTM described in Section 7.1.1. The vehicle dynamics controllers translate the prescribed motion demands into actuator demands and is divided into longitudinal and lateral dynamics components. The longitudinal closed-loop controller tracks the longitudinal velocity demand v_x^* by adjusting the total wheel torques. Together with a superimposed torque vectoring demand from the lateral dynamics controller, this determines the summed wheel torque demands M_{wL}^* and M_{wR}^* for the left wheels and right wheels respectively. These are then split equally between the front and rear wheels on the respective side. The lateral dynamics feedback controller is taken from the ROboMObil control software, which has the layout illustrated in Figure 6.9 and sets the steering angle demands δ_F^*, δ_R^* as well as the torque vectoring demand $M_{z,TV}^*$ to control the body side slip angle β and yaw rate $\dot{\psi}$. The closed-loop controlled actuators are adequately modelled by unitary gain low-order dynamics with saturation and slew-rate limits. Sensor models are realised as simple linear filters.

We now discuss the modelling of sensor and actuator faults. Sensor faults are simulated in a straightforward manner by modifying their corresponding measurement outputs. The actuator faults of interest are manifested as an offset of the actuator output measurements from their true values, which affects the actuator feedback control. Such faults are designated as Type-M in Section 7.4. Figure 7.8-left illustrates the effect for the case of a negative unit feedback control loop. Since this simulation uses black-box models of the controlled actuators with simplified closed-loop dynamics, the effect on the true physical output is simulated by adding the offset to the actuator demand (the input of the

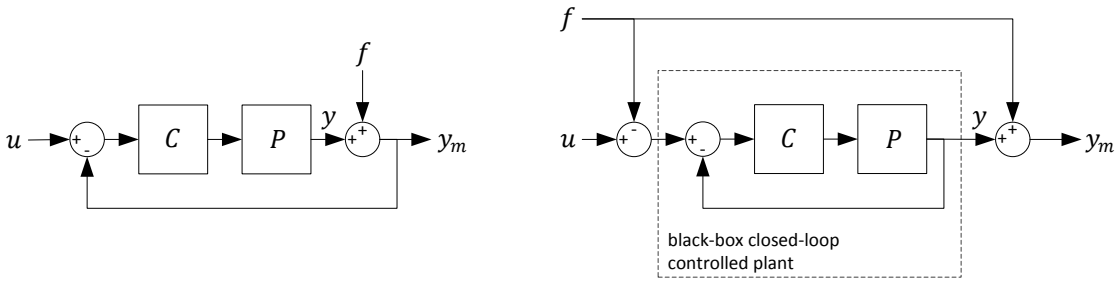

Figure 7.8: Left: Sensor fault injection into an actuator control loop. C and P denote the controller and plant respectively. Right: equivalent block diagram using the black-box controlled (fault-free) actuator models.

black-box). The erroneous measured value is recovered by subtracting this offset from the model output, as shown in Figure 7.8-right. The two block diagrams can be shown to be equivalent using basic block diagram manipulation. Another category of actuator faults to be detected are deviations outside of the feedback loop, which are designated as Type-P in Section 7.4. Despite having different transient behaviours on the physical and measurement outputs that are different to the set up described above, both fault categories possess identical steady state behaviours and hence Type-P is not additionally modelled.

7.6 Parameter Identification for the Single Track Model

As with any model-based method, achieving good performance from the fault diagnosis functions requires the design model to be an accurate representation of the real plant. The NKM contains only horizontal geometric parameters which can easily be gathered from vehicle construction data. The methods with which the parameters in the control-oriented STM can be determined for a real vehicle are now discussed. The parameters can be broadly divided into three groups:

- vehicle geometry (l_f, l_r) - the wheel base $l = l_f + l_r$ can be readily measured or obtained from construction data, while l_f or l_r defines the longitudinal position of the centre of mass, which can be measured using scales or determined from construction data.
- inertial parameters (m, J_z) - the total vehicle mass m can be measured using scales. J_z may be estimated from construction data or measured using special test rigs (e.g. [GMP11; Uys06]). If this is not feasible, a reasonable approximation of J_z for conventional passenger vehicles is $J_z \approx m\,(l/2)^2$ [Hey99].
- tyre force related parameters $(c_{\alpha F}, c_{\alpha R}, \sigma_\alpha)$ - the front and rear cornering stiffnesses $c_{\alpha F}, c_{\alpha R}$ are composite parameters arising from a combination of multiple factors, including tyre characteristics, tyre-road contact condition, chassis and suspension elasticity, and suspension and steering geometry. For a specific tyre-road contact condition, these parameters may be determined empirically from experimental data and this is the subject of the current section. The tyre relaxation length σ_α is a tyre dependent property that may be identified from tyre testing or driving experiments.

Cornering stiffness may be determined from testing procedures designed to decouple the effects of irrelevant unknown variables and isolate the parameter of interest. Many procedures employ a steady state cornering manoeuvre, in which the vehicle is driven on a circular path of constant radius with constant or slowly varying velocity. This allows the consideration of static relationships in which $\dot{\beta} = \ddot{\psi} = 0$. [WI09] presents a least-squares procedure to identify the front and rear cornering stiffness parameters together with the centre of mass position, where the slowly varying velocity v_x, δ_F, δ_R, β, $\dot{\psi}$ and a_y are available, and the parameters m and l are assumed to be known. [Tad12] assumes knowledge of vehicle mass and requires a quasi-steady state cornering experiment where the velocity is increased slowly. The velocity is determined at which $\beta = 0$, which then produces a simple expression for $c_{\alpha F}$ and subsequently $c_{\alpha R}$.

In applications where online identification is necessary, or where steady state data is unavailable, the identification procedure must cope with non-steady-state real world driving or experimental data. Online identification is attractive because the models in model-based control, estimation and fault diagnosis approaches can be updated with the latest parameter estimates online to improve the results. The recursive least squares method (RLS) presented in [LS09] and the adaptive full-order observer (AFO) [Kaw10] take the dynamic nature of the STM into consideration. Both require computation of the derivative of the yaw rate $\dot{\psi}$, which can be accurately measured with low-noise using a gyroscope. [Kaw10] uses the net yaw moment ($M_{z,total} = J_z\ddot{\psi}$) exclusively as the output variable $\boldsymbol{y}$ in the least squares set-up, while [LS09] sets the net front and rear lateral tyre forces (calculated from vehicle body accelerations) as the output variable $\boldsymbol{y}$. Additionally, [LS09] estimates the vertical load on the front and rear axles and identifies the load-dependent component of the cornering stiffness parameters. In this application, we forego running the identification online, and instead identify the cornering stiffness of the ROboMObil offline using non-steady-state experimental data.

7.6.1 Least Squares Identification of Cornering Stiffness

The identification of the cornering stiffness parameters is performed using the offline non-recursive least squares method. This method solves the following general problem [Lju99]:

$$\hat{\boldsymbol{\theta}}^* = \arg\min_{\boldsymbol{\theta}} \left(\boldsymbol{Y} - \boldsymbol{\Phi}\boldsymbol{\theta}\right)^T \boldsymbol{\Lambda}^{-1} \left(\boldsymbol{Y} - \boldsymbol{\Phi}\boldsymbol{\theta}\right) \ , \tag{7.73}$$

where $\boldsymbol{\Lambda}$ is a weighting matrix, $\boldsymbol{\theta}$ is the parameter vector to be estimated, $\hat{\boldsymbol{\theta}}^*$ its optimal estimate, and the process measurements are contained in the matrices $\boldsymbol{Y}$ and $\boldsymbol{\Phi}$ such that

$$\boldsymbol{Y} = \boldsymbol{\Phi}\boldsymbol{\theta} \ . \tag{7.74}$$

The output series $\boldsymbol{Y}$ and input series $\boldsymbol{\Phi}$ are formed by stacking measurement data $\boldsymbol{y}(k)$ and $\boldsymbol{\varphi}^T(k)$ over the time steps $k = 1, \ldots, N$ as follows:

$$\boldsymbol{Y} = \begin{bmatrix} \boldsymbol{y}(1) \\ \boldsymbol{y}(2) \\ \vdots \\ \boldsymbol{y}(N) \end{bmatrix}, \quad \boldsymbol{\Phi} = \begin{bmatrix} \boldsymbol{\varphi}^T(1) \\ \boldsymbol{\varphi}^T(2) \\ \vdots \\ \boldsymbol{\varphi}^T(N) \end{bmatrix}, \tag{7.75}$$

where the variables at the k-th time step are related by

$$\boldsymbol{y}(k) = \boldsymbol{\varphi}^T(k)\boldsymbol{\theta} \ . \tag{7.76}$$

In this instance, we aim to estimate $\boldsymbol{\theta} = [c_{\alpha F} \ c_{\alpha R}]^T$. We now proceed to deriving suitable $\boldsymbol{y}(k)$ and $\boldsymbol{\varphi}(k)$ from the STM equations. The model equations from Section 7.1.2 are first rewritten using only measured values, leaving $\boldsymbol{\theta}$ as the only unknowns. To begin with, the tyre slip angles can be written as

$$\alpha_F = \delta_F - \arctan\left(\frac{v_y + l_f\dot{\psi}}{v_x}\right) \tag{7.77}$$

$$\alpha_R = \delta_R - \arctan\left(\frac{v_y - l_r\dot{\psi}}{v_x}\right) \ . \tag{7.78}$$

Note that to account for the effects of relaxation length, the dynamic lateral tyre forces $F_{w,y,F}, F_{w,y,R}$ are given by filtering the steady state tyre force by a velocity-dependent first order filter corresponding to (7.38):

$$F_{w,y,j} + \frac{\sigma_\alpha}{v_x}\dot{F}_{w,y,j} = F_{w,y,j}^{stat} \tag{7.79}$$

$$= c_{\alpha,j}\alpha_j \tag{7.80}$$

where $j \in [F, R]$ denote the front and rear axles. Due to the linear slip-to-force relationship of the linear tyre model, the same effect can be achieved by filtering the tyre slip angles instead:

$$\alpha_j^* + \frac{\sigma_\alpha}{v_x}\dot{\alpha}_j^* = \alpha_j \tag{7.81}$$

where $\alpha_j^* = {}^{F_{w,y,j}}/_{c_{\alpha,j}}$ is defined as the dynamic tyre slip angle. For small steering angles δ_j, and when the road banking is zero, the force and moment balance equations of the STM (7.49) and (7.48) become:

$$ma_y = \alpha_F^* c_{\alpha F} + \alpha_R^* c_{\alpha R} \tag{7.82}$$

$$J_z\ddot{\psi} = \alpha_F^* l_f c_{\alpha F} - \alpha_R^* l_r c_{\alpha R} + M_{z,TV} \ . \tag{7.83}$$

Observe that a_y is a measured value, $M_{z,TV}$ is a known actuation input, and $\ddot{\psi}$ can be computed by differentiating the $\dot{\psi}$ measurement. Assuming that $\{m, J_z, l_f, l_r\}$ are

known parameters, (7.82) and (7.83) only contain $c_{\alpha F}$ and $c_{\alpha R}$ as unknowns, as desired. Rearranging the equations gives the following equation which is linear in the parameters $\boldsymbol{\theta}$ and in the necessary form of (7.76):

$$\underbrace{\begin{bmatrix} ma_y \\ J_z\ddot{\psi} - M_{z,TV} \end{bmatrix}}_{\boldsymbol{y}} = \underbrace{\begin{bmatrix} \alpha_F^* & \alpha_R^* \\ \alpha_F^* l_f & -\alpha_R^* l_r \end{bmatrix}}_{\boldsymbol{\varphi}^T} \underbrace{\begin{bmatrix} c_{\alpha F} \\ c_{\alpha R} \end{bmatrix}}_{\boldsymbol{\theta}} . \tag{7.84}$$

Once an appropriate $\boldsymbol{\Lambda}$ is chosen, the least squares problem is ready to be solved to give $\hat{\boldsymbol{\theta}}^*$. In this instance, the two components of $\boldsymbol{y}$ and all time steps are weighted equally, giving $\boldsymbol{\Lambda} = \boldsymbol{I}$. Efficient numerical computation algorithms are readily available to solve large least squares problems. Readers are referred to [Lju99] for details.

We now revisit the issue of determining the relaxation length σ_α. In this instance, it is estimated by a scalar optimisation over (7.73) to find the value $\hat{\sigma}_\alpha^*$ which minimises the optimal objective function. The optimisation formulation is shown below, with the dependency of $\boldsymbol{\Phi}$ on σ_α highlighted by expressing it as $\boldsymbol{\Phi}(\sigma_\alpha)$:

$$\hat{\sigma}_\alpha^* = \arg\min_{\sigma_\alpha} \left(\min_{\boldsymbol{\theta}} \left(\boldsymbol{Y} - \boldsymbol{\Phi}(\sigma_\alpha)\boldsymbol{\theta} \right)^T \boldsymbol{\Lambda}^{-1} \left(\boldsymbol{Y} - \boldsymbol{\Phi}(\sigma_\alpha)\boldsymbol{\theta} \right)^T \right) . \tag{7.85}$$

Since the presented identification procedure is based on the STM with small angle assumptions, it is only valid under moderate accelerations, at small angles of δ_F, δ_R and β, and at non-zero velocities. Therefore, only data samples at which the states of the vehicle satisfy the below list of criteria are selected for identification. Note that the chosen samples need not be in a contiguous block. The criteria are:

- $v_x > \underline{v}_x \approx 2$ m/s,
- $|a_y| < 4$ m/s^2,
- $|\delta_F| < \bar{\phi}, \quad |\delta_R| < \bar{\phi}, \quad |\beta| < \bar{\phi}$, where $\bar{\phi} \approx 10°$ denotes the upper angle limit,
- $|\rho| \approx |\dot{\psi}/v_x| < 0.15$ [1/m], where ρ denotes the steady-state path curvature.

The choice of data sets for the identification is free and not restricted only to quasi-steady-state manoeuvres. Nonetheless, low frequency stimulation is preferred to mask unmodelled transient effects which tend to have faster time constants, such as sensor filter dynamics, body roll dynamics, and elastokinematic effects.

The parameter identification is applied to data from a 40 second test drive sequence (see Figure 7.9) on a dry test track. The test drive contains phases including a double lane change, moderate braking and acceleration, quasi-steady state cornering, and oscillating steering inputs. The following cornering stiffness and relaxation length values are obtained:

$$\begin{aligned} c_{\alpha F} &= 71574 \text{ N/rad} \\ c_{\alpha R} &= 78812 \text{ N/rad} \\ \sigma_\alpha &= 0.8 \text{ m} \end{aligned}$$

We observe that these are plausible values that lie within the typical range of cornering stiffnesses of $20000 - 120000$ N/rad reported in literature [WI09]. The two components of the error vector $e_y = (\boldsymbol{y} - \boldsymbol{\varphi}^T \boldsymbol{\vartheta})$ are shown in the top plot of Figure 7.10 to demonstrate the fit of the identified parameters. The vector components of $\boldsymbol{y}$ are also plotted against those of $\boldsymbol{\varphi}^T \boldsymbol{\vartheta}$ in the second and third plots to illustrate the error sizes relative to the signal sizes.

7.6.2 Parameter Listing

The parameter relevant for the linearised STM of the ROboMObil, obtained as described by measurement, design data or identification, are listed in Table 7.5. The relaxation length σ_α is only used in the nonlinear simulation model and is therefore not listed here. On the other hand, s_l, s_r and r_w are used the NKM and are therefore included in the list.

Table 7.5: Key parameters of the ROboMObil models

Parameter	**Value**	**Unit**
$s_l,\ s_r$	0.7	m
l_f	1.288	m
l_r	1.112	m
m	1175	kg
J_z	1692	kgm^2
r_w	0.274	m
$c_{\alpha F}$	71574	N/rad
$c_{\alpha R}$	78812	N/rad

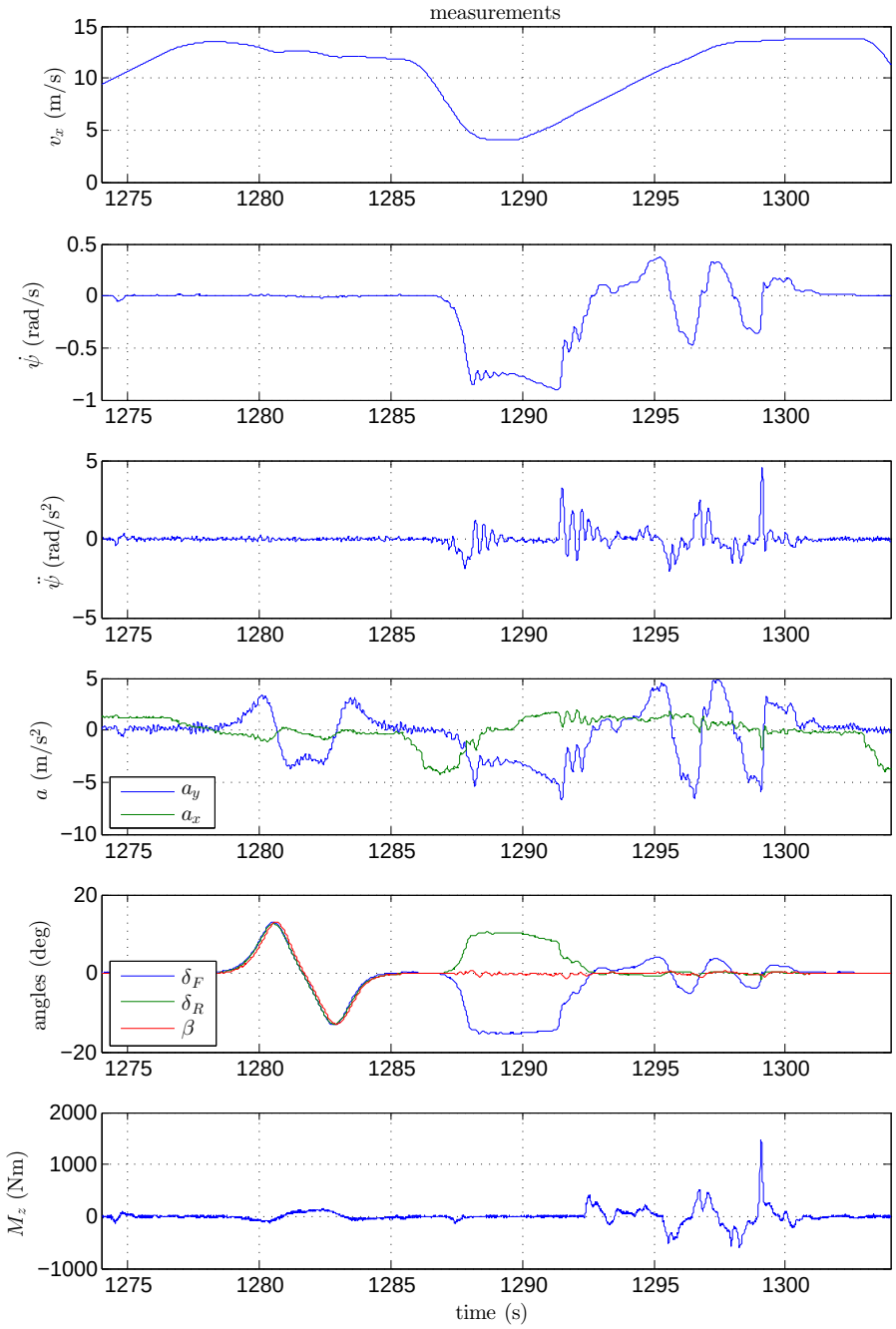

Figure 7.9: Experimental test drive data used for the cornering stiffness estimation

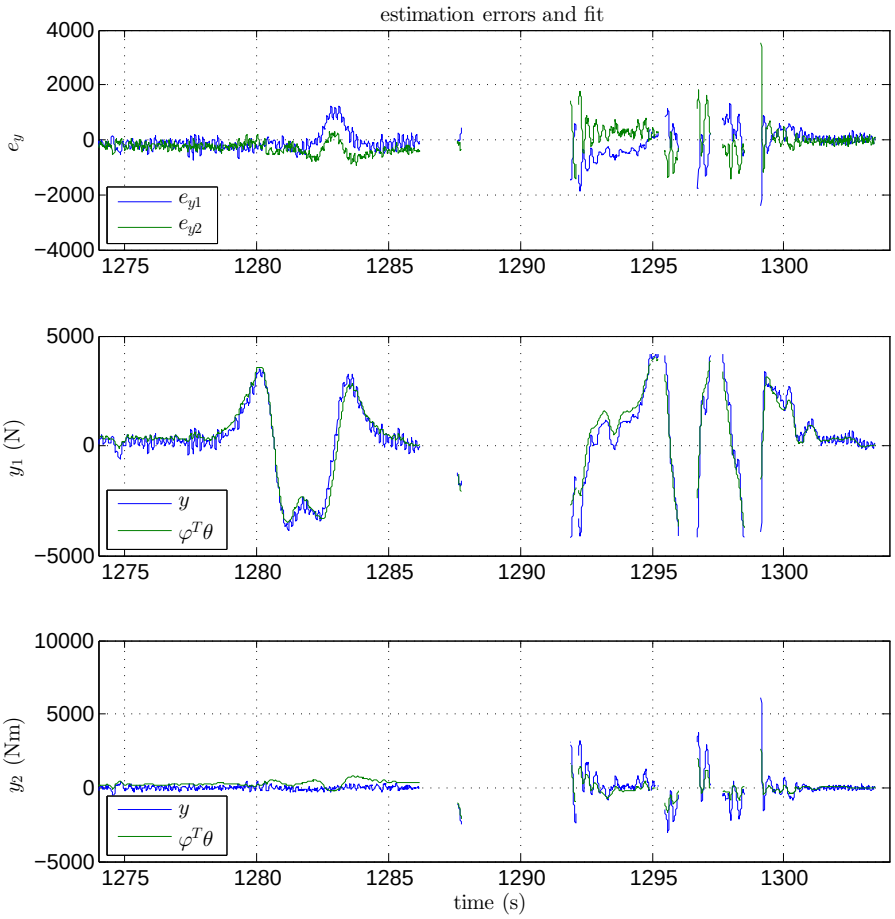

Figure 7.10: Top: identification errors, given as the components of $e_y = \boldsymbol{y} - \boldsymbol{\varphi}^T\boldsymbol{\vartheta}$. Middle and bottom: comparisons of the first and second components of $\boldsymbol{y}$ and $\boldsymbol{\varphi}^T\boldsymbol{\theta}$ respectively. Gaps in the plot represent the samples that are not used in the LS identification due to the violation of STM validity conditions.

7.7 Symbols Used

The symbols used in this chapter that are relevant to vehicle dynamics are listed in Tables 7.6 and 7.7 for easy reference in the next chapters.

Table 7.6: Table of symbols used in this chapter

Symbol	Meaning
$a,\ a'$	nominal and fault-affected values of variable a
f_a	additive fault of the variable a
a_x, a_y	body acceleration in the x and y directions at CoG
$c_{a,f}, c_{a,r}$	anti-roll bar stiffness at the front and rear axles
$c_{s,i}, k_{d,i}$	wheel suspension stiffness and damping for wheel i
C_a	aerodynamic drag constant
$c_{\alpha,i}$	cornering stiffness at the i-th wheel
$c_{\alpha F}, c_{\alpha R}$	combined cornering stiffness on the front and rear axles
$F_{max,i}$	maximum horizontal tyre force magnitude of the i-th wheel
$F_{x,i}, F_{y,i}$	tyre force at the i-th wheel in the x_U, y_U directions
$\boldsymbol{F}_{xy}$	vector containing $F_{x,i}, F_{y,i}$ for all wheels
$F_{x,ext}, F_{y,ext}, F_{z,ext}$	external forces at CoG in x, y, z directions of U coordinate system
$F_{w,x,i}, F_{w,y,i}$	tyre forces in x_{W_i}, y_{W_i} directions (also referred to as tangential and lateral) of the i-th wheel
$F_{w,y,i}^{stat}$	steady state lateral tyre force
$F_{z,i}, F_{z,0,i}, \Delta F_{z,i}$	wheel load (actual, resting, deviation from resting) at the i-th wheel
g	acceleration due to gravity
h	height of the body CoG over ground
l_i, s_i	x_U and y_U coordinates of the position of the i-th wheel
l_f, l_r	positive distances from CoG to front and rear wheels
l	wheelbase
i_m	traction motor current
J_x, J_y, J_z	body rotational inertias about the x, y, z directions
J_w	rotational inertia of a wheel about its rotating axis
m	vehicle mass
$M_{x,ext}, M_{y,ext}, M_{z,ext}$	external moment at CoG in x, y, z directions of U coordinate system
$M_{w,i}$	total wheel moment of the i-th wheel
M_{TM}, M_{DB}	wheel moments from traction motor and disc brake
$M_{z,TV}$	yaw moment through torque vectoring
P_b	brake pressure
r_w	effective wheel radius
s_l, s_r	positive distances from CoG to the left and right wheels
$\boldsymbol{v}, v, v_x, v_y$	body velocity vector at CoG, its magnitude, x, y components
$\boldsymbol{v}_{w,i}$	velocity of the body at the centre of the i-th wheel
$v_{w,x,i}, v_{w,y,i}$	x and y components of $\boldsymbol{v}_{w,i}$
$v_{x,\sigma}, v_{y,\sigma}, \dot{\psi}_\sigma$	body x, y velocities and yaw rate at sensor location σ

Table 7.7: Table of symbols used in this chapter (continued)

Symbol	**Meaning**
$\alpha_i, \alpha_F, \alpha_R$	wheel slip angle at the i-th wheel, front axle and rear axle
α_g, α_b	road grade and banking angles
β	body side-slip angle at CoG
δ_i	steering angle of the i-th wheel
δ_U, δ_A	steering angles in undercarriage and actuator coordinates
$\Delta z, \Delta z_i$	body vertical displacement from rest at CoG and i-th wheel
$\dot{\psi}$	body yaw rate
ω_i	rotational velocity of the i-th wheel
σ_α	tyre relaxation length
θ, ϕ	body pitch and roll angles

Chapter 8

Robust FDI using the Linearised Single Track Model

When a road vehicle is in cruising operation, faults in actuators and sensors of the lateral dynamics control system can be diagnosed using detectors based on STM. Figure 8.1 provides a schematic reminder of the parameters that define this cruising region in which the STM is valid. Based on this model, this chapter presents a design of the fault detection and isolation (FDI) system along the structure of Figure 8.2, comprising of a bank of residual generators and evaluators, as well as a pattern evaluation module. The presented design approach uses the tools developed in Chapters 4 and 5 for robust LPV residual generator design and residual evaluation respectively, and is applicable for diverse X-by-Wire vehicle architectures. It is presented here for the specific case of the ROboMObil, which is particularly challenging due to its high number of actuators and sensors.

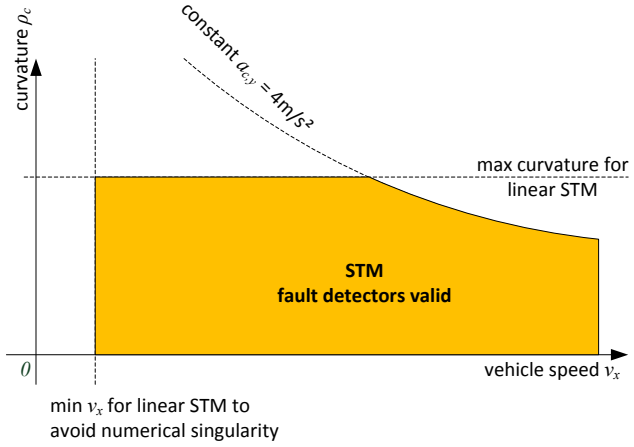

Figure 8.1: Validity regions of FDI based on the STM (based on Figure 6.19)

This chapter begins with a definition of the FDI problem, and then introduces adaptations to the STM presented in Chapter 7 to bring it into the required form for uncertain polytopic LPV synthesis. Sections 8.4 and 8.5 trace the application of the residual generator and evaluator design procedure to this model for one example residual. Subsequently

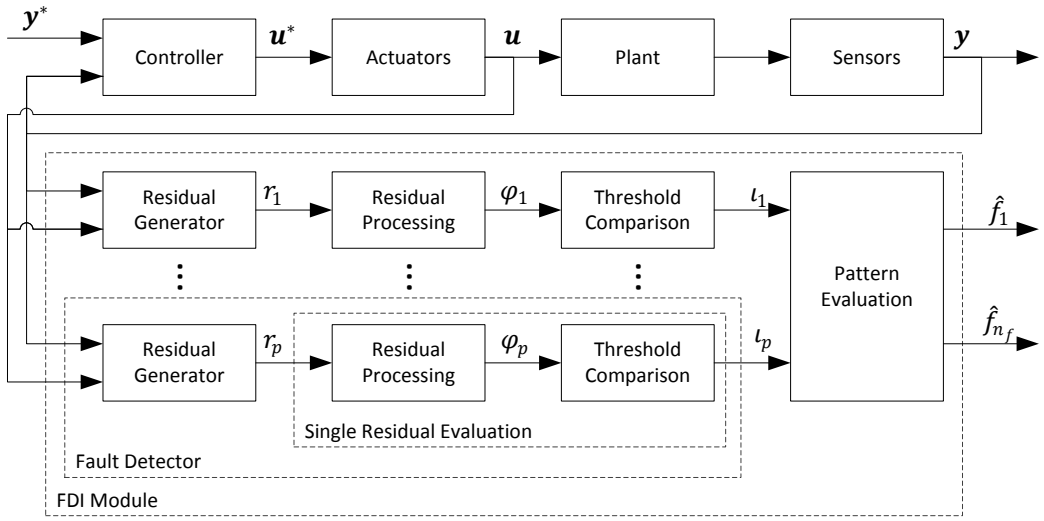

Figure 8.2: Residual-based FDI architecture used in the *STMFDI*

a suitable residual structure is designed for fault isolation, revealing some limits on the achievable degree of isolation using the presented procedure. After that, the behaviour of the resulting FDI functions is examined using simulations and experimental data, before the chapter closes with a discussion on the outcomes of the development. The content of this chapter extends the application sections of the publications [Ho16; Ho17].

8.1 Problem Definition and Assumptions

Besides being dependent on the measurable longitudinal velocity, the lateral dynamics of a road vehicle is also affected by a number of uncertain influences in its normal operation. Many of these manifest themselves as parameter uncertainties and unknown disturbances to the model. This work accounts for two significant and common effects, namely the uncertain cornering stiffness of the tyres and the unknown road banking disturbance. When these factors are included, the resulting STM is an uncertain LPV system, for which residual generators can be designed using the approach from Chapter 4.

This development handles situations when the ROboMObil is driving on predominantly flat and even terrain, reflecting the conditions on most test tracks on which driving experiments are conducted. This allows the road banking angle to be bounded to a low magnitude. On the other hand, the disturbances through lateral external force $F_{y,ext}$ and external yaw moment $M_{z,ext}$ are assumed to be negligible. Although these can arise through physical effects such as cross-winds with an offset centre of pressure, their occurrence with significant intensity during the operation of the ROboMObil is considered sufficiently seldom, and therefore they are neglected in this FDI design. In applications where larger disturbances can occur, measures such as parameter estimation can be applied to approximate their values under some assumptions. This is however beyond the scope of this work.

As already defined from the analysis in Section 6.4 and modelled in Section 7.4, the faults to be detected at the vehicle dynamics FDI level can be represented as additive faults at actuator and sensor components. Out of these faults, the STM lateral dynamics model possesses the necessary input and output structure to detect the following:

- Steering angle faults of the front and rear axles (f_{δ_F}, f_{δ_R})
- Torque vectoring fault (f_{tv}) - unwanted yaw moment due to asymmetrical (left/right) faults in the traction motor drives or disc brakes
- Body sensors faults
  - in the optical sensor measurement β (f_β),
  - in the IMU raw sensor measurements $\dot{\psi}$ and a_y ($f_{\dot{\psi}}$, f_{a_y}).

Note that f_β is analogous to the v_y sensor fault treated in Chapter 9, since $\beta \approx \frac{v_y}{v_x}$ when β is small, which holds during cruising operation.

In the next section, inputs representing the above faults will be added to the state space equations of the linearised STM presented in Section 7.1.2. Bounds on these fault variables will then be proposed and justified. Symmetrical wheel torque deviations, as well as faults in the a_x and v_x sensors only affect longitudinal motion and are therefore undetectable through fault detectors based on the linearised STM, which describes lateral dynamics only. Wheel speeds do not explicitly appear in the STM and faults in those sensors must be diagnosed by other means, such as the kinematic model-based FDI in Chapter 9.

The developments assume that at most one faults can be present at any time. As mentioned in the fault diagnosis overview in Chapter 2, the single fault assumption is common in fault-tolerant control literature and is reasonable in many automotive applications due to the low probability of a second fault occurring before the first fault is diagnosed and handled. The assumption is signifcant as it underlies the residual generation and structured residual methods presented in Chapters 4 and 5.

Finally, the range of vehicle velocities to be handled is restricted to $v = [\underline{v}, \bar{v}] = [3, 20]$m/s. This range corresponds with the usual operating velocities of the ROboMObil during experimental test drives, and would have to be adapted for other vehicles and applications. A wider range of this scheduling parameter would likely lead to a more conservative design, especially when using the polytopic LPV synthesis approach chosen in this work. The reason for this will become clear in Section 8.3.

8.2 Model Preparation

The synthesis model for residual generator design uses the control-oriented linearised STM presented in Section 7.1.2 as its starting point, with the velocity at the body CoG, v, treated as a scheduling parameter. This model takes the form of an LPV system. The six additive faults to be considered are aggregated into the physical fault vector $\tilde{\boldsymbol{f}}_p =$

$\begin{bmatrix} f_{\delta_F} & f_{\delta_R} & f_{tv} & f_\beta & f_{\dot\psi} & f_{a_y} \end{bmatrix}^T$. f_{δ_F} and f_{δ_R} are defined in (7.68). The torque vectoring fault f_{tv} is the erroneous yaw moment due to the traction motor fault $f_{M_{w,TM,i}}$ and disc brake torque fault $f_{M_{w,DB,i}}$ at each wheel with index i, themselves defined in (7.69) and (7.70) respectively, by

$$f_{tv} = \sum_{i=1}^{4} -\frac{s_i}{r_w}(f_{M_{w,TM,i}} + f_{M_{w,DB,i}}) \ . \tag{8.1}$$

Since the steering angle and torque vectoring faults occur on the input of the STM plant, they are characterised as actuator faults. The remaining faults, namely $\{f_\beta,\ f_{\dot\psi},\ f_{a_y}\}$ are labelled as sensor faults because they directly affect plant output measurements, with each entering only additively into the output equation for the corresponding element of $\boldsymbol{y}$. The road bank angle α_b disturbance is already modelled in the linearised STM in Section 7.1.2.

The residual generator synthesis procedure for polytopic LPV systems places constraints on the permitted dependency of the state space matrices on the scheduling parameters $\boldsymbol{\rho}$. The system matrices must be affine in $\boldsymbol{\rho}$, and furthermore all matrices of the measurement equation must be independent of $\boldsymbol{\rho}$. Inspection of (7.56)-(7.57) reveals that $\boldsymbol{C}$ is dependent on the parameter v, while $\boldsymbol{D}_u$ and $\boldsymbol{D}_d$ are independent. This incompatibility is alleviated by defining a new state ζ and fault input f_ζ via the state and input transformations

$$\zeta = \frac{\dot\psi}{v} \ , \qquad f_\zeta = \frac{f_{\dot\psi}}{v} \ .$$

A modified fault vector $\boldsymbol{f}_p$ is formed from $\tilde{\boldsymbol{f}}_p$ by replacing $f_{\dot\psi}$ with f_ζ. Also, ζ replaces $\dot\psi$ in the state vector $\boldsymbol{x}$ defined in (7.53). The modified plant equations resulting from this and the above fault representations can be written as

$$\dot{\boldsymbol{x}} = \boldsymbol{A}\boldsymbol{x} + \boldsymbol{B}_u\boldsymbol{u} + \boldsymbol{B}_d\boldsymbol{d}_p + \boldsymbol{B}_f\boldsymbol{f}_p \tag{8.2}$$

$$\boldsymbol{y} = \boldsymbol{C}\boldsymbol{x} + \boldsymbol{D}_u\boldsymbol{u} + \boldsymbol{D}_d\boldsymbol{d}_p + \boldsymbol{D}_f\boldsymbol{f}_p \tag{8.3}$$

where

$$\boldsymbol{x} = \begin{bmatrix} \beta \\ \zeta \end{bmatrix}, \ \boldsymbol{u} = \begin{bmatrix} \delta_F \\ \delta_R \\ M_{z,TV} \end{bmatrix}, \ \boldsymbol{y} = \begin{bmatrix} \beta \\ \zeta \\ a_y \end{bmatrix}, \ \boldsymbol{d}_p = \begin{bmatrix} d_{\alpha_b} \end{bmatrix}, \ \boldsymbol{f}_p = \begin{bmatrix} f_{\delta_F} \\ f_{\delta_R} \\ f_{tv} \\ f_\beta \\ f_\zeta \\ f_{a_y} \end{bmatrix}$$

$$\boldsymbol{A} = \begin{bmatrix} -\dfrac{c_{\alpha F} + c_{\alpha R}}{mv} & \dfrac{c_{\alpha R}l_R - c_{\alpha F}l_F}{mv} - v \\ \dfrac{c_{\alpha R}l_R - c_{\alpha F}l_F}{J_z v} & \dfrac{c_{\alpha R}l_R^2 - c_{\alpha F}l_F^2}{J_z v} \end{bmatrix}$$

$$
\boldsymbol{B}_u = \begin{bmatrix} \frac{c_{\alpha F}}{mv} & \frac{c_{\alpha R}}{mv} & 0 \\ \frac{c_{\alpha F} l_F}{J_z v} & -\frac{c_{\alpha R} l_R}{J_z v} & -\frac{2w}{J_z r_w v} \end{bmatrix}
$$

$$
\boldsymbol{C} = \begin{bmatrix} 1 & 0 \\ 0 & 1 \\ -\frac{c_{\alpha F} + c_{\alpha R}}{m} & \frac{c_{\alpha R} l_R - c_{\alpha F} l_F}{m} \end{bmatrix}
$$

$$
\boldsymbol{D}_u = \begin{bmatrix} 0 & 0 & 0 \\ 0 & 0 & 0 \\ \frac{c_{\alpha F}}{m} & \frac{c_{\alpha R}}{m} & 0 \end{bmatrix}, \quad \boldsymbol{B}_d = \begin{bmatrix} \frac{1}{v} \\ 0 \end{bmatrix}, \quad \boldsymbol{D}_d = \begin{bmatrix} 0 \\ 0 \\ 0 \end{bmatrix}
$$

$$
\boldsymbol{B}_f = \begin{bmatrix} \frac{c_{\alpha F}}{mv} & \frac{c_{\alpha R}}{mv} & 0 & 0 & 0 & 0 \\ \frac{c_{\alpha F} l_F}{J_z v} & -\frac{c_{\alpha R} l_R}{J_z v} & \frac{1}{J_z v} & 0 & 0 & 0 \end{bmatrix}
$$

$$
\boldsymbol{D}_f = \begin{bmatrix} 0 & 0 & 0 & 1 & 0 & 0 \\ 0 & 0 & 0 & 0 & 1 & 0 \\ \frac{c_{\alpha F}}{m} & \frac{c_{\alpha R}}{m} & 0 & 0 & 0 & 1 \end{bmatrix}.
$$

Since the terms v and $1/v$ both appear in the above state space matrices, they are not affine in the scheduling parameter v. To allow the application of the design methods, the parameter vector $\boldsymbol{\rho} = \left[\frac{1}{v} \; v\right]^T = [\rho_1 \; \rho_2]^T$ is defined. The dependency between its elements results in some conservatism, and this issue will be treated in the next section.

We now proceed to specifying those assumptions on the input signals and uncertain parameters that are required for residual generator design. Since the residual generator design approach employs approximate decoupling, when a fault is to be isolated in a residual, it is treated as a disturbance whose norm is upper-bounded. Although in general very large fault sizes are possible, it is reasonable to set the maximum fault size to the smallest fault that is not detectable by other diagnosis modules, such as those operating on subsystem levels or those using signal-based methods (e.g. range checks). Furthermore, the minimum fault sizes to be detected need to be specified. They are set so that smaller faults have insignificant or acceptable effects on vehicle motion when it is under feedback control. If necessary, they can be iteratively adjusted so that sufficient feasible residual generators can be synthesised to enable adequate fault isolation using structured residuals. The maximum disturbance size is set to its largest value expected during normal operation of this vehicle. In preparation for the synthesis of each residual generator, the plant model is normalised such that the minimum fault size to be detected and maximum disturbances and faults to be rejected have magnitudes of one, in order to be consistent with the problem definition in Chapters 3 and 4.

The minimum and maximum values for normalisation in residual generator design for the ROboMObil are listed in Table 8.1. Some justifications are now offered for these values,

starting with the maximums. Test data shows that road banking of $|\alpha_b| > 3°$ is seldom encountered during test operation. With regards to the steering angles, it is assumed here that offsets greater than $\sim 30°$ can be readily detected by the kinematic model-based FDI. The maximum possible wheel torque offset occurs due to worst-case undesired braking from the friction brakes. Assuming a maximum brake torque of 1000Nm, the maximum unwanted yaw moment is approximately given by $M_{z,TV} = 1000 \cdot ((s_l + s_r)/2)/r_w = 2555\text{Nm}$, with wheel radius $r_w = 0.274\text{m}$ and vehicle track $s_l + s_r = 1.4\text{m}$. The maximum sizes for the body sensor faults are offsets that produce sensor values beyond those that are feasible in normal cruising operation, and thus can be detected by range checks.

The minimum steering actuator fault sizes are chosen to correspond approximately to a lateral acceleration offset of 1m/s^2 at $v = 10\text{m/s}$. The minimum torque vectoring fault size is chosen to correspond to a yaw acceleration of about 0.3rad/s, at which point noticeable control errors can occur. Since the ROboMObil is closed-loop controlled in both the states β and $\dot{\psi}$, an additive fault in sensors measuring those states would result in a deviation from the intended trajectory. Values larger than the chosen minimum values are deemed to cause deviations difficult to handle for the human operator or for the higher level controllers. Finally, the lateral acceleration a_y is not directly used for control, but a deviation can result in erroneous supervisory decisions or faulty estimation outputs. A maximum of 2m/s^2 is considered to be acceptable. One can see that familiarity with the complete system design and a significant amount of operation experience and engineering judgement is involved in the determination of these parameters. They may have to be adjusted to alleviate issues encountered in operation.

Table 8.1: Normalisation values for faults and disturbances

fault / disturbance	**symbol**	**min** $\lvert\cdot\rvert$	**max** $\lvert\cdot\rvert$
disturbance: road banking	α_b	–	3°
actuator fault: front steering	f_{δ_f}	2.8°	30°
actuator fault: rear steering	f_{δ_r}	2.8°	30°
actuator fault: torque vectoring	f_{tv}	818Nm	2555Nm
sensor fault: side slip angle	f_β	3°	30°
sensor fault: yaw rate	$f_{\dot{\psi}}$	0.2rad/s	3rad/s
sensor fault: lateral acc	f_{a_y}	2m/s^2	15m/s^2

The parametrisation of the uncertainties is now treated. The cornering stiffnesses $c_{\alpha F}$ and $c_{\alpha R}$ describe the tyre-road contact behaviour, which can vary with road surface condition and the state of the tyre. For the robust operation of the fault detectors, variations in these parameters should be taken into account. However, considering the full range of possible conditions would result in such large uncertainties that only very poor fault sensitivity remains achievable. In this work, only dry asphalt is considered, and it is assumed that $c_{\alpha F}$ and $c_{\alpha R}$ vary within 1% of their nominal values. It has been found

iteratively that this parameter value yields an adequate quantity of feasible detectors (i.e. with guaranteed detection performance for worst-case inputs) for fault isolation, under the specified assumptions on sizes of disturbances and faults. It may be possible to increase the level of permissible uncertainty by adjusting these latter assumptions or by taking measures to reduce the conservatism of the residual generator design process - this is discussed in the Discussions and Future Research sections in Chapter 10.

The cornering stiffness parameters are expressed as nominal values with bounded additive uncertainties as follows:

$$\begin{aligned} c_{\alpha F} &= \tilde{c}_{\alpha F} + d_{cF}\delta_{c_{\alpha F}} \\ c_{\alpha R} &= \tilde{c}_{\alpha R} + d_{cR}\delta_{c_{\alpha R}} \\ |\delta_{c_{\alpha F}}| < 1,\ &|\delta_{c_{\alpha R}}| < 1 \end{aligned} \tag{8.4}$$

where $\tilde{c}_{\alpha F}$ ($\tilde{c}_{\alpha R}$) and d_{cF} (d_{cR}) denote the nominal value and the additive uncertainty upper-bound for $c_{\alpha F}$ ($c_{\alpha R}$).

The uncertain model can be expressed as an LFR (see Figure 3.4), in which the bounded uncertainties are extracted into a Δ block in a feedback interconnection with the nominal model. This is performed using numerical tools to produce a diagonal Δ with the form:

$$\Delta = \begin{bmatrix} \delta_{c_{\alpha F}} & 0 \\ 0 & \delta_{c_{\alpha R}} \end{bmatrix}. \tag{8.5}$$

The STM has now been adapted into the requisite form for the application of the robust LPV residual generator design procedure. The missing element is the definition of the polytope for the scheduling parameter vector $\boldsymbol{\rho}$, which will be addressed in the next section.

8.3 Polytopic LPV Representation

Since the two components of $\boldsymbol{\rho}$ are not independent, the feasible points in the two dimensional parameter space does not constitute a box defined by maximum and minimum bounds on each parameter. Rather, they lie on a hyperbolic curve $\rho_1 = 1/\rho_2$ with the end points $\bar{\boldsymbol{\rho}} = [\frac{1}{\bar{v}}\ \bar{v}]$ and $\underline{\boldsymbol{\rho}} = [\frac{1}{\underline{v}}\ \underline{v}]$. To reduce the conservatism arising from the imposition of the design constraints on infeasible parameter combinations within the polytope, the triangular polytope illustrated in Figure 8.3 is chosen as the convex parameter region for polytopic synthesis in order to minimise the enclosed area. It is bounded by the line joining the two endpoints of the curve, and the two tangents at the ends of the curve. Similar triangular polytopes are also used in [Zha14; VKM14] for controller or estimator design based on the LPV STM.

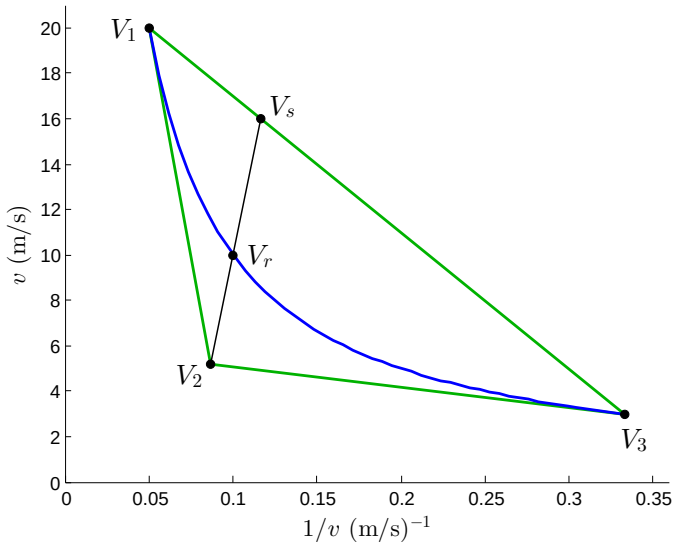

Figure 8.3: Triangular convex polytope enclosing the hyperbolic curve. The points V_r and V_s are used for interpolation.

The vertices of the polytope are given by the coordinates:

$$C_{V_1} = \left(\frac{1}{\bar{v}}, \bar{v}\right) \tag{8.6}$$

$$C_{V_2} = \left(\frac{2}{\bar{v}+\underline{v}}, \frac{2\bar{v}\underline{v}}{\bar{v}+\underline{v}}\right) \tag{8.7}$$

$$C_{V_3} = \left(\frac{1}{\underline{v}}, \underline{v}\right) . \tag{8.8}$$

The polytopic LPV residual generator at a specified parameter value is computed from the vertex instances by interpolation using (4.53). One can use any set of interpolation functions $\vartheta_i(\boldsymbol{\rho}),\ i = 1, 2, 3$ that satisfies (3.57), which can be expressed for this triangular polytope as

$$C_{V_r} = \sum_{i=1}^{3} \vartheta_i(\boldsymbol{\rho}) C_{V_i} \ , \quad \text{and} \quad 0 \leq \vartheta_i(\boldsymbol{\rho}) \leq 1,\ i = 1, 2, 3 \tag{8.9}$$

for the coordinate of any point V_r within the polytope. A generic approach to derive such a set of interpolation functions for any number of vertices is to first express the point V_r as a convex combination of two other points. Each of these could then be expressed as a convex combination of another two, and recursively repeated until the end point is a polytope vertex. For a triangular polytope this is a two step process. V_r is interpolated between the vertex V_2 and a point V_s which lies on the V_1V_3 line. The corresponding weighting factors $\vartheta_i(\boldsymbol{\rho})$ are ([Zha14]):

$$\vartheta_1(\boldsymbol{\rho}) = \frac{D_{V_2V_r}}{D_{V_2V_s}} \cdot \frac{D_{V_sV_3}}{D_{V_1V_3}} \tag{8.10}$$

$$\vartheta_2(\boldsymbol{\rho}) = \frac{D_{V_sV_r}}{D_{V_2V_s}} \tag{8.11}$$

$$\vartheta_3(\boldsymbol{\rho}) = \frac{D_{V_2V_r}}{D_{V_2V_s}} \cdot \frac{D_{V_1V_s}}{D_{V_1V_3}} \tag{8.12}$$

where $D_{V_a V_b}$ denotes the Euclidean distance between the points V_a and V_b. It can be verified by simple algebra that these weights $\vartheta_i(\boldsymbol{\rho})$ satisfy the necessary summation property (8.9).

8.4 Residual Generator Synthesis

This section and the subsequent one trace the design and validation of one of the bank of fault detectors selected to be part the structured residuals FDI scheme. The design of the residual structure will be covered later in Section 8.6, which requires individual fault detector design to be carried out for each of a list of potential fault signatures. The performance metrics calculated in the design procedure are then used as selection criteria to construct the minimal residual structure. The fault detector described in this section corresponds to index 284 in the aforementioned list of fault signatures. Its residual is designated r_{284} and has the fault signature specification

$$\begin{array}{c} \begin{array}{cccccc} f_{\delta_F} & f_{\delta_R} & f_{tv} & f_{\beta} & f_{\dot{\psi}} & f_{a_y} \end{array} \\ \begin{bmatrix} \times & 1 & \times & 1 & 0 & 0 \end{bmatrix} \end{array}$$

where the '×'s indicate indeterminate responses to $\{f_{\delta_F},\ f_{tv}\}$. As explained in Section 5.2.1, indeterminate entries are used in the signatures to avoid over-constraining the synthesis so that solutions with an adequate fault-vs-disturbance sensitivity ratio $\bar{\eta}$ can be found. The faults corresponding to the indeterminate entries are neglected in the residual generator synthesis, that is, their corresponding columns in the state space matrices are removed.

The LPV residual generator $\boldsymbol{F}(\boldsymbol{\rho})$ is designed by applying Procedure 4.2 to the normalised uncertain LPV STM in LFR form. Table 8.2 presents the design parameters chosen for the synthesis and the reasoning behind their selection.

The uncertainty block Δ, whose form is shown in (8.5), corresponds to the form designated "Blocks of Repeated Constant Real Scalar" in Section 3.5.1, as shown in (3.69). In this instance, each of the two diagonal blocks has size one, i.e., $m_i = 1,\ i = 1, 2$. The matching IQC multiplier $(\boldsymbol{\Psi}, \boldsymbol{M})$ and the LMI constraints on $\boldsymbol{M}$ are also presented in the same section, where $\boldsymbol{\Psi}$ has the state space representation provided in (3.79). The parameters of $\boldsymbol{\psi}_i,\ i = 1, 2$ are chosen iteratively to be $n_\psi = 1$ and $\alpha = 0.01$ for both blocks.

The synthesis yields an LPV residual generator $\boldsymbol{F}(\boldsymbol{\rho})$ of 6-th order. It has been verified that its frozen parameter instances at the vertices satisfy the pole location specifications. The optimal κ value of 2.2 is found using a golden section search (Figure 8.4 shows how the cost function $\bar{\eta}$ varies with κ), using which the minimum value of $\gamma^* = 0.36$ is reached in the SDP (4.56). The gains of the fault-to-residual reference filters at the vertices are $\boldsymbol{\Lambda}_1 = [1.4\ 1.0]^T$, $\boldsymbol{\Lambda}_2 = [1.1\ 1.1]^T$, and $\boldsymbol{\Lambda}_3 = [1.0\ 1.1]^T$. The residual generator's fault-vs-disturbance sensitivity metric η is upper bounded by $\eta \leq \bar{\eta} = 1.1$, which slightly exceeds

Table 8.2: Design parameters for LPV residual generator synthesis

parameter	**description**	**value**	**comments**
Ω	evaluation frequency range for H_- index	$[0, 1]$ rad	primarily interested in quasi-static faults
$W_{[i]},\ i \in [1, n_f]$	normalised fault to residual reference	$\frac{1}{0.1s+1}$	≈ 1 for $\omega \in \Omega$
$W_{f[i]},\ i \in [1, n_f]$	frequency weight for residual reference tracking	$\frac{1}{0.33s+1}$	attenuation for $\omega \notin \Omega$
$W_{d[j]}, j \in [1, n_d]$, $W_{u[k]}, k \in [1, n_u]$	frequency weight for disturbance and input rejection	1	reject disturbances and inputs at all frequencies
d_{cF}	uncertainty in $c_{\alpha F}$	1%	see discussion immediately before (3.79)
d_{cR}	uncertainty in $c_{\alpha R}$	1%	see discussion immediately before (3.79)
$[\underline{v}, \bar{v}]$	admissible range of scheduling signal	$[3, 20]$	velocity unit: m/s
$[\underline{Re(\sigma)}, \overline{Re(\sigma)}]$	pole-region constraint, [min,max] of real component	$[-300, -5]$	reasonable range of time constants
$\tan(\theta)$	pole-region - max damping ratio	$\tan(\frac{\pi}{12})$	≈ 0.27
κ	weighting factor, fault sensitivity vs. disturbance rejection	2.2	found by scalar optimisation

the upper limit of $\bar{\eta} = 1$ to guarantee reliable detection without false alarms. The value $\bar{\eta} = 1.1$ can be interpreted as follows: if the minimum fault sizes specified in Table 8.2 were increased by 10%, then the guarantee for fault detection would be guaranteed to hold. Due to the inherent conservatism of the condition $\bar{\eta} < 1$ as discussed in Chapter 4, it is relaxed to $\bar{\eta} < 2$ in the choice of feasible residual generators later on for residual structure design.

The performance of the residual generator for r_{284} is illustrated in Figure 8.5. The bode magnitude plots of the frozen parameter LTI systems are evaluated over a rough grid of scheduling and uncertain parameters. Although the behaviour during non-zero parameter rates of change are not described by these plots, they nonetheless offer useful insights into system behaviour. Within the specified low frequency region $\Omega = [0, 1]$rad/s and over the permissible range of the parameters $\{v, \delta_{c_{\alpha F}}, \delta_{c_{\alpha R}}\}$, the plots illustrate that the signals to be attenuated have about 20dB smaller effects on the residual compared to the faults to be detected.

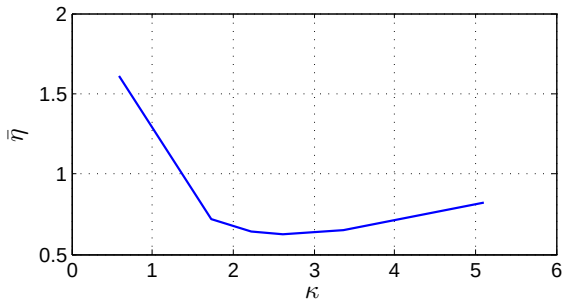

Figure 8.4: $\bar{\eta}$ vs κ over the linear search

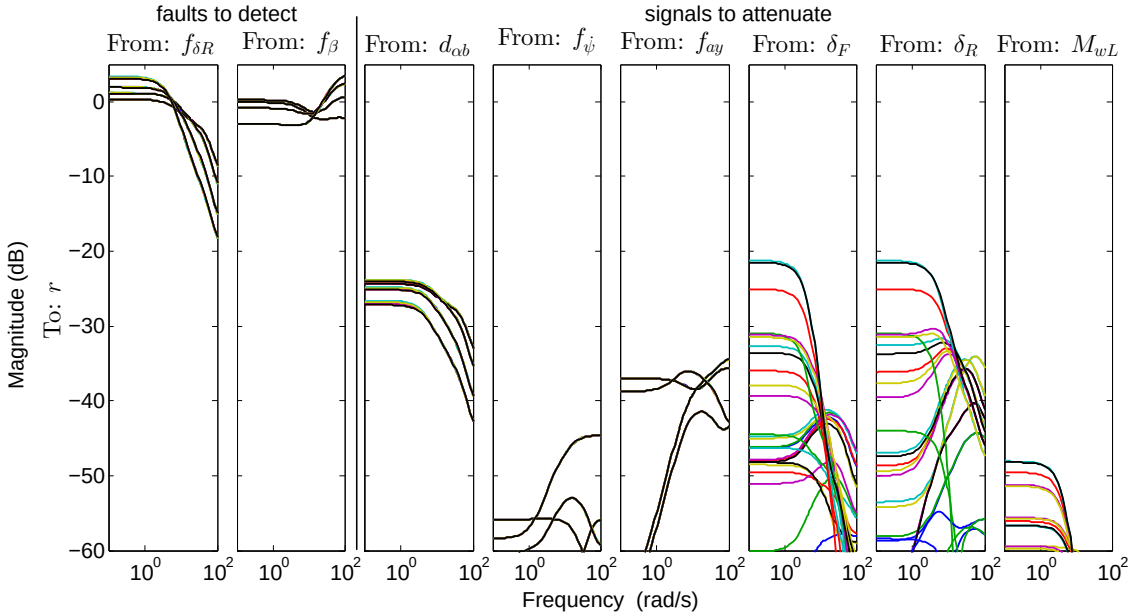

Figure 8.5: Bode magnitude plots of the connected plant-residual generator system over a 3×7 grid of frozen parameter values $v \in [3, 10, 20]$ and $\Delta \in [[0, 0],\ [0.01, 0],\ [0, 0.01],\ [0.01, -0.01],\ [0.01, 0.01],\ [-0.01, -0.01],\ [-0.01, 0.01]]$.

8.5 Residual Evaluation

The residual calculated by the residual generator is processed by a evaluation function and then compared to a threshold function to trigger an alarm. Here the approach in Section 5.1 is employed, using the truncated 2-norm as the evaluation function and the threshold function set according to Section 5.1.3. The design choices and parameter selection are now described, and the selected parameters for r_{284} are listed in the top row of Table 8.3.

Design of the residual evaluation and threshold functions involves establishing the following parameters:

1. decay times ζ_d and ζ_u
2. window length T_r
3. weighting functions $\boldsymbol{W}_d$ and $\boldsymbol{W}_u$
4. the bound ϵ_d on the RMS weighted disturbance

5. the worst-case gains γ_d and γ_u.

The weighting filters ($\boldsymbol{W}_u$, $\boldsymbol{W}_d$) and the worst-case gains (γ_u, γ_d) are determined through analysis of the transfer function matrices $\boldsymbol{G}_{ru}(\boldsymbol{\rho})$ and $\boldsymbol{G}_{rd}(\boldsymbol{\rho})$. Figure 8.6 shows the bode plots of the frozen parameter LTI systems over a grid of the permissible scheduling and uncertain parameters. Despite the bode plots suggesting that weighting may be possible for some inputs, it turns out that for the LPV system there is little scope for selecting $\boldsymbol{W}_u$ and $\boldsymbol{W}_d$ such that $|W_{u[k]}(j\omega)| > 1,\ k \in [1, n_u]$ and $|W_{d[j]}(j\omega)| > 1,\ j \in [1, n_d]$ for ω within a relevant range, without increasing the worst-case induced-$\mathcal{L}_2$ norms $\|\boldsymbol{G}_{ru}\|_\Delta$ and $\|\boldsymbol{G}_{rd}\|_\Delta$. Here, the relevant frequency range refers to the frequencies close to the frequency contents of $\boldsymbol{u}$ and $\boldsymbol{d}$. Therefore $\boldsymbol{W}_u = \boldsymbol{I}$ and $\boldsymbol{W}_d = \boldsymbol{I}$ are chosen for simplicity.

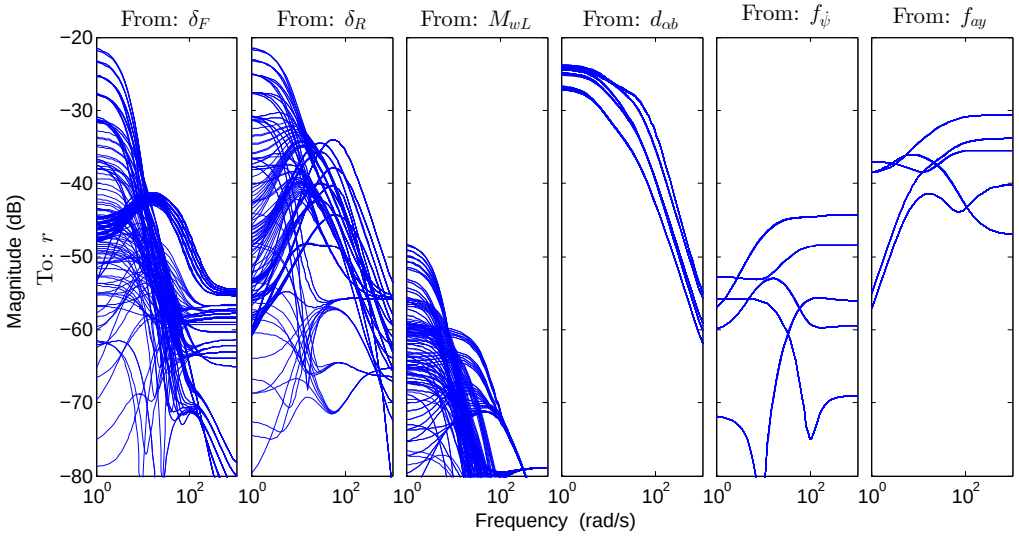

Figure 8.6: Bode plots of frozen parameter LTI systems over the grid of permissible scheduling and uncertain parameters

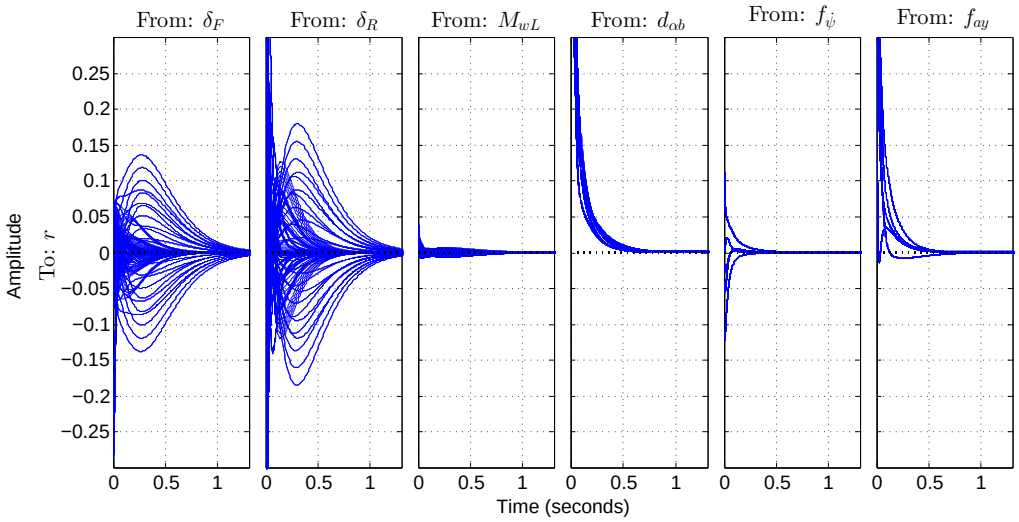

Figure 8.7: Impulse response plots of frozen parameter LTI systems over the grid of permissible scheduling and uncertain parameters

The basic approach for threshold generation described in Section 5.1.2 - 5.1.3 is adapted here in a similar manner to the illustrative example in Section 5.1.4, in which the residual bounds are split into separate components for sub-groups of elements within the $\boldsymbol{d}$ and $\boldsymbol{u}$ vectors, rather computed directly for those full vectors. Again this is done to further reduce conservatism and improve sensitivity. Consider first the contribution from the disturbance $\boldsymbol{d} = [\boldsymbol{d}_p \ f_{reject}]$ to the residual, where $\boldsymbol{d}_p = [d_{\alpha b}]$ denotes the physical plant disturbance and $f_{reject} = [f_{\psi} \ f_{a_y}]$ denotes the faults to be rejected. Notice that $\boldsymbol{d}_p$ is considered a norm-bounded input, while any single fault from f_{reject} can occur concurrently to $\boldsymbol{d}_p$. With respect to the ideal 2-norm, the worst-case contribution from $\boldsymbol{d}$ to the residual norm is given by

$$\epsilon_d = \|r_d\|_2 \leq \gamma_{d_p} \|\boldsymbol{d}_p\|_2 + \max_{f_i \in f_{reject}} \gamma_{f_i} |f_i| \ , \tag{8.13}$$

where

$$\begin{aligned} \gamma_{d_p} &= \sup_{\Delta \in \mathcal{D}} \|\boldsymbol{G}_{rd_p}\|_{i2} \\ \gamma_{f_i} &= \sup_{\Delta \in \mathcal{D}} \|\boldsymbol{G}_{rf[i]}\|_{i2} \ . \end{aligned}$$

The contribution from the actuation inputs $\boldsymbol{u}$ to the residuals can be similarly divided up into those of its scalar elements. Such an adaptation is especially beneficial when the elements u_i or sub-groups thereof have vastly different worst-case gains to the residual. Splitting $\boldsymbol{u}$ into k sub-groups of its components, the worst-case contribution from $\boldsymbol{u}$ to the residual norm is given by

$$\epsilon_u = \|r_u\|_2 \leq \sum_{i=1}^{k} \gamma_{u_i} \|\boldsymbol{u}_i\|_2 \ . \tag{8.14}$$

In this application, $\boldsymbol{u}$ is divided into its three actuation inputs. The presented approach can then be readily extended to the truncated norm by following the same principles outlined in Section 5.1.3. The decay time ζ from each system input group is estimated by inspecting the impulse response of its constituent scalar elements to r in Figure 8.7. In order to reduce the inherent conservatism of the proposed threshold computation method, it is decided that it would be reasonable to tune each ζ to half the actual decay time.

When applied to the nonlinear simulation or experimental test drive data, an additional contribution to the residual appears due to unmodelled dynamics and measurement noise. In the experimental case, this is compounded by uncertainties in parameters other than the cornering stiffnesses accounted for in the synthesis. To deal with these effects, a small additional constant component Φ_e added to the threshold to prevent false alarms. The evaluation window length T_r represents another tunable parameter. A longer T_r increases detection time but also improves sensitivity to persistent faults (see discussion in Section 5.1.3). $T_r = 2.0$s is deemed in this case to be a reasonable compromise. If extensive simulation and experimental data are available, these could be used to empirically optimise

these tuning parameters to find the desired trade-off between sensitivity, detection time, and false alarm rates.

Table 8.3: Residual evaluation parameters

res.#	$\gamma_{u_1}, \gamma_{u_2}, \gamma_{u_3}$	γ_{d_p}	$\gamma_{f_{reject}}$	ζ_u	ζ_d	T_r	$\tilde{d}_{RMS}$	Φ_e
284	$[0.065, 0.108, 0.004]$	0.088	$[0.01, 0.03]$	$[0.6, 0.6, 0.1]$	0.1	2.0	1.0	0.15
355	$[0.064, 0.065, 0.003]$	0.005	$[0.01, 0.03]$	$[0.5, 0.5, 0.5]$	0.3	2.0	1.0	0.20
311	$[0.055, 0.048, 0.001]$	0.112	$[0.27, 0.16]$	$[0.1, 0.4, 0.4]$	0.5	2.0	1.0	0.05
390	$[0.086, 0.130, 0.004]$	0.193	$[0.14, 0.03]$	$[0.3, 0.3, 0.1]$	0.1	1.5	1.0	0.05
145	$[0.049, 0.110, 0.003]$	0.098	$[0.28, 0.15]$	$[0.3, 0.3, 0.1]$	0.4	1.6	1.0	0.05
167	$[0.049, 0.091, 0.003]$	0.278	$[0.28, 0.15]$	$[0.5, 0.5, 0.3]$	0.3	2.0	1.0	0.10
165	$[0.057, 0.048, 0.002]$	0.282	$[0.30, 0.17]$	$[0.5, 0.5, 0.1]$	0.4	2.0	1.0	0.05
122	$[0.085, 0.122, 0.004]$	0.362	$[0.02, 0.01]$	$[0.6, 0.4, 0.1]$	0.3	2.0	1.0	0.05
231	$[0.469, 0.517, 0.025]$	0.794	$[0.91, 0.51]$	$[0.3, 0.3, 0.3]$	0.3	1.5	1.0	0.05
69	$[0.246, 0.462, 0.014]$	0.820	$[1.04]$	$[0.3, 0.3, 0.2]$	0.3	1.5	1.0	0.05

8.6 Residual Structure Design

Given a set of feasible fault detectors, and their respective fault signatures and cost measures, Section 5.2.4 describes a method to select the optimal set of fault detectors that maintains the fault isolation capability achieved by the full set. The cost $\bar{\eta}$ associated with each fault signature is computed by applying the residual generator design procedure to every possible signature. The choice of $\{0, 1, \times\}$ for each fault results in 3^{n_f} signature permutations for n_f faults. This exponential increase with n_f makes this cost evaluation step extremely computationally intensive, and therefore some measures are employed to reduce the number of permutations.

According to [FN01], when there are m known system outputs, it is only possible to perfectly decouple at most $(m-1)$ independent inputs in a residual. Although approximate decoupling residuals are being sought, this nonetheless provides useful insight. Since this guideline implies that attempts at attenuation of more inputs is less likely to succeed, the number of '0' entries is initially limited in each signature of the signature set. Furthermore, a signature generally contributes more to fault isolation if there less indeterminate entries, so only the signatures with fewer indeterminate '$\times$' entries than a threshold should be processed at the beginning. Only if insufficient adequate residual generators can be found, should further indeterminate entries be considered. Despite these guidelines, this procedure to prune the permutation set is iterative and ad-hoc to a degree. The idea is to

eventually reach a sufficiently large pool of residual generators with adequate performance to pass to the residual selection process.

In this application, signatures are chosen to have a maximum of three indeterminate '$\times$' entries and up to two insensitive '0' entries. Attempts to decouple more faults generally led to unusable residual generators with high values of $\bar{\eta}$. Out of the 423 signatures satisfying these criteria, 163 signatures produced residual generators that satisfy the relaxed performance criterion of $\bar{\eta} < 2$. This set of signatures constitutes the input data to the residual selection process and forms the starting point of the upcoming discussion.

By applying the selection procedure from Section 5.2.4 under the partial firing assumption, a residual structure is obtained which corresponds to the first eight rows of incidence matrix shown in Figure 8.8-right. The procedure ensures that this subset of fault detectors achieves the same fault isolation capability as the initial set and has the same fault matrix. This fault matrix is depicted in Figure 8.8-left, where the entries marked with $*$ and $\triangle$ are to be interpreted as '1's. It can be seen that full isolation, which corresponds to a diagonal matrix, proves to be unachievable. In particular, the torque vectoring fault f_{tv} is troublesome and the '$*$' in the $(f_{tv}, \text{no-fault})$ position indicates that it cannot be detected using this set of residuals. Inspection of the incidence matrix on the right reveals the cause - every selected residual is either indeterminate or insensitive to f_{tv}, which does not allow it to be detected. We can deduce that the initial set also suffers from this issue, since the selection procedure does not reduce isolation capability. A further blemish in this fault matrix is that f_{δ_F} and $f_{\dot{\psi}}$ cannot be isolated from each other.

In an attempt to recover the missing detection and isolation capabilities when larger faults are present, the performance requirement $\bar{\eta} < 2$ is further relaxed to yield a supplementary set of fault detectors with $2 < \bar{\eta} < 7$. Fault detectors from this supplementary set are selected if they contribute to an improvement in the fault isolation capability, producing the fault matrix in Figure 8.8-left where only the '$*$' are interpreted as '1's. The two bottommost fault detectors in Figure 8.8-right, whose numbers are each labelled with a $*$ superscript, are selected from this supplementary set. The $\bar{\eta}$ metric of all the selected residual generators are illustrated in Figure 8.9. The extended set of residuals achieves isolation between f_{δ_F} and $f_{\dot{\psi}}$, but is still unable to detect f_{tv}. Evidently, the effects of f_{tv} on the lateral dynamics are too weak compared to the permissible disturbances, uncertainties and other faults, and other measures need to be employed for its detection and isolation.

At runtime, the pattern evaluation function of Procedure 5.2 is applied at each time step to compute the set of fault candidates. The version accounting for partial firing is used.

8.7 Validation

The behaviour and effectiveness of the fault detectors are now verified by applying them to simulation and experimental data sets affected by faults. To generate the simulated

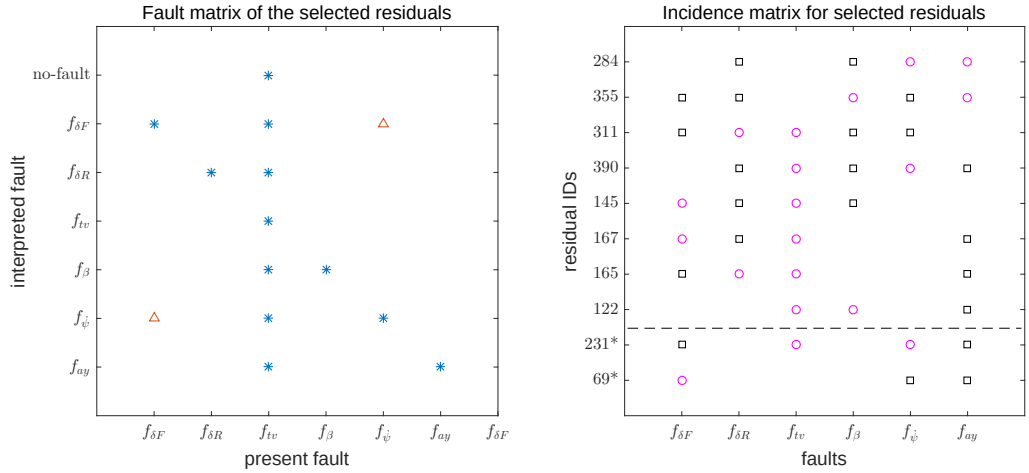

Figure 8.8: Properties of the selected residual set which provides the maximum isolation capability. Left: fault isolation matrix - a mark at (x,y) indicates that fault y explains fault x (the presence of fault x produces a residual pattern that can be interpreted as fault y). The fault matrix marked by just '$*$' arises from the residual set with the supplementary residuals, whereas the matrix including also the '$\triangle$' is produced when the supplementary residuals are excluded. Right: fault signatures of the selected residuals - $\square$: sensitive ('1'), $\circ$: insensitive ('0'), empty: indeterminate ('$\times$'). The supplementary residuals are labelled with a $*$ superscript and divided from the remainder with a dotted line.

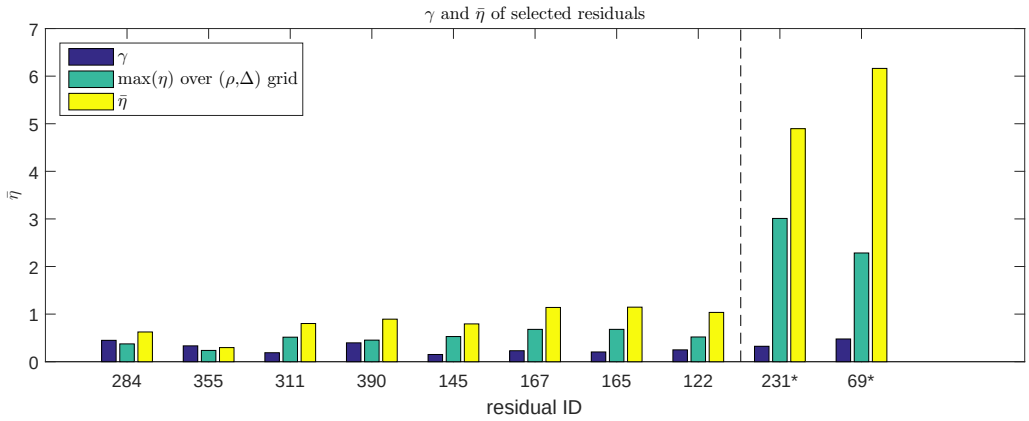

Figure 8.9: Properties and metrics of the selected residuals. A comparison is shown between the worst value of η evaluated over a parameter grid, and the more conservative upper bound $\bar{\eta}$ calculated from γ. The supplementary residuals are labelled with a $*$ superscript and divided from the remainder with a dotted line.

data sets, faults are modelled and simulated in conjunction with the vehicle and its control system. However, for the experimental data sets, faults are not injected during vehicle operation on safety grounds. Instead, the fault effects are superimposed retrospectively on the recorded data. This is not considered a major setback for this investigation, since the main focus of validation using experiment data is to verify adequate robustness against uncertainties, disturbances and nonlinearities on the real vehicle. Sensitivity to faults and fault isolation functionality can be satisfactorily investigated and validated through simulations. These have the additional advantage of being able to reproducibly simulate a large range of fault manifestations and occurrence times.

8.7.1 Using Simulation

Several simulations are presented to illustrate the behaviour of the fault detectors. They are listed in Table 8.4. In the first two cases, denoted A and B, their respective motion control references for v_x, β and $\dot{\psi}$ are constructed to contain a range of different dynamic behaviours while remaining within the cruising operating region. Case A is a 40s long simulation in which all the faults and disturbances are injected as square pulses to facilitate analysis of the responses of the residual to these inputs. In contrast, all the sub-cases of case B share another motion control reference, and each sub-case is injected with only a (different) single fault in a variety of manifestations. Finally, case C actually denotes the experimental test case in which both the actuator and body sensor outputs are replayed from recorded data. The faults are injected via the same set of pulses as in case A. The experimental test case will be described in more detail in the upcoming Section 8.7.2.

The plant signals and the diagnosis results of each validation case are presented in a consistent three plot format. The first displays the actuator outputs and the body sensor measurements of the vehicle, which constitute the $\boldsymbol{u}$ and $\boldsymbol{y}$ inputs to the fault detectors. The second plot shows the evaluated residual and threshold for the first three residuals from the selection $(r_{284}, r_{355}, r_{311})$ to demonstrate their time-domain behaviours in response to stimulation. To aid the intuitive distinction between the effects of the faults from those due to actuation inputs and disturbances, the evaluated residual from the corresponding fault-free simulation is also plotted concurrently. These three residuals are in fact sufficient for isolation between $\{f_{\delta_R}, f_\beta, f_{\dot{\psi}}\}$, and the fault hypotheses from this reduced fault isolation problem is shown on this same plot with the residuals. In the third plot, in order to save space and maintain clarity, the ten residuals for the full fault isolation problem are not displayed, but rather only the status of whether they have fired. The fault hypotheses for all six faults is then displayed.

Table 8.4: Validation cases

case	**sub-case**	**motion ref.**	**data**	**faults**
A	-	fictive 1 (long)	sim	square pulses - all faults
B	B1	fictive 2 (short)	sim	f_{δ_F} - alternative
	B2			f_{δ_R} - alternative
	B3			f_{tv} - alternative
	B4			f_β - alternative
	B5			$f_{\dot{\psi}}$ - alternative
	B6			f_{a_y} - alternative
C	-	-	exp	square pulses - all faults

Case A: Additive Faults in Constant Pulses

The trajectories of the fictive reference inputs and the resulting vehicle motion for case A are depicted in Figure 8.10a. The reference motion is defined by the triple $\{v_x, \beta, \dot{\psi}\}$, whose demand values are shown as blue dash-dotted lines in the respective plots. Each controller's tracking behaviour minimises the errors between the demand and the fault-affected feedback signal provided to it, causing the real variable to deviate from the reference when a sensor fault is present. Furthermore, it can be observed that the lateral dynamics controller compensates for the perturbations caused by the actuator faults.

The top three plots of Figure 8.10b displays the evaluated residuals for $r_{284}, r_{355}, r_{311}$ together with their respective dynamic thresholds. They demonstrate that these residuals are sensitive to the faults specified in their signatures while being successfully decoupled from the disturbance d_{α_b}, attenuated faults $\{f_{\dot{\psi}},\ f_{a_y}\}$, and actuation inputs. This performance is expected from the low to moderate $\bar{\eta}$ achieved with these residuals. The imperfect decoupling is evident by inspecting the fault-free residuals (shown by the black dotted line), which are small but non-zero in response to the disturbance d_{α_b} during $[1, 4]$s and to the moderate steering angle inputs in the time period $[25, 35]$s. Another observation is that a residual may fire in response to its indeterminate faults. For example, r_{284} fires in response to f_{δ_F} during $[8, 10.4]$s. This behaviour is normal and does not compromise fault isolation since it is considered in the residual structure design.

The bottom plot of Figure 8.10b shows that in the reduced isolation problem, reliable isolation is achieved when one of $\{f_{\delta_R}, f_\beta, f_{\dot{\psi}}\}$ is present during the periods $[12, 15]$s, $[24, 17]$s and $[30, 33]$s respectively. The reduced problem has the incidence matrix

$$\begin{array}{c} \\ r_{284} \\ r_{355} \\ r_{311} \end{array} \begin{array}{c} \begin{array}{ccc} f_{\delta_R} & f_\beta & f_{a_y} \end{array} \\ \begin{pmatrix} 1 & 1 & 0 \\ 1 & 0 & 1 \\ 0 & 1 & 1 \end{pmatrix} \end{array} .$$

This structure enables each fault to be uniquely identified even under the partial firing assumption. The plotted signals demonstrate the behaviour that before an occurred fault is uniquely identified, the set of fault hypotheses often contain more fault candidates than just the true one. This is a product of the different transient behaviour between the residuals, leading to partial firing for a short moment. The pattern evaluation algorithm (see Procedure 5.2) identifies the multiple faults which can induce the observed partial pattern, leading to a set of non-unique fault hypotheses. Another remark is that the faults which are not members of the reduced isolation problem, namely $\{f_{\delta_F}, f_{tv}, f_{a_y}\}$, violate the closed world assumption that requires all possible faults to be known. Their occurrences therefore lead to the erroneous fault hypotheses in this reduced problem.

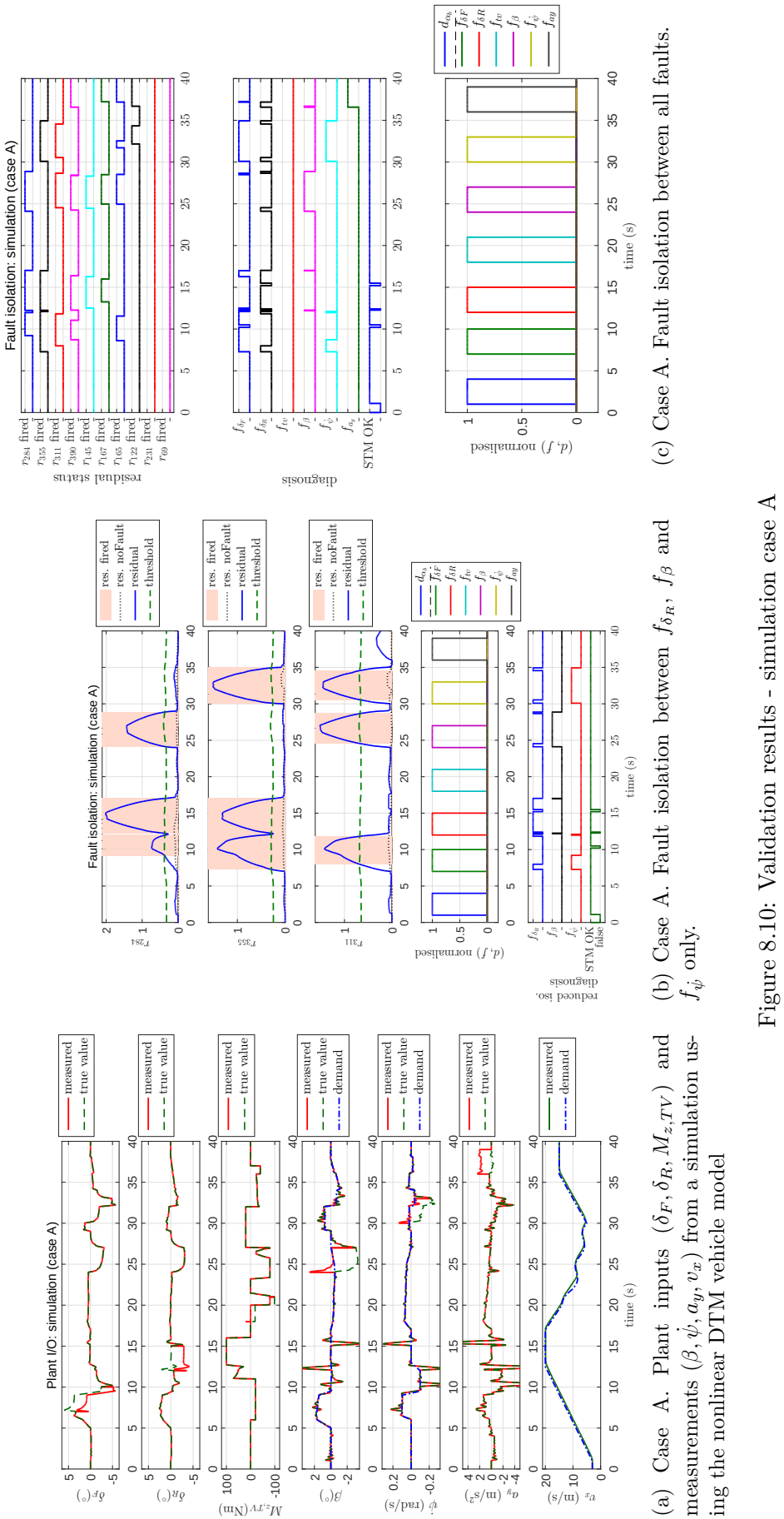

(a) Case A. Plant inputs $(\delta_F, \delta_R, M_{z,TV})$ and measurements $(\beta, \dot{\psi}, a_y, v_x)$ from a simulation using the nonlinear DTM vehicle model

(b) Case A. Fault isolation between f_{δ_R}, f_β and $f_{\dot{\psi}}$ only.

(c) Case A. Fault isolation between all faults.

Figure 8.10: Validation results - simulation case A

The full set of six faults is handled in the full isolation problem using all ten residuals. The firing status of these residuals are shown in the top plot of Figure 8.10c. The second plot then depicts the hypotheses for each of the six faults. We can see that f_{δ_F}, f_{δ_R}, f_β and $f_{\dot{\psi}}$ are uniquely isolated after the transitions have settled, whereas the presence of $f_{\dot{\psi}}$ triggers the faulty hypotheses for $\{f_{\delta_F}, f_{\dot{\psi}}\}$ in $[30, 35]$s. The phenomenon can be traced back to the fault matrix in Figure 8.8, which exposes that isolation between $\{f_{\delta_F}, f_{\dot{\psi}}\}$ is only possible by using supplementary residuals with $\bar{\eta} > 2$. The residuals r_{231} and r_{69} belong to this category and not unexpectedly, they did not fire in response to the faults in this example, whose magnitudes correspond to the specified minimum detectable faults sizes. The ability to eliminate the $f_{\dot{\psi}}$ hypothesis in the presence of f_{δ_F} is fortuitous and not predicted from the residual structure. The firing of r_{284}, which has an indeterminate response to f_{δ_F}, rules out the possibility of $f_{\dot{\psi}}$ which is rejected by r_{284}. The final observation is that the detection of f_{tv} is not possible with this set of residuals, which has already been revealed by the achieved fault matrix during residual structure design.

Having now analysed robustness and fault sensitivity, the other important performance measure of detection delay is now discussed. This property of the fault detector has not been addressed explicitly in the design procedure. It is a function of the fault sensitivity and dynamics of the residual generator, the window lengths in the residual evaluation, the robustness margins in the threshold selection, and also the fault manifestation (magnitude and evolution). As a rough indication of this aspect of the performance of fault detector 284, the detection delays are listed in Table 8.5 for the simulated fault occurrences. The isolation delay refers to the elapsed time from fault occurrence until the steady-state fault hypothesis is reached.

Table 8.5: Fault detection and isolation times from case A

fault	**rise time (s)**	**detection delay (s)**	**isolation delay (s)**
f_{δ_F}	7	0.3	1.7
f_{δ_R}	12	0.4	0.5
f_{tv}	18	n/a	n/a
f_β	24	0.1	0.5
$f_{\dot{\psi}}$	30	0.2	0.5
f_{a_y}	36	0.6	1.2

Since the *STMFDI* module has not been run in conjunction with fault tolerant control (FTC) functions, it is not possible to draw conclusions on the adequacy of the observed detection delays. In any case, it should be noted that the vehicle remains stable throughout the simulation in spite of the injected faults, showing that the closed-loop lateral dynamics controller is able to tolerate these fault sizes *passively* (i.e., without reconfiguration), although there are considerate excursions of the states from the demanded β and $\dot{\psi}$ (see 4th and 5th plots of Figure 8.10a). Nonetheless timely diagnosis is important in order to

minimise the duration of compromised vehicle handling, and to reduce the potential for further damage and the risk in case of a worsening fault. From vehicle testing experience, I would consider the achieved detection and isolation times to be adequate, but they must be investigated for specific applications.

On the other hand, larger faults can result in worse deviations from the demanded motion or even instability. For the purpose of maintaining stability and acceptable control, the detection times appear to be acceptable but the isolation times for f_{δ_F} and f_{a_y} may be marginal. However, this again needs to be verified with a suitable designed controller. It should be noted that detection time generally reduces with increasing fault size, so the isolation times may not prove to be an issue any longer for critically large faults. Furthermore, there is scope to influence the dynamics of the residual generator via the choice of frequency behaviour for the reference model and the bounds on the eigenvalues of the residual generator, both of which are tunable design parameters (see Table 8.2).

Case B: Single Faults in Alternative Manifestations

Having examined the residual's responses to step manifestations of the additive faults, several selected alternative manifestations are investigated under the umbrella of case B. Each simulation sub-case lasts 15s and share the same actuator and disturbance inputs as well as initial conditions. Due to the large quantity of results from case B, the description of the set up as well as the presentation and analysis of the results have been placed in Appendix A.

8.7.2 Using Road Test Data

Case C: Additive Faults in Constant Pulses

This section demonstrates the validity of the *STMFDI* when it is applied to measurement data from a real driving test. Compared to the simulation example, application to the real plant brings with it additional challenges, including measurement noise, extra uncertain parameters (including calibration and installation tolerances), and further unmodelled dynamics and disturbances.

The chosen data set was recorded during a double lane change test, in which the automated test manoeuvre in $t \in [9, 17]$s was followed by a driver-controlled turn-around ($t \in [18, 24]$s) and return drive ($t \in [24, 40]$s) towards the starting position. The GPS-recorded path is illustrated in Figure 8.11. For the test duration the vehicle was operated under closed-loop longitudinal and lateral dynamics control as in the simulation set up in the previous section. A noteworthy characteristic of the double lane change manoeuvre is that the ROboMObil maintained a constant orientation by setting equal front and rear steering angles. During the turn-around and return drive, the steering was performed more conventionally to produce a yaw component of motion as well. The trajectories of the plant inputs and outputs are shown in Figure 8.12a. The three plot figures have been shifted to the end of the chapter for readability reasons.

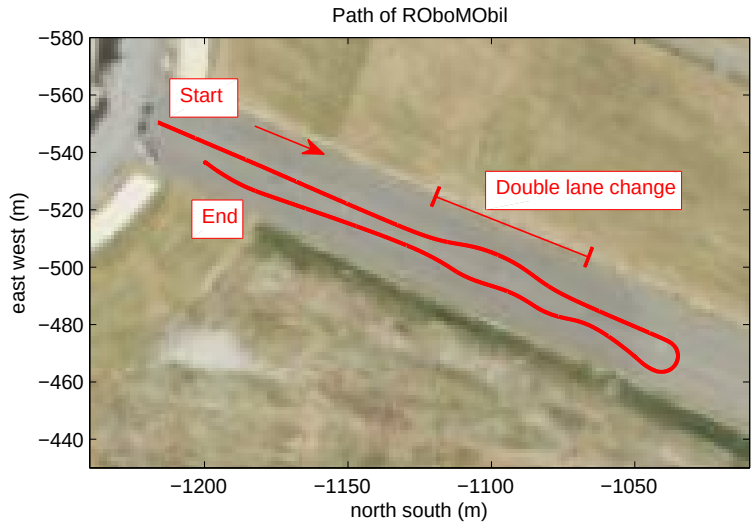

Figure 8.11: Path of the RObоMObil during the recorded test drive

With the exception of the very beginning and end of the drive, during the test the longitudinal velocity v_x varies in the range $[5, 14]$m/s, and the lateral acceleration a_y lies predominantly below 4m/s^2 with only brief peaks of 6m/s^2. Thus most of the time both v_x and a_y satisfy the validity constraints of the designed residual generators, namely $v_x \in [3, 20]$m/s and $|a_y| < 4$m/s. The former constraint reflects the permissible range of the scheduling parameter, while the latter ensures the validity of the underlying LPV STM. Furthermore, the angles δ_F, δ_R and β have magnitudes less than 15° so that the small angle assumptions in the LPV STM are still reasonable. The low-to-moderate longitudinal acceleration satisfies $|a_x| < 3\text{m/s}^2$, which is acceptable for the model, except for short peaks due to application of the friction brakes in $[17, 19]$s. When the operating states of the system violate any of these constraints, the diagnosis is invalidated and indicated in the plots by setting all the fault hypotheses to false.

As explained earlier, the test drive was performed without any fault simulation. The sensor faults are retrospectively injected by modifying the plant output measurements. In contrast, the reproduction of actuator fault effects in the same sense as for the DTM simulations requires the ability to influence the real actuator demand and states, which cannot be carried out retrospectively. An alternative approach is employed in which the actuator fault is subtracted from the actuator measurement signal.

It is acknowledged that this produces a more isolated and abrupt transient in the affected actuator measurement, without influencing vehicle motion as a real actuator fault would have. The effect of a steering actuator deviating from the demanded value can be seen in cases A, B1 and B2. After an initial transient, the lateral dynamics controller corrects the motion of the vehicle with the control efforts distributed over the available actuators. Despite this difference, the steady state behaviour of actuator fault simulation via retrospective injection is plausible and provides a useful check of fault sensitivity. Moreover, as mentioned earlier, the emphasis of validation using road test data is to verify

that false alarms are not triggered by the additional effects. These conclusions are not affected by the mode of fault injection.

The fault detectors demonstrate the behaviour displayed in Figures 8.12b and 8.12c. Compared to the DTM simulations, on occasions the evaluated residuals shown in Figure 8.12b deviate further from zero when the sensitive faults are absent. This is expected due to the greater mismatch between the model and the real physical plant, but the residual levels remain sufficiently low to recognise when a sensitive fault has occurred. Furthermore, the high residual values in $[19, 26]$s can be partly attributed to the high steering angles of up to 12° and 10° on the front and rear axles to negotiate the tight hairpin curve, which results in increased deviation from the small angle assumptions embedded in the linearised STM.

Figure 8.12c shows that the *STMFDI* module successfully isolates all the faults other than f_{tv}. We see from the "STM OK" signal that the validity conditions are intermittently violated. For $t > 38.7$s it is violated by $v_x < \underline{v}$, where $\underline{v} = 3$m/s is the minimum scheduling parameter of the LPV residual generators. During $[17.3, 19]$s the validity condition is violated by $|a_y| > 4\text{m/s}^2$. The diagnostic outputs are invalidated during these periods.

8.8 Discussion

The chapter has shown that an FDI module based on the linearised STM with time-varying velocity can be realised using fault detector and structured residual design procedures presented in Part-I of this thesis. Theoretical metrics and validation tests indicate that most faults at the minimum specified size can be reliably detected and isolated, with the exception of the torque vectoring fault f_{tv} and the isolation between f_{δ_F} and $f_{\dot{\psi}}$. The inability to detect f_{tv} can be attributed to its comparably weak effects on lateral dynamics in comparison to other inputs considered. However, f_{tv} is a composite fault composed from wheel torque faults (see Section 8.2), whose effects on longitudinal acceleration may offer a detection and isolation mechanism through considering both longitudinal and lateral dynamics concurrently. Such an investigation is beyond the scope of this work. Isolation between f_{δ_F} and $f_{\dot{\psi}}$ may yet be achievable through less conservative determination of residual evaluation parameters, since the supplementary residuals (r_{231} and r_{69}) responsible for their isolation have higher but still useful values of the $\bar{\eta}$ metric (see Figure 8.9). The proposed method for threshold computation from the analytical worst-case induced-$\mathcal{L}_2$ norm is inherently conservative and in cases where the level of conservatism cannot be tolerated, it offers a starting point for further optimisation.

The validation demonstrated that both for constant additive faults and other fault manifestations, reliable fault diagnosis depends on successfully handling the temporary occurrences of multiple fault hypotheses caused by partial firing in the transient phases. Furthermore, when a fault manifestation is equivalent to a time-varying additive fault, such as a frozen signal output or a gain error, the fault hypotheses may be extinguished

intermittently. Based on fault persistence assumptions, logical processing of the hypotheses enables reliable diagnostic conclusions to be drawn. For example, knowledge of the system and fault mechanisms may allow the designer to assume that once a fault has occurred, it persists for a certain extended duration or even indefinitely. In this instance a latch-type post-processing may be appropriate. An investigation into such measures is beyond the scope of this work, whose aim is to provide the tools to generate the fault hypotheses.

This chapter has also demonstrated that the proposed design and validation method is largely automatable once the model, perturbations and faults are specified. Since advanced vehicles can have diverse possibilities of sensing and actuation architectures, it precludes the use of FDI schemes developed specifically for the fixed structure of ESP systems on conventional vehicles, for which the sensor cluster architectures and braking actuation schemes are almost identical across most platforms. An automatable toolchain facilitates the systematic design and validation of STM-based fault diagnosis for more complex future architectures, represented in this work by the ROboMObil. The automation also improves the efficiency of the residual structure design. This process requires the determination of a sufficiently large pool of feasible fault signatures, which is obtained through running the residual generator design procedure on a large if not exhaustive set of signature permutations.

The STM-based FDI functions described in this chapter act in concert with the FDI functions based on the nonlinear kinematic model (NKM) to form the the model-based component of the Vehicle Dynamics FDI module. The use of two models allows a wider range of operating conditions to be covered than is possible using either of them alone. A brief practical perspective on the fusion of the diagnostic results from the two modules is given in Section 9.7 of the next chapter, after the presentation of the NKM-based FDI approach.

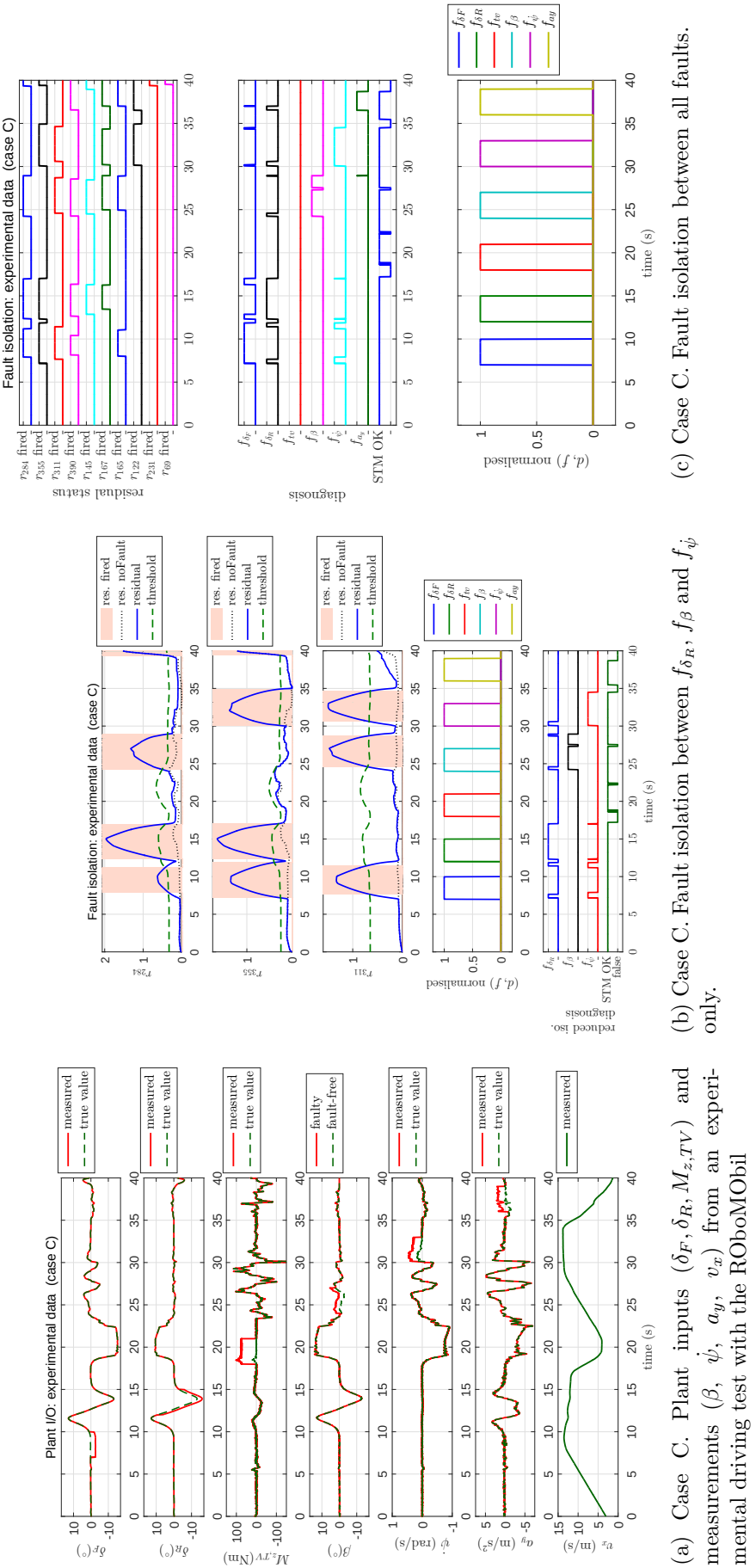

(a) Case C. Plant inputs ($\delta_F, \delta_R, M_{z,TV}$) and measurements ($\beta$, $\dot{\psi}$, a_y, v_x) from an experimental driving test with the ROboMObil

(b) Case C. Fault isolation between f_{δ_R}, f_β and $f_{\dot{\psi}}$ only.

(c) Case C. Fault isolation between all faults.

Figure 8.12: Validation results - experimental data (case C)

Chapter 9

FDI Design Using a Nonlinear Kinematic Model

For the purpose of model-based fault detection, a kinematic model is attractive because the model parameters can be readily and accurately obtained, as they only consist of vehicle geometry parameters. This low level of uncertainty is accompanied by its insensitivity to force and moment disturbances, since by definition a kinematic model does not contain kinetic relationships. On the other hand, a limitation of the kinematic model of horizontal vehicle dynamics is its prerequisite of negligible longitudinal and lateral tyre slips. This restricts its validity region to driving situations with low tyre forces, such as low speed manoeuvring or driving with modest accelerations at higher speeds. These characteristics make them suitable for complementing STM-based fault detectors in order to extend the coverage to a broader range of operating states, as intended by the concept from Section 6.4.3. The STM-based fault detectors were already presented in Chapter 8.

The kinematic FDI concept proposed in this chapter has its foundations in the seminal works of [DFD04; Fis07; Ise06a]. The fault detectors in these works utilise a combination of kinematic and steady state lateral dynamics models that are linearised about the near straight-ahead driving condition for conventional front wheel steered vehicles. These conditions become too restrictive when dealing with a vehicle navigating in tighter environments. This is exacerbated particularly for highly manoeuvrable vehicles such as the ROboMObil, which has large steering angle ranges controlled individually on multiple wheels. To address these challenges, the fault detectors in this chapter make use of a kinematic model without applying linearisations for steering angle trigonometry. It will henceforth be referred to as the nonlinear kinematic model (NKM), and is introduced in Section 9.1.3. This model is still able to provide accurate descriptions of the horizontal velocity relationships when driving on trajectories with high curvature or even predominantly sideways or rotational motion.

In residual-based fault detectors, a fault is deemed to have occurred if the measured values of specified variables deviate by more than a specified threshold from their independently estimated values. Given permissible tolerances on measurement errors and

parameter uncertainties, as well as the extent of violation of the no tyre slip assumption, a common empirical approach would be to choose the threshold by analysing the corresponding distributions of the residual values from Monte-Carlo simulations or experiments. This work proposes an alternative analytical approach for the NKM-based fault detectors, in which the bounded-in-bounded-out (BIBO) paradigm is used to determine the feasibility of a set of measured values under the constraints given by the tolerance bounds and model equations. Furthermore, a metric is proposed to determine whether the steering angles allow the NKM's slip-free assumption to be met. The derivation of this metric also produces estimates of body motion variables from the steering angles only, which offer the basis for further fault detectors.

The chapter begins with a more elaborate explanation of the motivating issue behind the development of the NKM-based FDI (*NKMFDI*). It is followed by some preliminaries, before the problem statement is presented. Subsequently several approaches for fault detection and model validation are derived and analysed. Following this, the kinematic model-based detectors are integrated into a structured residual scheme for fault isolation, before some supervision and implementation aspects are discussed. Validation results using simulation and experimental data are then presented. To conclude, fusion of the diagnostic results with those from *STMFDI* are briefly treated. The content of this chapter is based on the publication [HB16].

9.1 Motivation and Preliminaries

9.1.1 Challenges of High Manoeuvrability

We motivate the technical development with an outline of the fault detection approaches from [DFD04; Fis07]. Both employ essentially the same linear front wheel steered geometric model, whose five model relations are:

$$\text{front wheel speed difference:} \quad s_F\dot{\psi} = r_w(\omega_2 - \omega_1) \tag{9.1}$$

$$\text{rear wheel speed difference:} \quad s_R\dot{\psi} = r_w(\omega_4 - \omega_3) \tag{9.2}$$

$$\text{yaw rate from steering angle:} \quad \dot{\psi} = \frac{v}{l}\delta_F \tag{9.3}$$

$$\text{steady state cornering acceleration:} \quad a_y = v\dot{\psi} \tag{9.4}$$

$$\text{steady state yaw rate with wheel slip:} \quad \dot{\psi} = \frac{\delta_F}{l}\frac{v}{1+\left(\frac{v}{v_{ch}}\right)^2} \tag{9.5}$$

where r_w denotes the wheel radius, s_F (s_R) the front (rear) track, l the wheelbase, and δ_F the steering angle on the front axle. v_{ch} is the *characteristic vehicle velocity* defined in [MW04] as

$$v_{ch} = \sqrt{\frac{c_{\alpha F}c_{\alpha R}l^2}{m(c_{\alpha R}l_r - c_{\alpha F}l_f)}}\,,$$

where m, $c_{\alpha F}$, $c_{\alpha R}$, l_f and l_r are all parameters of the STM and are defined in Table 7.6.

The first two equations rely on a geometric interpretation with small steering angles and predominantly forward motion, while the the third one additionally assumes front wheel only steering. The fourth equation represents the centrifugal component of the lateral acceleration a_y, a relation that holds during steady state cornering and predominantly forward motion. Lastly, the fifth equation describes the steering angle to yaw rate relationship during steady state cornering, using the steady state STM to account for lateral wheel slip. Since this last equation is not a kinematic relation, it will not be considered further in this chapter.

For a vehicle with the high manoeuvrability of the ROboMObil, the linear assumptions of (9.1)-(9.3) are invalid over a large fraction of its motion possibilities. The four individually steered wheels with large angle ranges impart the vehicle with the potential to realise trajectories with high curvatures and body side-slip angles, enabling manoeuvres such as the parking sequence shown in Figure 9.1. When the steering angles are large, the nonlinearities resulting from the trigonometric relations can no longer be linearised and must be handled explicitly. As a result, the kinematic model equations (9.1) - (9.3) are inadequate, necessitating a more general representation of the kinematic relations. The NKM achieves this by additionally employing an intermediate Cartesian velocity-based representation of the wheel variables, rather than directly relating steering angles, wheel speeds and body motion to each other as in [DFD04; Fis07]. Section 9.1.3 describes this model in more detail, after the additional notation used in this chapter is introduced.

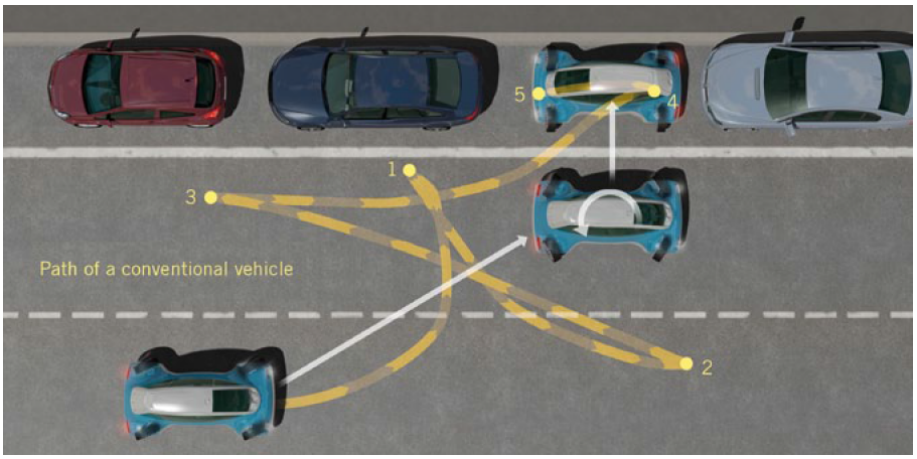

Figure 9.1: Possible parking manoeuvre of the ROboMObil [Sch11]

9.1.2 Notation

Most symbols and variables used in this chapter are already defined in Chapter 7 and listed in Tables 7.6 and 7.7. A selection of the additional ones are listed in Table 9.1, while others are introduced when they are used.

Table 9.1: Table of additional symbols used in this chapter

Symbol	Meaning
$l_*,\ s_*$	(x_U, y_U) coordinates (undercarriage system) of a point $*$
$\boldsymbol{v}_{w,i}$	horizontal velocity vector of the centre of the i-th wheel
$v_{w,i},\ \beta_i$	magnitude and direction (relative to x_U direction) of $\boldsymbol{v}_{w,i}$
$\tilde{v}_{w,i},\ \delta_i$	wheel perimeter speed and steering angle of the i-th wheel
$\Omega_w,\ \Delta_w$	vectors of all wheel velocities ω_i and steering angles δ_i respectively, for $i = 1, \ldots, 4$
$\mathbb{W}$	set of active wheel indices for an instance of fault detector
$y,\ \acute{y}$	nominal (measured) and true values of a sensor output variable y
$\hat{y}$	estimate of y
$p,\ \breve{p}$	nominal and true values of a parameter p
$\bar{e}_*$	upper bound on the error magnitude of variable $*$
r_*	a residual
b_*	a boolean fault status

9.1.3 Nonlinear Kinematic Model (NKM)

The NKM is a control-oriented simplification of the DTM introduced in Chapter 7, reached by extracting only the horizontal dynamics and assuming negligible tyre slips. The resulting planar model is kinematic only and relates body velocities to the wheel rotational velocities and steering angles.

The NKM assumes that the vehicle body obeys planar rigid body kinematics and rotates about an instantaneous centre of rotation (ICR), such that the velocity vector of any point on the body is perpendicular to the line joining it to the ICR. The body velocity vector at the i-th wheel is denoted as $\boldsymbol{v}_{w,i}$, which has magnitude $v_{w,i}$ and direction β_i in the undercarriage coordinate system (see Figure 9.2-right). When there is no tyre slip, these values are equal to the translational speed at the wheel perimeter $\tilde{v}_{w,i}$ and steering angle δ_i respectively. That is, $\beta_i = \delta_i$ and $v_{w,i} = \tilde{v}_{w,i}$, where $\tilde{v}_{w,i} = r_w \omega_i$ with r_w being the effective wheel radius and ω_i being the wheel rotational speed.

For a vehicle with four wheels, this negligible tyre slip assumption (NTSA) is only feasible if the steering angles are set such that all wheel axes intersect at the ICR as shown in Figure 9.2. Such a set of steering angles $\Delta_w = [\delta_1, \delta_2, \delta_3, \delta_4]$ is termed here *Ackermann-consistent*, which refers to an extension to the concept of Ackermann steering for front wheel steered vehicles. Even with independent four wheel steering, this condition will be approximately satisfied in most low to medium speed manoeuvring scenarios, since the minimisation of tyre slip is a usual control objective to reduce energy losses and tyre wear. The NTSA also demands that the wheel speeds $\Omega_w = [\omega_1, \omega_2, \omega_3, \omega_4]$ are proportional to the distance of the wheels from the ICR. This conditioned will be adequately fulfilled when the wheel torques are sufficiently low so that the tyres lie well within their limits of adhesion. A set of values $[\Delta_w, \Omega_w]$ that satisfies these criteria is said to be *no-slip kinematically consistent* (NSKC).

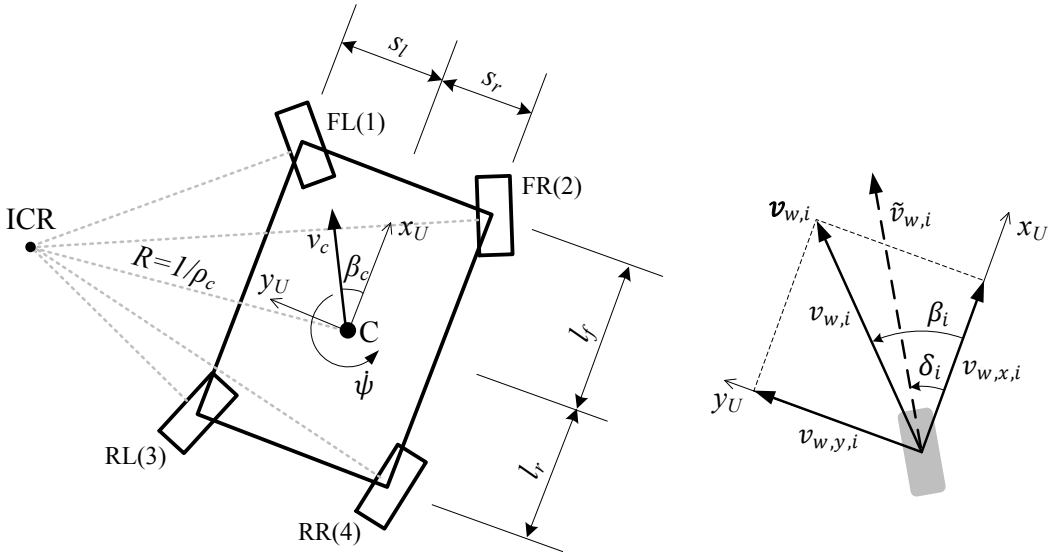

Figure 9.2: Left: NKM with an Ackermann-consistent set of steering angles Δ_w. R and ρ_c denote curve radius and curvature respectively. Right: relationship between the wheel variables.

Referring to the right diagram of Figure 9.2 which depicts the variables at the i-th wheel, β_i and $v_{w,i}$ are related to $\boldsymbol{v}_{w,i} = [v_{w,x,i}\ v_{w,y,i}]^T$ by the polar to Cartesian transformation:

$$\begin{aligned} v_{w,x,i} &= v_{w,i} \cos\beta_i \ , \\ v_{w,y,i} &= v_{w,i} \sin\beta_i \ . \end{aligned} \tag{9.6}$$

The vector $\boldsymbol{v}_w$ containing all wheel centre velocities is related to the generalised body velocity $\boldsymbol{q}_c$ at the vehicle reference point C by (7.17). It is restated here for convenient reference:

$$\boldsymbol{v}_w = \boldsymbol{G}\boldsymbol{q}_c \tag{9.7}$$

where

$$\begin{aligned} \boldsymbol{G} &= \begin{bmatrix} 1 & 0 & 1 & 0 & 1 & 0 & 1 & 0 \\ 0 & 1 & 0 & 1 & 0 & 1 & 0 & 1 \\ -s_1 & l_1 & -s_2 & l_2 & -s_3 & l_3 & -s_4 & l_4 \end{bmatrix}^T \\ \boldsymbol{v}_w &= \begin{bmatrix} v_{w,x,1} & v_{w,y,1} & v_{w,x,2} & v_{w,y,2} & v_{w,x,3} & v_{w,y,3} & v_{w,x,4} & v_{w,y,4} \end{bmatrix}^T \\ \boldsymbol{q}_c &= \begin{bmatrix} v_{c,x} & v_{c,y} & \dot{\psi} \end{bmatrix} \ . \end{aligned}$$

(l_i, s_i) is the coordinate pair for the i-th wheel centre in the (x_U, y_U) coordinate system. In this chapter, the wheel arrangement will be assumed to be rectangular as illustrated in

Figure 9.2, which yields

$$\begin{bmatrix} l_1 \\ l_2 \\ l_3 \\ l_4 \end{bmatrix} = \begin{bmatrix} l_f \\ l_f \\ -l_r \\ -l_r \end{bmatrix}, \qquad \begin{bmatrix} s_1 \\ s_2 \\ s_3 \\ s_4 \end{bmatrix} = \begin{bmatrix} s_l \\ -s_r \\ s_l \\ -s_r \end{bmatrix}.$$

In a general vehicle configuration, body motion sensors are not necessarily all located at reference point C. Such sensors augment the model in a manner that can be represented in two ways. Let the (x_U, y_U) location of a general sensor σ be (s_σ, l_σ) as illustrated in Figure 9.3. The IMU and optical velocity sensor are denoted with $\sigma = im$ and $\sigma = os$ respectively and their approximate location on the ROboMObil are also shown in the figure.

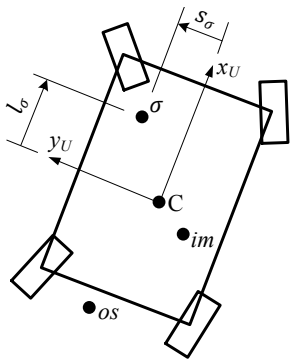

Figure 9.3: Location parameters for a general body motion sensor σ

The first representation form computes $\boldsymbol{v}_w$ and the generalised velocity vector at each body sensor location $\boldsymbol{q}_{im},\ \boldsymbol{q}_{os}$ from the velocity $\boldsymbol{q}_c$ at C:

$$\begin{bmatrix} \boldsymbol{v}_w \\ \boldsymbol{q}_{im} \\ \boldsymbol{q}_{os} \end{bmatrix} = \boldsymbol{G}_{as}\boldsymbol{q}_c \tag{9.8}$$

where

$$\boldsymbol{q}_{im} = \begin{bmatrix} v_{x,im} \\ v_{y,im} \\ \dot{\psi}_{im} \end{bmatrix}, \quad \boldsymbol{q}_{os} = \begin{bmatrix} v_{x,os} \\ v_{y,os} \\ \dot{\psi}_{os} \end{bmatrix}, \quad \boldsymbol{G}_{as} = \begin{bmatrix} \boldsymbol{G} \\ \boldsymbol{G}_{im,c} \\ \boldsymbol{G}_{os,c} \end{bmatrix}$$

$$\boldsymbol{G}_{\sigma,c} = \begin{bmatrix} 1 & 0 & -s_\sigma \\ 0 & 1 & l_\sigma \\ 0 & 0 & 1 \end{bmatrix}, \ \sigma \in \{im,\ os\}\ .$$

The second representation form eliminates the unmeasured variable $\boldsymbol{q}_c$ and replaces it with an equation for each body sensor location:

$$\boldsymbol{v}_w = \boldsymbol{G}_\sigma \boldsymbol{q}_\sigma, \quad \sigma \in \{im,\ os\} \tag{9.9}$$

where

$$\boldsymbol{G}_\sigma = \boldsymbol{G}_c \boldsymbol{G}_{\sigma,c}^{-1} = \begin{bmatrix} 1 & 0 & (s_\sigma - s_1) \\ 0 & 1 & (-l_\sigma + l_1) \\ 1 & 0 & (s_\sigma - s_2) \\ 0 & 1 & (-l_\sigma + l_2) \\ 1 & 0 & (s_\sigma - s_3) \\ 0 & 1 & (-l_\sigma + l_3) \\ 1 & 0 & (s_\sigma - s_4) \\ 0 & 1 & (-l_\sigma + l_4) \end{bmatrix} .$$

In summary, the full NKM for describing the kinematic analytical redundancy on a vehicle is a map between $\boldsymbol{q}_\sigma$, $\sigma \in \{im, os\}$ and $\{\Delta_w, \Omega_w\}$. It consists of the wheel variable transformation (9.6), the NTSA (such that $v_{w,i} = \tilde{v}_{w,i}$ and $\beta_i = \delta_i$ for $i = 1, \ldots, 4$) and the rectilinear rigid body kinematics equations (9.9) at each sensor σ.

9.1.4 Motivation: Simple Fault Detection Using Static Parity Relations

An intuitive way to implement fault detectors based on the NKM would be to first transform the steering angles Δ_w and wheel speeds Ω_w into wheel centre velocities $\boldsymbol{v}_w$ with the trigonometric relations (9.6). Then, using (9.9), subsets of the measurement variables can be estimated using an independent subset, and residuals are defined as the difference between the measured and estimated values. This could be performed for the following pairs of variables sets:

$$\text{residual in } \boldsymbol{v}_w: \quad \boldsymbol{r}_w = \boldsymbol{v}_w - \hat{\boldsymbol{v}}_w \quad = \boldsymbol{v}_w - \boldsymbol{G}\boldsymbol{q}_c \tag{9.10}$$

$$\text{residual in } \boldsymbol{q}_c: \quad \boldsymbol{r}_q = \boldsymbol{q}_c - \hat{\boldsymbol{q}}_c \quad = \boldsymbol{q}_c - \boldsymbol{G}^+\boldsymbol{v}_w \tag{9.11}$$

$$\text{residual in } \boldsymbol{v}_{w,i}: \quad \boldsymbol{r}_{w,i} = \boldsymbol{v}_{w,i} - \hat{\boldsymbol{v}}_{w,i} = \boldsymbol{v}_{w,i} - \boldsymbol{G}_i \boldsymbol{G}_{jkl}^+ \boldsymbol{v}_{w(jkl)} \tag{9.12}$$

where $\hat{y}$ denotes an estimate of a variable y and $\boldsymbol{A}^+$ denotes the Moore-Penrose pseudo-inverse of matrix $\boldsymbol{A}$. The first and third residuals differ in that the first one estimates $\boldsymbol{v}_w$ from $\boldsymbol{q}_c$, while the third one estimates wheel velocity $\boldsymbol{v}_{w,i}$ at one wheel from velocities at other wheels. Using different combinations of variables in the estimates achieves a variety of fault sensitivities in the residuals, providing the basis for fault isolation using structured residuals.

The residuals (9.10)-(9.12) represent the deviation from the measurement to the nominal estimate. To avoid false alarms, the thresholds must lie above maximum possible residual values in fault-free operation. Their deviations from zero may be caused by measurement tolerances due to imperfect sensors, model uncertainty, or violation of model assumptions. With regard to model uncertainties, while the horizontal vehicle geometric parameters are accurately measurable and the errors can be considered negligible, the wheel radius r_w can vary over a vehicle's lifetime. Furthermore, since pneumatic tyres can only transmit force to the road in the presence of tyre slip, some slip and therefore

mild breaches of the NTSA is inevitable even when operating with low accelerations. The simple residual-based approach does not suggest any means for determining appropriate residual threshold values.

Using knowledge of sensor, vehicle, and tyre properties, while restricting the fault detectors to only operate under low acceleration conditions, bounds may be set on sensor noise and bias, wheel radius variations, and tyre slip. It would be efficient to analytically derive thresholds and other relevant fault detector parameters from this knowledge, with the benefit that input-dependent thresholds can be employed to improve fault sensitivity. Therefore it is preferable to derive thresholds in this manner, rather than resorting to the common approaches of Monte-Carlo methods or other empirical means as mentioned in the introduction to this chapter.

An additional difficulty posed by individually steered vehicles is the potential for non-Ackermann-consistent angles to be commanded. Satisfaction of the NTSA, which is a prerequisite for the validity of kinematic vehicle models, requires the set of steering angles to be Ackermann-consistent. When using NKM-based fault detectors, NTSA violations must be detected to prevent false alarms from being raised. In the same vein, it is also crucial to recognise driving situations with potentially high tyre slips and deactivate the detectors accordingly. Methods to address these challenges are proposed in this chapter.

9.1.5 Problem Statement

In this section, we seek a flexible sensor fault detection and isolation approach that may be applied on vehicles with ROboMObil-like architectures as well as more conventional architectures for control, actuation and sensing. The sensor availability on three example vehicle classes is shown in Table 9.2.

Table 9.2: Measurement availability in selected vehicle architecture classes. •: available, ✓: the value is available and verified by local sensor monitoring

		Δ	Ω	$v_{\sigma,x}$	$v_{\sigma,y}$	$\dot{\psi}_\sigma$	$a_{\sigma,y}$	$a_{\sigma,x}$
1	Conventional road car with ESP	•	•			•	•	•
2	ROboMObil (with in-wheel traction drive)	•	✓	•	•	•	•	•
3	ROboMObil-like with central traction drive	•	•	•	•	•	•	•

The rest of this chapter addresses the third option, the fictive ROboMObil-like architecture with a centralised traction drive replacing the in-wheel motors. From a fault diagnosis perspective, this differs from the ROboMObil only in that the wheel speeds measurements cannot be locally verified, thus wheel speed faults must be diagnosed at the vehicle level. This choice is made to ensure that all potential faults from the three listed architectures are covered. With respect to body motion measurements, the ROboMObil has the vector:

$$\boldsymbol{y}_{romo} = [v_{os,x}\ v_{os,y}\ \dot{\psi}_{im}\ a_{im,x}\ a_{im,y}]^T\ . \tag{9.13}$$

However, to maintain the general applicability for more conventional vehicles, the FDI design shall not demand that measurements of the velocities in all three horizontal DOFs $v_x,\ v_y,\ \dot{\psi}$ are available.

To sum up, the goal of this work is to detect and isolate faults in sensors of this third architecture. Their corresponding additive fault variables are listed in Table 9.3 below.

Table 9.3: Sensor faults to be detected and isolated using the *NKMFDI*

fault name	**sensor variable**	**additive fault variable**
steering angle fault (i-th wheel)	δ_i	f_{δ_i}
wheel speed fault (i-th wheel)	ω_i	f_{ω_i}
optical sensor v_x fault	$v_{os,x}$	$f_{v_{os,x}}$
optical sensor v_y fault	$v_{os,y}$	$f_{v_{os,y}}$
IMU $\dot{\psi}$ fault	$\dot{\psi}_{im}$	$f_{\dot{\psi}_{im}}$
IMU a_x fault	$a_{im,x}$	$f_{a_{im,x}}$
IMU a_y fault	$a_{im,y}$	$f_{a_{im,y}}$

Just like in the *STMFDI*, it is assumed that only a single fault may occur at any time, and that the fault may be considered persistent with an additive manifestation as explained in Section 7.4. False alarms shall be avoided by robustly incorporating knowledge about the uncertainties and disturbances into the detector design, and also by monitoring the validity of the NKM. The NKM-based FDI and monitoring functions will be referred to by the name of *NKMFDI*.

9.2 Fault Detector Design

The development takes the following approach. Multiple types of fault detectors are first introduced to take advantage of the analytical redundancy offered by different sensor combinations, which then enables fault isolation using structured residuals. The detectors can be divided into these categories:

1. using wheel speeds and steering angles (Section 9.2.2) - transforms the wheel speeds and steering angles into Cartesian wheel velocities before asserting their consistency among each other or against body motion sensor measurements. These are the most important NKM-based detectors for fault isolation. Their outputs are Boolean variables rather than residuals.
2. using steering angles only (Section 9.2.3) - calculates the path geometry using the steering angles only, and offers consistency checks against *ratios* between body velocity measurements. The outputs are conventional residuals.
3. body motion sensors only (Section 9.2.4) - the residual outputs indicate the consistency among the body velocity and acceleration measurements.

Additionally, a metric for evaluating the Ackermann consistency of the steering angles is developed together with the steering angle only fault detectors in Section 9.2.3. The

equations defining detector outputs and metrics are highlighted with boxes for ease of reading. Fault isolation using structured residuals and the validity criteria will be covered in Section 9.3 and Section 9.5.1 respectively.

We begin with the detectors in the first group, those using both wheel speeds and steering angles. The principle behind the development of these fault detectors is to derive tight tests of consistency between sets of measurements. These tests take the form of either comparison of a scalar measurement to thresholds, or direct constraint satisfaction problems. The development follows a deterministic paradigm, in which the permissible values of uncertainties and unknowns are considered bounded. Fault sensitivity is not explicitly considered at detector design stage, but rather analysed after a fault detector has been created. Before we derive the fault detectors, Section 9.2.1 first studies the potential sources of deviations of the real vehicle behaviour from that of the nominal model and parameters during low speed manoeuvring. Constraints are then formulated to describe the bounds on these deviations.

9.2.1 Constraints on the Deviations

The most significant deviations stem from three different types of sources: measurement tolerances, parameter uncertainties, and violation of model assumptions. Each type is described separately below before constraints on the combined deviations are given.

Measurement Tolerances

Discrepancies between the output signal of a fault-free sensor and the true value of the measured variable may arise through tolerated bias and gain errors due to finite measurement and calibration accuracy, imperfect mounting orientation, and measurement noise. It will be assumed that bounding values are available for deviations due to these sources. Then for any fault-free sensor, with y denoting its output signal and $\acute{y}$ the true variable value, the values satisfy

$$|\acute{y} - y| \leq \bar{e}_y \tag{9.14}$$

where $\bar{e}_y$ is the upper bound on the magnitude of combined sensor tolerances. The output value y will also be referred to as the *nominal* or *measured* value.

Parameter Uncertainties

It is assumed that the wheel location parameters $[l_f, l_r, s_l, s_r]$ and sensor locations (s_σ, l_σ), $\sigma \in \{im, os\}$ can be determined with sufficient accuracy by measurement or from construction data, which leaves the parameter uncertainties in the effective wheel radius $r_{w,i}$ for each wheel. This may vary due to tyre dimension tolerances, tyre pressure, as well as its rolling properties. For a vehicle that is fit for operation, it can be assumed that its true value

$\check{r}_{w,i}$ at the i-th wheel is close to the nominal value r_w such that

$$|r_w - \check{r}_{w,i}| \leq \bar{e}_{r_w} \tag{9.15}$$

where $\bar{e}_{r_w}$ is the upper bound on the wheel radius deviation magnitude. Due to this effect and the measurement tolerance on the wheel speed ω_i, the true wheel speed $\acute{v}_{w,i}$ has a bounded deviation from its nominal value $\tilde{v}_{w,i}$:

$$\begin{aligned} |\acute{v}_{w,i} - \tilde{v}_{w,i}| &= |\check{r}_{w,i}\acute{\omega}_i - r_w\omega_i| \\ &\lesssim r_w\bar{e}_\omega + \bar{e}_{r_w}\,|\omega_i| \ , \end{aligned} \tag{9.16}$$

where $\bar{e}_\omega$ denotes the wheel speed sensor tolerance, following the notation in (9.14).

Violation of Assumptions

The central assumption of the NKM is that of zero tyre slip, but even at low accelerations a small but non-negligible amount of tyre slip is inevitable. Under these conditions, the tyres operate in the quasi-linear regions of their tyre force characteristics, where slip is approximately proportional to the transmitted force. Therefore, limiting the maximum accelerations and wheel torques in the validity region of the fault detector allows a bound to be set on the longitudinal and lateral tyre slips. Longitudinal tyre slip results in a deviation of the wheel centre velocity magnitude $v_{w,i}$ from the true wheel perimeter speed $\acute{v}_{w,i}$. Longitudinal slip is defined as (see (7.29b)):

$$\begin{aligned} s_{v,i} &= \frac{v_{w,i} - \acute{v}_{w,i}}{v_{w,i}} \\ &\approx \frac{v_{w,i} - \acute{v}_{w,i}}{\acute{v}_{w,i}} \qquad \text{for small slips.} \end{aligned} \tag{9.17}$$

Similarly, lateral tyre slip leads to a deviation of the wheel centre velocity direction β_i from the steering angle δ_i:

$$\alpha_i = \beta_i - \delta_i \ , \tag{9.18}$$

where α_i is commonly known as the slip angle.

Letting the slips be bounded by $|s_{v,i}| < \bar{e}_{sv,i}$ and $|\alpha_i| < \bar{e}_{\alpha_i}$ results in:

$$|v_{w,i} - \acute{v}_{w,i}| < \bar{e}_{sv,i}\,|\acute{v}_{w,i}| \tag{9.19}$$

$$|\beta_i - \delta_i| < \bar{e}_{\alpha_i} \tag{9.20}$$

Since longitudinal tyre slip is approximately proportional to the applied wheel torque, $\bar{e}_{sv,i}$ may be set to be dependent on wheel torque $M_{w,i}$ when this measurement is available:

$$\bar{e}_{sv,i} = \bar{e}_{svn}M_{w,i} \tag{9.21}$$

where $\bar{e}_{svn}$ denotes the proportionality constant.

Combined Bounds

By aggregating the three categories of deviation sources, the total bounds on the fault-free deviations can now be expressed. For the body motion sensors, the only source is measurement tolerance. Hence under fault-free conditions we can write for the j-th element $q_{\sigma,j}$ of the measurement vector $\boldsymbol{q}_\sigma$:

$$q_{\sigma,j} \in [\acute{q}_{\sigma,j} - \bar{e}_{q_{\sigma,j}},\ \acute{q}_{\sigma,j} + \bar{e}_{q_{\sigma,j}}] \ . \tag{9.22}$$

The deviation of the true wheel centre velocity magnitude $v_{w,i}$ from the nominal wheel perimeter speed $\tilde{v}_{w,i}$ consists of a combination of measurement error, parameter uncertainty and longitudinal tyre slip. Summing the contributions from (9.16) and (9.19) yields the expression:

$$v_{w,i} \in [\underbrace{\tilde{v}_{w,i} - \bar{e}_{v,i}}_{\underline{v}_{w,i}},\ \underbrace{\tilde{v}_{w,i} + \bar{e}_{v,i}}_{\overline{v}_{w,i}}] \tag{9.23}$$

where

$$\bar{e}_{v,i} = r_w \bar{e}_\omega + \bar{e}_{r_w}\,|\omega_i| + \bar{e}_{sv,i} r_w |\acute{\omega}_i| \tag{9.24a}$$

$$\approx r_w \bar{e}_\omega + (\bar{e}_{r_w} + \bar{e}_{sv,i} r_w)|\omega_i| \ . \tag{9.24b}$$

The bound $\bar{e}_{v,i}$ is calculated by observing that $|\tilde{v}_{w,i} - v_{w,i}| \leq |\tilde{v}_{w,i} - \acute{v}_{w,i}| + |\acute{v}_{w,i} - v_{w,i}|$ by the triangle inequality, and substituting in (9.16) and (9.19). The approximation from (9.24a) to (9.24b) is valid for small tolerances. The grouping in the (9.24b) highlights that the error bound $\bar{e}_{v,i}$ comprises an absolute (speed-independent) and a relative (speed-dependent) component.

Finally, the deviation of a wheel centre velocity direction β_i from its measured value δ_i is a combination of measurement error and lateral tyre slip. These can be expressed by:

$$\beta_i \in [\underbrace{\delta_i - \bar{e}_{\delta,i}}_{\underline{\beta}_i},\ \underbrace{\delta_i + \bar{e}_{\delta,i}}_{\overline{\beta}_i}] \tag{9.25}$$

where

$$\bar{e}_{\delta,i} = \bar{e}_\delta + \bar{e}_{\alpha,i} \ .$$

Wheel Velocity Bounds in xy-Coordinates

For the application of the linear equations (9.8) and (9.9), the above tolerances for $v_{w,i}$ and β_i have to be transformed from polar coordinates into the (x_U, y_U) coordinate system.

Considering the $v_{w,i}$ and β_i deviations to be independent gives the Cartesian tolerance region $\mathbb{V}_{w,i}$ for $\boldsymbol{v}_{w,i}$ shown in Figure 9.4.

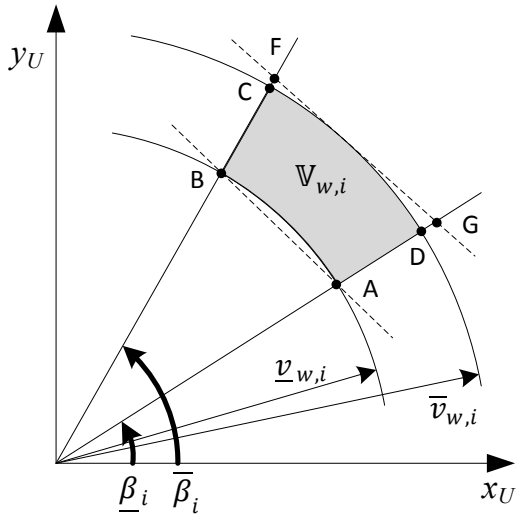

Figure 9.4: Construction of the (shaded) tolerance region $\mathbb{V}_{w,i}$ for $\boldsymbol{v}_{w,i}$, which is fully contained within its polytopic convex hull BAGF

It is clear by inspection that the constraint $\boldsymbol{v}_{w,i} \in \mathbb{V}_{w,i}$ is nonlinear and non-convex. To facilitate solutions to the upcoming feasibility and optimisation problems, it is approximated by linear convex constraints that restrict $\boldsymbol{v}_{w,i}$ to lie in a convex bounding polygon for $\mathbb{V}_{w,i}$. The construction of this polygon, denoted BAGF, is illustrated in Figure 9.4. There, the line GF is tangent with arc CD at its midpoint. The vertices of BAGF have the coordinates:

$$
\begin{aligned}
B &: \left[\underline{v}_{w,i}\cos\overline{\beta}_i,\ \underline{v}_{w,i}\sin\overline{\beta}_i\right] \\
A &: \left[\underline{v}_{w,i}\cos\underline{\beta}_i,\ \underline{v}_{w,i}\sin\underline{\beta}_i\right] \\
G &: \left[\overline{v}_{w,i}\frac{\cos\underline{\beta}_i}{\cos\left(\frac{\underline{\beta}_i+\overline{\beta}_i}{2}\right)},\ \overline{v}_{w,i}\frac{\sin\underline{\beta}_i}{\cos\left(\frac{\underline{\beta}_i+\overline{\beta}_i}{2}\right)}\right] \\
F &: \left[\overline{v}_{w,i}\frac{\cos\overline{\beta}_i}{\cos\left(\frac{\underline{\beta}_i+\overline{\beta}_i}{2}\right)},\ \overline{v}_{w,i}\frac{\sin\overline{\beta}_i}{\cos\left(\frac{\underline{\beta}_i+\overline{\beta}_i}{2}\right)}\right] .
\end{aligned}
$$

The constraint that $\boldsymbol{v}_{w,i}$ lies within the region BAGF can be written as four linear inequalities, each expressing the constraint for $\boldsymbol{v}_{w,i}$ to lie on the side of the lines BA, AG, GF and FB respectively that correspond to the interior of BAGF:

$$
\boldsymbol{P}_k\boldsymbol{v}_{w,i} \leq \boldsymbol{Q}_k,\ k \in \{\mathrm{BA}, \mathrm{AG}, \mathrm{GF}, \mathrm{FB}\}\ . \tag{9.26}
$$

This can then be generalised to multiple wheels. To enhance readability, the following expressions are given for the wheel set $\mathbb{W} = \{1, 2, 3, 4\}$, although they are applicable to $\mathbb{W}$ containing any subset of wheel indices. The constraint that the wheels $i \in \mathbb{W}$ each satisfies $\boldsymbol{v}_{w,i} \in \mathbb{V}_{w,i}$ can be expressed as:

$$\boldsymbol{v}_{w,\mathbb{W}} \in \mathbb{V}_{w,\mathbb{W}} \tag{9.27}$$

where

$$\begin{aligned} \mathbb{V}_{w,\mathbb{W}} &= \mathbb{V}_{w,1} \times \mathbb{V}_{w,2} \times \mathbb{V}_{w,3} \times \mathbb{V}_{w,4} \\ \boldsymbol{v}_{w,\mathbb{W}} &= \begin{bmatrix} \boldsymbol{v}_{w,1}^T & \boldsymbol{v}_{w,2}^T & \boldsymbol{v}_{w,3}^T & \boldsymbol{v}_{w,4}^T \end{bmatrix}^T . \end{aligned}$$

Then, the nonlinear constraint (9.27) can be approximated by applying (9.26) on all $i \in \mathbb{W}$ and combining them into the linear inequality constraint:

$$\boldsymbol{P}_{\mathbb{W}} \boldsymbol{v}_{w,\mathbb{W}} \leq \boldsymbol{Q}_{\mathbb{W}} , \tag{9.28}$$

where

$$\begin{aligned} \boldsymbol{P}_{\mathbb{W}} &= diag(\boldsymbol{P}_1, \boldsymbol{P}_2, \boldsymbol{P}_3, \boldsymbol{P}_4) \\ \boldsymbol{Q}_{\mathbb{W}} &= \begin{bmatrix} \boldsymbol{Q}_1^T & \boldsymbol{Q}_2^T & \boldsymbol{Q}_3^T & \boldsymbol{Q}_4^T \end{bmatrix}^T . \end{aligned}$$

9.2.2 Fault Detectors from Wheel Variables

Armed with the linear inequality constraints to represent the tolerance regions of each variable of the NKM, we now move to derive the fault detectors. They are designed to assess the compatibility between NSKC-compliance and the requirement for each variable to lie within its tolerance region, the former being represented as equality constraint (9.8) or (9.9). The fault detectors answer the following two questions to verify the feasibility that a set of variable values is produced by fault-free sensors:

1. *NSKC Check*: Given a subset of variables from $\boldsymbol{y} \subseteq \boldsymbol{v}_{w,\mathbb{W}}$, is there a set of values lying within their respective tolerance regions such that the NSKC-constraint (9.8) is fulfilled?
2. *Body Velocity Check:* Given a scalar body velocity variable $q_{\sigma,j}$ and a subset of wheels $\mathbb{W}$, does the value of $q_{\sigma,j}$ lie within an interval that is consistent with the measurement tolerances $\bar{e}_{q_{\sigma,j}}$, $\boldsymbol{v}_{w,\mathbb{W}} \in \mathbb{V}_{w,\mathbb{W}}$ and NSKC-constraints (9.9)?
3. *Body Acceleration Check:* same as the *Body Velocity Check*, replacing $q_{\sigma,j}$ with acceleration variables $a_{\sigma,k}$.

The first question corresponds to a feasibility problem with a Boolean fault indicator output, while the second and third questions can be simplified into checking whether the scalar measurement $q_{\sigma,j}$ / $a_{\sigma,k}$ lies between feasible upper and lower bounds. The Body

Velocity and Acceleration Checks have similarities to residual-based approaches, but their outputs are nonetheless presented as Boolean decisions. The Boolean outputs follow the convention that a true value indicates an inconsistency / faulty condition.

NSKC Check

Consider $\boldsymbol{v}_{w,\mathbb{W}}$ for $\mathbb{W} \subseteq \{1,2,3,4\}$, with $n_{\mathbb{W}}$ being the length of $\mathbb{W}$. Let $\boldsymbol{G}_s$ consist of the rows of $\boldsymbol{G}_{as}$ such that $\boldsymbol{v}_{w,\mathbb{W}} = \boldsymbol{G}_s \boldsymbol{q}_c$. The *NSKC Check* searches for a feasible solution for $\boldsymbol{v}_{w,\mathbb{W}}$ under these two constraints:

1. $\boldsymbol{P}_{\mathbb{W}} \boldsymbol{v}_{w,\mathbb{W}} \leq \boldsymbol{Q}_{\mathbb{W}}$ (see (9.28))
2. $\boldsymbol{v}_{w,\mathbb{W}} \in \text{col}(\boldsymbol{G}_s)$ where $\text{col}(\boldsymbol{G}_s) : \{\boldsymbol{y} | \boldsymbol{y} = \boldsymbol{G}_s \boldsymbol{q}_c,\ \boldsymbol{q}_c \in \mathbb{R}^3\}$ denotes the *column space* of $\boldsymbol{G}_s$.

Requirement 2 can be expressed as a set of $(2n_{\mathbb{W}} - 3)$ equality constraints by defining a matrix $N_G \in \mathbb{R}^{(2n_{\mathbb{W}}-3, n_{\mathbb{W}})}$ whose rows form a null space basis to $\text{col}(\boldsymbol{G}_s)$. The equality constraint is:

$$N_G \boldsymbol{v}_{w,\mathbb{W}} = 0 \ . \tag{9.29}$$

The set of $\boldsymbol{v}_{w,\mathbb{W}}$ satisfying the two above constraints is denoted by $\mathcal{C}_{\mathbb{W}}$. The Boolean output of the *NSKC Check* is defined as:

$$\boxed{b_{nskc,\mathbb{W}} := (\mathcal{C}_{\mathbb{W}} = \emptyset) \ .} \tag{9.30}$$

The computation of $b_{nskc,\mathbb{W}}$ is a linear programming (LP) feasibility problem that can be solved efficiently.

Body Velocity Check

The *Body Velocity Check* asserts that the measured value of a body velocity variable $q_{\sigma,j}$ is taken to lie within its permissible bounds, whose values are based on (9.22). In this equation, the true variable value $\acute{q}_{\sigma,j}$ lies within its feasible interval $[\underline{\hat{q}}_{\sigma,j,\mathbb{W}},\ \overline{\hat{q}}_{\sigma,j,\mathbb{W}}]$, which contains the range of values that are consistent with NSKC wheel velocities given by $\boldsymbol{v}_{w,\mathbb{W}} \in \mathcal{C}_{\mathbb{W}}$. The *Body Velocity Check* is expressed more precisely as asserting that:

$$\underline{q}_{\sigma,j} \leq q_{\sigma,j} \leq \overline{q}_{\sigma,j} \tag{9.31}$$

where

$$\underline{q}_{\sigma,j,\mathbb{W}} = \underline{\hat{q}}_{\sigma,j,\mathbb{W}} - \bar{e}_{\sigma,j} \tag{9.32}$$

$$\overline{q}_{\sigma,j,\mathbb{W}} = \overline{\hat{q}}_{\sigma,j,\mathbb{W}} + \bar{e}_{\sigma,j} \tag{9.33}$$

$$\underline{\hat{q}}_{\sigma,j,\mathbb{W}} = \min_{\boldsymbol{v}_{w,\mathbb{W}} \in \mathcal{C}_{\mathbb{W}}} (\boldsymbol{G}_{\sigma}^{+})_j \boldsymbol{v}_{w,\mathbb{W}} \tag{9.34}$$

$$\overline{\hat{q}}_{\sigma,j,\mathbb{W}} = \max_{\boldsymbol{v}_{w,\mathbb{W}} \in \mathcal{C}_{\mathbb{W}}} (\boldsymbol{G}_{\sigma}^{+})_j \boldsymbol{v}_{w,\mathbb{W}} \tag{9.35}$$

and $(\boldsymbol{G}_{\sigma}^{+})_j$ denotes the row of the pseudo-inverse $\boldsymbol{G}_{\sigma}^{+}$ corresponding to the $q_{\sigma,j}$. It should be noted that since $\boldsymbol{v}_{w,\mathbb{W}}$ is constrained to the column space of $\boldsymbol{G}_{\sigma}$, the expression $(\boldsymbol{G}_{\sigma}^{+})_j \boldsymbol{v}_{w,\mathbb{W}}$ produces an exact inverse, i.e. $\boldsymbol{G}_{\sigma}\boldsymbol{G}_{\sigma}^{+}\boldsymbol{v}_{w,\mathbb{W}} = \boldsymbol{v}_{w,\mathbb{W}}$. Expressions (9.34) and (9.35) represent LP optimisation problems that can be solved efficiently.

Note that the *Body Velocity Check* is only defined if $b_{nskc,\mathbb{W}} = 0$. Otherwise $\mathcal{C}_{\mathbb{W}} = \emptyset$ and $\underline{\hat{q}}_{\sigma,j,\mathbb{W}}$, $\overline{\hat{q}}_{\sigma,j,\mathbb{W}}$ are undefined.

The Boolean output of the *Body Velocity Check* is given by:

$$\boxed{b_{B\{\mathbb{W}\}\{k\}} := \sim \left(\underline{q}_{\sigma,j,\mathbb{W}} \leq q_{\sigma,j} \leq \overline{q}_{\sigma,j,\mathbb{W}} \right) \ ,} \tag{9.36}$$

where $\sim$ denotes the negation operator and $k = 1, 2, 3$ refers to the position of the corresponding velocity variables $q_{\sigma,j}$ in the $\boldsymbol{y}_{romo}$ vector:

$$\begin{aligned} k = 1 \quad &\longrightarrow \quad q_{\sigma,j} = v_{os,x} \\ k = 2 \quad &\longrightarrow \quad q_{\sigma,j} = v_{os,y} \\ k = 3 \quad &\longrightarrow \quad q_{\sigma,j} = \dot{\psi}_{im} \ . \end{aligned}$$

$\mathbb{W} \subseteq \{1, 2, 3, 4\}$ denotes the subset of wheel variables used, while the subscript B is the designation for the *Body Velocity / Acceleration Check* detectors.

Body Acceleration Check

According to the problem definition, not only do faults in the body velocity sensors need to be detected, but also those in the acceleration sensors. The horizontal accelerations of the ROboMObil are measured in the IMU, corresponding to the variables $a_{im,x}$ and $a_{im,y}$. Since these are not velocity variables, they cannot be directly handled using the kinematic model equation referenced to the IMU (see (9.9)). However, under certain conditions, the body accelerations are dominated by the steady-state cornering terms that are products of variables from the $\boldsymbol{q}_{im}$ vector, thus allowing bounds to be set.

Let us first examine the lateral acceleration. The subscript im will be omitted in this section for notational clarity. The acceleration a_y can be expressed as:

$$a_y = \dot{v}_y \underbrace{+ v_x \dot{\psi}}_{a_{y,s}} \tag{9.37}$$

where $a_{y,s}$ denotes the steady-state cornering component.

The conditions under which $\dot{v}_y$ will be small can be deduced from its following expansion. Denote the body speed as $v = \sqrt{v_x^2 + v_y^2}$, and write $v_y = v \sin(\beta)$. Applying the product rule for differentiation yields:

$$\dot{v}_y = \dot{v} \sin(\beta) + v \dot{\beta} \cos(\beta) \tag{9.38}$$

Then $\dot{v}_y$ will be small when both terms are small, i.e. either:

1. $\dot{\beta}$ and $\dot{v}$ are small, or
2. $\dot{\beta}$ and β are small.

The conditions are fulfilled for the first case during smooth parking manoeuvres in which accelerations are generally limited to low values, whereas the second case applies to conventional driving with predominantly forward motion and low rate of change of the steering angles. By specifying bounds on $\dot{\beta}$, β and $\dot{v}$ for the operating conditions of the fault detector, the term $\dot{v}_y$ can be bounded by $|\dot{v}_y| \leq \bar{e}_{\dot{v}_y}$ and treated as part of the measurement tolerance of a_y. The compliance with these bounds can be monitored using only $\{\Delta_w, \Omega_w\}$ and their derivatives, which can be incorporated into the validity check.

We now consider the steady-state cornering term $a_{y,s} = v_x \dot{\psi}$. In the previous section maximum and minimum estimates for the body velocities were determined from the wheel variables. Using the notation from (9.34) and (9.35), we can write $v_x \in \mathcal{V}_x,\ \dot{\psi} \in \Psi$, where $\mathcal{V}_x = [\underline{\hat{v}}_x,\ \overline{\hat{v}}_x]$ and $\Psi = [\underline{\hat{\dot{\psi}}},\ \overline{\hat{\dot{\psi}}}]$. The bilinear expression $a_{y,s} = v_x \dot{\psi}$ takes on its minimum and maximum values at vertices of the set $\mathcal{V}_x \times \Psi$. This can be expressed as:

$$\underline{\hat{a}}_{y,s} \leq a_{y,s} \leq \overline{\hat{a}}_{y,s} \tag{9.39}$$

where $\underline{\hat{a}}_{y,s},\ \overline{\hat{a}}_{y,s}$ are the minimum and maximum bounds on $a_{y,s}$ calculated from the wheel variables.

The fault-free measurement a_y is then bounded by:

$$\underline{a}_y \leq a_y \leq \overline{a}_y$$

where

$$\underline{a}_y = \underline{\hat{a}}_{y,s} - \bar{e}_{\dot{v}_y} - \bar{e}_{a_y}$$
$$\overline{a}_y = \overline{\hat{a}}_{y,s} + \bar{e}_{\dot{v}_y} + \bar{e}_{a_y}$$

and $\bar{e}_{a_y}$ denotes the measurement tolerance of a_y.

Bounds on the longitudinal acceleration can be determined using a similar treatment, starting from the expression:

$$a_x = \dot{v}_x \underbrace{-v_y\dot{\psi}}_{a_{x,s}} \tag{9.40}$$

where $a_{x,s}$ denotes the steady-state cornering term.

In summary, the Boolean outputs of the *Body Acceleration Check* are given by:

$$\boxed{b_{B\{\mathbb{W}\}\{4\}} = \sim \left(\underline{\hat{a}}_{x,s} \leq a_{x,s} \leq \overline{\hat{a}}_{x,s}\right)} \tag{9.41a}$$

$$\boxed{b_{B\{\mathbb{W}\}\{5\}} = \sim \left(\underline{\hat{a}}_{y,s} \leq a_{y,s} \leq \overline{\hat{a}}_{y,s}\right)} \tag{9.41b}$$

The subscripts 4 and 5 denote the indices of $a_{im,x}$ and $a_{im,y}$ in the $\boldsymbol{y}_{romo}$ vector.

Summary

The fault detectors derived in this section are listed in Table 9.4.

Table 9.4: Fault detectors from wheel variables

Symbol	Description
$b_{nskc,\mathbb{W}}$	*NSKC Check* with wheel set $\mathbb{W}$
$b_{B,\mathbb{W},k}$	*Body Velocity / Acceleration Check* with wheel set $\mathbb{W}$ and k-th component of $\boldsymbol{y}_{romo}$

9.2.3 Fault Detectors from Steering Angles Only

If only the steering angles but no wheel speed measurements are available, then the approach from the previous section cannot be applied. Let us first assume that it is possible to compute or estimate the ICR from the steering angles. Knowledge of the ICR allows the ratios between any two of the three elements in $\boldsymbol{q}_\sigma$ to be calculated, since the ratio removes the speed information contained in $\boldsymbol{q}_\sigma$ and leaves only planar motion geometry, which is fully described by the ICR. These estimated ratios are denoted $\hat{\gamma}_\sigma$, $\hat{\rho}_{\sigma,x}$ and $\hat{\rho}_{\sigma,y}$ and given by:

$$\hat{\gamma}_\sigma := \frac{\hat{v}_{\sigma,y}}{\hat{v}_{\sigma,x}} \,, \qquad \hat{\rho}_{\sigma,x} := \frac{\hat{\dot{\psi}}}{\hat{v}_{\sigma,x}} \,, \qquad \hat{\rho}_{\sigma,y} := \frac{\hat{\dot{\psi}}}{\hat{v}_{\sigma,y}} \,. \tag{9.42}$$

By comparing these estimates against the respective ratios of the measured values, faults in sensors measuring $\boldsymbol{q}_\sigma$ can be detected and possibly isolated. Furthermore, these ratios are also related to the more familiar motion geometry variables of side-slip angle $\hat{\beta}_\sigma$

and curvature $\hat{\rho}_\sigma$ at the sensor location σ by:

$$\hat{\beta}_\sigma = \arctan \hat{\gamma}_\sigma \ , \qquad \hat{\rho}_\sigma = \frac{\hat{\rho}_{\sigma,x}\hat{\rho}_{\sigma,y}}{\sqrt{\hat{\rho}_{\sigma,x}^2 + \hat{\rho}_{\sigma,y}^2}} \ . \tag{9.43}$$

When the set of steering angles Δ_w are perfectly Ackermann-consistent, the ICR and above estimates may be derived in a straightforward manner by applying trigonometric relations on Δ_w. However, in cases with more than two independently steered wheels, perfect Ackermann-consistency does not hold in general. The ICR determination problem is then over-constrained and must be solved approximately. Interestingly, it turns out that the derivation of the approximate solution also provides a metric to assess the degree of Ackermann consistency of Δ_w. Having this assessment in the *NKMFDI* is essential because this condition is a prerequisite for NSKC, and therefore Ackermann consistency must be adequately satisfied for the detectors in the previous section to produce meaningful results. This section is structured to first trace the derivation of this metric, and the $\boldsymbol{q}_\sigma$ ratio estimates are then computed from the intermediate variables.

Motivation for the Proposed Approach

Intuitively, the calculation of a metric to assert Ackermann-consistency can be posed as finding a $\boldsymbol{q}_c$ that corresponds to slip-free steering angles closest to the measured ones Δ_w. Due to the speed independence of Ackermann-consistency, the speed DOF must be constrained in the search, such as by $\|\boldsymbol{q}_c\|_2 = 1$. Such a consistency metric can be expressed by the following optimisation formulation:

$$\tilde{e}_\Delta = \min_{\substack{\boldsymbol{q}_c \\ \|\boldsymbol{q}_c\|_2=1}} \|f_\Delta(\boldsymbol{G}\boldsymbol{q}_c) - \Delta_w\|_2 \tag{9.44}$$

where $f_\Delta(\cdot)$ is a function that computes the steering angles from a wheel velocity vector $\boldsymbol{v}_w$. The body velocity ratios can then be computed from the optimal $\boldsymbol{q}_c$ using (9.42).

The nonlinearity of $f_\Delta(\cdot)$ complicates the optimisation, and motivates the search for an alternative formulation. By specifying an arbitrary non-zero normalising speed, the speed degree of freedom is constrained and the angle consistency problem may be converted into a velocity consistency problem in $\boldsymbol{v}_w$ space. This may be stated as finding wheel centre translational speeds $\boldsymbol{v}_{ws} = [v_{w,1} \ \dots \ v_{w,4}]^T$ and $\boldsymbol{q}_c$ to minimise the resulting value of $\|f_{v_w}(\boldsymbol{v}_{ws}, \Delta_w) - \boldsymbol{G}\boldsymbol{q}_c\|_2$, where $f_{v_w}(\cdot)$ is a function that computes $\boldsymbol{v}_w$ from $\boldsymbol{v}_{ws}$ and Δ. The metric $\tilde{e}_{v_w}$ is defined as this minimum value. It is more precisely described by:

$$\tilde{e}_{v_w} = \min_{\substack{\boldsymbol{v}_{ws} \\ \|\boldsymbol{v}_{ws}\|_2=1}} \left[\min_{\boldsymbol{q}_c} \|f_{v_w}(\boldsymbol{v}_{ws}, \Delta_w) - \boldsymbol{G}\boldsymbol{q}_c\|_2 \right] \ . \tag{9.45}$$

It can be shown that $f_{v_w}(\cdot)$ is linear in $\boldsymbol{v}_{ws}$, thus the cost function is linear in all optimisation variables.

The norm constraint is applied to $\boldsymbol{v}_{ws}$ here but could equally have been applied to $f_{v_w}(\boldsymbol{v}_{ws}, \Delta_w)$, $\boldsymbol{G}\boldsymbol{q}_c$ or $\boldsymbol{q}_c$. Observe that without this norm constraint, the optimisation is simply a nested linear least-squares problem, for which each stage can be solved using a pseudo-inverse rather than an explicit optimisation. This motivates our approach which modifies the norm constraint such that this is possible.

Proposed Ackermann-Consistency Metric

In the proposed method, the norm constraint is replaced with a constraint on an arbitrary wheel centre speed. In the derivation, wheel 1 is chosen and its wheel centre speed is set to $v_{w,1} = b$, where b is any non-zero value. In the case that a singularity occurs for motions where the vehicle is rotating about an axis close to wheel 1, the normalised speed can be applied to another wheel instead. Excluding this case, and having set $v_{w,1} = b$, the undetermined (free) wheel speed variables of the remaining wheels are collected into $\boldsymbol{v}_{w,f} = [v_{w,2}\ v_{w,3}\ v_{w,4}]^T$. $\boldsymbol{v}_w$ can then be expressed as a function of the wheel speeds by

$$\boldsymbol{v}_w = \begin{bmatrix} b\cos\delta_1 \\ b\sin\delta_1 \\ v_{w,2}\cos\delta_2 \\ v_{w,2}\sin\delta_2 \\ v_{w,3}\cos\delta_3 \\ v_{w,3}\sin\delta_3 \\ v_{w,4}\cos\delta_4 \\ v_{w,4}\sin\delta_4 \end{bmatrix} = \boldsymbol{W}\boldsymbol{D}\begin{bmatrix} b \\ \boldsymbol{v}_{w,f} \end{bmatrix} = f_{v_w}\left(\begin{bmatrix} b \\ \boldsymbol{v}_{w,f} \end{bmatrix}, \Delta_w\right) \tag{9.46}$$

where

$$\boldsymbol{W} = diag\left(\begin{bmatrix} \cos\delta_1 \\ \sin\delta_1 \\ \cos\delta_2 \\ \sin\delta_2 \\ \cos\delta_3 \\ \sin\delta_3 \\ \cos\delta_4 \\ \sin\delta_4 \end{bmatrix}\right),\ \boldsymbol{D} = \left[\begin{array}{c|ccc} 1 & 0 & 0 & 0 \\ 1 & 0 & 0 & 0 \\ 0 & 1 & 0 & 0 \\ 0 & 1 & 0 & 0 \\ 0 & 0 & 1 & 0 \\ 0 & 0 & 1 & 0 \\ 0 & 0 & 0 & 1 \\ 0 & 0 & 0 & 1 \end{array}\right] = \left[\begin{array}{c|c} \boldsymbol{D}_1 & \boldsymbol{D}_f \end{array}\right] .$$

The metric $\tilde{e}_{v_w}$ can be adapted to be calculated using this set up. Define a new, closely related metric e_{v_w} that is given by:

$$e_{v_w} = \frac{e'_{v_w}}{\|\boldsymbol{G}\hat{\boldsymbol{q}}_c\|_2} \tag{9.47}$$

where

$$e'_{v_w} = \min_{\boldsymbol{v}_{w,f}} \left(\min_{\boldsymbol{q}_c} \|\boldsymbol{e}_v\|_2 \right) \tag{9.48}$$

$$\boldsymbol{e}_v = \boldsymbol{v}_w - \boldsymbol{G}\boldsymbol{q}_c \tag{9.49}$$

and $\hat{\boldsymbol{q}}_c$ denotes the optimal value of $\boldsymbol{q}_c$.

For a fixed $\boldsymbol{v}_{w,f}$ in the inner optimisation of (9.48), the cost function $\|\boldsymbol{e}_v\|_2$ is minimised by choosing $\boldsymbol{q}_c$ to be the least squares solution computed with the help of the Moore-Penrose pseudo-inverse, that is,

$$\begin{aligned} \hat{\boldsymbol{q}}_c &= \boldsymbol{G}^+ \boldsymbol{v}_w \\ &= \boldsymbol{G}^+ \boldsymbol{W} \boldsymbol{D} \begin{bmatrix} b \\ \boldsymbol{v}_{w,f} \end{bmatrix} . \end{aligned} \tag{9.50}$$

Using this optimal estimate $\hat{\boldsymbol{q}}_c$, $\boldsymbol{e}_v$ can then be expressed as a linear function of $\boldsymbol{v}_{w,f}$ for the outer optimisation:

$$\begin{aligned} \boldsymbol{e}_v &= \boldsymbol{v}_w - \boldsymbol{G}\hat{\boldsymbol{q}}_c \\ &= \left(\boldsymbol{I} - \boldsymbol{G}\boldsymbol{G}^+\right) \boldsymbol{v}_w \\ &= \left(\boldsymbol{I} - \boldsymbol{G}\boldsymbol{G}^+\right) \boldsymbol{W}\boldsymbol{D} \begin{bmatrix} b \\ \boldsymbol{v}_{w,f} \end{bmatrix} \\ &= \left(\boldsymbol{I} - \boldsymbol{G}\boldsymbol{G}^+\right) \boldsymbol{W}\boldsymbol{D}_1 b + \left(\boldsymbol{I} - \boldsymbol{G}\boldsymbol{G}^+\right) \boldsymbol{W}\boldsymbol{D}_f \boldsymbol{v}_{w,f} \\ &= \boldsymbol{A}_1 b + \boldsymbol{A}_f \boldsymbol{v}_{w,f} \end{aligned} \tag{9.51}$$

Since b is a fixed value, the outer optimisation of (9.48) has now been cast into the standard form for a linear least squares problem. The optimal value of the argument $\boldsymbol{v}_{w,f}$, denoted $\boldsymbol{v}^*_{w,f}$, is again calculated by using the Moore-Penrose pseudo-inverse:

$$\boldsymbol{v}^*_{w,f} = \boldsymbol{A}_f^+ \left(-\boldsymbol{A}_1 b\right) . \tag{9.52}$$

Back-substitution of $\boldsymbol{v}_{w,f}$ into (9.51) yields $\boldsymbol{e}_v$:

$$\begin{aligned} \boldsymbol{e}_v &= \boldsymbol{A}_1 b + \boldsymbol{A}_f \boldsymbol{v}^*_{w,f} \\ &= \left(\boldsymbol{A}_1 - \boldsymbol{A}_f \boldsymbol{A}_f^+ \boldsymbol{A}_1\right) b . \end{aligned} \tag{9.53}$$

Upon inspection of this expression, it would appear logical to normalise $\boldsymbol{e}_v$ by the arbitrarily specified scalar b. However, this does not provide comparable metrics of $\|\boldsymbol{e}_v\|_2$ across all possible steering configurations and arbitrary choice of the reference wheel (wheel 1 in this derivation). Instead, a normalisation by the norm of the least square estimates of the wheel centre velocities is used, similar to that proposed in metric $\tilde{e}_{v_w}$ (see (9.45)). The resulting metric e_{v_w} is given by:

$$
\begin{aligned}
e_{v_w} &= \frac{\|\boldsymbol{e}_v\|_2}{\|\boldsymbol{G}\hat{\boldsymbol{q}}_c\|_2} \\
&= \frac{\|\boldsymbol{A}_1 - \boldsymbol{A}_f\boldsymbol{A}_f^+\boldsymbol{A}_1\|_2}{\|\boldsymbol{G}\boldsymbol{G}^+\boldsymbol{W}\boldsymbol{D}\begin{bmatrix}1\\ -\boldsymbol{A}_f^+\boldsymbol{A}_1\end{bmatrix}\|_2} \ .
\end{aligned} \tag{9.54}
$$

where the second expression is reached from the first by substitutions and cancelling out the b in both numerator and denominator.

Although e_{v_w} can be used to assess the Ackermann consistency of Δ_w, it would be convenient to have an intuitive metric that is related to angular errors. Here, an alternative metric e_{AC} is proposed with a simple interpretation related to $\tilde{e}_\Delta$ (see (9.44)). It is defined as the average of the absolute differences between the elements of measured Δ_w and the Ackermann-consistent $\hat{\Delta}_w = [\hat{\delta}_1 \ ... \ \hat{\delta}_4]$ that correspond to $\hat{\boldsymbol{q}}_c$. e_{AC} is calculated by:

$$
\boxed{e_{AC} := \frac{1}{4}\sum_{i=1}^{4}\left|\delta_i - \hat{\delta}_i\right|} \tag{9.55}
$$

where

$$
\begin{aligned}
\hat{\delta}_i &= \arctan\frac{\hat{v}_{w,y,i}}{\hat{v}_{w,x,i}} \\
\hat{\boldsymbol{v}}_w &= \begin{bmatrix}\hat{v}_{w,x,1} & \hat{v}_{w,y,1} & \dots & \hat{v}_{w,x,4} & \hat{v}_{w,y,4}\end{bmatrix}^T = \boldsymbol{G}\hat{\boldsymbol{q}}_c \ .
\end{aligned}
$$

The e_{AC} metric is chosen over the one based on the 2-norm used in (9.44) for better comparability between metrics computed with different sizes of the set $\mathbb{W}$. The sensitivity of e_{AC} to the violation of Ackermann-consistency is demonstrated by a numerical example. The steering angles are set to correspond, under NTSA, to path variables $\beta_c = 5°$ and $\rho_c = 1\ [1/m]$ measured at the body reference point C. Figure 9.5 illustrates the value of e_{AC} when a steering angle offset ϵ_{δ_2} is added to δ_2, showing that e_{AC} increases linearly with the offset for $|\epsilon_{\delta_2}| \lesssim 20°$. The threshold for permissible e_{AC} values is chosen as $J_{e_{AC}} = 1°$ for the later application, which corresponds to approximately 2.5° angle mismatch in wheel 2.

Body Velocity Ratio Estimates

The body ratio estimates $\hat{\gamma}_\sigma$, $\hat{\rho}_{\sigma,x}$ and $\hat{\rho}_{\sigma,y}$ can now be calculated using (9.42) from the components of the estimated body velocity vector $\hat{\boldsymbol{q}}_\sigma$ at the locationσ, which is given by:

$$
\begin{aligned}
\hat{\boldsymbol{q}}_\sigma &= [\hat{v}_{\sigma,x} \ \hat{v}_{\sigma,y} \ \hat{\dot{\psi}}]^T \\
&= \boldsymbol{G}_\sigma^+\boldsymbol{W}\boldsymbol{D}\begin{bmatrix}1\\ -\boldsymbol{A}_f^+\boldsymbol{A}_1\end{bmatrix} b \ .
\end{aligned} \tag{9.56}
$$

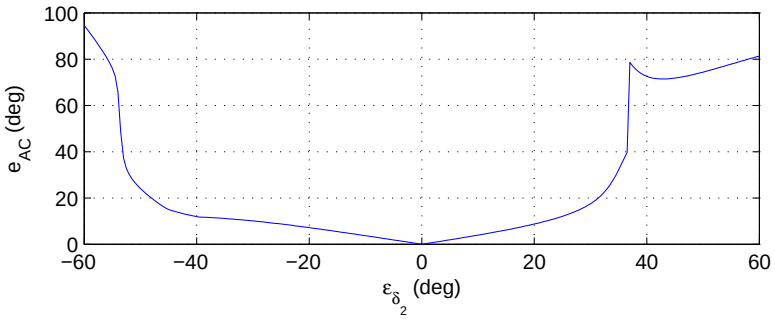

Figure 9.5: Variation of e_{AC} with ϵ_{δ_2} (δ_2 offset) in the illustrative example

The residuals (9.57)-(9.59) can then be computed if the contained measurements are available. The indices jk in a residual variable $r_{A\{\mathbb{W}\}\{jk\}}$ denote the positions of the two variables in the ratio within the $\boldsymbol{y}_{romo}$ vector.

$$r_{A,\mathbb{W},21} = \hat{\gamma}_{os} - \frac{v_{os,y}}{v_{os,x}} \tag{9.57}$$

$$r_{A,\mathbb{W},31} = \hat{\rho}_{os,x} - \frac{\dot{\psi}_{im}}{v_{os,x}} \tag{9.58}$$

$$r_{A,\mathbb{W},32} = \hat{\rho}_{os,y} - \frac{\dot{\psi}_{im}}{v_{os,y}} \tag{9.59}$$

Note that the value of $\dot{\psi}_\sigma$ is independent of sensor location, so $\dot{\psi}_{im}$ is used together with os measurements in the residuals.

Similarly to the fault indicators from Section 9.2.2, the consistency check and the estimates can be calculated using a subset of two or three wheels for the purpose of fault isolation. Further by-products from these derivations are estimates of the more familiar path variables of side-slip angle β_c and curvature ρ_c at point C. These are calculated by (9.43) with $\sigma = C$. They are repeated here for convenient reference:

$$\hat{\beta}_c = \arctan \hat{\gamma}_c \ , \qquad \hat{\rho}_c = \frac{\hat{\rho}_{c,x}\hat{\rho}_{c,y}}{\sqrt{\hat{\rho}_{c,x}^2 + \hat{\rho}_{c,y}^2}} \ . \tag{9.60}$$

The accuracy of these estimates is demonstrated by the validation results in Section 9.6.

Summary

The validity metrics, fault detectors, and estimates derived in this section are listed in Table 9.5.

9.2.4 Other Fault Detectors

Even though the next residual generators do not make use of the NKM, they are included here for completeness because they are mentioned in the key literature of [DFD04; Fis07]

Table 9.5: Validity metrics, fault detectors and estimates from steering angles

Symbol	Description
e_{AC}	Angle deviation metric of the Ackermann consistency check
$r_{A\{\mathbb{W}\}\{jk\}}$	Body Velocity Ratio residuals with wheel set $\mathbb{W}$ and components j, k of $\boldsymbol{y}_{romo}$
$\hat{\beta}_c,\ \hat{\rho}_c$	steady state path variable estimates at C

named in the introduction. They also contribute to the fault isolation capability as will be demonstrated in Section 9.3. They are based on relations concerning accelerations of rotating bodies and are valid regardless of whether the Ackermann consistency condition and NTSA hold. The two resulting relationships are:

$$a_{\sigma,x} = \dot{v}_{\sigma,x} - v_{\sigma,y}\dot{\psi} \tag{9.61}$$

$$a_{\sigma,y} = \dot{v}_{\sigma,y} + v_{\sigma,x}\dot{\psi}\ . \tag{9.62}$$

The reader is reminded here of the ROboMObil's measurement vector $\boldsymbol{y}_{romo} = [v_{os,x}, v_{os,y}, \dot{\psi}_{im}, a_{im,x}, a_{im,y}]^T$. The different measurement locations require transformation of all variables to the *im* location where the accelerations are measured. This gives the adapted and rearranged relations:

$$\begin{aligned} \dot{v}_{im,x} &= a_{im,x} + (v_{os,y} + (l_{im} - l_{os})\dot{\psi})\dot{\psi} \\ &= f_{v_x}(a_{im,x}, v_{os,y}, \dot{\psi})\ , \end{aligned} \tag{9.63}$$

$$\begin{aligned} \dot{v}_{im,y} &= a_{im,y} - (v_{os,x} - (s_{im} - s_{os})\dot{\psi})\dot{\psi} \\ &= f_{v_y}(a_{im,y}, v_{os,x}, \dot{\psi})\ . \end{aligned} \tag{9.64}$$

To avoid taking direct derivatives, a recursive filter may be set up from each of these relations and the estimation error may be taken as the residuals r_{C,a_x} and r_{C,a_y} respectively. To illustrate, r_{C,a_x} would be calculated by such a filter, where K_{v_x} is a filter gain:

$$\boxed{\begin{aligned} \dot{\hat{v}}_{im,x} &= f_{v_x}(a_{im,x}, v_{os,y}, \dot{\psi}) - K_{v_x}((v_{os,x} - (s_{im} - s_{os})\dot{\psi}) - \hat{v}_{im,x}) \\ r_{C,a_x} &= (v_{os,x} - (s_{im} - s_{os})\dot{\psi}) - \hat{v}_{im,x}\ . \end{aligned}} \tag{9.65}$$

Summary

The fault detectors derived in this section are listed in Table 9.6.

Table 9.6: Fault detectors from body motion measurements only

Symbol	Description
$r_{C,a_x},\ r_{C,a_y}$	residuals checking consistency between OS velocity measurements, IMU accelerations, and IMU yaw rate

9.3 Fault Isolation

In sensor fault detection, each fault detector is sensitive to faults in the sensors whose measurements are used in calculating the fault alarm. The availability of a bank of alarms, each sensitive to different faults, enables the use of the structured residual approach to isolate individual or groups of faults. The "residual" structure is composed of the detector outputs shown in Table 9.7. To keep the size of the table manageable for detectors with outputs $b_{B\{\mathbb{W}\}\{k\}}$ and $b_{nskc,\mathbb{W}}$, only those with $\mathbb{W} = \{1,3,4\}$ or $\{2,3,4\}$ are shown. These are relevant for isolating between faults in wheels 1 and 2.

Table 9.7: Residual structure. Group 1: body motion sensors only; Group 2: Ω_w unavailable; Group 3: Ω_w available

Gr.	$\mathbb{W}$	detector	eq. ref.	$f_{\delta 1}$	$f_{\delta 2}$	$f_{\omega 1}$	$f_{\omega 2}$	$f_{v_{os,x}}$	$f_{v_{os,y}}$	$f_{\dot{\psi}}$	$f_{a_{im,x}}$	$f_{a_{im,y}}$
1	-	r_{C,a_x}	(9.65)	0	0	0	0	1	1	1	1	0
	-	r_{C,a_y}	"	0	0	0	0	1	1	1	0	1
2	all	$r_{A\{\text{all}\}\{21\}}$	(9.57)	1	1	0	0	1	1	0	0	0
	all	$r_{A\{\text{all}\}\{31\}}$	(9.58)	1	1	0	0	1	0	1	0	0
	all	$r_{A\{\text{all}\}\{32\}}$	(9.59)	1	1	0	0	0	1	1	0	0
3	all	$b_{nskc\{\text{all}\}}$	(9.30)	1	1	1	1	0	0	0	0	0
		$b_{nskc\{134\}}$	"	1	0	1	0	0	0	0	0	0
		$b_{B\{134\}\{1\}}$	(9.36)	1	0	1	0	1	0	0	0	0
	134	$b_{B\{134\}\{2\}}$	"	1	0	1	0	0	1	0	0	0
		$b_{B\{134\}\{3\}}$	"	1	0	1	0	0	0	1	0	0
		$b_{B\{134\}\{4\}}$	(9.41)	1	0	1	0	0	0	0	1	0
		$b_{B\{134\}\{5\}}$	"	1	0	1	0	0	0	0	0	1
		$b_{nskc\{234\}}$	(9.30)	0	1	0	1	0	0	0	0	0
		$b_{B\{234\}\{1\}}$	(9.36)	0	1	0	1	1	0	0	0	0
	234	$b_{B\{234\}\{2\}}$	"	0	1	0	1	0	1	0	0	0
		$b_{B\{234\}\{3\}}$	"	0	1	0	1	0	0	1	0	0
		$b_{B\{234\}\{4\}}$	(9.41)	0	1	0	1	0	0	0	1	0
		$b_{B\{234\}\{5\}}$	"	0	1	0	1	0	0	0	0	1

It can be seen that each fault does indeed have a unique signature in the residual structure, which is sufficient for isolation under the single fault assumption. Additionally, the structure is robust to false isolation during partial firing, since it is unidirectional strong isolating in that transforming one signature into another requires turning at least a $\{0,1\}$ pair of entries into $\{1,0\}$. This topic was explained in more detail in Chapter 5 and not described further here.

The detectors are divided in Table 9.7 into three groups:

1. consistency checks between body motion sensors (NKM-independent)
2. fault detectors from steering angles only (without wheel speed)
3. fault detectors from wheel variables (with wheel speed).

It should be noted that residuals $r_{A\{all\}\{jk\}}$ from Group 2 are not actually required for isolation. However, in the event when wheel speeds are unavailable or not sufficiently

accurate, they provide degraded fault isolation capability. An instance of this situation occurs with hall effect wheel speed sensors found in conventional ABS systems, which suffer from reduced accuracy and increased signal delays at low speeds due to its physical measurement principle. When wheel speeds are available, Group 3 residuals alone are sufficient for fully isolating the faults listed in Table 9.7. Moreover, if both body velocity and acceleration measurements are available like on the ROboMObil, then the Group 1 residuals offer fault detection on these sensors irrespective of the validity of the NKM. However, fault isolation in general requires the other fault detector groups.

9.4 Fault Sensitivity Analysis

The *NSKC Check* and *Body Velocity / Acceleration Checks* from Section 9.2.2 are, by design, robust to disturbances including modelling errors and measurement deviations within the specified tolerances, since knowledge of their bounds are explicitly incorporated in the design method. On the other hand, it was declared from the outset of this chapter that unlike the *STMFDI* method in Chapter 8, fault sensitivity is not explicitly assured by design and must be analysed after detector design. This section presents an approach for analysing and visualising the fault sensitivity of the detectors over a range of system states.

It should be noted that the presented test cases and analysis conditions are by no means exhaustive. Rather, the aim of this section is to demonstrate the interpretation of the analysis results, and to provide insights into the sensitivity behaviours of the detectors. In an actual application, more exhaustive analysis based on these procedures should be conducted to better cover the operating conditions.

Analysis Method

The presented analysis results are produced by running the fault detectors on sets of sensor outputs $\{\Delta_w, \Omega_w, \boldsymbol{q}_{im}, \boldsymbol{q}_{os}, \boldsymbol{a}_{im}\}$ computed from vehicle motion descriptions generated by 1-D "sweeps" over chosen parameters. Since the fault detectors being analysed are memoryless, their outputs are only dependent on the motion variables from one sample in time. Therefore the time dimension can be ignored altogether, permitting the efficient use and visualisation of this analysis method. The sensor outputs at each grid point in the sweep are generated by calculating the body sensor measurements $\boldsymbol{q}_\sigma$ and $\boldsymbol{a}_\sigma$ from the reference vehicle motion $\boldsymbol{q}_c$ as well as the wheel variables $\{\Omega_w, \Delta_w\}$ under the NTSA. Instead of directly specifying the generalised velocity $\boldsymbol{q}_c$ at the body centre, we use the more intuitive equivalent parameter vector $\boldsymbol{p}_c = [v_c \ \beta_c \ \rho_c]^T$ to specify a trajectory based on the speed v_c, side slip angle β_c and path curvature ρ_c. $\boldsymbol{q}_c$ and $\boldsymbol{p}_c$ are related by:

$$v_{c,x} = v_c \cos\beta_c \ , \quad v_{c,y} = v_c \sin\beta_c \ , \quad \dot{\psi}_c = v_c \rho_c \ .$$

The 1-D grids are then produced by sweeping over a component of $\boldsymbol{p}_c$ while fixing the other components. In the example analyses in this section, the following nominal values of $\boldsymbol{p}_c$ (for the fixed components) and the swept range of values are used:

$\boldsymbol{p}_c$ component	nominal value	sweep value range
v_c	5 m/s	$[-8, 8]$m/s
β_c	-5 °	$[-95, 95]°$
ρ_c	0.05 [1/m]	$[-0.3, 0.3]$ [1/m]

The plots in Figures 9.6 illustrate the behaviour of the thresholds $\underline{q}_{\sigma,j,\mathbb{W}}$ and $\overline{q}_{\sigma,j,\mathbb{W}}$ in sweeps over v_c, β_c and ρ_c respectively. To aid visualisation, the fault-free (true) value of the measurement variable is subtracted from the thresholds to give the normalised values:

$$\tilde{\overline{q}}_{\sigma,j,\mathbb{W}} = \overline{q}_{\sigma,j,\mathbb{W}} - q_{\sigma,j}$$
$$\tilde{\underline{q}}_{\sigma,j,\mathbb{W}} = \underline{q}_{\sigma,j,\mathbb{W}} - q_{\sigma,j} \ .$$

The sensitivity to an additive sensor fault for $q_{\sigma,j}$ is given by the distances from the fault-free variable to either threshold, which are in turn simply the normalised threshold values shown in the plots.

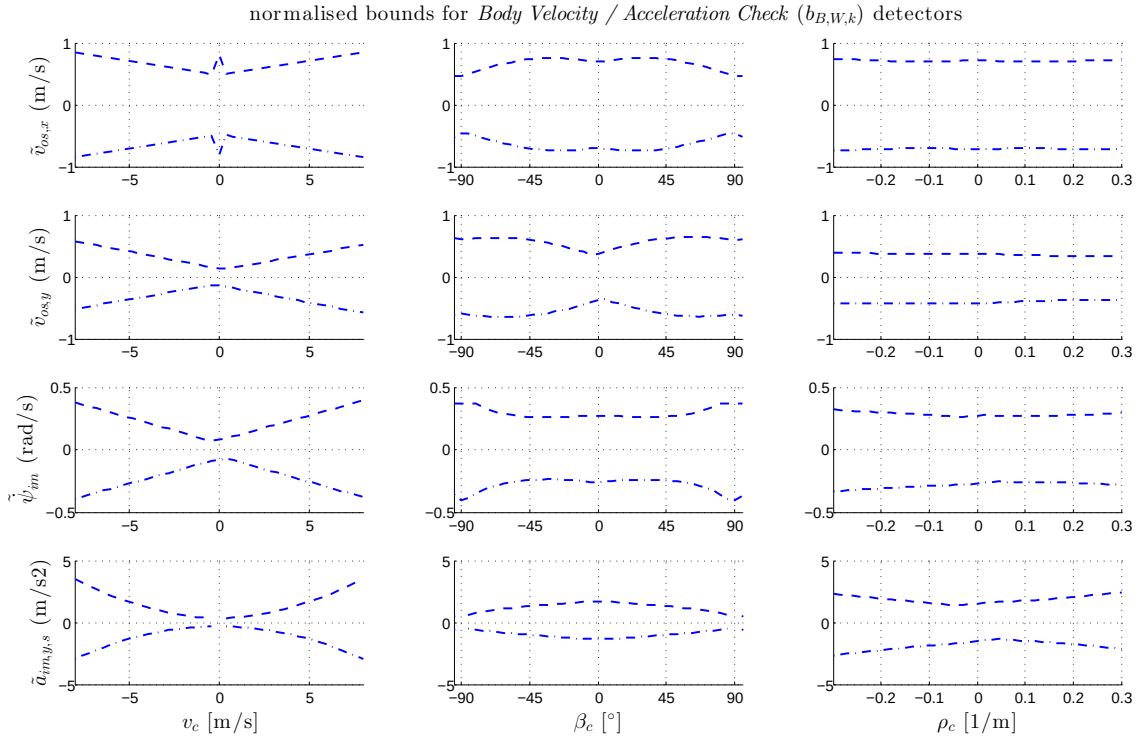

Figure 9.6: Sensitivity of $b_{B\{\mathbb{W}\}\{k\}}$ to body motion sensor faults. The three plots examine the effects as the components of $\boldsymbol{p}_c$ vary. The minimum detectable fault size, which is considered a measure for fault sensitivity, is given by the magnitude of these normalised thresholds. The $\mathbb{W}$ subscript is omitted from the labels.

In contrast, it is not possible to determine the fault sensitivity of $b_{nskc,\mathbb{W}}$ using only outputs from the fault-free calculation because the Boolean outputs to the feasibility

problems provide no indication of the proximity to infeasibility. Instead, its sensitivity to a wheel speed fault, here chosen as f_{ω_1}, is computed by evaluating the Boolean output over a sweep of the fault magnitude for a given $\boldsymbol{p}_c$. Faults in other wheel speed sensors exhibit similar behaviours. To condense the information for visualisation, the Boolean output of the *NSKC Check* is augmented by the firing status of the corresponding *Body Velocity / Acceleration Checks* ($b_{B\{\mathbb{W}\}\{k\}}$) into a discrete output. The following encoding is used:

discrete code	$b_{nskc,\mathbb{W}}$ **fired**	**number of fired** $b_{B\{\mathbb{W}\}\{k\}}$
0	no	0
n (≥ 1)	no	n
-1	yes	n/a

The plots in Figure 9.7 visualise the variation of the discrete output with fault size and a component of $\boldsymbol{p}_c$ in a 2-D colourmap, where the x-axis denotes the swept $\boldsymbol{p}_c$ component, the y-axis denotes the fault expressed as a percentage of ω_1. The discrete output value is conveyed by the colour at the grid point.

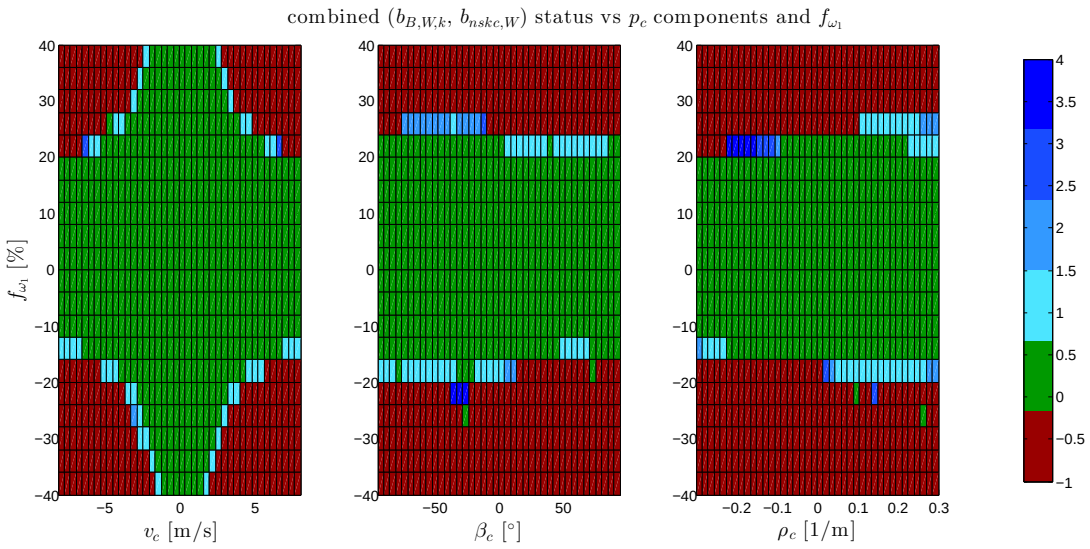

Figure 9.7: Sensitivity of $b_{B\{\mathbb{W}\}\{k\}}$ and $b_{nskc,\mathbb{W}}$ to f_{ω_1}. The three plots examine the effects over a range of values of $\boldsymbol{p}_c$ components. f_{ω_1} is swept in the range $[-40, +40]$%. The colour designations are: Green(0): no fault detected, Red(-1): $b_{nskc,\mathbb{W}} = 1$, i.e. wheel speed fault detected. Blue(1-4): $b_{nskc,\mathbb{W}} = 0$, but one or more $b_{B\{\mathbb{W}\}\{k\}}$ alarms are raised (the number is given by the output value), so the fault is detected but not isolated to a wheel speed sensor.

In a thorough analysis, fault sensitivity would be evaluated over a 3-D grid of $\boldsymbol{p}_c$ components and condensed into more manageable output metrics. Due to the difficulty of visualising such sweeps, the illustrative sweeps over only one $\boldsymbol{p}_c$ component are preferred in this work to demonstrate the dependencies on vehicle motion.

The explanations so far merely illustrate the nominal fault sensitivity when the variable deviations are all zero. At the worst-case tolerances, the measured value $q_{\sigma,j}$ lies by

definition at either the upper or the lower threshold. The worst-case fault sensitivity arises through a sensor fault that cancels out this deviation, resulting in a fault sensitivity of $\overline{q}_{\sigma,j,\mathbb{W}} - \underline{q}_{\sigma,j,\mathbb{W}}$, i.e., the gap between the upper and lower thresholds. With the *NSKC Check* the situation is more complex, but a similar logic can be applied and the worst-case fault sensitivity of a wheel variable is roughly the value in the nominal case plus the wheel variable tolerance. In practice, a persistent cancellation between the fault and the time-varying deviation is unlikely, and therefore the nominal sensitivity is a sufficient indicator of detector performance.

The fault detector parameters used for the generation of the analysis results are the same as those used in their validation on the ROboMObil in Section 9.6, which are listed in Table 9.11. Two further parameters also affect detector behaviours - the wheel set $\mathbb{W}$ and the wheel torque magnitudes $|M_{w,i}|,\ i = 1,\ldots,4$, the latter of which affects the longitudinal tyre slip tolerances. For the analysis here, $\mathbb{W} = \{1,2,3,4\}$ and $|M_{w,i}| = 40\text{Nm},\ i = 1,\ldots,4$ are specified.

Interpretation of Results

Figure 9.6 shows that the fault sensitivity of the *Body Velocity / Acceleration Checks* demonstrate a significant dependency on v_c, but β_c and ρ_c have lower influence over their full ranges. Care should be taken when interpreting the plots for $\tilde{a}_{im,y,s}$, because beyond small values of β_c the steady state "centrifugal" component $a_{y,s}$ tends to no longer be dominant in a_y, as explained in the subsection *Body Acceleration Check* in Section 9.2.2. The appearance of improving fault sensitivity beyond $[-20°, 20°]$ is therefore misleading. The v_c sweep of the $\tilde{v}_{os,x}$ bounds shows that at close to zero speed, the trend in sensitivity to $f_{v_{os,x}}$ abruptly changes. This is an artifact of the wheel speed tolerance being the sum of an absolute and a relative component, and the absolute component becomes dominant when v_c approaches zero.

We also observe that the shape of the dependency of the bounds on β_c is due to the difference in the wheel velocity tolerances in the longitudinal ($\bar{e}_{v,i}$) and lateral wheel ($\bar{e}_{\delta,i}$) directions. For example, the non-zero (40Nm) wheel torques result in increased values of $\bar{e}_{v,i}$ without affecting the $\bar{e}_{\delta,i}$ values. This causes more marked variations of the bounds on $\tilde{v}_{os,x}$ and $\tilde{v}_{os,y}$ over a β_c sweep, as the (x_U, y_U) directions become more or less aligned with the wheel directions. At $\beta_c = 0°$, the $\tilde{v}_{os,x}$ thresholds are determined by $\bar{e}_{v,i}$, whereas at $\beta_c = 90°$, they would be determined by $\bar{e}_{\delta,i}$ instead.

The parabolic increase of the $\tilde{a}_{im,y,s}$ thresholds with v_c makes them too insensitive to faults to be useful at higher speeds. However, at lower speeds where the *NKMFDI* usually operates, the thresholds are tight enough to offer reasonable fault sensitivity.

In Figure 9.7, the $b_{nskc,\mathbb{W}}$ output of the *NSKC Check* is assessed against the multiplicative wheel speed fault f_{ω_1} over a range of magnitudes. Here, a value of 0% denotes fault-free. From the plots, we can recognise a trend where increasing magnitude of f_{ω_1} first triggers an alarm from the *Body Velocity / Acceleration Checks*, before slightly larger

wheel speed faults trigger the *NSKC Check*. Alarms from *NSKC Checks* provide better isolation since a body motion sensor fault can be ruled out.

According to the leftmost plot of Figure 9.7, the detectors are very insensitive at close to zero v_c. This is caused by the presence of an absolute wheel speed tolerance, whose effects dominate over the relative speed tolerance at low wheel speeds. It is added to account for the speed invariant measurement noise, but results in the penalty of reduced sensitivity to multiplicative wheel speed sensor faults at low speeds. In comparison, the sensitivity does not vary significantly over β_c and ρ_c in the nominal vehicle configuration.

Steering angle sensor faults are not treated in this sensitivity study. Since the steering angle sensor is used in closed-loop control of the actuator, a steering angle fault causes a deviation in the physical steering angle, bringing the set of physical steering angles out of an Ackermann consistent configuration. The effect on vehicle motion and therefore detector behaviour is strongly dependent on kinetic (as opposed to kinematic) vehicle parameters. Limited investigations show that large sensor errors are detectable, but the sensitivity to small angle deviations is poor. A more detailed study is necessary to gain further insights, but this is outside the scope of this work.

9.5 Supervision and Implementation

Implementing the NKM fault detectors in a practical application demands some additional supervisory measures. Due to the limited validity region of the NKM fault detectors, it is crucial to determine whether the current driving situation falls within this region and fulfils the necessary assumptions. Only when the validity is asserted should the fault detectors be evaluated. The execution sequence is summarised as pseudo-code in this section. Besides supervisory aspects, other implementation topics specific to the ROboMObil's embedded hardware and software are also covered.

9.5.1 Asserting Validity of the NKM

The validity condition of the NKM revolves around negligible tyre-slip, which is satisfied when:

1. The steering angles Δ_w are Ackermann-consistent (for feasibility of motion without lateral-tyre-slip),
2. Wheel torques lie within the low slip region of the current tyre-road friction characteristics, and
3. Body acceleration normal to the path (i.e. in the direction of the ICR) is low.

The verification of condition 1 is handled by comparing the Ackermann-consistency metric e_{AC} against an appropriate threshold $J_{e_{AC}}$. This was treated in Section 9.2.3. Verification of condition 2 involves knowledge of the maximum transmissible tangential tyre force for a specified low tyre slip threshold, which can be determined from tyre test

data or road tests and could even be made dependent on environmental conditions and system state. It will be assumed that the maximum wheel torque on the i-th wheel in this low-slip region is given by a parameter $\overline{M}_{w,i}$ as shown in (9.21).

To achieving tighter bounds for improved fault detection performance, the maximum tangential slip tolerance $\bar{e}_{sv,i} = \bar{e}_{svn} M_{w,i}$ is treated as a wheel-torque dependent parameter. The coefficient $\bar{e}_{svn}$ can be determined by assuming a worst-case (lowest) longitudinal tyre stiffness, which may be readily estimated from tyre or driving test data.

Verification of the third condition of low acceleration is more challenging because the constraint verification involves variables from potentially fault-affected sensors. Direct measurements or estimates of path-normal acceleration at the reference point C, $a_{c,n}$, uses variables that are monitored by the NKM fault detectors. This difficulty is overcome by evaluating the criteria using multiple methods based on different estimates of acceleration, and then applying the single-fault assumption in the decision logic. These methods are described in Table 9.8.

Table 9.8: Methods for monitoring the path-normal acceleration condition

#	Method	Description
1	use body acceleration measurements	Even though the path-normal direction is unknown from only acceleration measurements, $a_{c,n} \leq \lvert\boldsymbol{a}_c\rvert$. Since the IMU is mounted close to the vehicle centre, $\boldsymbol{a}_{im} \approx \boldsymbol{a}_c$. **Check**: $\sqrt{a_{im,x}^2 + a_{im,x}^2} \leq \bar{a}_n$
2	estimate acceleration from measurements of v_x, v_y and $\dot{\psi}$	in steady-state cornering, $a_{c,n} = \lvert\boldsymbol{v}_c\rvert\dot{\psi}$. Approximating $a_{c,n}$ by $a_{os,n}$ gives the following: **Check**: $\dot{\psi}\sqrt{v_{os,x}^2 + v_{os,y}^2} \leq \bar{a}_n$
3	estimate acceleration using measurements of steering angles and wheel speeds	The Ackermann-consistency check can yield the curvature estimate $\hat{\rho}_{w,i}$ at any wheel centre location. Together with the wheel speed the normal acceleration at the wheel location can be estimated, which approximates the body centre acceleration. **Check**: $\hat{\rho}_{w,i}(r_w\omega_i)^2 < \bar{a}_n$ at each wheel i
4	estimate acceleration using measurements of steering angles and yaw rate	combining estimates from 2 and 3, and using $a_{c,n} = \dot{\psi}^2/\rho_c$: **Check**: $\dfrac{\dot{\psi}^2}{\hat{\rho}_c} \leq \bar{a}_n$

Table 9.9 illustrates the signal dependency of each verification method in tabular form. By exploiting the single-fault assumption, a reliable outcome can be inferred when the

outputs are consistent between any group of two or more methods that share no common variables. Out of those listed in Table 9.8, these groups are:

$$\mathcal{E} = \{\{1, 2, 3.\text{x}\}, \{1, 2\}, \{1, 3.\text{x}\}, \{2, 3.\text{x}\}, \{1, 4\}\} \tag{9.66}$$

where 3.x denotes any of the four variants (one for each wheel) of method 3.

Table 9.9: Measurement dependency of path-normal acceleration estimates

#	δ_1	δ_2	δ_3	δ_4	ω_1	ω_2	ω_3	ω_4	$v_{os,x}$	$v_{os,y}$	$a_{im,x}$	$a_{im,y}$	$\dot{\psi}_{im}$
1											•	•	
2									•	•			•
3.1	•	•	•	•	•								
3.2	•	•	•	•		•							
3.3	•	•	•	•			•						
3.4	•	•	•	•				•					
4	•	•	•	•									•

The value of $\bar{a}_n$ can be set according to the level of lateral tyre-slip tolerated in the fault detectors. To provide a rough reference, if the cornering stiffness C_α of the tyre is known and each "quarter car" is treated independently, then we can set for the i-th wheel:

$$\bar{a}_n = \frac{4}{m} C_\alpha \bar{e}_{\alpha,i} \ . \tag{9.67}$$

where $\bar{e}_{\alpha,i}$ is the tolerated lateral tyre slip. For the ROboMObil, the parameter values are taken as $C_\alpha = 35000$ Nm/rad (per wheel) and $m = 1080$kg (see Section 7.6). Setting $\bar{e}_{\alpha,i} = 1.0°$ results in $\bar{a}_n = 2.3$ m/s.

9.5.2 FDI Procedure

The procedure for applying the NKM-based fault detectors is summarised in Procedure 9.1. The expressions for computing the metrics, residuals and fault alarms are listed in the incidence matrix in Table 9.7.

The presented procedure is concerned with FDI at one computation time step. In an actual application, the resulting residuals and fault indicators would be evaluated regularly and post-processed by temporal evaluation measures such as filters and debouncers.

9.5.3 Practical Implementation

In this subsection, some topics arising from the limitations of real sensors and embedded controller hardware are briefly discussed.

Procedure 9.1 FDI using the NKM-based Fault Detectors

Input: Ω_w, Δ_w, $\boldsymbol{q}_\sigma$, $\boldsymbol{a}_\sigma$

Compute Ackermann-consistency metric e_{AC} ▷ from Δ_w
if $e_{AC} \leq J_{e_{AC}}$ AND $|M_{w,i}| \leq \overline{M}_{w,i} \quad i \in [1 \dots 4]$ **then**
    Evaluate the acceleration conditions $|\hat{a}_n| < \bar{a}_n$ ▷ see Table 9.8
    Find subsets from $\mathcal{E}$ with consistent estimates ▷ see (9.66) for $\mathcal{E}$
    if $|\hat{a}_n| < \bar{a}_n$ for all consistent sets **then** ▷ NKM pre-requisites fulfilled
        if confidence in Ω_w is low **then**
            Compute the $r_{A\{\text{all}\}\{jk\}}$ residuals ▷ detect $\boldsymbol{q}_\sigma$ sensor ratio faults
        else
            Compute 4-wheeled $b_{nskc\{\text{all}\}}$ ▷ check if $\boldsymbol{v}_w$ is NSKC within tolerances
            Compute 3-wheeled $b_{nskc\{\mathbb{W}\}}$ ▷ for fault isolation
            if not NSKC **then**
                Isolate faulty wheel variable (structured residuals) ▷ see Table 9.8
            else
                Compute $b_{B\{\mathbb{W}\}\{k\}}$ ▷ detect and isolate $\boldsymbol{q}_\sigma$, $\boldsymbol{a}_\sigma$ faults
                if $b_{B\{\mathbb{W}\}\{k\}} \neq 0$ for at least one $(\mathbb{W}, k)$ pair **then**
                    Isolate faulty sensor using structured residuals ▷ see Table 9.8
                end if
            end if
        end if
    else
        no FDI possible
    end if
else
    no FDI possible
end if
Compute r_{C,a_x} and r_{C,a_y} residuals ▷ detect some $\boldsymbol{q}_\sigma$ sensor faults

Signal Smoothing

To reduce the effect of noise on residuals and fault detection, it is common to pre-process the measured signals by filtering. For this fault detection approach, extra care must be taken when choosing the filter time constant. Since some of the fault detectors solve a feasibility or optimisation problem using only the signal values from one time instant, there is no inherent smoothing effect as in the case of observer or filter-based approaches. Hence any causal filtering that significantly alters the value of a signal beyond its measurement tolerance may trigger a fault alarm. This can be mitigated by observing two guidelines:

- If using a causal filter, choose a sufficiently high bandwidth compared to the maximum rate of change of the noise-free signal to limit the maximum difference between its input and output.
- Use an acausal smoothing algorithm with a finite window size to avoid introducing a lag into the output signal. The parameters should be chosen to again limit the worst-case input-output difference in view of known signal properties. The use of an acausal smoother is realisable in real-time by delaying the evaluation of the fault detectors at each time step by half the window size.

Computational Load

The residual structure proposed in Table 9.7 contains 40 LP problems when it is extrapolated to detectors for all three-wheel combinations for $\mathbb{W}$. Due to the large number of optimisations, the computation load of solving them in every time step may become excessive for real-time implementation. If this is the case, one way to alleviate this is to save a set of filtered / smoothed data into a buffer, and compute one (or more) fault detector or validity check at every time step. At the same time, measurements can be buffered for the next evaluation window. In the case of the ROboMObil with its 4 ms sample time on the central control unit, the configuration of solving only one LP problem per time step results in a fault detection cycle time of 160 ms. This constitutes the worst-case additional detection delay, which remains an acceptable value since it lies well below the vehicle dynamics time constants.

9.6 Validation

9.6.1 Simulation

The proposed approach to FDI of vehicle sensors is first validated in a simulation of the ROboMObil, consisting of the nonlinear double track model (DTM) introduced in Chapter 7, together with sensor models which process the outputs of the DTM. The inputs to the DTM are Δ_w and wheel motor torques $\boldsymbol{M}_w$, while Ω_w and the body motion measurement vector $\boldsymbol{y}_{romo} = [v_{os,x}, v_{os,y}, \dot{\psi}_{im}, a_{im,x}, a_{im,y}]$ are outputs from the sensor models. To simulate representative motion commands, the inputs Δ_w and $\boldsymbol{M}_w$ are extracted from data recorded on an experimental test drive at low to medium speed.

Figure 9.8 illustrates the actuator inputs and the wheel speeds, while the measured signals plotted in Figure 9.10 provide an overview of the vehicle body motion. It is worth mentioning that from $t = 29$s onwards, the vehicle drives along a straight line and uses its four wheel steering to engage in a superimposed yawing motion. This induces a fluctuating value of β_c and also of the related variable $v_{c,y}$. The results will show that the FDI functions can handle this unconventional motion as well as the higher curvature in $t \in [24\text{s}, 28\text{s}]$.

The sizes of the injected faults are chosen to reflect a moderate fraction of the range of normal operating values. The parameters of the sensor faults are listed in Table 9.10. Besides the multiplicative wheel speed sensor faults $f_{\omega 1}$ and $f_{\omega 2}$, the remaining faults are additive and constant over their durations. The multiplicative faults are simulated as additive faults proportional to their variable values. The fault occurrence times are also displayed in Figure 9.11 to provide a better overview for later reference. Outside of its specified time period an additive fault variable is set to zero.

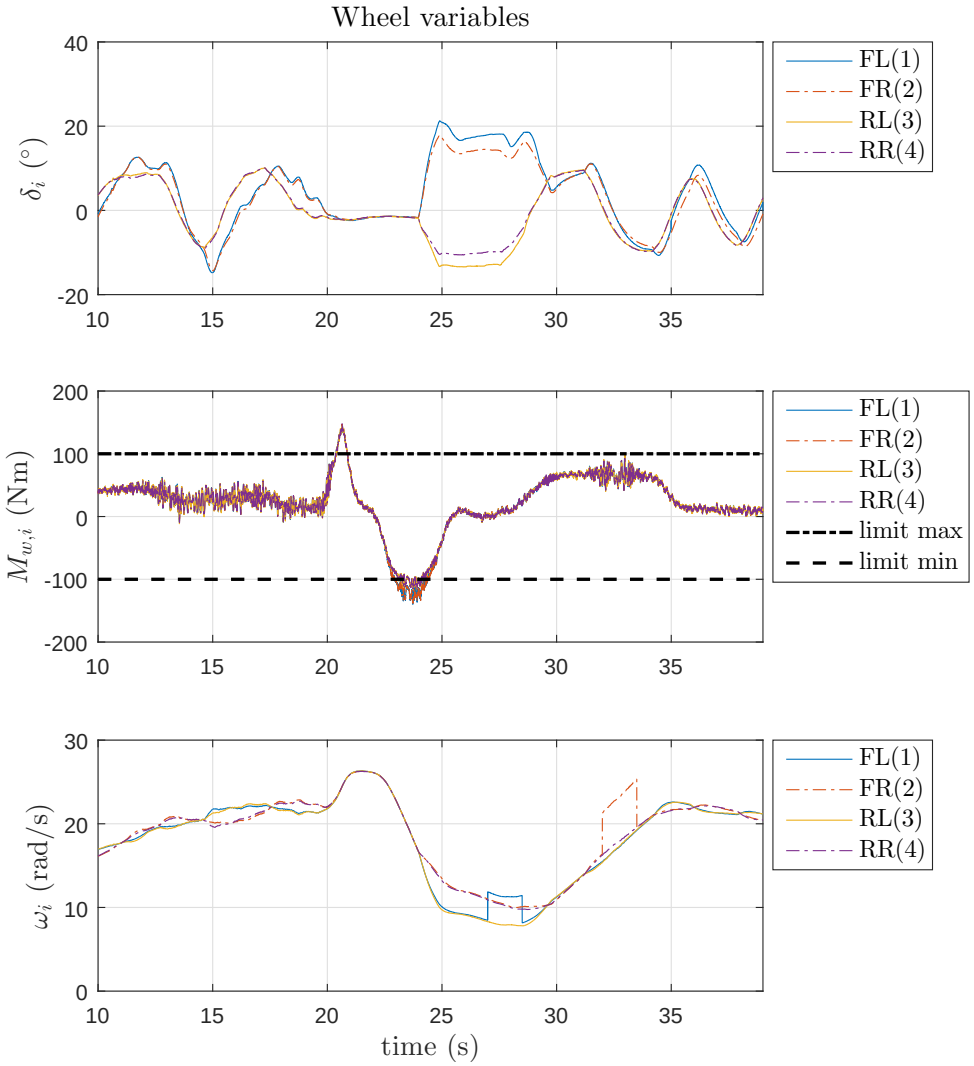

Figure 9.8: Simulation test case: wheel variables δ_i (steering angles), $M_{w,i}$ (wheel torques), and ω_i (wheel speeds). Occurrences of f_{ω_1} and f_{ω_2} are visible in the wheel speed plot.

Table 9.10: Fault sizes and times: simulation test case

Fault	**Size**	**Time (s)**
$f_{v_{os,x}}$	+0.9m/s	$[21, 22.5]$
$f_{v_{os,y}}$	+0.9m/s	$[18, 19.5]$
$f_{\dot{\psi}_{im}}$	+0.5rad/s	$[15, 16.5]$
$f_{a_{im,y}}$	+3m/s^2	$[12, 13.5]$
$f_{\omega 1}$	+30%	$[24, 25.5]$
$f_{\omega 2}$	+30%	$[27, 28.5]$
$f_{\delta 1}$	+2°	$[35, 39]$

The NKM-based fault detectors are configured with the parameters listed in Table 9.11. The parameters are determined by first setting initial values according to plant and environment knowledge, and then further empirically tuned using training data from experimental test drives. From experimentally acquired cornering stiffness parameters for the ROboMObil tyre, it was deduced that restricting $\|[a_{c,x}\ a_{c,y}]\| \leq 4\text{m/s}^2$ results in

$\bar{e}_{\alpha,i} \approx 1.7°$. Furthermore, the longitudinal tyre slip tolerance per unit wheel torque was estimated to be $\bar{e}_{svn} \approx 3 \times 10^{-4}$[1/Nm]), which equates to $\bar{e}_{sv,i} = 4.8\%$ slip at the full wheel moment of $|M_{w,i}| = 160$Nm.

Table 9.11: Fault detector parameters used in validation tests on the ROboMObil

Parameter	**Symbol**	**Value**	**Unit**	**Comments**	**Eq. ref.**
wheel speed sensor tolerance	$\bar{e}_{\omega}$	1	rad/s	absolute tol. component	(9.14)
wheel radius tolerance	$\bar{e}_{r_w}$	0.18	m	0.05 relative tol. component	(9.15)
longitudinal tyre slip tolerance per unit wheel torque	$\bar{e}_{svn,i}$	0.0003	1/Nm		(9.21)
steering angle sensor tolerance	$\bar{e}_{\delta}$	1.3	°		(9.14)
lateral tyre slip tolerance	$\bar{e}_{\alpha,i}$	1.7	°	for $i = 1, \ldots, 4$	(9.20)
sensor tolerance: $a_{im,x}$	$\bar{e}_{a_{im,x}}$	0.3	m/s^2		(9.14)
sensor tolerance: $a_{im,y}$	$\bar{e}_{a_{im,y}}$	0.3	m/s^2		(9.14)
sensor tolerance: $\dot{\psi}_{im}$	$\bar{e}_{\dot{\psi}_{im}}$	0.05	rad/s		(9.14)
sensor tolerance: $v_{os,x}$	$\bar{e}_{v_{os,x}}$	0.2	m/s		(9.14)
sensor tolerance: $v_{os,y}$	$\bar{e}_{v_{os,y}}$	0.2	m/s		(9.14)
Ackermann-consistency threshold	$J_{e_{AC}}$	1.0	°		

The first step of the FDI procedure described in Procedure 9.1 is the evaluation of the e_{AC} metric to check Ackermann-consistency. Figure 9.9 shows that $e_{AC} < J_{e_{AC}}$ during the test interval. Following this, it could be confirmed that the NKM validity conditions of $|a_{c,n}| < \bar{a}_n$ and $|M_{w,i}| < \overline{M}_{w,i}, \quad i = 1, \ldots, 4$ are satisfied, thus the *NKMFDI* diagnosis outputs are valid.

Since the wheel speeds are available, we proceed to the evaluation of $b_{nskc,\{\mathbb{W}\}}$ and $b_{B\{\mathbb{W}\}\{k\}}$ for all time steps. The fault alarm $b_{nskc\{134\}}$ is displayed in Figure 9.10. It is found that $b_{nskc\{134\}} = 1$ during $t \in [27\text{s}, 28.5\text{s}]$, meaning that $\{\Omega_{\mathbb{W}}, \Delta_{\mathbb{W}}\}$ do not fulfil the *NSKC Check*. Evaluation of the remaining 3-wheel variants of $b_{nskc\{\mathbb{W}\}}$ (see Figure 9.11) produces the residual pattern of

$$[b_{nskc\{123\}}\ b_{nskc\{124\}}\ b_{nskc\{134\}}\ b_{nskc\{234\}}] = [1\ 1\ 1\ 0]\ .$$

Since only the wheel set $\mathbb{W} = \{2, 3, 4\}$ is NSKC and all other sets contain wheel 1, the fault is isolated to wheel 1. All the computed $b_{nskc\{\mathbb{W}\}}$ are displayed in the second plot of Figure 9.11, and the isolation outcomes can be seen in the fourth plot. When the residual pattern does not match a fault signature exactly, then the partial firing considerations apply as discussed in Chapter 5. For example, during $[32, 33.5]$s, a 0 value of the

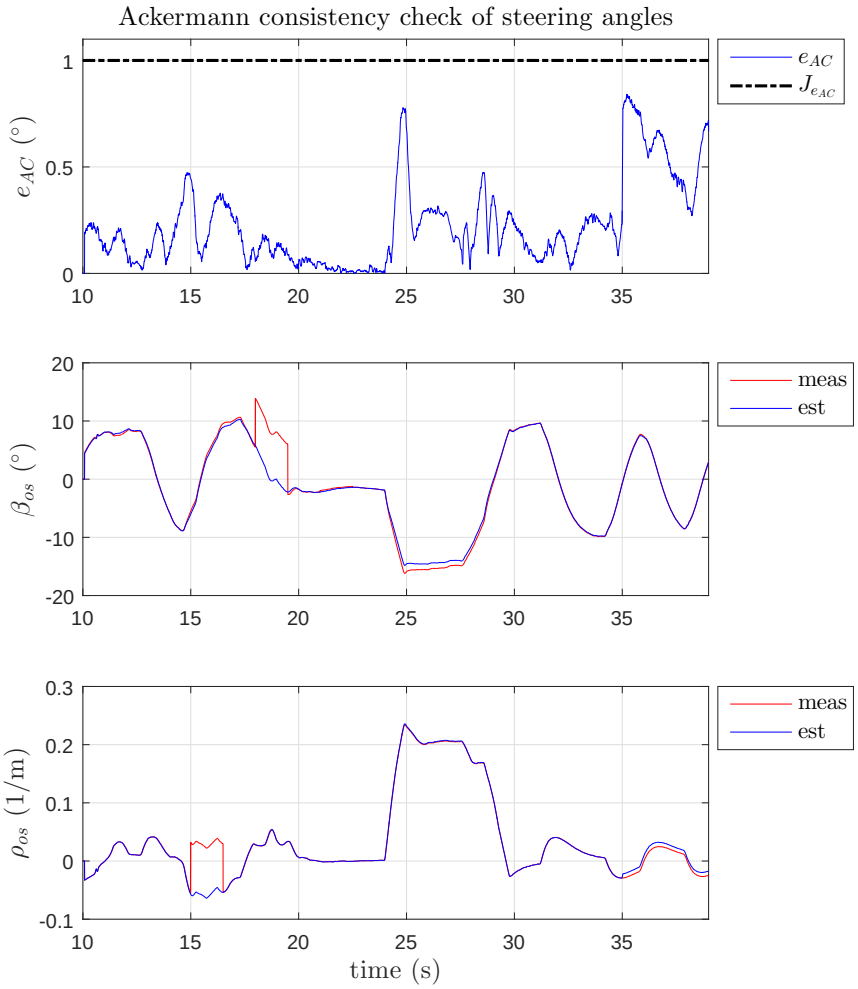

Figure 9.9: Simulation test case: e_{AC} and $J_{e_{AC}}$ from the Ackermann-consistency check (top) and the estimates $\{\hat{\beta}_c, \hat{\rho}_c\}$ using only Δ_w (remaining plots)

intermittently firing $b_{nskc\{123\}}$ results in a pattern which is a subset of both those for a fault at wheels 2 and 4 (right-front and right-rear), so both of these are considered fault candidates.

When the *NSKC Check* returns a fault-free diagnosis, the 20 residuals

$$r_{B\{\mathbb{W}\}\{j\}} \quad \text{for } j = 1, \ldots, 5, \ \mathbb{W} \in \{\{1,2,3\},\{1,2,4\},\{1,3,4\},\{2,3,4\}\}$$

are evaluated to detect and isolate faults in the body motion measurements. In order to visualise the measurement signal value in the same plot as the bounds, the measurements of $\boldsymbol{y}_{romo}$ are plotted together with their upper and lower thresholds in Figure 9.10. Only the detector signals for $\mathbb{W} = \{1,3,4\}$ are depicted to illustrate their behaviours. For each body motion measurement, Figure 9.10 shows the measured value, the nominal pseudo-inverse estimate from $\{\Omega_w, \Delta_w\}$ (see (9.11)), and the lower and upper bounds of the tolerance band. As expected from the fault sensitivity analysis, the width of the dynamic tolerance band is dependent on vehicle speed and steering inputs, providing more sensitive fault detection than constant residual thresholds. It can also be seen that each fault-affected measurement violates the bounds when its sensor fault occurs, whereas it remains within

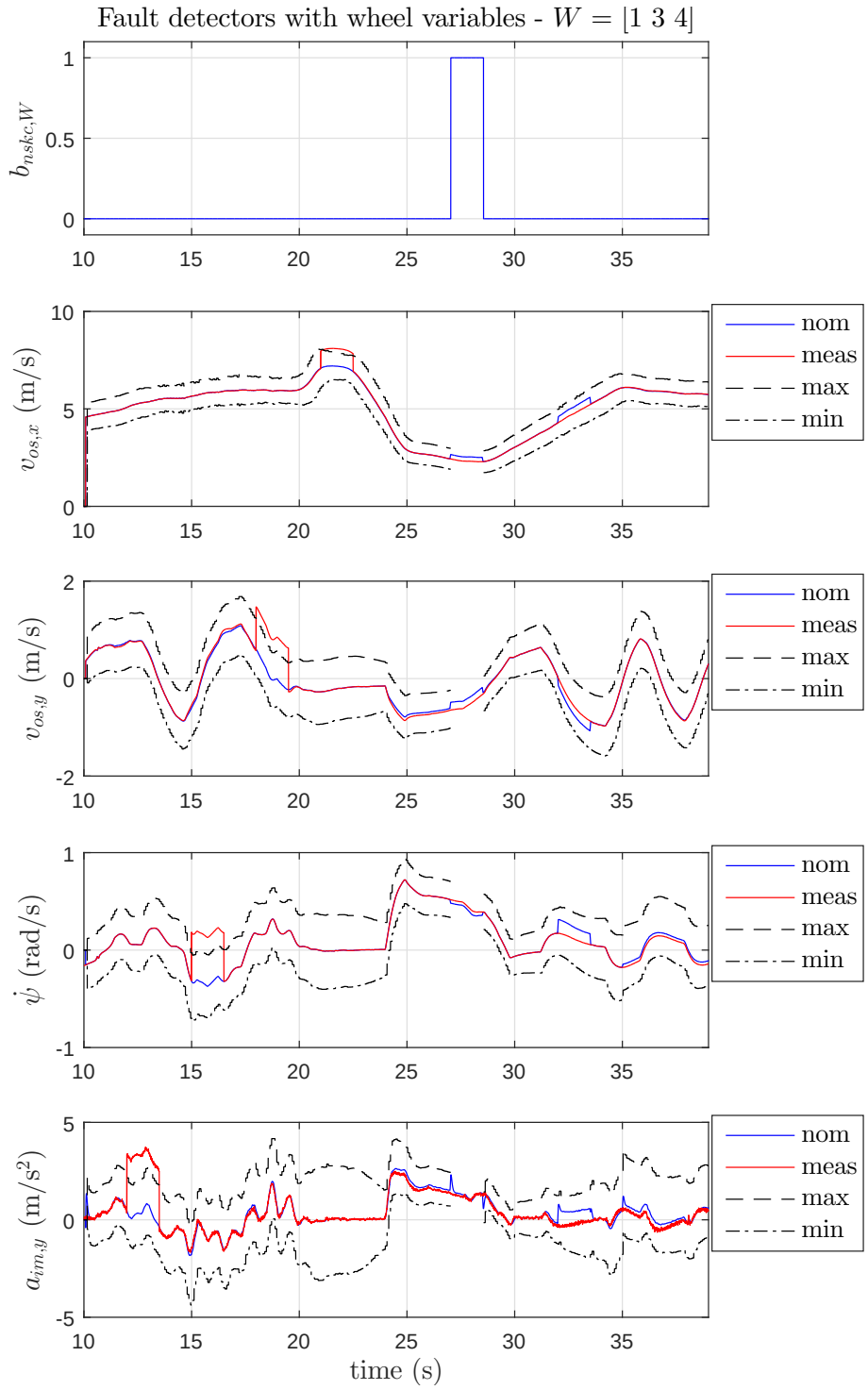

Figure 9.10: Simulation test case: *NSKC Check* of $\boldsymbol{v}_{w,\{134\}}$ (top) and $\boldsymbol{q}_{\sigma,j}$ components toegher with their bounds for the *Body Velocity / Acceleration Check* (remaining plots). $\boldsymbol{v}_{w,\{134\}}$ denotes the elements of $\boldsymbol{v}_w$ for wheels $\{1, 3, 4\}$.

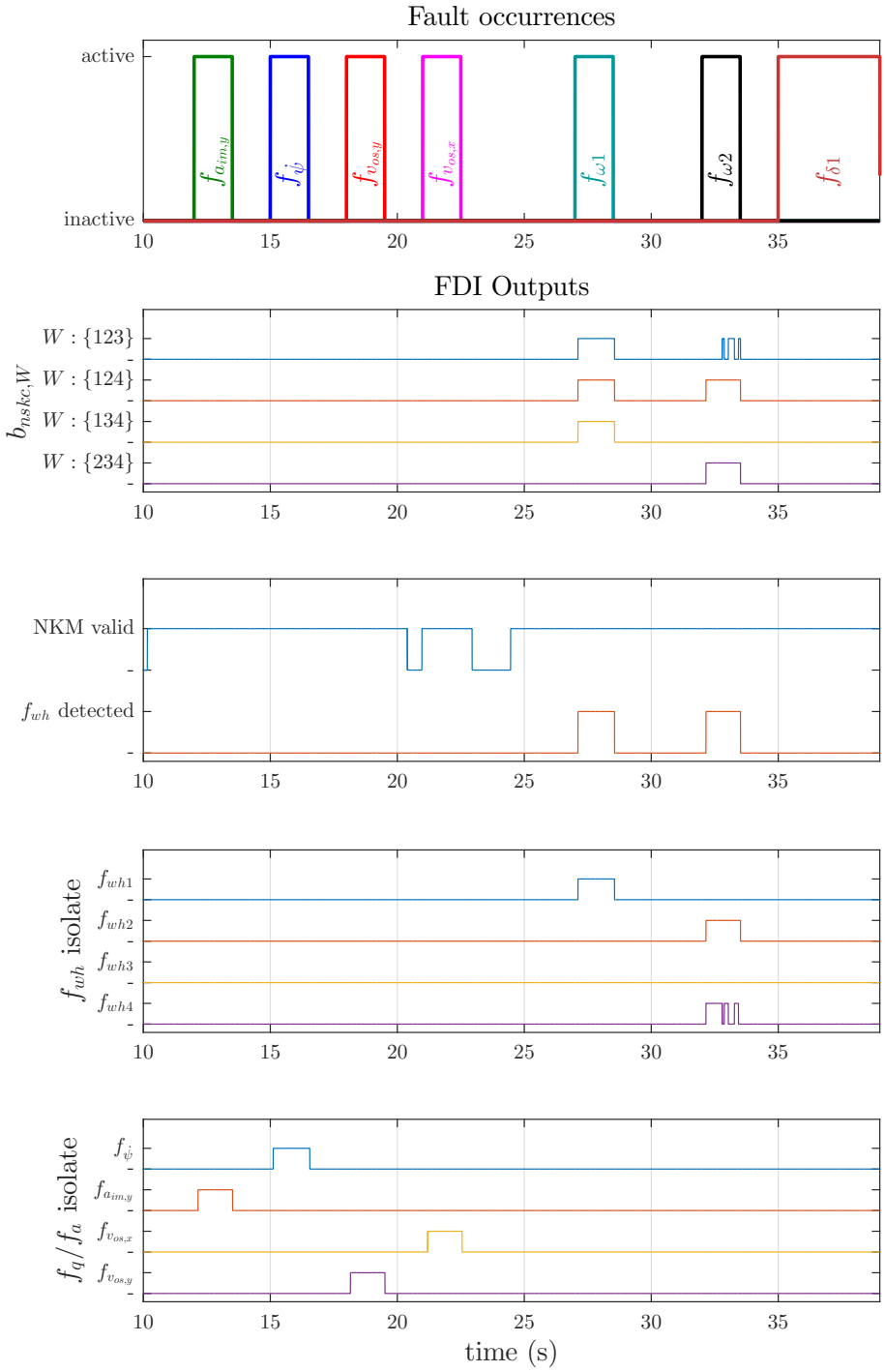

Figure 9.11: Simulation test case: Fault occurrences and FDI outputs. The top plot shows the timing of the injected faults. The second plot shows all four $b_{nskc,\mathbb{W}}$ outputs, and the third plot shows the NKM validity check output and detection of any wheel variable fault. The fourth plot shows isolation of wheel variable faults using the pattern of $b_{nskc,\mathbb{W}}$ residuals, and f_{wh*} denotes f_{ω_*} or f_{δ_*}. The bottom plot shows the fault detection status for the body motion sensors.

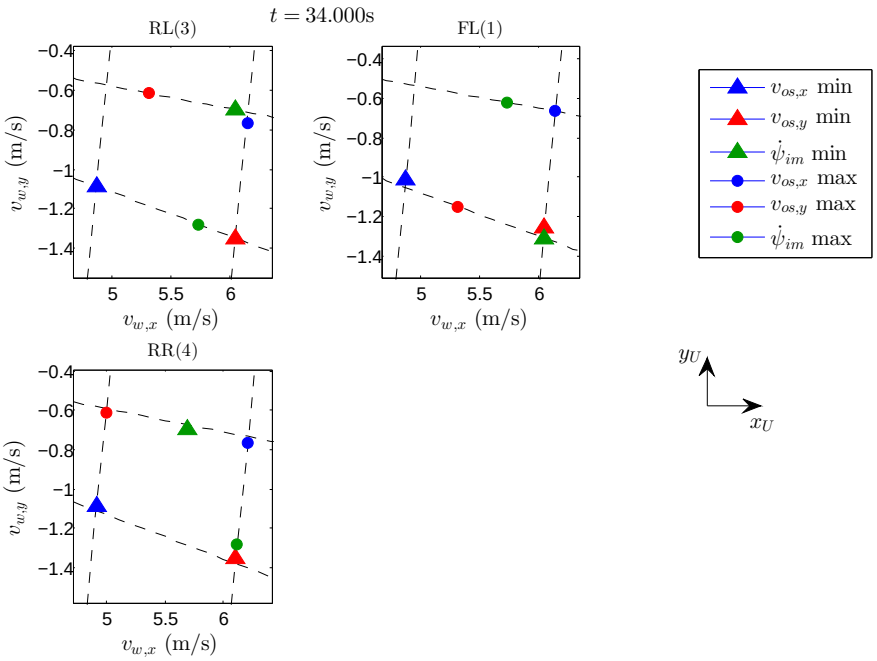

Figure 9.12: Simulation test case: $\boldsymbol{v}_{w,\{134\}}$ arguments of the LP solutions at $t = 34.0$s for the upper and lower bounds for the body motion variables $v_{os,x}$, $v_{os,y}$ and $\dot{\psi}_{im}$.

the bounds at other times despite occasional deviations from the nominal estimate. The sensor measuring the j-th component of $\boldsymbol{y}_{romo}$ is deemed faulty if $b_{B\{\mathbb{W}\}\{j\}}$ fires for just one of the tested $\mathbb{W}$. The fault detection results for the body motion sensors are shown in the bottom plot of Figure 9.11.

To gain an insight into the $\boldsymbol{q}_\sigma$ bounds, Figure 9.12 plots the $\boldsymbol{v}_{w,i},\ i \in \{1,3,4\}$ arguments of the LP optimisation solutions corresponding to the upper and lower bounds for each $\boldsymbol{q}_\sigma$ component at the time instant $t = 34.0$s. The polygon approximation of the tolerance region $\mathbb{V}_{w,i}$ is also plotted for each $\boldsymbol{v}_{w,i}$ (see Figure 9.4) using dotted lines. At the evaluated instant, all four wheels were steered to the right by approximately 10° and $\boldsymbol{v}_w$ is close to perfectly NSKC. One can observe that most of the six solutions consist of $\boldsymbol{v}_{w,i}$ lying close to the polygon boundaries for all the wheels to optimise the $\boldsymbol{q}_\sigma$ component of concern, but some $\boldsymbol{v}_{w,i}$ arguments lie slightly in the interior due to the requirement for each solution to maintain NSKC. As the deviation of $\{\Delta_w, \Omega_w\}$ from NSKC increases, more of the solution arguments will tend to move towards the polygon interior.

9.6.2 Experimental Test Drive

Next the effectiveness of the *NKMFDI* is demonstrated by applying it to experimental measurements of the wheel and body sensors from a driving test with the real vehicle. The ROboMObil was first manoeuvred slowly at a speed below 3m/s with large steering angles of up to 25° before it was stopped and then rotated about its central yaw axis. Since the sensitivity to body motion sensor faults has already been studied in Section 9.4 and demonstrated in simulation, the primary purpose of validation using experimental

data is to check that no false alarm is triggered throughout the extended range of motion of the physical RObоMObil. Nonetheless, faults have been injected retrospectively into the sensor data with the parameters listed in Table 9.12 to evaluate the fault responses.

Table 9.12: Fault sizes and times: experimental test case

Fault	**Size**	**Time**
$f_{v_{os,x}}$	$+50\%$	$[6, 8]$s
$f_{v_{os,y}}$	frozen at 0	$[14, 16]$s
$f_{\dot{\psi}_{im}}$	$+0.6$rad/s	$[39, 41]$s
$f_{a_{im,y}}$	$+2\text{m/s}^2$	$[18, 20]$s
$f_{\omega 1}$	$+100\%$	$[10, 12]$s
$f_{\omega 2}$	$+5$rad/s	$[22, 24]$s
$f_{\delta 1}$	$+2^\circ$	$[35, 39]$s

Figure 9.13 plots the wheel variables, showing that the phase of rotational motion begins from $t = 32.2$s, when the steering angles are set to magnitudes of approximately 60° with the vehicle stopped, before rotating in a anti-clockwise direction. In the top plot of Figure 9.14, the e_{AC} metric breaching its threshold during the periods $[32.2\text{s}, 33.4\text{s}]$ and $[43.3\text{s}, 44.4\text{s}]$ indicates that the steering angles failed to fulfil the Ackermann consistency requirement. In these periods, the steering angles of the stationary vehicle are being changed from the longitudinal to the rotational configuration. On the RObоMObil, they must inevitably pass through Ackermann inconsistent configurations due to the large but still finite steering angle range of each wheel, which results in separated feasible ICR regions (as shown in Figure 6.8). The diagnosis outputs are invalidated during these periods.

Figure 9.15 again shows the behaviours of the fault detectors for $\mathbb{W} = \{1, 3, 4\}$. The top plot shows that the *NSKC Check* does not raise false alarms even at high steering angles and predominantly rotational motion, and it is sensitive to the wheel speed fault at $t = 15$s as desired. The remaining plots of Figure 9.15 demonstrate that the body sensor signals remain within the calculated bounds throughout the motion under fault-free conditions, while their faults are promptly detected. The excursion of the $a_{im,y}$ measurement outside the bounds after $t = 37.5$s is an anomaly most likely caused by a glitch in sensor processing. This is suggested by its non-zero value even when the vehicle has ceased moving after $t = 41.5$s, which cannot be caused by erroneous geometric parameters. The diagnostic results are summarised by the logical outputs displayed in Figure 9.16.

The presented plots highlight some of the adaptations of the algorithm necessary to deal with the properties of real sensors. The optical velocity sensors ($\sigma = os$) are configured to set its velocity outputs to zero below a threshold speed. This effect is handled in the bound calculations by appropriate relaxation of the bounds at very low speeds. Both this sensor and the acceleration sensor ($\sigma = im$) also become significantly noisier at low speed, and false alarms are minimised by smoothing the Boolean outputs, realised by requiring them to fire over a number of consecutive samples before an alarm is raised.

Furthermore, Figure 9.14 shows how the β_{os} and ρ_{os} signals estimated from steering angles may be useful. Due to the sensor properties at low speed, both measurements are extremely noisy and unsuitable for use in dynamic or supervisory control. The much smoother estimated signals provide an alternative source in such situations.

Finally, another snapshot of the tolerance regions and the $\boldsymbol{v}_w$ arguments of the LP solutions is offered in Figure 9.17, this time at an instant when the vehicle is executing the rotational motion at $t = 38.0$s. The diagonal sides of the polygon regions reflect the large steering angles of approximately $\pm 60°$. At the low wheel speeds during this manoeuvre, the absolute component of the wheel speed tolerance becomes dominant and results in a larger tolerance of each $\boldsymbol{v}_{w,i}$ in the longitudinal wheel direction than in the lateral direction. This effect is visible in the elongated shape of the tolerance regions. The alignment of these rectangles with the $\pm 60°$ steering angles produces a higher body velocity tolerance in the body y-direction than the x-direction, and this is reflected in the wider bounds for $v_{os,y}$ than $v_{os,x}$. This illustrates the sensitivity advantage of the presented approach, in which the tolerance regions for $\boldsymbol{v}_{w,i}$ are derived with separate, possibly dynamic tolerance parameters for longitudinal and lateral wheel directions. This stands in contrast to the alternative approach of norm bounding the errors on the Cartesian wheel velocities $\boldsymbol{v}_{w,i}$, where this directional sensitivity would not be possible.

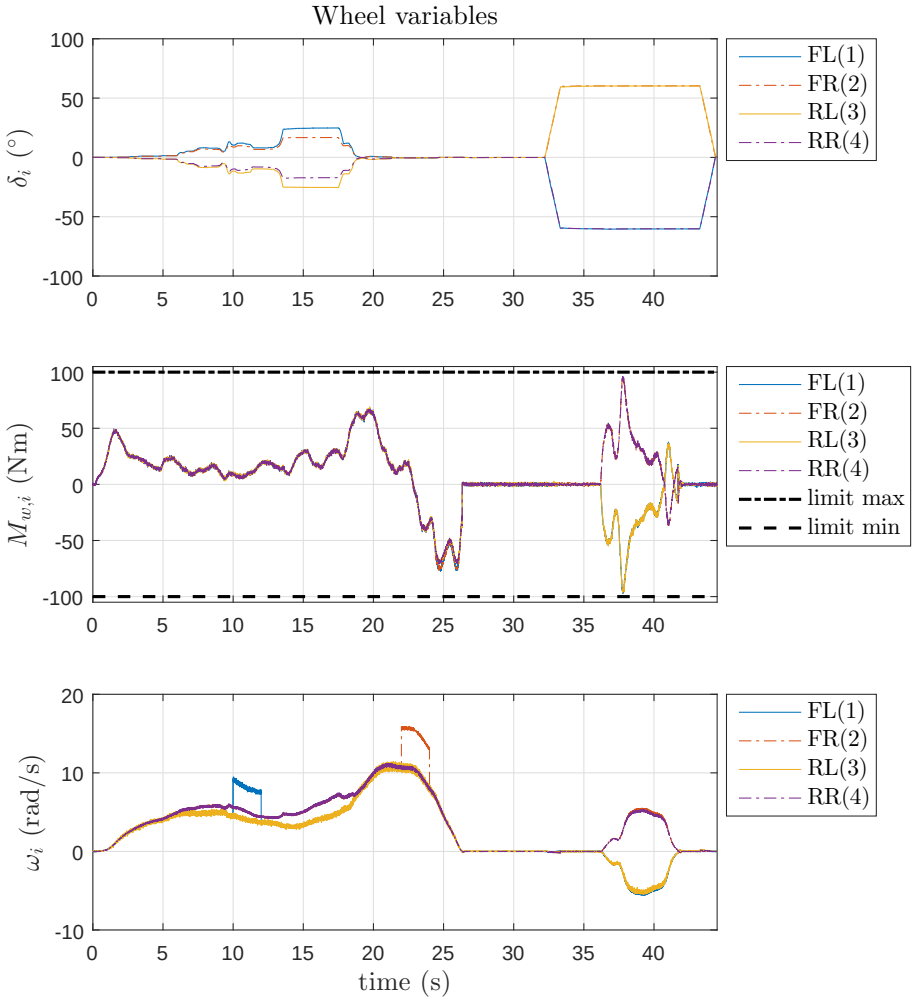

Figure 9.13: Experimental test case: wheel variables δ_i (steering angles), $M_{w,i}$ (wheel torques), and ω_i (wheel speeds). Occurrences of f_{ω_1} and f_{ω_2} are visible in the wheel speed plot.

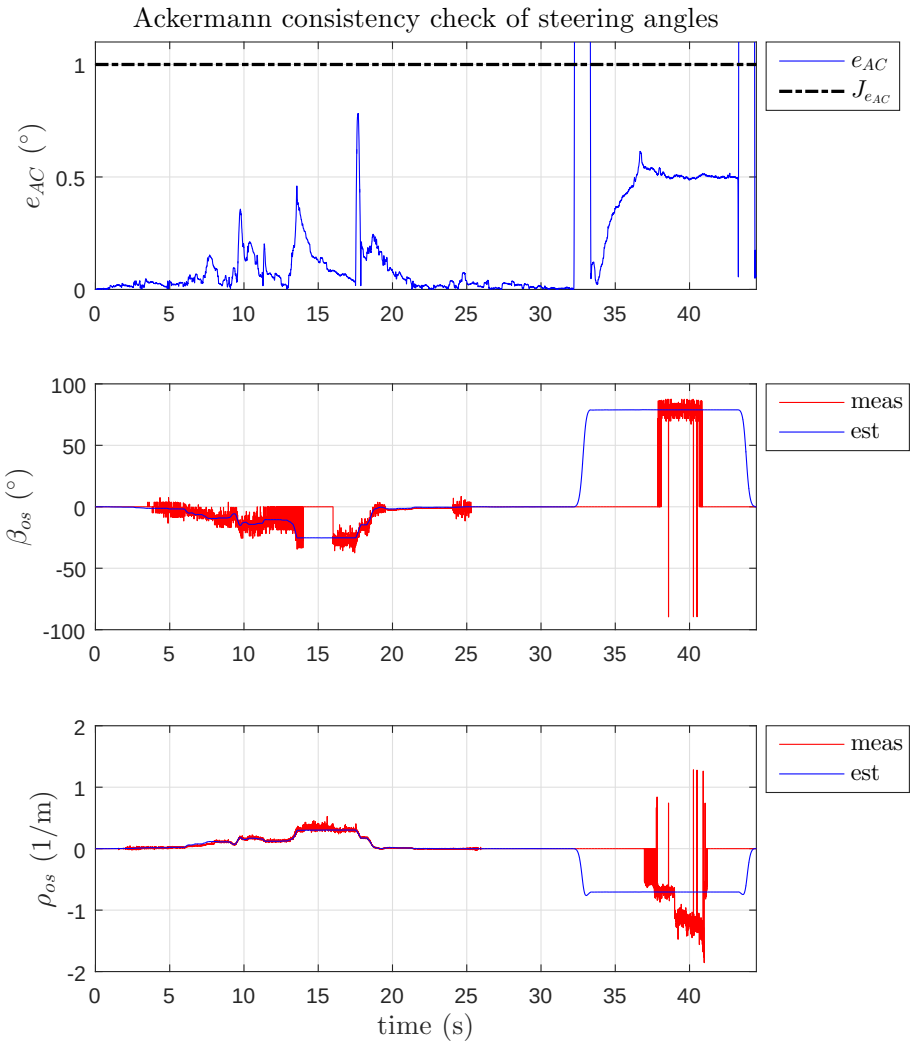

Figure 9.14: Experimental test case: e_{AC} and $J_{e_{AC}}$ from the Ackermann-consistency check (top) and the estimates $\{\hat{\beta}_c, \hat{\rho}_c\}$ using only Δ_w (remaining plots)

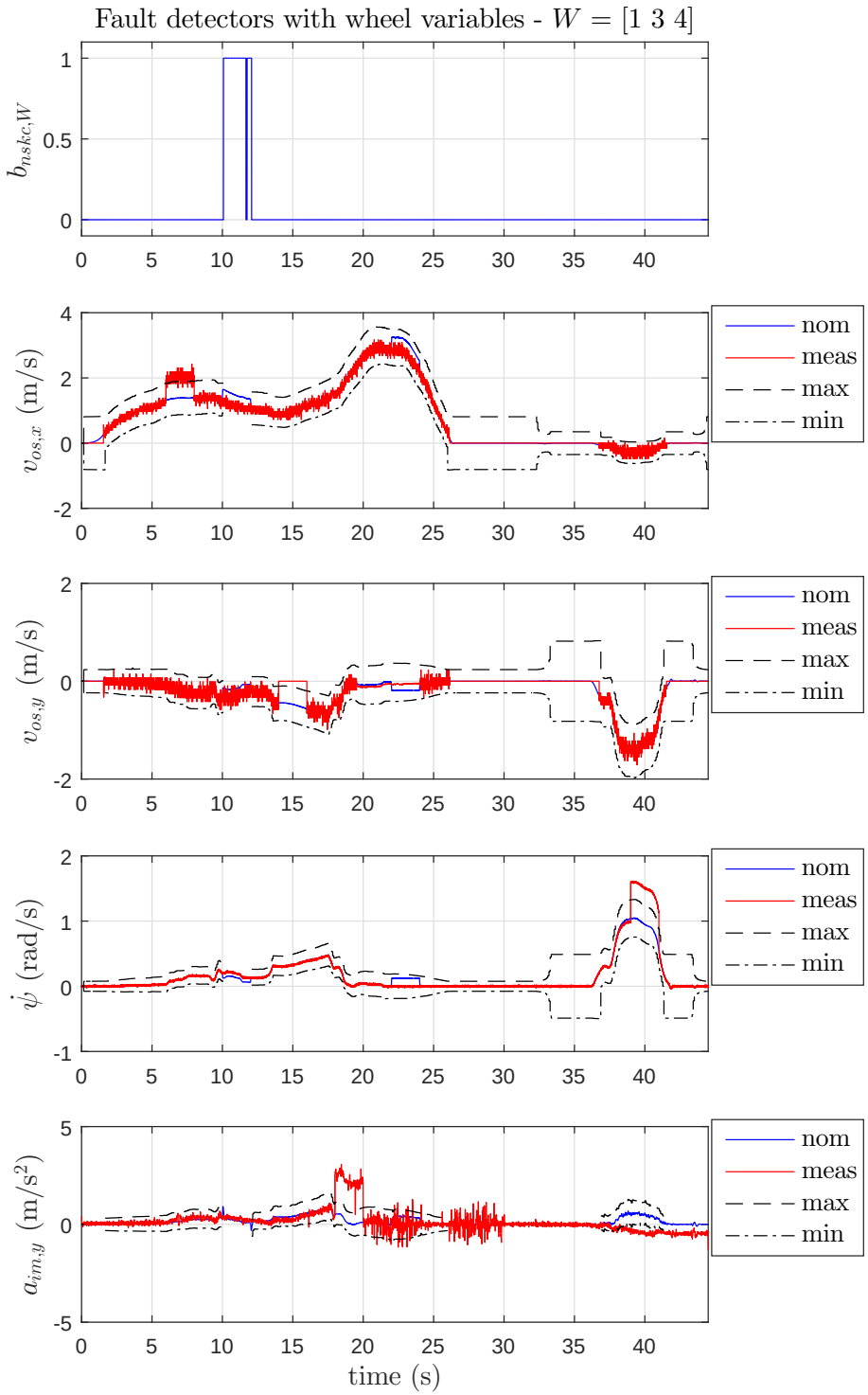

Figure 9.15: Experimental test case: *NSKC Check* of $\boldsymbol{v}_{w,134}$ (top) and bounds on $\boldsymbol{q}_c$ components calculated from $\boldsymbol{v}_{w,134}$ (remaining plots). $\boldsymbol{v}_{w,134}$ denotes the elements of $\boldsymbol{v}_w$ for wheels $\{1, 3, 4\}$.

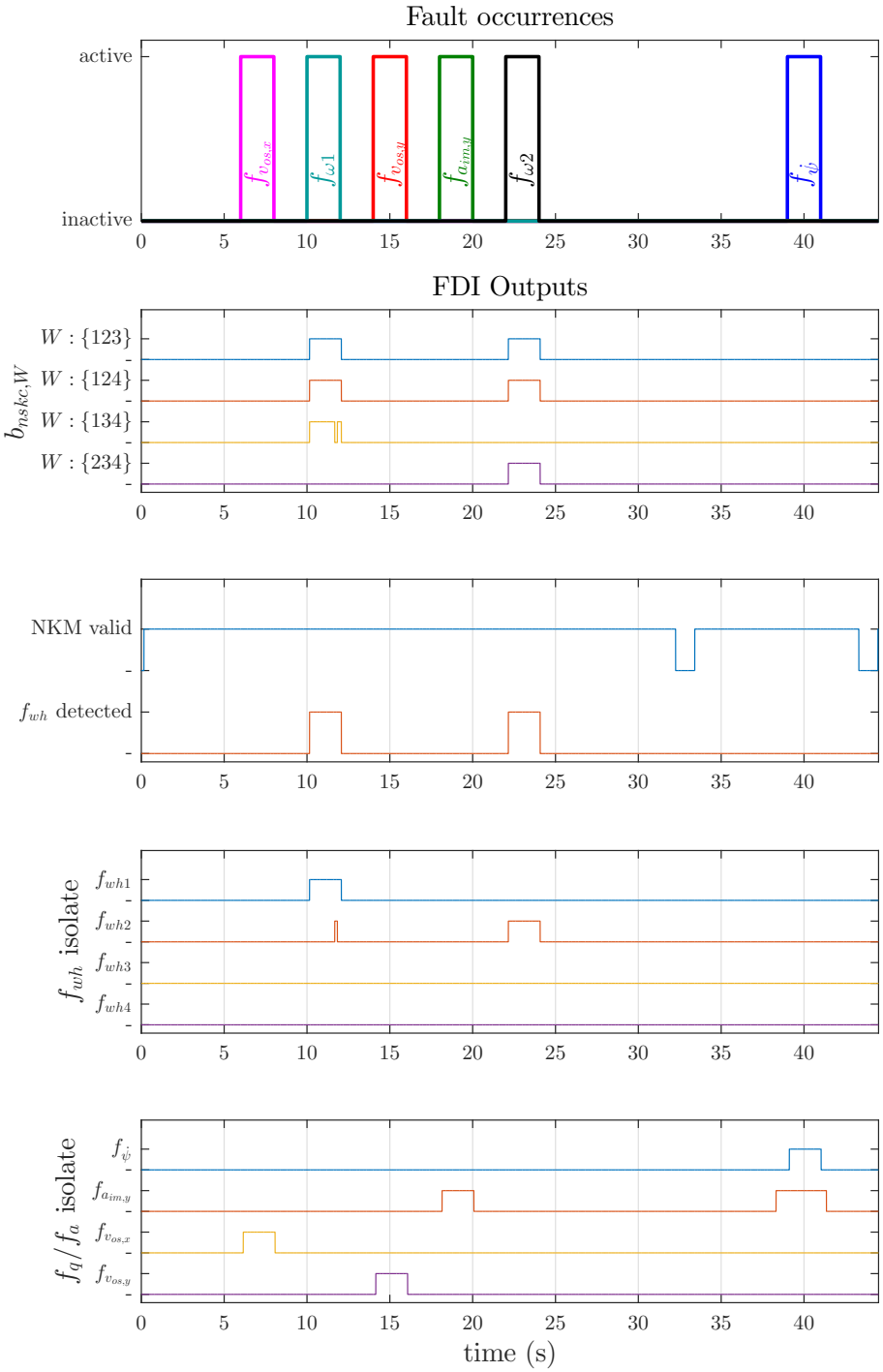

Figure 9.16: Experimental test case: Fault occurrences and FDI outputs. The top plot shows the timing of the injected faults. The second plot shows all four $b_{nskc,\mathbb{W}}$ outputs, and the third plot shows the NKM validity check output and detection of any wheel variable fault. The fourth plot shows isolation of wheel variable faults using the pattern of $b_{nskc,\mathbb{W}}$ residuals, and f_{wh*} denotes f_{ω_*} or f_{δ_*}. The bottom plot shows the fault detection status for the body motion sensors.

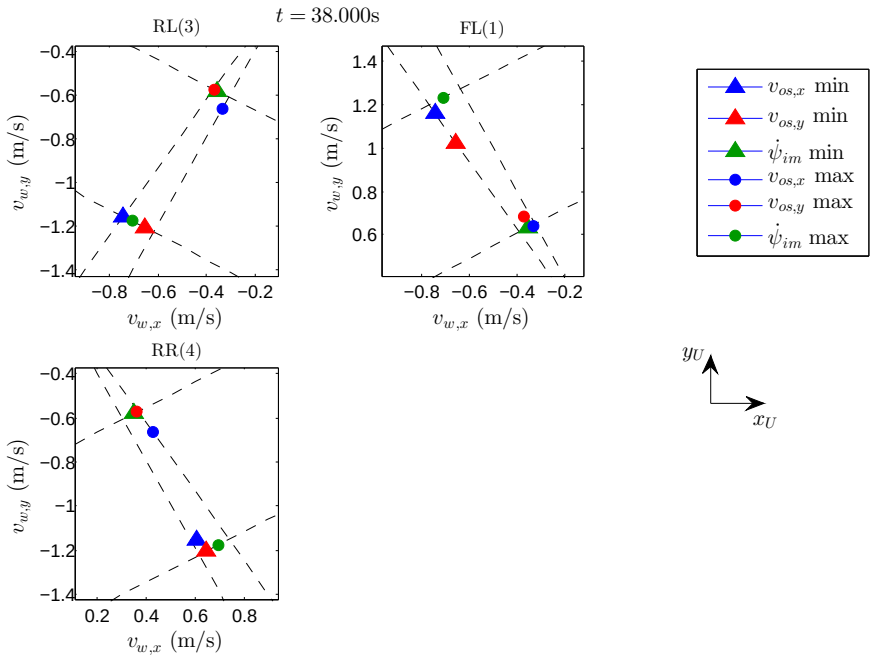

Figure 9.17: Experimental test case: $\boldsymbol{v}_w, \{134\}$ arguments of the LP solutions at $t = 38.0$s for the upper and lower bounds for the body motion variables $v_{os,x}$, $v_{os,y}$ and $\dot{\psi}_{im}$.

9.7 Fusion with Other Diagnostic Outputs

In this and the previous chapter, the complementary model-based FDI functions of *NKMFDI* and *STMFDI* have been developed and analysed independently. Although this thesis only sets out to develop and evaluate these components of vehicle dynamics FDI without addressing their integration into the overall FDI module, some ideas to take advantage of the synergies between these two functions are briefly explored here.

As already explained in Section 6.4.3 the NKM and STM are valid in different but overlapping operating regions. In addition, the two FDI approaches also deal with different subsets of the faults to be detected by the vehicle dynamics FDI, which are given in Table 6.3. These subsets are:

- STM: $\boldsymbol{f}_{stm} = \begin{bmatrix} f_{\delta_F} & f_{\delta_R} & f_{tv} & f_{\beta_{os}} & f_{\dot{\psi}_{im}} & f_{a_{im,y}} \end{bmatrix}^T$
- NKM: $\boldsymbol{f}_{nkm} = \begin{bmatrix} f_{\omega_1} \cdots f_{\omega_4} & f_{\delta_1} \cdots f_{\delta_4} & f_{\dot{\psi}_{im}} & f_{v_{os,x}} & f_{v_{os,y}} & f_{a_{im,x}} & f_{a_{im,y}} \end{bmatrix}^T$

Between these two sets, the common faults are:

- steering angle faults ($f_{\delta_F}, f_{\delta_R}$ / $f_{\delta_1} \cdots f_{\delta_4}$). Note that f_{δ_F} is a function of the two faults $f_{\delta_1}, f_{\delta_2}$, and f_{δ_R} is a function of $f_{\delta_3}, f_{\delta_4}$. However, as already mentioned in the fault sensitivity analysis, *NKMFDI* is not able to detect steering faults of small magnitudes, and its ability to isolate between them is also not proven.
- lateral dynamics body motion sensor faults ($f_{\beta_{os}}, f_{\dot{\psi}_{im}}, f_{a_{im,y}}$). Note that the $f_{\beta_{os}}$ and $f_{v_{os,y}}$ are different representations of the same fault, since the variables β_{os} and $v_{os,y}$ are related by $\beta_{os} = \tan^{-1} \frac{v_{os,y}}{v_{os,x}}$.

The situation can be represented by the following diagram:

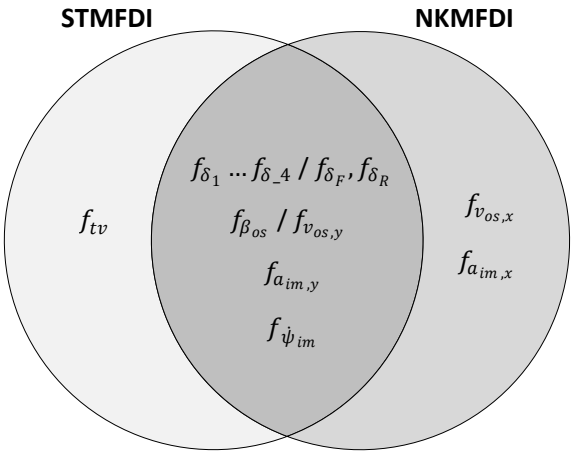

Figure 9.18: Overlap between faults detectable by the *NKMFDI* and *STMFDI* approaches

In the operating regions when only one of the FDI modules can be activated, and for faults that are only covered by one model, there is a single diagnosis and no further processing is necessary. When both FDI modules are activated, the faults that are detected by both models correspond to two diagnostic outputs. A simple approach to fuse these outputs is to apply the logical OR to the two diagnostic outputs to improve the sensitivity of the diagnosis. For a given fault, it is reasonable to also apply the logical OR between diagnostic outputs from these two model-based FDI functions and other model-free diagnostic functions. In general, for any fault covered by multiple diagnosis modules forming a set $\mathcal{D}$, the combined diagnostic output would be given by applying the logical OR to the outputs from the valid subset:

$$diagnostic\ output = \bigvee_{i \in \mathcal{D}} (alarm_i \wedge valid_i) \ .$$

More sophisticated logic and knowledge-based techniques to combine the diagnostic outputs can potentially improve the robustness of the diagnosis. Generally such extensions are founded upon assumptions on the temporal behaviour of the faults, in particular those related to their manifestation and recovery. For example, assume it is known that a particular fault does not recover once it has occurred. Then the diagnoses at different times from various modules can confirm each other over time, as the time-varying operating conditions and fault sizes validate different FDI modules and trigger different diagnostic alarms. Although the inclusion of such measures is essential to fully exploit the capabilities of the diagnostic modules, investigations into this reasoning stage is left for future research.

Chapter 10

Conclusions and Suggestions for Future Research

The goal of the thesis was to develop methods for systematic design of model-based global vehicle-level diagnosis of horizontal vehicle dynamics systems, which complements the model-free and subsystem-level diagnosis functions. Tackling vehicle level FDI design for the ROboMObil, the DLR's highly manoeuvrable and over-actuated X-by-Wire test platform, demanded an approach that is valid over both its predominant modes of motion, namely cruising and manoeuvring. This was addressed by using two complementary models with partly overlapping validity regions, with the NKM covering lower speed manoeuvring and the LPV STM covering higher speed cruising. New concepts were presented for FDI design using these models, addressing robustness issues in residual computation in both cases by taking the bounding characteristics of uncertainties and disturbances into account. Based on the NKM, the parity-relation approach was extended by propagation of input tolerances through the model. Meanwhile, based on the LPV STM, residual generators were designed by applying the reference model matching design approach based on robust estimator synthesis. It was determined that the use of a residual generator synthesis approach with a fixed fault-to-residual reference could compromise the solution quality, and this insight motivated an adaptation to allow relevant parameters in the reference model to be optimised concurrently in the estimator synthesis SDPs. Both the STM-based and NKM-based approaches could be automated to a high degree once the system and input properties are established, making them also suitable for efficiently and objectively assessing the diagnostic characteristics of candidate vehicle architectures.

Following a discussion of the outcomes of this thesis, this chapter also outlines some possibilities for future research and development.

10.1 Discussions

Part-I of this thesis introduced a procedure for FDI design for uncertain LPV systems. By applying the structured residuals approach, the fault isolation problem was divided

into a series of residual generation and evaluation problems, each with its own fault sensitivity specification. The reference model matching method for residual generation proved to be suitable for the task, especially as the state-of-the-art and cutting edge methods could be leveraged from the robust control framework to solve the contained uncertain polytopic LPV estimator synthesis problem. In particular, recent advances in the use of IQCs in analysis and synthesis for perturbed systems were employed, opening the door to incorporating not just parameter uncertainties into this method, but also a range of other perturbations such as saturations and diverse nonlinearities. The optimisation of reference model gains were incorporated into the synthesis SDP, which permits the reference model to be established concurrently to the synthesis, rather than in a prior step by applying an alternative reference-free method to a nominal model.

This improved efficiency can be significant for medium-to-large fault isolation problems, in which a high number of residual generators need to be assessed by subjecting them to the synthesis procedure. However, there are limitations to this way of determining the reference model. The inability to adapt the frequency behaviour is mitigated by the use of the fault weighting filter to relax the reference model matching constraint outside of a narrow frequency range of interest. Hence, the current method does not optimally handle cases where fault sensitivity is specified by a measure evaluated over a wider frequency range.

The residual evaluation procedure proposed for single residuals was developed to exploit analytical knowledge about the interconnection between the plant and residual generator. The residual evaluation function and the threshold function were based on the 2-norm, thus maintaining a tie to the 2-norm based measure of optimality in the synthesis stage. Adjustments were made to the common realisations of the truncated 2-norm approximation to ensure that the analytical system induced-norm could be used as a basis for the input-dependent dynamic threshold function. This approach admittedly comes at the penalty of some conservatism and memory-intensive computation, and the lack of weighting of recent over past residual values adversely affects detection times. In a practical application, this approach provides a starting point and benchmark for adaptations through e.g., recursive approximations to the truncated norm and forgetting factors.

For the task of fault isolation, automated procedures were presented for assessing the isolation capability of a residual structure and based on that, for selection of a minimal necessary subset of residuals to achieve maximum possible isolation. A procedure for online pattern evaluation was also presented. It was shown that the achievable isolation capability is tightly coupled with assumptions on the relationship between fault occurrence and residual firing, which is in turn a product of the residual generation and single residual evaluation steps. The short treatment on this topic took some steps in treating all these components in an integrated manner, but there is still much scope to be explored in future investigations.

Part-II presented a development of model-based diagnosis components based on global vehicle dynamics, with the ROboMObil as the concrete application. It was shown that the

requirements for the vehicle level diagnostic component should be derived from an analysis of the full vehicle dynamics system and its diagnostic needs, followed by a hierarchical decomposition of the diagnostic functions to divide them into manageable modules. Such an analysis and decomposition defines the set of faults to be diagnosed in the global FDI module in terms of type, size, and possibly even temporal behaviour. These constraints connect the practical requirements with theoretical assumptions of the fault detection algorithms, which in the case of the methods developed in Part-I specify the maximum and minimum fault magnitudes as well as their persistence once they occur.

Application of the procedure from Part-I to the LPV STM produced a diagnosis module with useful FDI capability, being able to detect and in most cases, isolate faults in steering angle sensors, sensors for body side-slip angle, yaw rate and lateral acceleration. Its effectiveness was first shown in a medium fidelity simulation, and then using experimental data. Moreover, the complete design procedure has been shown to be automatable to a high degree, requiring less manual tuning and iterative decision making than many procedures in literature. This enables diagnostic assessment of complex X-by-Wire architectures already at an early concept design stage.

It was found that the current approach did not reliably detect and isolate all faults of the minimum specified size. The wheel torque faults of the traction motor and the disc brake proved to be especially problematic, since its total effect on lateral dynamics was relatively weak, making it difficult to distinguishing them from disturbances and other faults. Preliminary investigations in [HO14] demonstrated that joint evaluation of STM-based diagnostics and longitudinal dynamics-based diagnostics could improve the detection and isolation capability for this fault, while case-specific measures based on system and fault knowledge could also be beneficial. The traction motor fault is all the more relevant due to the widespread adoption of electric vehicles.

Apart from the wheel torque faults, the presented realisation of *STMFDI* proved adequate for the assumptions specified in this thesis. However, the specified uncertainty range of $\pm 1\%$ in the cornering stiffness is lower than typical variations encountered in real world driving conditions, which may arise due to changes in tyre-road friction properties and wheel load, among other factors. Although the current solution is not sufficient to handle these more generic conditions, the proposed approach nevertheless provides a basis on which this range may be extended through less conservative handling of the permissible scheduling parameter trajectories and uncertainties. Moreover, currently no assumption is made on the frequency content of the actuation inputs. More accurate knowledge of their expected evolution during vehicle operation would permit the use of frequency weights to potentially increase permissible uncertainty levels. The next section provides some suggestions for future research areas related to these issues.

Finally, a diagnosis approach was presented based on the kinematic model to cover the wide range of motion possibilities of the ROboMObil, including rotating, driving sideways and along tightly curved paths. The parity relations based approaches applicable on conventional vehicles were extended with propagation of input tolerances through the

model using a bounded-in-bounded-out approach, in order to account for measurement tolerances and model uncertainties that inevitably arise through a simple model which assumes no tyre slip. The diagnostic functions were again tested in simulation and on experimental data, and the analyses of the sensitivity to faults were shown for some illustrative examples, demonstrating promising results. The trade-off for the analytical propagation of the tolerance bounds is the need to solve LP optimisation problems online, with a significant increase in computation complexity compared to a standard parity relation approach. However, this should not be a major concern for future vehicle generations running complex control algorithms.

A challenge for reliable deployment would be to robustly recognise when the underlying models and the diagnostic results are valid, without this recognition being affected by potential faults to be detected. A solution has been proposed for monitoring the forces on the vehicle through multiple calculations of the total horizontal accelerations, but it remains to be validated whether this behaves adequately over all vehicle operating conditions. Such supervisory issues for the STM-based diagnostics could be approached in a similar manner, but it was omitted in this thesis due to time constraints. To conclude the development, a rudimentary proposal was made for joining the results from both model-based diagnostic modules. It is expected that more potential and reliability can be realised through a more thorough analysis and application specific concepts, together with signal and logic post-processing measures common in industrial applications. These are topics to be addressed in future work.

10.2 Future Research

The proposed methods and procedures for model-based FDI design have demonstrated great promise in meeting the challenges posed by upcoming mechatronic vehicle dynamics architectures. However the approach is still at an early stage of development, and there is much potential to improve aspects of diagnostic function performance and the quality of their assessment. These are outlined below both for the theoretical and application oriented developments in the thesis.

It is known that the polytopic LPV relaxation often delivers conservatism analysis and synthesis results, in particular in the STM-based diagnostic application where the actual parameter region is overbounded to handle the nonlinear parameter dependency. The polytopic relaxation has been chosen over a grid-based alternative due to the theoretical guarantee that it offers for the upper bound of the induced norm. The use of the gridding approach together with parameter-dependent Lyapunov matrix function has the potential for less conservatism in the synthesis and more representative performance measures for the residual generator. If the polytopic LPV relaxation is maintained, conservatism may also be reduced using affine parameter-dependent Lyapunov functions rather than the constant ones used in this work. Furthermore, reduced-order estimator synthesis techniques may

be worth pursuing for higher order systems, if the order of the residual generator is a concern.

The STM-based diagnostics show significant potential in the residual evaluation stage. As mentioned in the earlier discussion, the current work only presents the result from the automated design procedure based on sequential residual generation, signal evaluation and pattern evaluation. A more holistic view of these three stages, together with considering the full horizontal vehicle dynamics including longitudinal dynamics, and fusion with diagnostic results from the NKM, is likely to yield improvements in the diagnostic capabilities. Information on fault manifestations, as is often provided in aerospace FDI projects from failure mode knowledge for the specified aircraft, can also be integrated if it is available. The full capability of the model-based approach can only be revealed through such a holistic development strategy.

Virtual validation and certification of vehicle functions are hot topics today, and diagnosis functions are also subject to this trend. In the simulation-based assessment of the STM-based FDI in this thesis, only the results using one set of model parameters and several cases of input signals were presented. Typically virtual validation entails the assessment of diagnosis performance metrics over a large set of simulations that adequately covers the variability of real world operating conditions, which is manifested in the simulation model as uncertain parameters and different evolutions of system inputs. Methods such as Monte-Carlo simulations or worst-case search (*anti-optimisation*) provide means of assessing worst-case performance over these variations. Moreover, a suitable optimisation design tool, such as the DLR's Multi-Objective Parameter Synthesis (MOPS) tool [Joo02], enables the FDI module parameters to be concurrently tuned to optimise the worst-case performance.

It has been emphasised in this thesis that model-based diagnosis is only reliable when the assumptions of the underlying models are adequately fulfilled. The two control-oriented models, STM and NKM, are both invalidated through dynamic driving, albeit with different tolerance thresholds. There is little research on how to reliably detect such conditions when the possibility of faults in the available measurements has to be considered. A simple proposal based on redundant evaluation of vehicle acceleration has been presented in this work, but model dynamics knowledge and signal evolution over time can be considered for future work to enhance this recognition. A solution is key to the viability of model-based diagnostic functions, and for maximising the coverage over the operating states and therefore their benefits.

Appendix A

Simulation Results - Validation of *STMFDI*

This appendix contains the results from case B of the simulative validation of the *STMFDI* approach proposed in Chapter 8. For details on the connection of this case to the validation arrangements, refer to Section 8.7.

Case B contains several sub-cases which investigate single faults in various manifestations, as opposed to the rectangular pulses used exclusively in cases A and C. Each simulation sub-case lasts 15s and use the same actuator and disturbance inputs as well as initial conditions. The reference longitudinal velocity v_x lies in [8, 18]m/s while the references for β and $\dot{\psi}$ are again chosen to keep the lateral accelerations in the low-to-medium range. In this instance no torque vectoring is commanded. The simulated fault types are based on those presented in the fault modelling section in Section 7.4 and are listed in Table A.1. Where the fault is an additive bias (constant or time-varying), the maximum magnitude is chosen to be slightly above the specified minimum detectable fault size.

Table A.1: Fault types simulated in sub-cases of case B

sub-case	**fault**	**type**	**occurred time (s)**
B1	f_{δ_F}	time-varying bias within $[-3, 3]^\circ$	$[4.5, 11]$
B2	f_{δ_R}	constant bias (-3°)	$[4.5, 11]$
B3	f_{tv}	undesired braking on left-rear wheel	$[4.5, 11]$
B4	f_β	sensor output gain error (factor 0.5)	$[9, 13]$
B5	$f_{\dot{\psi}}$	time-varying bias within $[-0.3, 0.3]$rad/s	$[4.5, 11]$
B6	f_{a_y}	sensor output frozen at 0	$[4.5, 11]$

Sub-Case B1 - f_{δ_F} (Figure A.1)

An arbitrary moderately-slow time-varying offset in the range $[-6, 6]^\circ$ is added to the steering angle sensor of the front-left steering actuator during $t \in$ [4.5 11]s. With no fault

on the front-right steering, in a linear model this would be equivalent to an additive fault f_{δ_F} of half this size. Figure A.1b shows that the residual dips below the threshold when the time-varying additive fault value is small, as one would expect. Faults that are manifested as intermittent additive faults induce such residual behaviour, and their reliable diagnosis requires processing of the temporal behaviour of the Boolean alarm signal. This additional step is beyond the scope of this work.

Sub-Case B2 - f_{δ_R} (Figure A.2)

A constant bias is added to the steering angle of both wheels of the rear axle. A one-sided steering bias on the rear is not simulated as it leads to a loss of vehicle stability with the nonlinear simulation model. This occurs because such a fault effectively reduces the rear cornering stiffness, and in this simulation the controller is not adapted to cope with this change upon fault diagnosis. The fault is successfully isolated in both the reduced and full isolation problems.

Sub-Case B3 - f_{tv} (Figure A.3)

Undesired braking of 500Nm on the left rear wheel produces differential wheel torque and therefore a torque vectoring fault $f_{tv} = 1270\text{Nm}$ during $t \in [9, 13]\text{s}$. This sub-case serves to show that the third to ninth residuals are all insensitive to the fault as per their specifications. Since no residual in the selected set is specified to be sensitive to f_{tv}, its detection is not possible.

Sub-Case B4 - f_β (Figure A.4)

The β sensor measurement is afflicted with a gain error such that it outputs a signal 0.5 times the actual vehicle state β. Due to closed-loop control using this faulty signal, the actual β state of the vehicle is effectively commanded to twice the reference value. The residuals fire intermittently since the effective additive fault size depends on the magnitude of the state β. Smaller additive fault values are not reliably detected, but nevertheless the fault can be isolated during $t \in [6.7, 9.5]\text{s}$.

Sub-Case B5 - $f_{\dot{\psi}}$ (Figure A.5)

The $\dot{\psi}$ sensor measurement is injected with a time-varying bias within the range $[-0.3, 0.3]\text{rad/s}$ whose value can be deduced from the $\dot{\psi}$ plot in Figure A.5a. The fault's time-varying nature causes the residual to only fire when the additive fault is sufficiently large. Moreover, the supplementary residuals r_{231} and r_{69} only fire for faults that are much larger than the minimum specified size. Since the injected faults are not sufficiently large to cause them to fire, it is not possible to distinguish between f_{δ_F} and $f_{\dot{\psi}}$ in this case. Inspection of the fault hypothesis plot identify these two faults as the most likely candidates.

Sub-Case B6 - f_{a_y} (Figure A.6)

The a_y sensor measurement is frozen at zero. This is equivalent to a time-varying additive fault f_{a_y} which is the negation of the true lateral acceleration. This takes on

substantial non-zero values in $[7.2, 9.5]$s, which causes the sensitive residuals to fire and trigger the correct diagnosis.

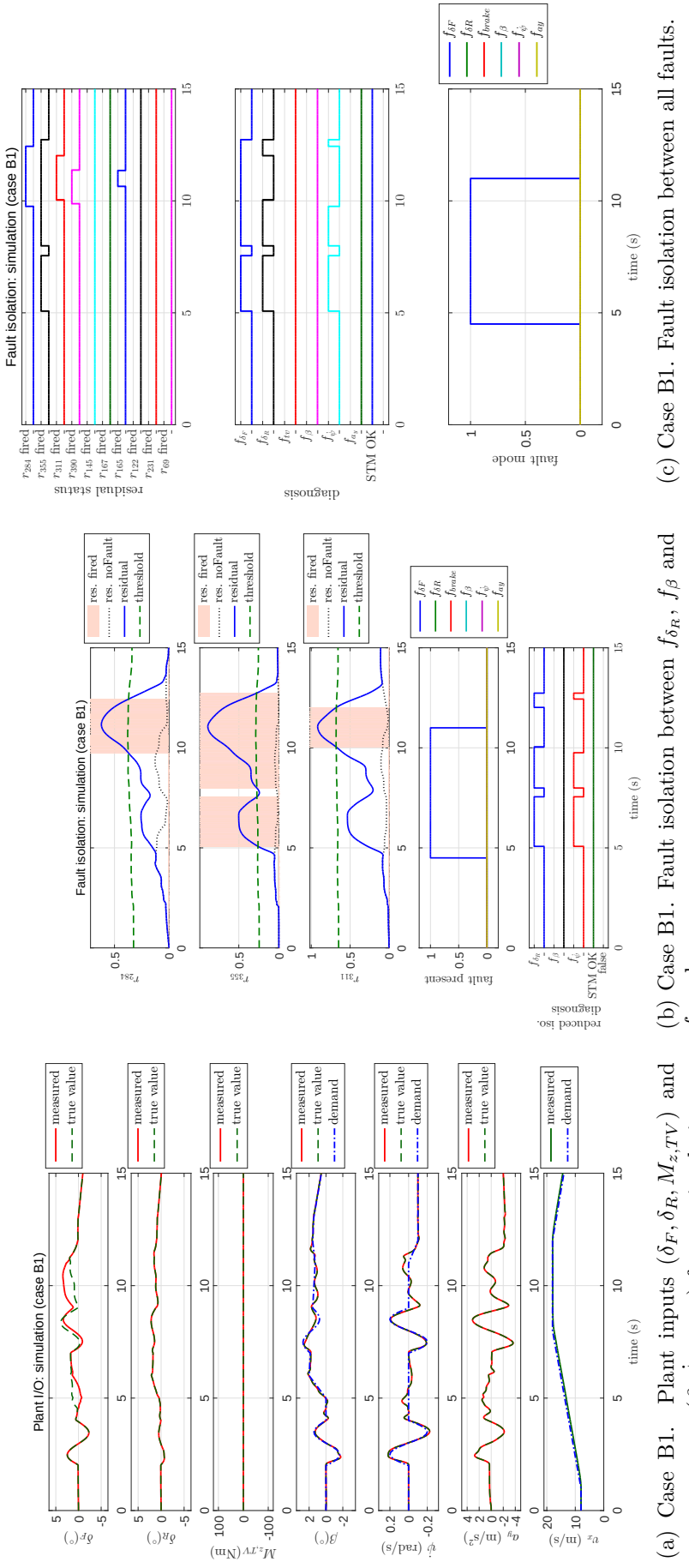

(a) Case B1. Plant inputs $(\delta_F, \delta_R, M_{z,TV})$ and measurements $(\beta, \dot{\psi}, a_y, v_x)$ from a simulation using the nonlinear DTM vehicle model

(b) Case B1. Fault isolation between f_{δ_R}, f_β and $f_{\dot{\psi}}$ only.

(c) Case B1. Fault isolation between all faults.

Figure A.1: Validation results - simulation case B1

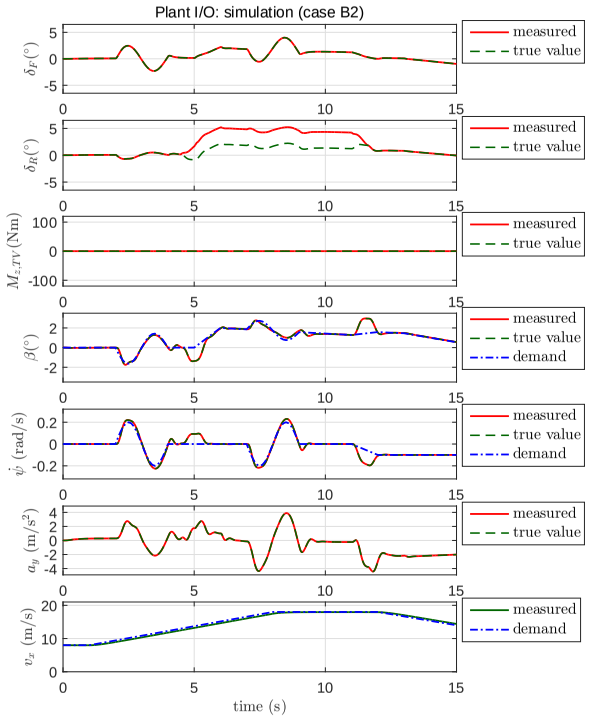

(a) Case B2. Plant inputs $(\delta_F, \delta_R, M_{z,TV})$ and measurements $(\beta, \dot{\psi}, a_y, v_x)$ from a simulation using the nonlinear DTM vehicle model

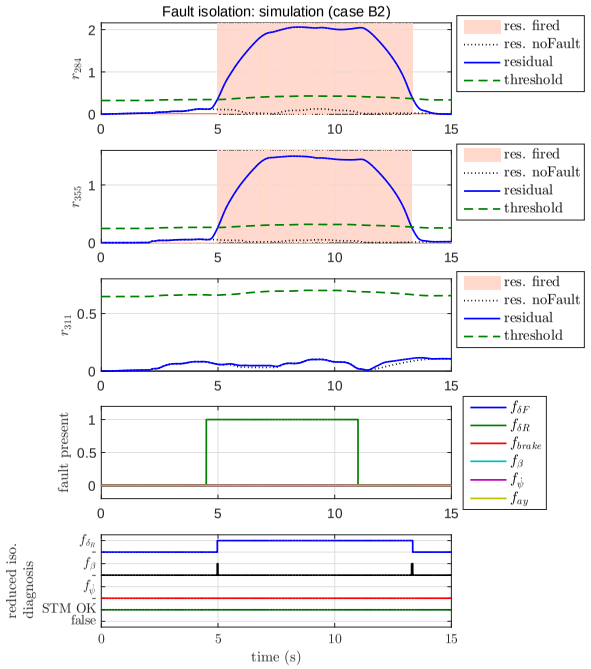

(b) Case B2. Fault isolation between f_{δ_R}, f_β and $f_{\dot{\psi}}$ only.

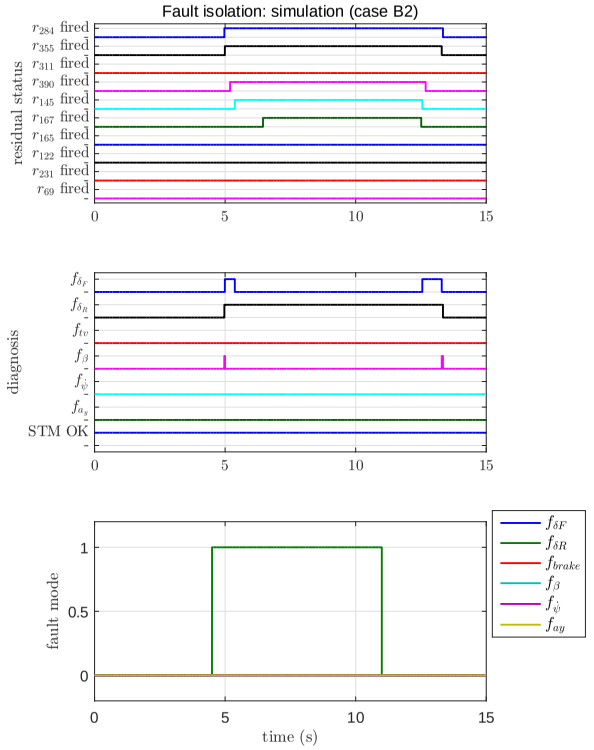

(c) Case B2. Fault isolation between all faults.

Figure A.2: Validation results - simulation case B2

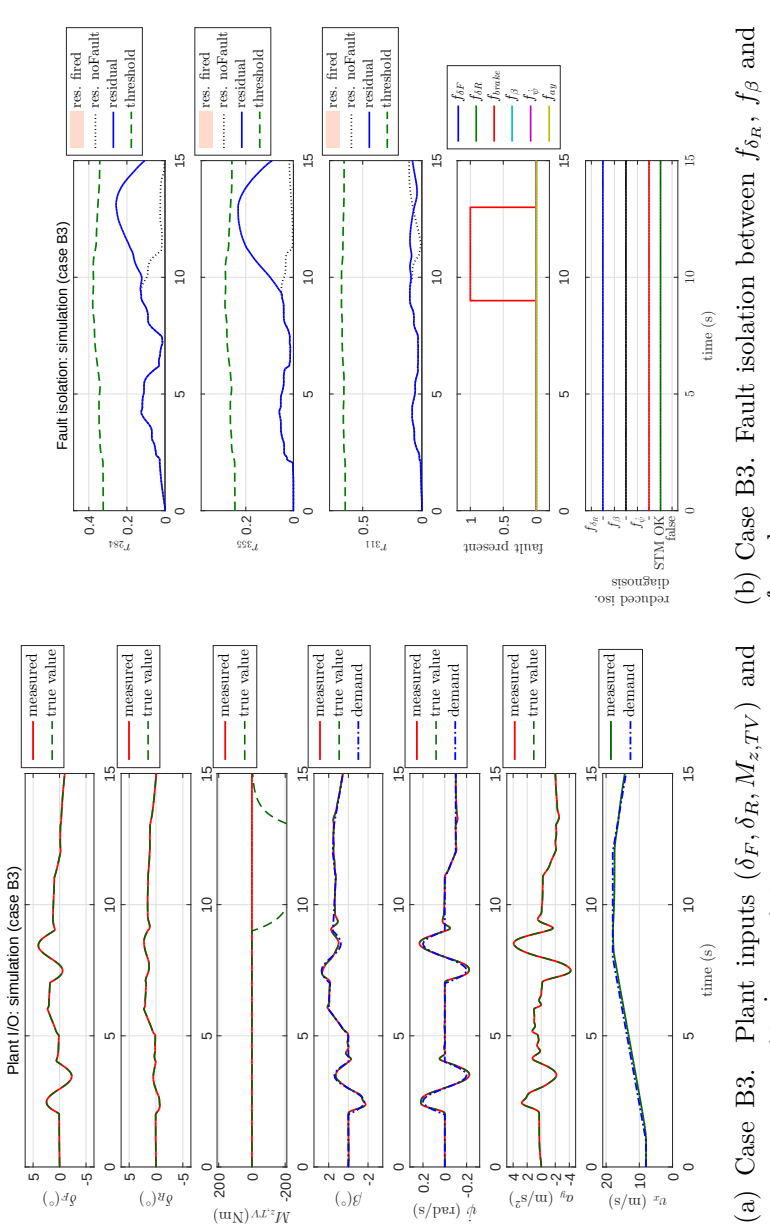

(a) Case B3. Plant inputs $(\delta_F, \delta_R, M_{z,TV})$ and measurements $(\beta, \dot{\psi}, a_y, v_x)$ from a simulation using the nonlinear DTM vehicle model

(b) Case B3. Fault isolation between f_{δ_R}, f_β and $f_{\dot{\psi}}$ only.

(c) Case B3. Fault isolation between all faults.

Figure A.3: Validation results - simulation case B3

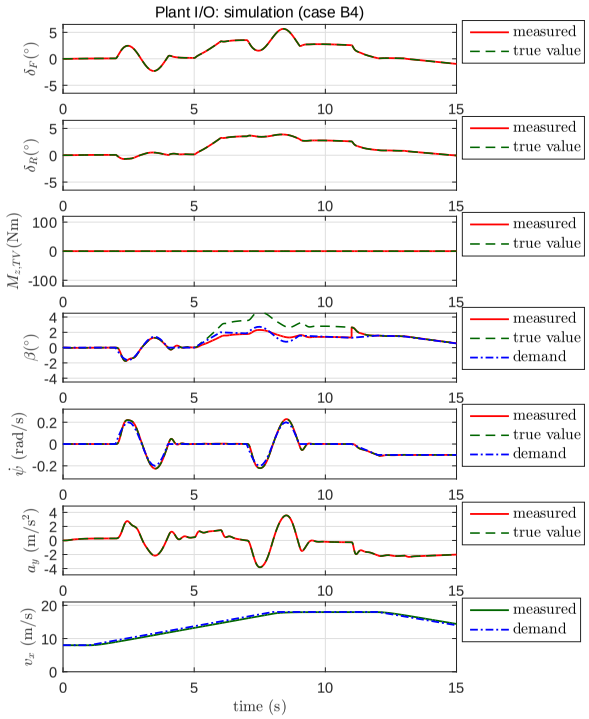

(a) Case B4. Plant inputs $(\delta_F, \delta_R, M_{z,TV})$ and measurements $(\beta, \dot{\psi}, a_y, v_x)$ from a simulation using the nonlinear DTM vehicle model

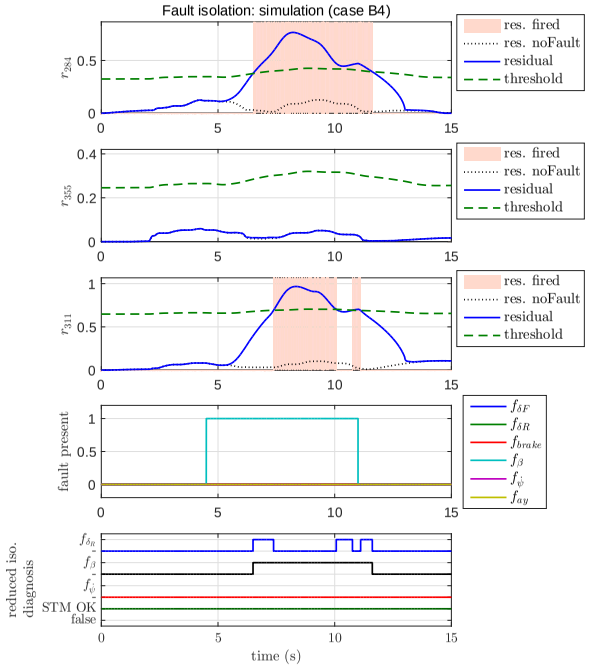

(b) Case B4. Fault isolation between f_{δ_R}, f_β and $f_{\dot{\psi}}$ only.

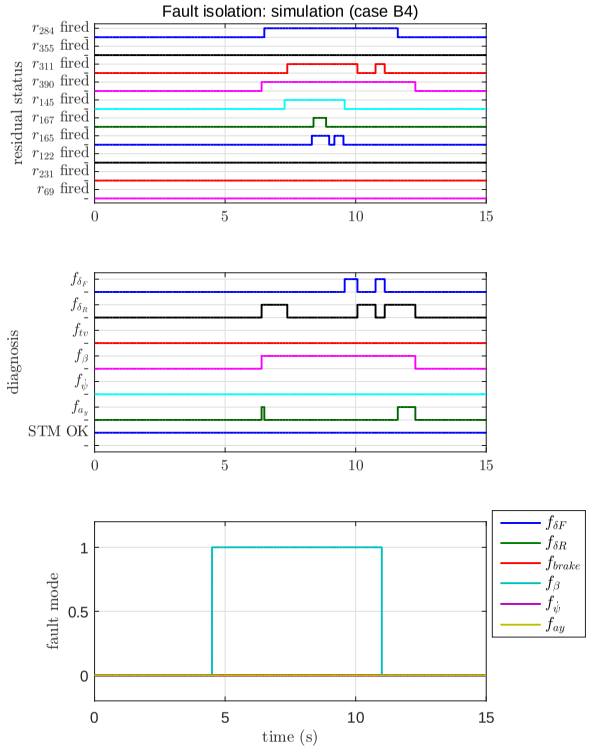

(c) Case B4. Fault isolation between all faults.

Figure A.4: Validation results - simulation case B4

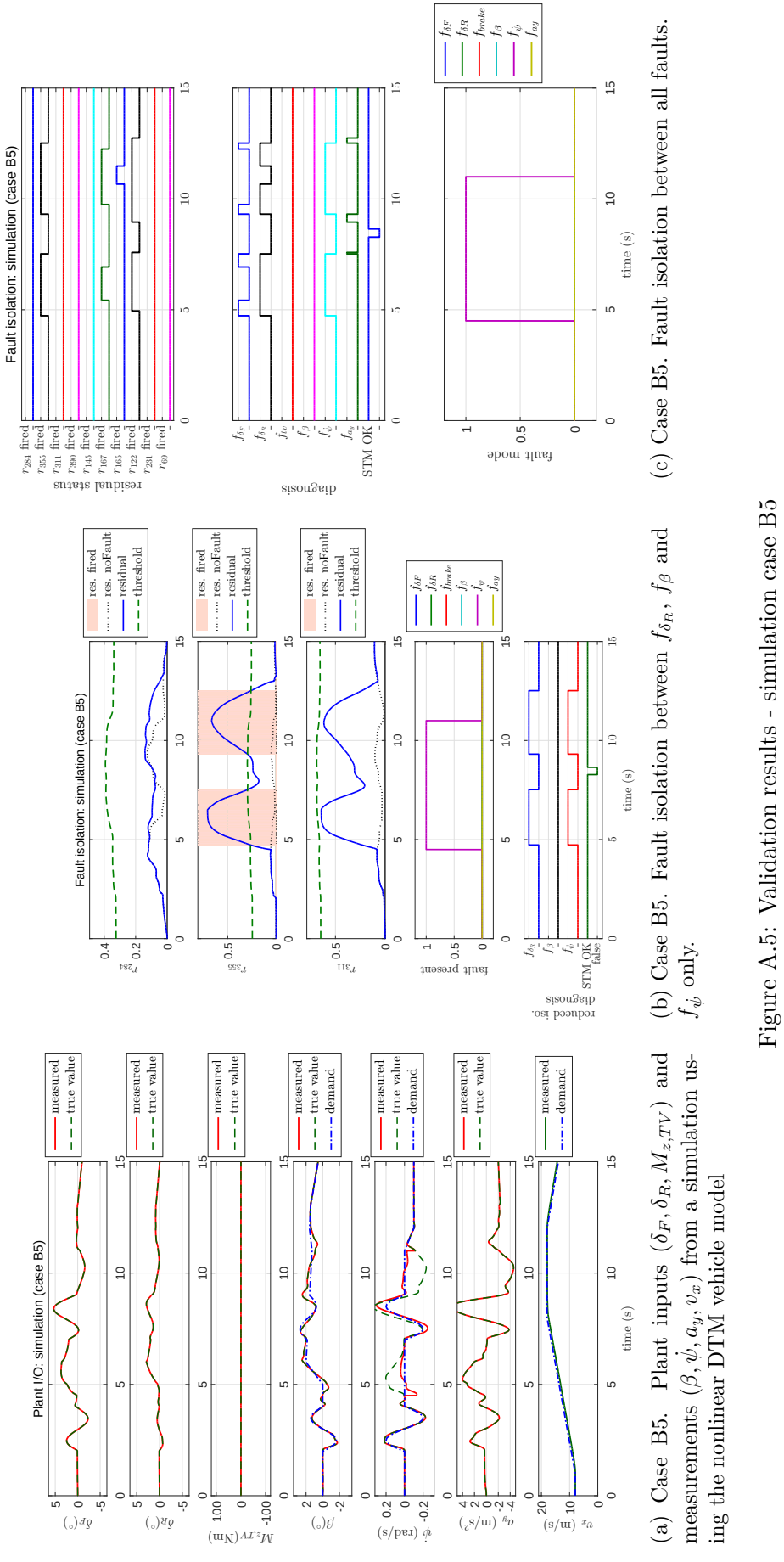

(a) Case B5. Plant inputs $(\delta_F, \delta_R, M_{z,TV})$ and measurements $(\beta, \dot{\psi}, a_y, v_x)$ from a simulation using the nonlinear DTM vehicle model

(b) Case B5. Fault isolation between f_{δ_R}, f_β and $f_{\dot{\psi}}$ only.

(c) Case B5. Fault isolation between all faults.

Figure A.5: Validation results - simulation case B5

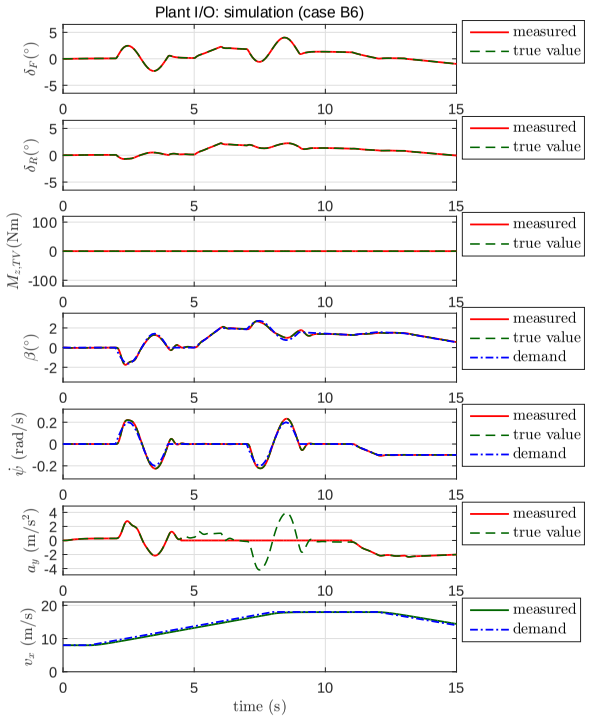

(a) Case B6. Plant inputs $(\delta_F, \delta_R, M_{z,TV})$ and measurements $(\beta, \dot{\psi}, a_y, v_x)$ from a simulation using the nonlinear DTM vehicle model

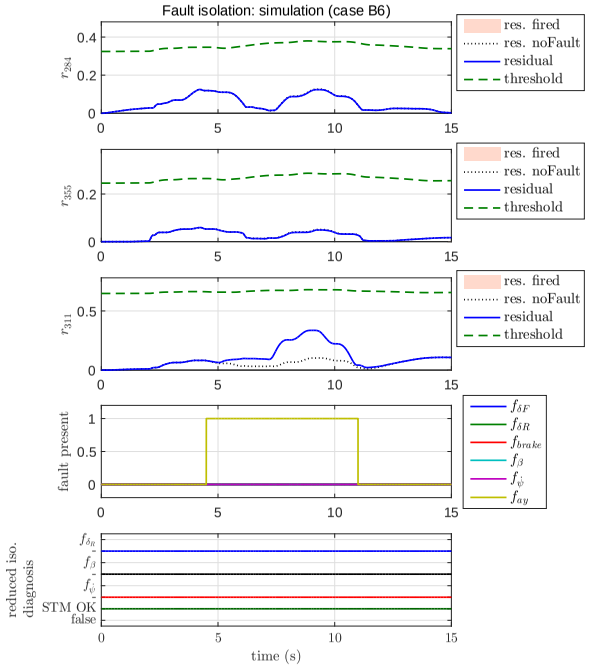

(b) Case B6. Fault isolation between f_{δ_R}, f_β and $f_{\dot{\psi}}$ only.

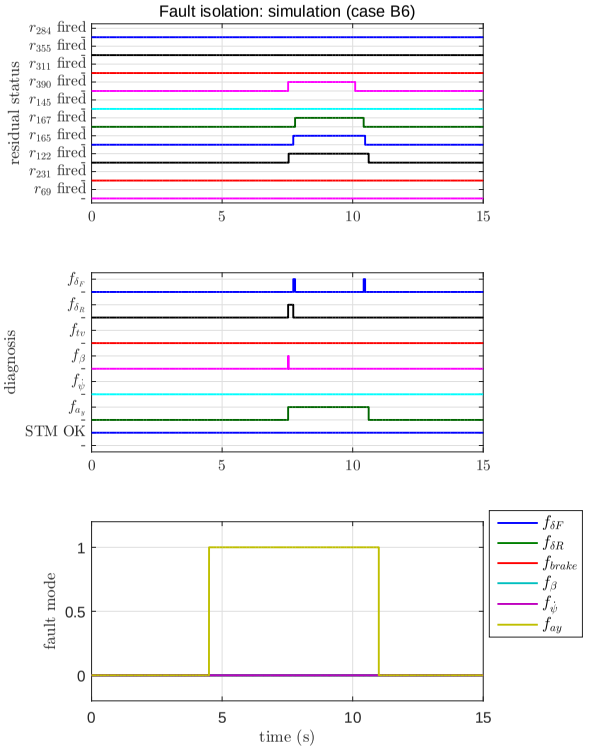

(c) Case B6. Fault isolation between all faults.

Figure A.6: Validation results - simulation case B6

References

[Abd09] Abdo, A, Saijai, J, Damlakhi, W and Ding, S X. "An Observer-based Fault Detection Approach for Vehicle Lateral Dynamics Control System". In: *7th Workshop on Advanced Control and Diagnosis*. 2009 (cit. on p. 16).

[AGB95] Apkarian, Pierre, Gahinet, Pascal and Becker, Greg. "Self-scheduled H-infinity control of linear parameter-varying systems: a design example". In: *Automatica* 31.9 (1995), pp. 1251–1261 (cit. on pp. 26, 28, 41).

[Ala15] Alameh, Kawthar, Cité, Nicolas, Hoblos, Ghaleb and Barakat, Georges. "Fault Detection and Isolation for Permanent Magnet Synchronous Machines". In: *22nd International Congress on Sound and Vibration (ICSV22)* (2015) (cit. on p. 108).

[Arm06] Armbruster, Michael, Zimmer, Eduard, Lehmann, Matthias, Reichel, Reinhard, Sieglin, Erik, Spiegelberg, Gernot and Sulzmann, Armin. "Affordable X-By-Wire technology based on an innovative, scalable E/E platform-concept". In: 2006, pp. 3016–3020 (cit. on p. 9).

[Arm09] Armengol, Joaquim et al. "Minimal Structurally Overdetermined sets for residual generation : A comparison of alternative approaches". In: *7th IFAC Symposium on Fault Detection, Supervision and Safety of Technical Processes*. 2009, pp. 1480–1485 (cit. on p. 11).

[Bal09] Balaban, Edward, Saxena, Abhinav, Bansal, Prasun, Goebel, Kai F. and Curran, Simon. "Modeling, detection, and disambiguation of sensor faults for aerospace applications". In: *IEEE Sensors Journal* 9.12 (2009), pp. 1907–1917 (cit. on p. 111).

[Bar13] Bartys, Michal. "Generalized reasoning about faults based on the diagnostic matrix". In: *International Journal of Applied Mathematics and Computer Science* 23.2 (2013), pp. 407–417 (cit. on p. 52).

[Bau11] Baumgartner, Daniel. "Konzeption eines Drive-by-Wire Lenkungsprüfstands mit flexibler Multibody-Simulation im ROboMObil Projekt". MA thesis. Technical University of Munich, 2011 (cit. on p. 109).

[BB04] Bokor, J. and Balas, G. "Detection filter design for LPV systems-a geometric approach". In: *Automatica* 40.3 (Mar. 2004), pp. 511–518 (cit. on pp. 13, 49, 69, 70).

[Bea71] Beard, Richard Vernon. “Failure accommodation in linear systems through self-reorganization”. PhD thesis. Massachusetts Institute of Technology, 1971 (cit. on pp. 12, 14, 85).

[Bec93] Becker, Gregory, Packard, Andy, Philbrick, Doug and Balas, Gary J. “Control of Parametrically-Dependent Linear Systems: A Single Quadratic Lyapunov Approach”. In: *American Control Conference*. 1993, pp. 2795–2799 (cit. on pp. 23, 28).

[Ben14] Bengler, Klaus, Dietmayer, Klaus, Farber, Berthold, Maurer, Markus, Stiller, Christoph and Winner, Hermann. “Three decades of driver assistance systems: Review and future perspectives”. In: *IEEE Intelligent Transportation Systems Magazine* 6.4 (2014), pp. 6–22 (cit. on p. 1).

[Bla06] Blanke, M, Kinnaert, M, Lunze, J and Staroswiecki, M. *Diagnosis and Fault-Tolerant Control*. 2nd. 2006 (cit. on pp. 7, 8, 11, 13, 14, 75, 78, 85, 102, 103).

[Boy94] Boyd, Stephen, El Chaoui, Larent, Feron, Eric and Balakrishnan, Venkataramanan. *Linear Matrix Inequalities in System and Control Theory*. 1994 (cit. on pp. 22, 24, 26).

[BR93] Burckhardt, Manfred and Reimpell, Jörnsen. *Fahrwerktechnik, Radschlupf-Regelsysteme*. Vogel, 1993 (cit. on p. 131).

[Bre11] Brembeck, J, Ho, L M, Schaub, A, Satzger, C, Tobolar, J, Bals, J and Hirzinger, G. “ROMO - The robotic electric vehicle”. In: *IAVSD International Symposium on Dynamics of Vehicle on Roads and Tracks*. 2011 (cit. on pp. 4, 96).

[BS09] Bokor, József and Szabó, Zoltán. “Fault detection and isolation in nonlinear systems”. In: *Annual Reviews in Control* 33.2 (Dec. 2009), pp. 113–123 (cit. on p. 12).

[Buc12] Buckl, Christian, Camek, Alexander, Kainz, Gerd, Simon, Carsten, Mercep, Ljubo, Stähle, Hauke and Knoll, Alois. “The software car: Building ICT architectures for future electric vehicles”. In: *2012 IEEE International Electric Vehicle Conference, IEVC 2012*. 2012 (cit. on p. 1).

[Bün14] Bünte, Tilman, Ho, Lok Man, Satzger, Clemens and Brembeck, Jonathan. “Central Vehicle Dynamics Control of the Robotic Research Platform ROboMObil”. In: *ATZ Elektronik* 9.3 (2014), pp. 58–64 (cit. on pp. 97, 99, 100, 102).

[Cas08] Casavola, A., Famularo, D., Franze, G. and Patton, R.J. “A Fault Detection filter design method for a class of linear time-varying systems”. In: *2008 16th Mediterranean Conference on Control and Automation*. 2008 (cit. on p. 13).

[CBB15] Castro, Ricardo de, Bünte, Tilman and Brembeck, Jonathan. “Design and Validation of the Second Generation of the Robomobil ’ s Vehicle Dynamics Controller”. In: *International Symposium on Dynamics of Vehicles on Road and Tracks*. 2015 (cit. on pp. 100–103).

[CFF05] Casavola, A, Famularo, D and Franze, G. “A robust deconvolution scheme for fault detection and isolation of uncertain linear systems: an LMI approach”. In: *Automatica* 41.8 (2005), pp. 1463–1472 (cit. on p. 55).

[CFF08] Casavola, Alessandro, Famularo, Domenico and Franzè, Giuseppe. “Robust fault detection of uncertain linear systems via quasi-LMIs”. In: *Automatica* 44 (2008), pp. 289–295 (cit. on p. 55).

[CG96] Chilali, Mahmoud and Gahinet, Pascal. “H-inf design with pole placement constraints: An LMI approach”. In: *IEEE Transactions on Automatic Control* 41.3 (1996), pp. 358–367 (cit. on p. 25).

[Che08] Chen, Xi. “Requirements and Concepts for Future Automotive Electronic Architectures from the View of Integrated Safety”. PhD thesis. Universität Fridericiana Karlsruhe, 2008 (cit. on p. 9).

[CMA91] Cormier R., Jr., Matsumura, T and Asano, M. “A New Method of Failure Detection and Isolation for Sensors and Actuators”. In: *Industrial Electronics, Control and Instrumentation, 1991. Proceedings. IECON ’91., 1991 International Conference on*. 2. Nov. 1991, 2139–2144 vol.3 (cit. on p. 16).

[CP99] Chen, Jie and Patton, Ron J. *Robust model-based fault diagnosis for dynamic systems*. Kluwer Academic Publishers, 1999 (cit. on pp. 7, 9, 11, 12, 50).

[CW84] Chow, E and Willsky, A. “Analytical redundancy and the design of robust failure detection systems”. In: *Automatic Control, IEEE Transactions on* 29.7 (1984), pp. 603–614 (cit. on pp. 11, 12).

[De 11] De Lira, S., Puig, V., Quevedo, J. and Husar, A. “LPV observer design for PEM fuel cell system: Application to fault detection”. In: *Journal of Power Sources* 196.9 (2011), pp. 4298–4305 (cit. on p. 13).

[DFD04] Ding, E.L., Fennel, H. and Ding, S.X. “Model-based diagnosis of sensor faults for ESP systems”. In: *Control Engineering Practice* 12.7 (2004), pp. 847–856 (cit. on pp. 15, 179–181, 201).

[Din00] Ding, S X, Jeinsch, T, Frank, P M and Ding, E L. “A unified approach to the optimization of fault detection systems”. In: *International Journal of Adaptive Control and Signal Processing* (2000), pp. 725–745 (cit. on p. 51).

[Din05] Ding, S.X., Schneider, S., Ding, E.L. and Rehm, A. “Fault tolerant monitoring of vehicle lateral dynamics stabilization systems”. In: *IEEE Conference on Decision and Control*. 2005 (cit. on p. 15).

[Din13] Ding, Steven X. *Model-Based Fault Diagnosis Techniques*. 2nd ed. Springer, 2013 (cit. on pp. 12, 14, 50, 52, 55, 73–76, 78).

[FD97] Frank, P M and Ding, X. “Survey of robust residual generation and evaluation methods in observer-based fault detection”. In: *Journal of Process Control* 7.6 (1997), pp. 403–424 (cit. on pp. 12, 14, 78).

[Fis07] Fischer, D., Börner, M., Schmitt, J. and Isermann, R. “Fault detection for lateral and vertical vehicle dynamics”. In: *Control Engineering Practice* 15.3 (2007), pp. 315–324 (cit. on pp. 15, 179–181, 201).

[FN01] Frisk, Erik and Nyberg, Mattias. “A minimal polynomial basis solution to residual generation for fault diagnosis in linear systems”. In: *Automatica* 37 (2001), pp. 1417–1424 (cit. on p. 166).

[FN06] Frisk, Erik and Nielsen, Lars. “Robust residual generation for diagnosis including a reference model for residual behavior”. In: *Automatica* 42.3 (Mar. 2006), pp. 437–445 (cit. on pp. 55, 57).

[Fra96] Frank, P.M. “Analytical and qualitative model-based fault diagnosis - a survey and some new results”. In: *European Journal of Control* 2 (1996), pp. 6–28 (cit. on p. 12).

[GAC96] Gahinet, Pascal, Apkarian, Pierre and Chilali, Mahmoud. “Affine parameter-dependent Lyapunov functions and real parametric uncertainty”. In: *IEEE Transactions on Automatic Control* 41.3 (1996), pp. 436–442 (cit. on p. 28).

[Gan77] Gantmacher, F.R. *The Theory of Matrices, Vol.I.* Chelsea Publishing Company, New York, 1977 (cit. on p. 40).

[Ger98] Gertler, Janos. *Fault Detection and Diagnosis in Engineering Systems.* CRC Press, 1998 (cit. on pp. 14, 52, 85–87).

[GGB09] Galli, G, Grasso, M and Bocchiola, C. *Protection circuit for permanent magnet synchronous motor in field weakening operation.* 2009 (cit. on p. 113).

[GHZ08] Grenaille, Sylvain, Henry, David and Zolghadri, Ali. “A method for designing fault diagnosis filters for LPV polytopic systems”. In: *Journal of Control Science and Engineering* 2008 (2008) (cit. on p. 13).

[GL15] Gordon, T.J. and Lidberg, M. “Automated driving and autonomous functions on road vehicles”. In: *Vehicle System Dynamics* 53.7 (2015), pp. 958–994 (cit. on p. 1).

[GM11] Goupil, Philippe and Marcos, Andres. “Advanced Diagnosis for Sustainable Flight Guidance and Control: The European ADDSAFE Project”. In: *SAE Technical Paper.* SAE International, 2011 (cit. on p. 2).

[GM95] Gertler, Janos and Monajemy, Ramin. “Generating Directional Residuals with Dynamic Parity Relations”. In: *Automatica* 31.4 (1995), pp. 627–635 (cit. on p. 14).

[GMP11] Gobbi, M., Mastinu, G. and Previati, G. “A method for measuring the inertia properties of rigid bodies”. In: *Mechanical Systems and Signal Processing* 25.1 (2011), pp. 305–318 (cit. on p. 144).

[Gou11] Goupil, Philippe. “AIRBUS state of the art and practices on FDI and FTC in flight control system”. In: *Control Engineering Practice* 19.6 (June 2011), pp. 524–539 (cit. on p. 8).

[Gou15] Goupil, Philippe, Boada-Bauxell, Josep, Marcos, Andres, Rosa, Paulo, Kerr, Murray and Dalbies, Laurent. “An overview of the FP7 RECONFIGURE project: Industrial, scientific and technological objectives”. In: *IFAC Proceedings Volumes (IFAC-PapersOnline)* 48.21 (2015), pp. 976–981 (cit. on p. 2).

[GR03] Ganguli, Ankur and Rajamani, Rajesh. “Fault Diagnostics for GPS-based Lateral Vehicle Control”. In: *Vehicle System Dynamics* 39.2 (Feb. 2003), pp. 99–120 (cit. on p. 16).

[GYG04] Gadda, Christopher D, Yih, Paul and Gerdes, J Christian. “Incorporating a Model of Vehicle Dynamics in a Diagnostic System for Steer-by-Wire Vehicles”. In: *AVEC*. 2004 (cit. on p. 16).

[HB16] Ho, Lok Man and Bünte, Tilman. “Sensor Fault Detection and Isolation using a Non-linear Planar Kinematic Model of Vehicle Dynamics”. In: *IEEE Multi-Conference on Systems and Control*. 2016 (cit. on pp. 17, 180).

[Hey99] Heydinger, Gary J., Bixel, Ronald a., Garrott, W. Riley, Pyne, Michael, Howe, J. Gavin and Guenther, Dennis a. “Measured Vehicle Inertial Parameters-NHTSA’s Data Through November 1998”. In: *SAE 1999 Transactions - Journal of Passenger Cars - V108-6* (1999) (cit. on p. 144).

[HH14] Hwang, Woohyun and Huh, Kunsoo. “Fault Detection and Estimation for Electromechanical Brake Systems Using Parity Space Approach”. In: *Journal of Dynamic Systems, Measurement, and Control* 137.1 (2014) (cit. on p. 110).

[HN03] Hugemann, Wolfgang and Nickel, Markus. “Longitudinal and Lateral Accelerations in Normal Day Driving”. In: *Proceedings of the Institute of Traffic Accident Investigators Conference (ITAI ’03)*. 2003 (cit. on p. 119).

[Ho13] Ho, Lok Man. “Structural Analysis of a Vehicle Dynamics Model for Fault Detection and Isolation on the ROboMObil”. In: *International Conference on Control and Fault-Tolerant Systems (SysTol)*. IEEE, 2013 (cit. on p. 103).

[HO14] Ho, Lok Man and Ossmann, Daniel. “Fault Detection and Isolation of Vehicle Dynamics Sensors and Actuators for an Overactuated X-by-Wire Vehicle”. In: *IEEE Conference on Decision and Control*. 2014 (cit. on pp. 15, 17, 229).

[Ho16] Ho, Lok Man. “H-infinity Structured Residual Generator Synthesis Using Residual Reference Models with Application to Lateral Vehicle Dynamics”. In: *European Control Conference*. 2016 (cit. on pp. 17, 48, 52, 154).

[Ho17] Ho, Lok Man. “Robust Residual Generator Synthesis for Uncertain LPV Systems Applied to Lateral Vehicle Dynamics”. In: *submitted to IEEE Transactions on Control Systems Technology* (2017) (cit. on pp. 17, 48, 154).

[HP96] Hou, M and Patton, Ron J. “An LMI Approach to H-/H_inf Fault Detection Filters”. In: *UKACC International Conference on Control*. 1996 (cit. on p. 51).

[HV06] Hecker, S. and Varga, A. “Symbolic manipulation techniques for low order LFT-based parametric uncertainty modelling”. In: *International Journal of Control* 79.11 (2006), pp. 1485–1494 (cit. on p. 30).

[HZ05] Henry, D. and Zolghadri, A. “Design of fault diagnosis filters: A multi-objective approach”. In: *Journal of the Franklin Institute* 342 (2005), pp. 421–446 (cit. on pp. 51, 55, 59).

[Int07] International Rectifier. *Data Sheet No. PD60347A, High Voltage 3 Phase Gate Driver IC with DC Bus Over Voltage Protection*. 2007 (cit. on p. 113).

[Ise06a] Isermann, Rolf. *Fahrdynamikregelung*. Springer Vieweg, 2006 (cit. on pp. 120, 133, 179).

[Ise06b] Isermann, Rolf. *Fault Diagnosis Systems*. Springer, 2006 (cit. on p. 10).

[ISO09] ISO. *Road vehicles Functional safety Part 10 : Guideline*. Tech. rep. 2009 (cit. on p. 8).

[ISS02] Isermann, Rolf, Schwarz, Ralf and Stölzl, Stefan. “Drive-by-Wire Systems Recent Devlopments Drive-by-Wire Structures with and Drive-by-Wire Systems”. In: *IEEE Control Systems Magazine* October (2002), pp. 64–81 (cit. on pp. 7, 9, 100, 115).

[IWI09] Isermann, R, Wesemeier, D and Isermann R., Wesemeier D. “Indirect Vehicle Tire Pressure Monitoring with Wheel and Suspension Sensors”. In: *7th IFAC Symposium on Fault Detection, Supervision and Safety of Technical Processes* (2009), pp. 917–922 (cit. on p. 2).

[JLM05] Jaimoukha, Imad M, Li, Zhenhai and Mazars, Emmanuel F M. “Linear Matrix Inequality Solution to the H-/H-infinity Fault Detection Problem”. In: *IASTED International Conference*. 2005, pp. 183–188 (cit. on p. 50).

[Joo02] Joos, Hans-dieter, Bals, Johann, Looye, Gertjan, Schnepper, Klaus and Varga, Andras. “A multi-objective optimisation-based software environment for control systems design”. In: *IEEE International Symposium on Computer Aided Control Design*. 2002 (cit. on p. 231).

[Jun15] Jung, Daniel, Khorasgani, Hamed, Frisk, Erik, Krysander, Mattias and Biswas, Gautam. “Analysis of fault isolation assumptions when comparing model-based design approaches of diagnosis systems”. In: *IFAC Symposium on Fault Detection, Supervision and Safety for Technical Processes (SAFEPROCESS)*. Elsevier Ltd., 2015 (cit. on pp. 52, 86).

[JW07] Jonasson, Mats and Wallmark, Oskar. “Stability of an electric vehicle with permanent-magnet in-wheel motors during electrical faults”. In: *World Electric Vehicle Journal* 1.1 (2007), pp. 100–107 (cit. on p. 113).

[JW08] Jonasson, Mats and Wallmark, Oskar. “Control of electric vehicles with autonomous corner modules: implementation aspects and fault handling”. In: *International Journal of Vehicle Systems Modelling and Testing* 3.3 (2008), pp. 213–228 (cit. on p. 9).

[Kab02] Kabbaj, N., Doncescu, A., Dahhou, B. and Roux, G. “Wavelet based residual evaluation for fault detection and isolation”. In: *Proceedings of the IEEE International Symposium on Intelligent Control* (2002) (cit. on p. 14).

[Kad02] Kadirkamanathan, V., Li, P., Jaward, M. H. and Fabri, S. G. "Particle filtering-based fault detection in non-linear stochastic systems". In: *International Journal of Systems Science* 33.4 (Jan. 2002), pp. 259–265 (cit. on p. 13).

[KAN08] Krysander, M, Aslund, J and Nyberg, M. "An Efficient Algorithm for Finding Minimal Overconstrained Subsystems for Model-Based Diagnosis". In: *Systems, Man and Cybernetics, Part A: Systems and Humans, IEEE Transactions on* 38.1 (2008), pp. 197–206 (cit. on pp. 11, 103).

[Kas06] Kashi, K, Nissing, D, Kesselgruber, D and Soffker, D. "Diagnosis of active dynamic control systems using virtual sensors and observers". In: *Mechatronics, 2006 IEEE International Conference on*. 2006, pp. 113–118 (cit. on p. 15).

[Kaw10] Kawashima, Kiyotaka, Uchida, Toshiyuki, Oh, Sehoon and Hori, Yoichi. "Robust bank angle estimation for rolling stability control on electric vehicle". In: *International Workshop on Advanced Motion Control, AMC* (2010), pp. 448–453 (cit. on p. 145).

[Khe11] Kheirandish, Azadeh, Husain, A Rashid, Kazemi, M Saeed, Gatavi, Ehsan and Ahmad, M Noh. "Robust fault detection and isolation of steer by wire system under various class of fault and system uncertainties". In: *4th International Conference on Modeling, Simulation and Applied Optimization (ICMSAO)*. 2011, pp. 3–6 (cit. on p. 16).

[Kho14] Khorasgani, Hamed, Jung, Daniel E, Biswas, Gautam, Frisk, Erik and Krysander, Mattias. "Robust Residual Selection for Fault Detection". In: *IEEE Conference on Decision and Control*. 2014 (cit. on p. 15).

[Kie53] Kiefer, J. "Sequential minimax search for a maximum". In: *Proceedings of the American Mathematical Society* 4.3 (1953), pp. 502–506 (cit. on p. 61).

[Kis16] Kistler. *Datasheet: Kistler Correvit S-HR Sensors - Non-Contact Optical Sensors*. 2016 (cit. on p. 98).

[KIT16] KIT. *OmniSteer*. 2016. URL: `http://www.share.kit.edu/omnisteer/` (visited on 20/09/2016) (cit. on p. 97).

[KM99] Krautstrunk, Alexander and Mutschler, P. "Fault Detection and Identification for Permanent Magnet Synchronous Motor Drives". In: *Proceedings of The International Intelligent Motion Conference*. Intertec International, Inc. 1999, pp. 161–166 (cit. on p. 108).

[KN02] Krysander, Mattias and Nyberg, Mattias. "Structural Analysis utilizing MSS Sets with Application to a Paper Plant". In: *Proc. 13th Int. Workshop Principles Diagnosis*. Department of Electrical Engineering. Semmering, Austria, 2002, pp. 51–57 (cit. on pp. 73, 85, 87–89, 103).

[KN05] Kiencke, Uwe and Nielsen, Lars. *Automotive Control Systems - for Engine, Driveline and Vehicle*. 2nd ed. Springer, 2005 (cit. on pp. 125, 126, 138).

[Kop94] Kopetz, Hermann. "A solution to an automotive control system benchmark". In: *Real-Time Systems Symposium*. 1994 (cit. on p. 9).

[Kop97] Kopetz, Hermann. *Real-Time Systems - Design Principles for Distributed Embedded Applications*. Kluwer Academic Publishers, 1997 (cit. on p. 7).

[LBC13] Lovera, Marco, Bergamasco, Marco and Casella, Francesco. "LPV Modelling and Identification: An Overview". In: *Robust Control and Linear Parameter Varying Approaches - Application to Vehicle Dynamics*. Ed. by Sename, Olivier, Gaspar, Peter and Bokor, Jozsef. Springer-Verlag, 2013. Chap. 1, pp. 3–24 (cit. on p. 23).

[LDD16] Linden, Franciscus Leendert Johannes, Dreyer, Nikolaus and Dorkel, André. "EMA Health Monitoring: An overview." In: *Recent Advances in Aerospace Actuation Systems and Components* (2016), pp. 21–26 (cit. on p. 109).

[Lea05] Leaphart, Eldon G, Czerny, Barbara J, Ambrosio, Joseph G D, Denlinger, Christopher L and Littlejohn, Deron. "Survey of Software Failsafe Techniques for Safety-Critical Automotive Applications". In: *SAE Technical Paper* 2005-01-07 (2005) (cit. on p. 111).

[Len14] Lenz, Tobias. "Modelling and Simulation of Component Faults in an X-by-Wire Electric Vehicle". MA thesis. Fachhochschule Köln, 2014 (cit. on p. 110).

[Leo68] Leondes, C.T., ed. *Advances in Control Systems: Theory and Applications*. 6th ed. Academic Press, New York, 1968 (cit. on p. 34).

[Liu06] Liu, Li. "Robust Fault Detection and Diagnosis for Permanent Magnet Synchronous Motors". PhD thesis. Florida State University, 2006 (cit. on p. 108).

[Lju99] Ljung, Lennart. *System identification - Theory for the User*. 2nd ed. Prentice-Hall, 1999 (cit. on pp. 145, 147).

[LL00] Leith, D. J. and Leithead, W. E. "Survey of gain-scheduling analysis and design". In: *International Journal of Control* 73 (2000), pp. 1001–1025 (cit. on pp. 13, 23).

[LMG04] Line, C., Manzie, C. and Good, M. "Control of an electromechanical brake for automotive brake-by-wire systems with an adapted motion control architecture". In: *SAE Technical Papers* (2004) (cit. on p. 139).

[Löf04] Löfberg, J. "YALMIP : A Toolbox for Modeling and Optimization in MATLAB". In: *Proceedings of the CACSD Conference*. Taipei, Taiwan, 2004 (cit. on p. 22).

[LS09] Lundquist, Christian and Schön, Thomas B. "Recursive Identification of Cornering Stiffness Parameters for an Enhanced Single Track Model". In: *IFAC Symposium on System Identification*. 2009, pp. 1726–1731 (cit. on p. 145).

[LSC10] Lii, Neal Y., Sturm, Stefan and Coombs, Timothy a. "Redundant Dissimilar Sensor Fusion with Dynamic Driver Input Classification and Graceful Degradation for Drive-by-Wire Applications". In: *2010 IEEE 71st Vehicular Technology Conference* (2010), pp. 1–5 (cit. on p. 9).

[LT10] Lin, Wei-song and Tang, Tao-en. “Active Safety Diagnosis of Brake-by-Wire Systems with Unscented Kalman Filter”. In: *IEEE International Conference on Vehicular Electronics and Safety (ICVES)*. 2010, pp. 1–6 (cit. on pp. 13, 16).

[Ma07] Ma, Yan. “Integrated design of observer based fault diagnosis systems and its application to vehicle lateral dynamic control systems”. PhD thesis. Universität Duisburg-Essen, 2007 (cit. on p. 15).

[Man95] Mangoubi, Rami S. “Robust Estimation and Failure Detection for Linear Systems.pdf”. PhD thesis. Massachusetts Institute of Technology, 1995 (cit. on p. 12).

[Mar12] Marzat, J., Piet-Lahanier, H., Damongeot, F. and Walter, E. “Model-based fault diagnosis for aerospace systems: a survey”. In: *Proceedings of the Institution of Mechanical Engineers, Part G: Journal of Aerospace Engineering* 226.10 (2012), pp. 1329–1360 (cit. on pp. 111, 142).

[Mas86] Massoumnia, Mohammad-Ali. “A geometric approach to the synthesis of failure detection filters”. In: *IEEE Transactions on Automatic Control* 31.9 (1986), pp. 839–846 (cit. on p. 12).

[MBI09] Muenchhof, Marco, Beck, Mark and Isermann, Rolf. “Fault-tolerant actuators and drivesStructures, fault detection principles and applications”. In: *Annual Reviews in Control* 33.2 (Dec. 2009), pp. 136–148 (cit. on pp. 8, 109).

[MR97] Megretski, Alexandre and Rantzer, Anders. “System analysis via integral quadratic constraints”. In: *IEEE Transactions on Automatic Control* 42.6 (1997), pp. 819–830 (cit. on pp. 31–35, 45).

[MVW89] Massoumnia, Mohammad-Ali, Verghese, George C and Willsky, Alan S. “Failure Detection and Identification”. In: *IEEE Transactions on Automatic Control* 34.3 (1989), pp. 316–321 (cit. on p. 49).

[MW04] Mitschke, Manfred and Wallentowitz, Henning. *Dynamik der Kraftfahrzeuge*. 4th ed. Springer Verlag, 2004 (cit. on p. 180).

[Nas10] Nasri, Othman, Shraim, Hassan, Dague, Philippe, Heron, Olivier and Cartron, Mickael. “Model-based decentralized embedded diagnosis inside vehicles: Application to Smart Distance Keeping function”. In: *Conference on Control and Fault-Tolerant Systems (SysTol)*. Oct. 2010, pp. 17–23 (cit. on p. 11).

[Nus13] Nussbaumer, P, Macek, C, Ploechl, M and Wolbank, T M. “Dynamics of four-wheel-drive electric vehicle during machine fault condition”. In: *15th European Conference on Power Electronics and Applications (EPE)*. 2013 (cit. on p. 108).

[Ore06] Orend, Ralf. “Integrierte Fahrdynamikregelung mit Einzelradaktorik: ein Konzept zur Darstellung des fahrdynamischen Optimums”. PhD thesis. Universität Erlangen-Nürnberg, 2006 (cit. on pp. 125, 130, 131, 133).

[Oss13] Ossmann, Daniel. “Fehlerdetektion, -Isolation und -Identifikation in elektrohydraulischen Aktuatorensystemen moderner, ziviler Flugzeuge”. PhD thesis. Technische Universität München, 2013 (cit. on pp. 75, 87).

[Oss14] Ossmann, Daniel. “Optimization Based Tuning of Fault Detection and Diagnosis Systems for Safety Critical Systems”. In: *IFAC World Congress*. 2014, pp. 8570–8575 (cit. on pp. 14, 75).

[OV09] Orchard, M. E. and Vachtsevanos, G. J. “A particle-filtering approach for online fault diagnosis and failure prognosis”. In: *Transactions of the Institute of Measurement and Control* 31.3-4 (June 2009), pp. 221–246 (cit. on p. 13).

[Oxf15] Oxford Technical Solutions. *Datasheet: RT4000 - GNS/INSS for high dynamic vehicle testing*. 2015 (cit. on p. 98).

[Pac02] Pacejka, H.B. *Tyre and Vehicle Dynamics*. Oxford: Society of Automotive Engineers and Butterworth-Heinemann, 2002 (cit. on pp. 131, 132).

[PFH12] Papageorgiou, Christos, Falkeborn, Rikard and Hansson, Anders. “IQC-Based Analysis Techniques for Clearance”. In: *Optimization Based Clearance of Flight Control Laws: A Civil Aircraft Application*. Ed. by Varga, Andreas and Puyou, Guilhem. 1st ed. Springer-Verlag, 2012. Chap. 10 (cit. on p. 46).

[PI01] Persis, C. De and Isidori, a. “A geometric approach to nonlinear fault detection and isolation”. In: *IEEE Transactions on Automatic Control* 46.6 (2001), pp. 853–865 (cit. on p. 49).

[Pre07] Press, William H., Teukolsky, Saul A., Vetterling, William T. and Flannery, Brian P. *Numerical Recipes - The Art of Scientific Computing*. 3rd. Cambridge University Press, 2007 (cit. on p. 61).

[PS14] Pfifer, Harald and Seiler, Peter. “Robustness analysis of linear parameter varying systems using integral quadratic constraints”. In: *International Journal of Robust and Nonlinear Control* (2014) (cit. on pp. 27, 34, 35).

[Puh87] Puhn, Fred. *Brake Handbook*. HP Trade, 1987, p. 176 (cit. on p. 110).

[Raj01] Rajamani, Rajesh, Howell, Adam S, Chen, Chieh, Hedrick, J Karl and Tomizuka, Masayoshi. “A complete fault diagnostic system for automated vehicles operating in a platoon”. In: *IEEE Transactions on Control Systems Technology* 9.4 (July 2001), pp. 553–564 (cit. on p. 16).

[Rei06] Reichel, R, Armbruster, M, Zimmer, E, Tjaden, H, Mutikani, W, Gandhi, S, Sulzmann, A and Spiegelberg, G. “FlexRay Communication Protocol for an Innovative Scalable X-by-Wire Platform”. In: *2nd Conference Active Safety through Driver Assistance*. 2006 (cit. on p. 111).

[Ril13] Rill, Georg. “TMeasy A Handling Tire Model based on a three-dimensional slip approach”. In: *Proceedings of the XXIII International Symposium on Dynamics of Vehicles on Roads and Tracks (IAVSD2013)*. Quingdao, China, 2013 (cit. on p. 131).

[Rit13] Ritzer, Peter. “Model Based Vehicle Dynamics Control For Modern Vehicle Architectures”. MA thesis. 2013 (cit. on p. 102).

[RN99] Rank, Mike Lind and Niemann, Henrik. “Norm based design of fault detectors”. In: *International Journal of Control* 72.9 (1999), pp. 773–783 (cit. on pp. 51, 53, 55, 60, 61).

[Rod13] Rodrigues, Mickael, Sahnoun, Mariem, Theilliol, Didier and Ponsart, Jean Christophe. “Sensor fault detection and isolation filter for polytopic LPV systems: A winding machine application”. In: *Journal of Process Control* 23.6 (2013), pp. 805–816 (cit. on p. 13).

[RS00] Rugh, Wilson J and Shamma, Jeff S. “Research on gain scheduling”. In: *Automatica* 36 (2000), pp. 1401–1425 (cit. on pp. 13, 23).

[RS14] Ridley, Justin and Stefula, Denise M. “The MRV: Next-Gen Automobile?” In: *NASA Game On Annual Magazine* (2014) (cit. on p. 97).

[RTC05] RTCA. *DO-297 Integrated Modular Avionics (IMA) Development Guidance and Certification Considerations*. 2005 (cit. on p. 1).

[RWT16] RWTH Aachen. *SpeedE*. 2016. URL: `https://www.ika.rwth-aachen.de/en/research/projects/e-mobility/1863-speede.html` (visited on 20/09/2016) (cit. on p. 97).

[SB17] Schaub, Alexander and Burschka, Darius. “Single Point Velocity Estimation from Pseudo-Stereo”. In: 2017 (cit. on p. 98).

[Sch01] Scherer, C. W. “LPV control and full block multipliers”. In: *Automatica* 37.3 (2001), pp. 361–375 (cit. on p. 28).

[Sch05] Schulz, Hans-Gerd. “Modellgestüztzte Fehlerdiagnose der Sensoren für die Fahrzeug-Querdynamik”. PhD thesis. Universität Duisburg-Essen, 2005 (cit. on pp. 13, 15).

[Sch11] Schaub, Alexander, Brembeck, Jonathan, Burschka, Darius and Hirzinger, Gerd. “Robotic Electric Vehicle with Camera-Based Autonomy Approach”. In: *ATZ Elektronik* (Feb. 2011), pp. 4–9 (cit. on p. 181).

[Sei15] Seiler, Peter. “Stability Analysis with Dissipation Inequalities and Integral Quadratic Constraints”. In: *IEEE Transactions on Automatic Control* 60.6 (2015), pp. 1704–1709 (cit. on pp. 32, 34).

[SGC97] Scherer, Carsten, Gahinet, Pascal and Chilali, Mahmoud. “Multiobjective output-feedback control via LMI optimization”. In: *IEEE Transactions on Automatic Control* 42.7 (1997), pp. 896–911 (cit. on p. 25).

[SK05] Schaefer, Ingolf and Kayser, Andreas. “Smart EMA: An approach to avoid unscheduled maintenance”. In: *AIAA 5th Aviation, Technology, Integration, and Operations Conference (ATIO)*. 2005 (cit. on p. 109).

[SK08] Scherer, Carsten W. and Köse, I. Emre. “Robustness with dynamic IQCs: An exact state-space characterization of nominal stability with applications to robust estimation”. In: *Automatica* 44.7 (2008), pp. 1666–1675 (cit. on pp. 40, 45).

[SK16] Siciliano, Bruno and Khatib, Oussama (Eds.) *Springer Handbook of Robotics*. 2nd ed. Springer-Verlag Berlin-Heidelberg, 2016 (cit. on p. 1).

[SN10] Svärd, Carl and Nyberg, Mattias. “Residual Generators for Fault Diagnosis Using Computation Sequences With Mixed Causality Applied to Automotive Systems”. In: *IEEE Transactions on Systems, Man, and Cybernetics* 40.6 (2010), pp. 1310–1328 (cit. on p. 103).

[SNF11] Svärd, Carl, Nyberg, Mattias and Frisk, Erik. “A Greedy Approach for Selection of Residual Generators”. In: *22nd International Workshop on Principles of Diagnosis (DX-11), Murnau, Germany*. 2011, pp. 1–8 (cit. on p. 89).

[SNF13] Svärd, Carl, Nyberg, Mattias and Frisk, Erik. “Realizability Constrained Selection of Residual Generators for Fault Diagnosis with an Automotive Engine Application”. In: *IEEE Transactions on Systems, Man and Cybernetics: Systems* 43.6 (2013), pp. 1354–1369 (cit. on p. 15).

[SW05] Scherer, Carsten W. and Weiland, Siep. *Linear Matrix Inequalities in Control*. November. 2005 (cit. on p. 25).

[Tad12] Tadday, Sebastian. “Improvement of the vehicle dynamics of an electrical car by using torque vectoring - Diploma Thesis”. MA thesis. Munich University of Applied Sciences, 2012 (cit. on p. 145).

[TB06] Thomsen, J S and Blanke, M. “Fault-tolerant actuator system for electrical steering of vehicles”. In: *IEEE Industrial Electronics, IECON 2006 - 32nd Annual Conference on*. Paris, France, 2006, pp. 3597–3602 (cit. on p. 109).

[Tjø08] Tjønnås, Johannes. “Nonlinear and Adaptive Dynamic Control Allocation”. PhD thesis. Norwegian University of Science and Technology, 2008 (cit. on p. 102).

[Tou05] Touloupis, Emmanuel, Flint, James A, Chouliaras, Vassilios A and Ward, David D. “A Fault-Tolerant Processor Core Architecture for Safety-Critical Automotive Applications”. In: *SAE Technical Paper*. SAE International, 2005 (cit. on p. 9).

[Uys06] Uys, P.E., Els, P.S., Thoresson, M.J., Voigt, K.G. and Combrinck, W.C. “Experimental Determination of Moments of Inertia for an Off-Road Vehicle in a Regular Engineering Laboratory”. In: *International Journal of Mechanical Engineering Education* 34.4 (2006), pp. 291–314 (cit. on p. 144).

[Van11] Vanek, Bálint, Seiler, Peter, Bokor, József and Balas, Gary J. “Robust model matching for geometric fault detection filters: a commercial aircraft example”. In: *IFAC Proceedings Volumes (IFAC-PapersOnline)* 18.1 (2011), pp. 7256–7261 (cit. on p. 57).

[Var07] Varga, Andras. “On Designing Least Order Residual Generators for Fault Detection and Isolation”. In: *16th International Conference on Control Systems and Computer Science*. Bucharest, Romania, 2007 (cit. on pp. 49, 85).

[Var11a] Varga, Andras. *Linear FDI-Techniques and Software Tools*. Tech. rep. DLR, 2011 (cit. on p. 15).

[Var11b] Varga, Andras. “On Parametric Solution of Fault Detection Problems”. In: *IFAC World Congress*. Ed. by Sergio, Bittanti. Aug. 2011, pp. 6697–6702 (cit. on p. 14).

[Var11c] Varga, Andras. “Synthesis of robust gain scheduling based fault detection filters for a class of parameter uncertain nonlinear systems”. In: *Control and Automation (MED), 19th Mediterranean Conference on*. 2011, pp. 467–472 (cit. on p. 13).

[Vie12] Viehweider, Alexander, Nam, Kanghyun, Fujimoto, Hiroshi and Hori, Yoichi. “A Fault Detection and Isolation Scheme for Lateral Vehicle Dynamics of EVs using a Quantitative Parity Space Approach”. In: *IECON 2012 - 38th Annual Conference on IEEE Industrial Electronics Society*. 2012, pp. 4630–4636 (cit. on p. 16).

[VKM14] Varrier, Sébastien, Koenig, Damien and Martinez, John J. “Robust fault detection for uncertain unknown inputs LPV system”. In: *Control Engineering Practice* 22 (2014), pp. 125–134 (cit. on pp. 13, 16, 159).

[VO14] Varga, Andreas and Ossmann, Daniel. “LPV model-based robust diagnosis of flight actuator faults”. In: *Control Engineering Practice* 31 (2014), pp. 135–147 (cit. on p. 13).

[VOJ14] Varga, A., Ossmann, D. and Joos, H. D. “A fault diagnosis based reconfigurable longitudinal control system for managing loss of air data sensors for a civil aircraft”. In: *IFAC World Congress*. 2014, pp. 3489–3496 (cit. on pp. 8, 103).

[VS16] Venkataraman, Raghu and Seiler, Peter. “Robust LPV Estimator Synthesis Using Integral Quadratic Constraints”. In: *American Control Conference*. 2016 (cit. on pp. 37, 39, 40, 43).

[Wan13] Wanner, Daniel. “Faults and their influence on the dynamic behaviour of electric vehicles - Licentiate Thesis”. MA thesis. KTH, 2013 (cit. on p. 113).

[Wan15] Wanner, Daniel. “Controlling over-actuated road vehicles during failure conditions”. PhD thesis. KTH, 2015 (cit. on p. 9).

[WDT14] Wanner, Daniel, Drugge, Lars and Trigell, Annika Stensson. “Fault classification method for the driving safety of electrified vehicles”. In: *Vehicle System Dynamics* 52.5 (Apr. 2014), pp. 704–732 (cit. on pp. 108, 115).

[WI09] Wesemeier, Daniel and Isermann, Rolf. “Identification of vehicle parameters using stationary driving maneuvers”. In: *Control Engineering Practice* 17.12 (2009), pp. 1426–1431 (cit. on pp. 145, 148).

[Wil05] Wilwert, Cedric, Navet, Nicolas, Song, Ye Qiong and Simonot-Lion, Francoise. "Design of Automotive X-by-Wire Systems". In: *The Industrial Communication Technology Handbook*. CRC Press, 2005 (cit. on pp. 9, 111).

[Wu95] Wu, Fen. "Control of Linear Parameter Varying Systems". PhD thesis. University of California at Berkeley, 1995 (cit. on pp. 23, 28).

[Wu96] Wu, F, Yang, X H, Packard, A and Becker, G. "Induced L2-norm control for LPV systems with bounded parameter variation rates". In: *International Journal of Robust and Nonlinear Control* 6 (1996), pp. 983–998 (cit. on p. 24).

[WYL07] Wang, Jian Liang, Yang, Guang Hong and Liu, Jian. "An LMI approach to H- index and mixed H- / Hinf fault detection observer design". In: *Automatica* 43 (2007), pp. 1656–1665 (cit. on pp. 50, 55).

[Xu15] Xu, Jin, Yang, Kui, Shao, Yi Ming and Lu, Gong Yuan. "An experimental study on lateral acceleration of cars in different environments in sichuan, southwest China". In: *Discrete Dynamics in Nature and Society* (2015) (cit. on p. 120).

[YDW02] Ye, Hao, Ding, S X and Wang, Guizeng. "Integrated Design of Fault Detection Systems in Time-Frequency Domain". In: *IEEE Transactions on Automatic Control* 47.2 (2002), pp. 2368–2373 (cit. on p. 14).

[YJ04] You, Song and Jalics, Laci. "Hierarchical Component-based Fault Diagnostics for By-Wire Systems". In: *SAE 2004 World Congress & Exhibition*. 2004 (cit. on pp. 11, 112–114).

[ZA08] Zheng, Bing and Anwar, Sohel. "Fault-Tolerant Control of the Road Wheel Subsystem in a Steer-By-Wire System". In: *International Journal of Vehicular Technology* 2008 (2008), pp. 1–8 (cit. on p. 9).

[ZDG95] Zhou, Kemin, Doyle, John C. and Glover, Keith. *Robust and Optimal Control*. 1st ed. Pearson, 1995, p. 596 (cit. on pp. 29, 30).

[ZF16] ZF. *ZF Advanced Urban Vehicle*. 2016. URL: `https://www.zf.com/corporate/en_de/products/technologietrends/smart_urban_vehicle/advanced_urban_vehicle.html` (visited on 20/09/2016) (cit. on p. 97).

[Zha14] Zhang, Hui, Huang, Xiaoyu, Wang, Junmin and Karimi, Hamid Reza. "Robust energy-to-peak sideslip angle estimation with applications to ground vehicles". In: *Mechatronics* (2014) (cit. on pp. 159, 160).

[ZP09] Zhang, Xian and Pisu, Pierluigi. "Model-based fault diagnosis for a vehicle chassis system". In: *2009 American Control Conference*. 2009, pp. 1116–1121 (cit. on p. 15).